Ministry of Education and Science of the Russian Federation
Saint Petersburg National Research University of Information
Technologies, Mechanics, and Optics

NANOSYSTEMS:

PHYSICS, CHEMISTRY, MATHEMATICS

2019, volume 10(2)

Наносистемы: физика, химия, математика

2019, том 10, № 2

NANO Ф&Х&М

NANOSYSTEMS:

PHYSICS, CHEMISTRY, MATHEMATICS

Address: University ITMO, Kronverkskiy pr., 49, St. Petersburg 197101, Russia.
Phone: +7(812)232-67-65, **Journal site:** http://nanojournal.ifmo.ru/,
E-mail: popov1955@gmail.com

AIM AND SCOPE

The scope of the journal includes all areas of nano-sciences. Papers devoted to basic problems of physics, chemistry, material science and mathematics inspired by nanosystems investigations are welcomed. Both theoretical and experimental works concerning the properties and behavior of nanosystems, problems of its creation and application, mathematical methods of nanosystem studies are considered.

The journal publishes scientific reviews (up to 30 journal pages), research papers (up to 15 pages) and letters (up to 5 pages). All manuscripts are peer-reviewed. Authors are informed about the referee opinion and the Editorial decision.

CONTENT

NANOSYSTEMS: PHYSICS, CHEMISTRY, MATHEMATICS, 2019, 10 (2), P. 115–123

Inverse dynamic problem for the wave equation with periodic boundary conditions

A. S. Mikhaylov[1,2], V. S. Mikhaylov[1,2]

[1]Saint Petersburg Department of V. A. Steklov Institute of Mathematics of the Russian Academy of Sciences, 7, Fontanka, Saint Petersburg, 191023 Russia

[2]Saint Petersburg State University, 7/9 Universitetskaya nab., Saint Petersburg, 199034 Russia

mikhaylov@pdmi.ras.ru, vsmikhaylov@pdmi.ras.ru

DOI 10.17586/2220-8054-2019-10-2-115-123

We consider the inverse dynamic problem for the wave equation with a potential on an interval $(0, 2\pi)$ with periodic boundary conditions. We use a boundary triplet to set up the initial-boundary value problem. As inverse data we use a response operator (dynamic Dirichlet-to-Neumann map). Using the auxiliary problem on the whole line, we derive equations of the inverse problem. We also establish the relationships between dynamic and spectral inverse data.

Keywords: inverse problem, Boundary Control method, Schrödinger operator.

Received: 10 January 2019

Revised: 24 January 2019

1. Introduction

Inverse problems for one-dimensional continuous and discrete systems plays an important role for the creation of new nano-devices, to mention just [1, 2] and references therein. In the present paper, we set up and study the inverse dynamic problem for a wave equation with a potential on an interval with periodic boundary conditions. The control problems for dynamical systems for wave equation with periodic boundary conditions (the density allows certain dependence on time) were considered in [3, 4]. The spectral problem for a Schrödinger operator on an interval with periodic and anti-periodic boundary conditions are used for treating the spectral problem for a Schrödinger operator with periodic potential on $\mathbb{R}$, see [5]. The inverse spectral problem with periodic boundary conditions for Schrödinger operator plays an important role for studying inverse problems on graphs with cycles [6].

In the previous papers by the authors, the "dynamic" approach to inverse spectral problems based on ideas of the Boundary Control method [7, 8] was developed in the cases of Schrödinger operator on a half-line [9–12] and finite and semi-infinite Jacobi matrices [13, 14]. We believe that our "dynamic" methods will help us to establish new relationships and develop new tools for studying the inverse problems with periodic potential, and will also stimulate studying inverse problems on graphs with cycles [6, 15].

For a potential $q \in C^2(0, 2\pi)$ we consider an operator H in $L_2(0, 2\pi)$ given by:

$$(Hf)(x) = -f''(x) + q(x)f(x), \quad x \in (0, 2\pi),$$
$$\operatorname{dom} H = \left\{ f \in H^2(0, 2\pi) \,|\, f(0) = f'(0) = f(2\pi) = f'(2\pi) = 0 \right\}.$$

Then

$$(H^*f)(x) = -f''(x) + q(x)f(x), \quad x \in (0, 2\pi),$$
$$\operatorname{dom} H^* = \left\{ f \in H^2(0, 2\pi) \right\}.$$

For a continuous function g we introduce the notations:

$$g_0 := \lim_{\varepsilon \to 0} g(0 + \varepsilon), \quad g_{2\pi} := \lim_{\varepsilon \to 0} g(2\pi - \varepsilon).$$

Let $B := \mathbb{R}^2$. The *boundary operators* $\Gamma_{0,1} : \operatorname{dom} H^* \mapsto B$ are introduced by the rules:

$$\Gamma_0 w := \begin{pmatrix} w_0 - w_{2\pi} \\ w'_0 - w'_{2\pi} \end{pmatrix}, \quad \Gamma_1 w := \frac{1}{2} \begin{pmatrix} w'_0 + w'_{2\pi} \\ -w_0 - w_{2\pi} \end{pmatrix}.$$

Integration by parts for $u, v \in \operatorname{dom} H^*$ shows that the abstract second Green identity holds:

$$(H^*u, v)_{L_2(0,2\pi)} - (u, H^*v)_{L_2(0,2\pi)} = (\Gamma_1 u, \Gamma_0 v)_B - (\Gamma_0 u, \Gamma_1 v)_B.$$

The mapping

$$\Gamma := \begin{pmatrix} \Gamma_0 \\ \Gamma_1 \end{pmatrix} : \operatorname{dom} H^* \mapsto B \times B$$

is surjective. Then a triplet $\{B, \Gamma_0, \Gamma_1\}$ is a *boundary triplet* for H^* (see [16]).

Let $T > 0$ be fixed. We use the triplet $\{B, \Gamma_0, \Gamma_1\}$ to set up the following initial-boundary value problem:

$$\begin{cases} u_{tt} + H^* u = 0, \quad t > 0, \\ (\Gamma_0 u)(t) = \begin{pmatrix} f_1(t) \\ f_2'(t) \end{pmatrix}, \quad t > 0, \\ u(\cdot, 0) = u_t(\cdot, 0) = 0. \end{cases} \tag{1}$$

Here the vector function $F = \begin{pmatrix} f_1 \\ f_2 \end{pmatrix}$, $f_1\, f_2 \in L_2(0, T)$, is interpreted as a *boundary control*. The solution to (1) is denoted by u^F. The *response operator* is introduced by the rule

$$\left(R^T F\right)(t) := \left(\Gamma_1 u^F\right)(t), \quad t > 0.$$

The speed of the wave propagation in the system (1) equal to one, which is why the natural set up of the dynamic inverse problem (IP) is to find a potential $q(x)$, $x \in (0, 2\pi)$ from the knowledge of a response operator $R^{2\pi}$ (see also [7, 8, 17, 18]).

In the second section, we derive the representation formula for the solution u^F, introduce the auxiliary dynamical system on the real line (see also [19]), and use the finiteness of the speed of wave propagation to establish relationships between the problem with periodic boundary conditions and problem on $\mathbb{R}$. In the third section, on the basis of this relationship, we obtain the suitable version of Krein and Gelfand-Levitan equations of the dynamic inverse problem. In the last section we derive the spectral representation of the response operator and dynamic representation of a Weyl function associated with $\{B, \Gamma_0, \Gamma_1\}$.

2. Forward problem, auxiliary dynamical system

We introduce the *outer space* of the system (1), the space of controls as $\mathcal{F}^T := L_2(0, T; \mathbb{R}^2)$, $F \in \mathcal{F}^T$, $F = \begin{pmatrix} f_1 \\ f_2 \end{pmatrix}$. By q we also denote the same potential, periodically continued to the whole real line: $q(x+2\pi) = q(x)$, $x \in \mathbb{R}$.

Theorem 1. *The solution to (1) with a control $F \in \mathcal{F}^T \cap C_0^\infty(\mathbb{R}_+)$, admits the following representation:*

1) *For $0 < t < 2\pi$*

$$\begin{aligned} u^F(x,t) &= u_1^{F_+}(x,t) + u_1^{F_-}(x,t) \\ &= \frac{1}{2} f_1(t-x) - \frac{1}{2} f_2(t-x) + \int_x^t w_1^0(x,s) f_1(t-s) + w_2^0(x,s) f_2(t-s)\, ds \\ -\frac{1}{2} f_1(t+x-2\pi) - \frac{1}{2} f_2(t+x-2\pi) &+ \int_{2\pi-x}^t w_1^{2\pi}(x,s) f_1(t-s) + w_2^{2\pi}(x,s) f_2(t-s)\, ds. \end{aligned} \tag{2}$$

where kernels $w_{1,2}^{0,2\pi}(x,t)$ *satisfy the following Goursat problems:*

$$\begin{cases} w_{1\,tt}^{0}(x,t) - w_{1\,xx}^{0}(x,t) + q(x)w_1^0(x,t) = 0, \quad 0 < x < t, \\ \dfrac{d}{dx}w_1^0(x,x) = -\dfrac{q(x)}{4}, \quad x > 0, \\ {w_1^{2\pi}}_{tt}(x,t) - {w_1^{2\pi}}_{xx}(x,t) + q(x)w_1^{2\pi}(x,t) = 0, \quad 0 < 2\pi - x < t, \\ \dfrac{d}{dx}w_1^{2\pi}(x,2\pi - x) = -\dfrac{q(x)}{4}, \quad x > 0, \\ w_1^0(0,s) = w_1^{2\pi}(2\pi,s), \\ w_{1\,x}^{0}(0,s) = {w_1^{2\pi}}_{x}(2\pi,s). \end{cases} \tag{3}$$

$$\begin{cases} w_{2\,tt}^{0}(x,t) - w_{2\,xx}^{0}(x,t) + q(x)w_2^0(x,t) = 0, \quad 0 < x < t, \\ \dfrac{d}{dx}w_2^0(x,x) = \dfrac{q(x)}{4}, \quad x > 0, \\ {w_2^{2\pi}}_{tt}(x,t) - {w_2^{2\pi}}_{xx}(x,t) + q(x)w_2^{2\pi}(x,t) = 0, \quad 0 < 2\pi - x < t, \\ \dfrac{d}{dx}w_2^{2\pi}(x,2\pi - x) = -\dfrac{q(x)}{4}, \quad x > 0, \\ w_2^0(0,s) = w_2^{2\pi}(2\pi,s), \\ w_{2\,x}^{0}(0,s) = {w_2^{2\pi}}_{x}(2\pi,s). \end{cases} \tag{4}$$

2) *On* $0 < t < 4\pi$

$$\begin{aligned} u^F(x,t) &= u_1^{F_+}(x,t) + u_1^{F_-}(x,t) + u_2^{F_+}(x,t) + u_2^{F_-}(x,t) \\ &= \frac{1}{2}f_1(t-x) - \frac{1}{2}f_2(t-x) + \int_x^t w_1^0(x,s)f_1(t-s) + w_2^0(x,s)f_2(t-s)\,ds \\ -\frac{1}{2}f_1(t+x-2\pi) &- \frac{1}{2}f_2(t+x-2\pi) + \int_{2\pi-x}^t w_1^{2\pi}(x,s)f_1(t-s) + w_2^{2\pi}(x,s)f_2(t-s)\,ds \\ &+ \frac{1}{2}f_1(t-2\pi-x) - \frac{1}{2}f_2(t-2\pi-x) \\ &+ \int_x^{t-2\pi} \widetilde{w}_1^0(x,s)f_1(t-2\pi-s) + \widetilde{w}_2^0(x,s)f_2(t-2\pi-s)\,ds \\ &- \frac{1}{2}f_1(t+x-4\pi) - \frac{1}{2}f_2(t+x-4\pi) \\ &+ \int_{2\pi-x}^{t-2\pi} \widetilde{w}_1^{2\pi}(x,s)f_1(t-2\pi-s) + \widetilde{w}_2^{2\pi}(x,s)f_2(t-2\pi-s)\,ds. \end{aligned}$$

where the integral kernels $w_{1,2}^{0,2\pi}$, $\widetilde{w}_{1,2}^{0,2\pi}$ *satisfy certain Goursat problems and the following compatibility conditions:*

$$\begin{aligned} w_{1,2}^0(0,s) = w_{1,2}^{2\pi}(2\pi,s),\ {w_{1,2}^0}_x(0,s) = {w_{1,2}^{2\pi}}_x(2\pi,s), \quad 0 < s < 4\pi, \\ w_{1,2}^0(2\pi,s) = \widetilde{w}_{1,2}^0(0,s-2\pi),\ {w_{1,2}^0}_x(2\pi,s) = {\widetilde{w}_{1,2}^0}_x(0,s-2\pi), \quad 0 < s < 4\pi, \\ w_{1,2}^{2\pi}(0,s) = \widetilde{w}_{1,2}^{2\pi}(2\pi,s-2\pi),\ {w_{1,2}^{2\pi}}_x(0,s) = {\widetilde{w}_{1,2}^{2\pi}}_x(2\pi,s-2\pi), \quad 0 < s < 4\pi. \end{aligned}$$

3) *On* $0 < t < 2n\pi$, $n > 1$:

$$u^F(x,t) = u_1^{F_+}(x,t) + u_1^{F_-}(x,t) + \ldots + u_n^{F_+}(x,t) + u_n^{F_-}(x,t), \tag{5}$$

where

$$\begin{aligned} u_k^{F_+}(x,t) &= \frac{1}{2}f_1(t-x-2(k-1)\pi) - \frac{1}{2}f_2(t-x-2(k-1)\pi) \\ &+ \int_{x+2(k-1)\pi}^t w_1(x+2(k-1)\pi,s)f_1(t-s) + w_2(x+2(k-1)\pi,s)f_2(t-s)\,ds \\ u_k^{F_-}(x,t) &= -\frac{1}{2}f_1(t+x-2k\pi) - \frac{1}{2}f_2(t+x-2k\pi) \\ &+ \int_{2k\pi-x}^t w_1(x-2k\pi,s)f_1(t-s) + w_2(x-2k\pi,s)f_2(t-s)\,ds \end{aligned}$$

and kernels $w_{1,2}$ satisfy the following Goursat problem:

$$\begin{cases} w_{1tt}(x,t) - w_{1xx}(x,t) + q(x)w_1(x,t), \quad 0 < |x| < t < 2n\pi, \\ \dfrac{d}{dx}w_1(x,x) = -\dfrac{q(x)}{4}, \quad x > 0, \\ \dfrac{d}{dx}w_1(x,-x) = -\dfrac{q(x)}{4}, \quad x < 0, \end{cases} \tag{6}$$

$$\begin{cases} w_{2tt}(x,t) - w_{2xx}(x,t) + q(x)w_2(x,t), \quad 0 < |x| < t < 2n\pi, \\ \dfrac{d}{dx}w_2(x,x) = \dfrac{q(x)}{4}, \quad x > 0, \\ \dfrac{d}{dx}w_2(x,-x) = -\dfrac{q(x)}{4}, \quad x < 0. \end{cases} \tag{7}$$

Several remarks have to be made.

Remark 1. *The proof of the representation (2) is straightforward and similar to one in [19]. If $F \in \mathcal{F}^T$, the function u^F defined by (2) is a generalized solution to (1) for $t \in (0, 2\pi)$.*

Remark 2. *The compatibility conditions in (3), (4) is used in the next subsection to relate the solution of the problem with periodic boundary conditions with one of the problem on the whole line.*

Since we consider the periodic boundary conditions, sometimes it would be convenient for us to interpret the interval as a ring:

Remark 3. *The compatibility conditions in 2) allows one to construct the "general" Goursat problems in 3). The physical meaning of the representation (5) is clear: the members of the sum indexed with "+" corresponds to waves that move clockwise, ones indexed with "−" correspond to waves moving counterclockwise.*

The *response operator* $R^T : \mathcal{F}^T \mapsto \mathcal{F}^T$ with the domain $D_R = \left\{\mathcal{F}^T \cap C_0^\infty(0,T;\mathbb{R}^2)\right\}$ is defined by the rule

$$(R^T F)(t) := \left(\Gamma_1 u^F\right)(t), \quad 0 < t < T.$$

Representation (2) implies the following

Corollary 1. *The response operator has a form:*

1) *on an interval $(0, 2\pi)$:*

$$\left(R^T F\right)(t) = -\frac{1}{2}\begin{pmatrix} f_1'(t) \\ -f_2(t) \end{pmatrix} + R * \begin{pmatrix} f_1 \\ f_2 \end{pmatrix}. \tag{8}$$

where

$$R(t) := \begin{pmatrix} r_{11}(t) & r_{12}(t) \\ r_{21}(t) & r_{22}(t) \end{pmatrix} = \begin{pmatrix} w_{1x}^0(0,t) & w_{2x}^0(0,t) \\ -w_1^0(0,t) & -w_2^0(0,t) \end{pmatrix} = \begin{pmatrix} w_1^{2\pi}{}_x(0,t) & w_2^{2\pi}{}_x(0,t) \\ -w_1^{2\pi}(0,t) & -w_2^{2\pi}(0,t) \end{pmatrix}$$

is a response matrix*,*

2) *on an interval $(0, 2n\pi)$:*

$$\left(R^T F\right)(t) = \left(-\frac{1}{2}\sum_{k=1}^{n}\begin{pmatrix} \delta'(t-2k\pi) & 0 \\ 0 & -\delta(t-2k\pi) \end{pmatrix} + \widetilde{R}(t)\right) * \begin{pmatrix} f_1 \\ f_2 \end{pmatrix}, \tag{9}$$

where the integral kernel $\widetilde{R}$ is expressed in terms of solutions to Goursat problems (6), (7).

Remark 4. *Due to the finite speed of wave propagation in system (1), the natural set up of IP is to recover the potential on $(0, 2\pi)$ from $R^{2\pi}$, that is why, for solving IP we can consider the system for times less or equal 2π.*

2.1. Auxiliary problem on $\mathbb{R}$

We introduce the the potential $\widetilde{q}$ by the rule

$$\widetilde{q}(x) = \begin{cases} q(x), \quad 0 < x < 2\pi, \\ 0, \quad x > 2\pi, \\ q(x+2\pi), \quad -2\pi < x < 0, \\ 0, \quad x < -2\pi, \end{cases} \tag{10}$$

For this potential, we consider an operator $\widetilde{H}$ in $L_2(\mathbb{R})$ given by:

$$(\widetilde{H}f)(x) = -f''(x) + \widetilde{q}(x)f(x), \quad x \in \mathbb{R},$$
$$\operatorname{dom}\widetilde{H} = \left\{f \in H^2(\mathbb{R}) \,|\, f(0) = f'(0) = 0\right\}.$$

Then:

$$(\widetilde{H}^*f)(x) = -f''(x) + \widetilde{q}(x)f(x), \quad x \in \mathbb{R},$$
$$\operatorname{dom}\widetilde{H}^* = \left\{f \in L_2(\mathbb{R}) \,|\, f \in H^2(-\infty,0),\, f \in H^2(-\infty,0)\right\}.$$

For a continuous function g we denote:

$$g_\pm := \lim_{\varepsilon\to 0} g(0 \pm \varepsilon).$$

The *boundary operators* $\widetilde{\Gamma}_{0,1} : \operatorname{dom} H^* \mapsto B$ are introduced by the rules

$$\widetilde{\Gamma}_0 w := \begin{pmatrix} w_+ - w_- \\ w'_+ - w'_- \end{pmatrix}, \quad \widetilde{\Gamma}_1 w := \frac{1}{2}\begin{pmatrix} w'_+ + w'_- \\ -w_+ - w'_- \end{pmatrix}.$$

We consider the initial boundary value problem for an auxiliary dynamical system on $\mathbb{R}$:

$$\begin{cases} v_{tt} + v_{xx} + \widetilde{q}v = 0, \quad x \in \mathbb{R}, \quad 0 < t < 2\pi, \\ (\Gamma_0 v)(t) = \begin{pmatrix} f_1(t) \\ f'_2(t) \end{pmatrix}, \quad 0 < t < 2\pi, \\ v(\cdot,0) = v_t(\cdot,0) = 0. \end{cases} \tag{11}$$

In [19] the dynamic IP for (11) was studied, where as a inverse data the authors used the *response operator*, introduced by the rule:

$$\left(\widetilde{R}^T F\right)(t) := \left(\widetilde{\Gamma}_1 v^F\right)(t), \quad t > 0.$$

On comparing the representation (2) with one obtained in [19] in Theorem 1, one deduce that for $0 < t < 2\pi$ the following equality holds:

$$v^F(x,t) = \begin{cases} u_1^{F_+}(x,t), & 0 < x < 2\pi, \\ u_1^{F_-}(x+2\pi,t), & -2\pi < x < 0. \end{cases} \tag{12}$$

Moreover, one has that:

$$R^{2\pi}F = \Gamma_1 u^F = \widetilde{\Gamma}_1 v^F = \widetilde{R}^{2\pi}F, \quad 0 < t < 2\pi. \tag{13}$$

Thus we reduced our initial IP to the IP for dynamical system (11) of recovering the potential $\widetilde{q}(x)$, on the interval $-\pi < x < \pi$ from $\widetilde{R}^{2\pi}$.

3. Equations of IP

In this section, we briefly outline the results of [19] in applying to our situation. Fix a parameter $0 < T \leqslant \pi$ and introduce the *inner space*, the space of states of the system (11) as $\mathcal{H}^T := L_2(-T,T)$. The representation (12) and Theorem 1 imply that $v^F(\cdot,T) \in \mathcal{H}^T$.

A *control operator* $W^T : \mathcal{F}^T \mapsto \mathcal{H}^T$ is defined by the formula $W^T F := v^F(\cdot,T)$. The *reachable set* is defined by the rule:

$$U^T := W^T\mathcal{F}^T = \left\{v^F(\cdot,T) \,\middle|\, F \in \mathcal{F}^T\right\}.$$

It will be convenient for us to associate the outer space $\mathcal{H}^T = L_2(-T,T)$ with a vector space $L_2(0,T;\mathbb{R}^2)$ by setting for $a \in L_2(-T,T)$ (we keep the same notation for a function)

$$a = \begin{pmatrix} a_1(x) \\ a_2(x) \end{pmatrix} \in L_2(0,T;\mathbb{R}^2), \quad a_1(x) := a(x),\, a_2(x) := a(-x),\, x \in (0,T).$$

Theorem 2. *The control operator is a boundedly invertible isomorphism between $\mathcal{F}^T$ and $\mathcal{H}^T$, and $U^T = \mathcal{H}^T$.*

The *connecting operator* $C^T : \mathcal{F}^T \mapsto \mathcal{F}^T$ is introduced via the quadratic form:

$$\left(C^T F_1, F_2\right)_{\mathcal{F}^T} = \left(v^{F_1}(\cdot,T), v^{F_2}(\cdot,T)\right)_{\mathcal{H}^T}.$$

The crucial fact in the Boundary Control method is that the connecting operator is expressed in terms of inverse dynamic data:

Theorem 3. *The connecting operator C^T admits the following representation:*

$$\left(C^T F\right)(t) = \frac{1}{2}\begin{pmatrix} f_1(t) \\ f_2(t) \end{pmatrix} + \int_0^T C(t,s)\begin{pmatrix} f_1(s) \\ f_2(s) \end{pmatrix} ds,$$

where

$$C_{1,1}(t,s) = p_1(2T-t-s) - p_1(|t-s|), \quad p_1(s) = \int_0^s r_{11}(\alpha)\, d\alpha,$$

$$C_{1,2}(t,s) = \widetilde{p}_1(2T-t-s) - \widetilde{p}_1(t-s), \quad \widetilde{p}_1(s) = \begin{cases} \displaystyle\int_0^s r_{12}(\alpha)\, d\alpha, \; s>0, \\ \displaystyle -\int_0^{-s} r_{12}(\alpha)\, d\alpha, \; s<0, \end{cases}$$

$$C_{2,1}(t,s) = -\widetilde{r}_{21}(t-s) - \widetilde{r}_{21}(2T-t-s), \quad \widetilde{r}_{21}(s) = \begin{cases} r_{21}(s), \; s>0, \\ -r_{21}(-s), \; s<0, \end{cases}$$

$$C_{2,2}(t,s) = -r_{22}(|t-s|) - r_{22}(2T-t-s).$$

3.1. Krein equations

Let $y(x)$ be a solution to the following Cauchy problem:

$$\begin{cases} -y'' + \widetilde{q}y = 0, \quad x \in (-T,T), \\ y(0) = 0, \; y'(0) = 1. \end{cases} \tag{14}$$

We set up the *special control problem*: to find $F \in \mathcal{F}^T$ such that $W^T F = y$ in $\mathcal{H}^T$. By the Theorem 2, such a control F exists, but we can say even more:

Theorem 4. *The solution to a special control problem is a unique solution to the following Krein equation:*

$$\left(C^T F\right)(t) = (T-t)\begin{pmatrix} 1 \\ 0 \end{pmatrix}, \quad t \in (0,T). \tag{15}$$

Representation formulas (2) and (12) imply that that the solution F to a special control problem satisfies relations:

$$y(T) = v^F(T,T) = \frac{1}{2}f_1(0) - \frac{1}{2}f_2(0),$$
$$y(-T) = v^F(-T,T) = -\frac{1}{2}f_1(0) - \frac{1}{2}f_2(0).$$

Thus solving (15) for all $T \in (0,\pi)$, we recover the solution $y(x)$ to (14) on the interval $(-\pi,\pi)$. Then the potential $\widetilde{q}(x)$, $x \in (-\pi,\pi)$ can be recovered as $\widetilde{q}(x) = \dfrac{y''(x)}{y(x)}$, $x \in (-\pi,\pi)$, and consequently

$$q(x) = \begin{cases} \widetilde{q}(x), \quad 0 < x < \pi, \\ \widetilde{q}(x-2\pi), \quad \pi < x < 2\pi. \end{cases}$$

3.2. Gelfand-Levitan equations

We introduce the notations:

$$C^T = \frac{1}{2}(I+C), \quad (Cf)(t) = 2\int_0^T C(t,s)\begin{pmatrix} f(s) \\ g(s) \end{pmatrix} ds,$$
$$J^T : \mathcal{F}^T \mapsto \mathcal{F}^T, \quad \left(J^T F\right)(t) = F(T-t),$$

$$\widetilde{C} = J^T C J^T, \quad \left(\widetilde{C}F\right)(t) = \int_0^T \widetilde{C}(t,s)F(s)\, ds. \tag{16}$$

Let $m(x,t) \in C\left((0,\pi)^2, R^{2\times 2}\right)$ denotes a matrix-valued function such that $m(x,t) = 0$ when $x > t$. In [13] it was proved the following

Theorem 5. *The unique solution to the Gelfand-Levitan equation*

$$m(x,s) + \widetilde{C}(x,s) + \int_0^\pi \widetilde{C}(x,\alpha) m(\alpha,s)\, d\alpha = 0, \quad 0 < x < s < \pi.$$

where the kernel $\widetilde{C}$ is defined by (16), determines the potential by the formula:

$$q(x) = \begin{cases} 2\dfrac{d}{dx}\left(m_{11}(x,x) - m_{12}(x,x)\right), & x \in (0,\pi), \\ -2\dfrac{d}{dx}\left(m_{11}(2\pi - x, 2\pi - x) + m_{12}(2\pi - x, 2\pi - x)\right), & x \in (\pi, 2\pi). \end{cases}$$

4. Relationship between dynamic and spectral inverse data

The problem of finding relationships between different types of inverse data is very important in inverse problems theory. We can mention [9, 10, 13, 20–22] on some recent results in this direction. Below we show the relationships between the dynamic response function, matrix spectral measure and Weyl matrix.

4.1. Response function and spectral measure

Consider two solutions to the equation:

$$-\phi'' + q(x)\phi = \lambda\phi, \quad 0 < x < 2\pi, \tag{17}$$

satisfying the Cauchy data:

$$\varphi(0,\lambda) = 0,\ \varphi'(0,\lambda) = 1,\ \theta(0,\lambda) = 1,\ \theta'(0,\lambda) = 0.$$

The eigenvalues and normalized eigenfunctions of (17) with periodic boundary conditions:

$$\phi(0) = \phi(2\pi), \quad \phi'(0) = \phi'(2\pi). \tag{18}$$

are denoted by $\{\lambda_n, y_n\}_{n=1}^\infty$. Let $\beta_n, \gamma_n \in \mathbb{R}$ be such that:

$$y_n(x) = \beta_n \varphi(x,\lambda_n) - \gamma_n \theta(x,\lambda_n),$$

we point out that there can be eigenvalues of multiplicity two.

We evaluate:

$$\begin{aligned} y_n(0) &= -\gamma_n, \quad y_n(2\pi) = \beta_n\varphi(2\pi,\lambda_n) + \gamma_n\theta(2\pi,\lambda_n), \\ y_n'(0) &= \beta_n, \quad y_n'(2\pi) = \beta_n\varphi'(2\pi,\lambda_n) + \gamma_n\theta'(2\pi,\lambda_n). \end{aligned}$$

Then:

$$\Gamma_1 y_n = \frac{1}{2}\begin{pmatrix} y_n'(0) + y_n'(2\pi) \\ -y_n(0) - y_n(2\pi) = \end{pmatrix} = \begin{pmatrix} \beta_n \\ \gamma_n \end{pmatrix}. \tag{19}$$

Let $F \in \mathcal{F}^T \cap C_0^\infty(0,T;\mathbb{R}^2)$, and u^F be a solution to (1). On multiplying (1) by y_n and integrating by parts, we get the following relation:

$$\begin{aligned} 0 = \int_0^{2\pi} u_{tt}^F y_n\, dx - \int_0^{2\pi} u_{xx}^F y_n\, dx + \int_0^{2\pi} q(x) u^F y_n\, dx &= \int_0^{2\pi} u_{tt}^F y_n\, dx \\ &+ \left(u^F, Hy_n\right) + \left(\Gamma_1 u^F, \Gamma_0 y_n\right)_B - \left(\Gamma_0 u^F, \Gamma_1 y_n\right)_B \\ = \int_0^{2\pi} u_{tt}^F y_n\, dx + \lambda_n \left(u^F, y_n\right) - \left(\begin{pmatrix} f_1(t) \\ f_2'(t) \end{pmatrix}, \begin{pmatrix} \beta_n \\ \gamma_n \end{pmatrix}\right)_B. \end{aligned}$$

Looking for the solution to (1) in the form:

$$u^F = \sum_{k=1}^\infty c_k(t) y_k(x), \tag{20}$$

we plug (20) into (1) and multiply by y_n and integrate over $(0, 2\pi)$ to get:

$$\int_0^{2\pi} \sum_{k=1}^\infty c_k''(t) y_k(x) y_n(x)\, dx + \int_0^{2\pi} \sum_{k=1}^\infty c_k(t) y_k(x) \lambda_n y_n(x)\, dx = \left(\begin{pmatrix} f_1(t) \\ f_2'(t) \end{pmatrix}, \begin{pmatrix} \beta_n \\ \gamma_n \end{pmatrix}\right)_B.$$

Thus we obtain that $c_n(t)$, $n \geqslant 1$, satisfies the following Cauchy problem:

$$\begin{cases} c_n''(t) + \lambda_n c_n(t) = \left(\begin{pmatrix} f_1(t) \\ f_2'(t) \end{pmatrix}, \begin{pmatrix} \beta_n \\ \gamma_n \end{pmatrix} \right)_B, \\ c_n(0) = 0,\ c_n'(0) = 0. \end{cases}$$

the solution of which is given by the formula:

$$c_n(t) = \int_0^t \frac{\sin \sqrt{\lambda_n}(t-s)}{\sqrt{\lambda_n}} \left(f_1(s)\beta_n + f_2'(s)\gamma_n\right) ds.$$

Then for u^F (20) we have the expansion:

$$\begin{aligned} u^F(x,t) &= \sum_{k=1}^{\infty} \int_0^t \frac{\sin \sqrt{\lambda_n}(t-s)}{\sqrt{\lambda_n}} \left(f_1(s)\beta_n + f_2'(s)\gamma_n\right) ds \left(\beta_n \varphi(x,\lambda_n) - \gamma_n \theta(x,\lambda_n)\right) \\ &= \sum_{k=1}^{\infty} \int_0^t \frac{\sin \sqrt{\lambda_n}(t-s)}{\sqrt{\lambda_n}} \left(\begin{pmatrix} \beta_n \\ \gamma_n \end{pmatrix} \otimes \begin{pmatrix} \beta_n \\ \gamma_n \end{pmatrix} \begin{pmatrix} f_1(s) \\ f_2'(s) \end{pmatrix}, \begin{pmatrix} \varphi(x,\lambda_n) \\ -\theta(x,\lambda_n) \end{pmatrix} \right) \\ &= \int_{-\infty}^{\infty} \int_0^t \frac{\sin \sqrt{\lambda}(t-s)}{\sqrt{\lambda}} \left(d\Sigma(\lambda) \begin{pmatrix} f_1(s) \\ f_2'(s) \end{pmatrix}, \begin{pmatrix} \varphi(x,\lambda) \\ -\theta(x,\lambda) \end{pmatrix} \right). \end{aligned} \tag{21}$$

Where $d\Sigma(\lambda)$ is a matrix measure (see [5]) introduced by the rule:

$$\Sigma(\lambda) = \sum_{\{k \,|\, \lambda_k < \lambda\}} \begin{pmatrix} \beta_n \\ \gamma_n \end{pmatrix} \otimes \begin{pmatrix} \beta_n \\ \gamma_n \end{pmatrix}. \tag{22}$$

Thus, the response operator R^T is given by:

$$\begin{aligned} (RF)(t) = \Gamma_1 v^F &= \sum_{k=1}^{\infty} c_k(t) \Gamma_1 y_k = \sum c_k(t) \begin{pmatrix} \beta_k \\ \gamma_k \end{pmatrix} \\ &= \sum_{k=1}^{\infty} \int_0^t \frac{\sin \sqrt{\lambda_k}(t-s)}{\sqrt{\lambda_k}} \left(f_1(s)\beta_k + f_2'(s)\gamma_k\right) ds \begin{pmatrix} \beta_k \\ \gamma_k \end{pmatrix} \\ &= \int_{-\infty}^{\infty} \int_0^t \frac{\sin \sqrt{\lambda}(t-s)}{\sqrt{\lambda}} d\Sigma(\lambda) \begin{pmatrix} f_1(s) \\ f_2'(s) \end{pmatrix} ds, \quad 0 < t. \end{aligned} \tag{23}$$

4.2. Weyl function and response function

Let $N_\lambda := \ker\left(H^* - \lambda I\right)$, we observe that any $\psi(x,\lambda) \in N_\lambda$ is given by:

$$\psi(x,\lambda) = c_1 \varphi(x,\lambda) + c_2 \theta(x,\lambda). \tag{24}$$

We evaluate:

$$\begin{aligned} \psi_0 = c_2, \quad \psi_{2\pi} = c_1 \varphi(2\pi) + c_2 \theta(2\pi), \\ \psi_0' = c_1, \quad \psi_{2\pi}' = c_1 \varphi'(2\pi) + c_2 \theta'(2\pi). \end{aligned}$$

Thus the following relations hold:

$$\Gamma_0 \psi = \begin{pmatrix} -\varphi(2\pi) & 1 - \theta(2\pi) \\ 1 - \varphi'(2\pi) & -\theta'(2\pi) \end{pmatrix} \begin{pmatrix} c_1 \\ c_2 \end{pmatrix},$$

$$\Gamma_1 \psi = \frac{1}{2} \begin{pmatrix} 1 + \varphi'(2\pi) & \theta'(2\pi) \\ -\varphi(2\pi) & -\left(1 + \theta(2\pi)\right) \end{pmatrix} \begin{pmatrix} c_1 \\ c_2 \end{pmatrix}.$$

The Weyl matrix is given by (see [16]):

$$M(\lambda) = \Gamma_1 \left(\Gamma_0|_{N_\lambda}\right)^{-1},$$

so we have:

$$M(\lambda) = \frac{1}{2} \begin{pmatrix} 1 + \varphi'(2\pi) & \theta'(2\pi) \\ -\varphi(2\pi) & -\left(1 + \theta(2\pi)\right) \end{pmatrix} \frac{1}{\det \Gamma_0} \begin{pmatrix} -\theta'(2\pi) & -\left(1 - \varphi'(2\pi)\right) \\ -\left(1 - \theta(2\pi)\right) & -\varphi(2\pi) \end{pmatrix}^T.$$

Evaluating the last expression we get the following formula for the Weyl matrix:

$$M(\lambda) = \frac{1}{2\left(F(2\pi,\lambda)-2\right)} \begin{pmatrix} -2\theta'(2\pi,\lambda)\left(1-\varphi'(2\pi,\lambda)\right) & -\varphi'(2\pi,\lambda)+\theta(2\pi,\lambda) \\ -\varphi'(2\pi,\lambda)+\theta(2\pi,\lambda) & 2\varphi(2\pi,\lambda) \end{pmatrix},$$

where

$$F(x,\lambda) = \varphi'(x,\lambda) + \theta(x,\lambda)$$

is a Lyapunov function.

In [9] the authors established the relationship between the Weyl function and the kernel of dynamic response operator (see also [10, 13, 22]). Note that one needs to know the response for all $t > 0$. Then, cf. (9):

$$M(k^2) = \int_0^\infty \left(-\frac{1}{2} \sum_{k=1}^{\infty} \begin{pmatrix} \delta'(t-2k\pi) & 0 \\ 0 & -\delta(t-2k\pi) \end{pmatrix} + \widetilde{R}(t) \right) e^{ikt}\, dt,$$

where this equality is understood in a weak sense.

Acknowledgements

The research of Victor Mikhaylov was supported by RFBR 17-01-00529. Alexandr Mikhaylov was supported by RFBR 17-01-00099; A. S. Mikhaylov and V. S. Mikhaylov were partly supported by RFBR 18-01-00269 and by the Ministry of Education and Science of Republic of Kazakhstan under grant AP05136197.

References

[1] Rietman E.A. *Molecular Engineering of Nanosystems*. Berlin, Springer Science & Business Media, 2013.
[2] Voda A. *Micro, Nanosystems and Systems on Chips: Modeling, Control, and Estimation*. New York, John Wiley & Sons, 2013.
[3] Avdonin S.A., Belinskiy B.P. and Ivanov S.A. On controllability of an elastic ring. *Appl. Math. Optim.*, 2009, **60**(1), P. 71103.
[4] Avdonin S.A., Belinskiy B.P. and Pandolfi L. Controllability of a nonhomogeneous string and ring under time dependent tension. *Math. Model. Nat. Phenom.*, 2010, **5**(4), P. 4-31.
[5] Levitan B.M. *Inverse Sturm-Liouville problems*. VNU Science Press, Utreht, the Netherlands, 1987.
[6] Kurasov P.B. Inverse problems for Aharonov-Bohm rings. *Math. Proc. Cambridge Philos. Soc.*, 2010, **148**(2), P. 331-362.
[7] Belishev M.I. Recent progress in the boundary control method, *Inverse Problems*, 2007, **23**(5), P. R1–R67.
[8] Belishev M.I. Boundary control and tomography of Riemannian manifolds (the BC-method). *Uspekhi Matem. Nauk*, 2017, **72**(4), P. 3–66 (in Russian).
[9] Avdonin S.A., Mikhaylov V.S., Rybkin A.V. The boundary control approach to the Titchmarsh-Weyl $m-$function. *Comm. Math. Phys.*, 2007, **275**(3), P. 791–803.
[10] Mikhaylov A.S., Mikhaylov V.S. Relationship between different types of inverse data for the one-dimensional Schrödinger operator on the half-line. *J. Math. Sci.* (N.Y.), 2017, **226**(6), P. 779–794.
[11] Mikhaylov A.S., Mikhaylov V.S. Inverse dynamic problems for canonical systems and de Branges spaces. *Nanosystems: Physics, Chemistry, Mathematics*, 2018, **9**(2), P. 215–224.
[12] Mikhaylov A.S., Mikhaylov V.S. Boundary Control method and de Branges spaces. Schrödinger operator, Dirac system, discrete Schrödinger operator. *Journal of Mathematical Analysis and Applications*, 2018, **460**(2), P. 927–953.
[13] Mikhaylov A.S., Mikhaylov V.S., Simonov S.A. On the relationship between Weyl functions of Jacobi matrices and response vectors for special dynamical systems with discrete time. *Mathematical Methods in the Applied Sciences*, 2018, **41**(16), P. 6401–6408.
[14] Mikhaylov A.S., Mikhaylov V.S. *Dynamic inverse problem for Jacobi matrices*, 2019, (to appear in Inverse Problems and Imaging).
[15] Belishev M.I., Wada N. On revealing graph cycles via boundary measurements. *Inverse Problems*, 2009, **25**(10), P. 105011-21.
[16] Behrndt J., Malamud M.M., Neidhart H. Scattering matrices and Weyl functions. *Proc. London Math. Soc.*, 2008, **97**, P. 568-598.
[17] Avdonin S.A., Mikhaylov V.S. The boundary control approach to inverse spectral theory. *Inverse Problems*, 2010, **26**(4), P. 045009-19.
[18] Belishev M.I., Mikhaylov V.S. Unified approach to classical equations of inverse problem theory. *Journal of Inverse and Ill-posed Problems*, 2012, **20**(4), P. 461–488.
[19] Mikhaylov A.S., Mikhaylov V.S. On an inverse dynamic problem for the wave equation with a potential on a real line. *Zapiski Seminarov POMI*, 2017, **461**, P. 212–231.
[20] Belishev M.I. On relation between spectral and dynamical inverse data. *J. Inv. Ill-posed problems*, 2001, **9**(6), P. 647-665.
[21] Belishev M.I. On a relation between data of dynamic and spectral inverse problems. *Zap. Nauchn. Sem. S.-Peterburg. Otdel. Mat. Inst. Steklov. (POMI)*, 2003, **297**, P. 30–48, translation in *J. Math. Sci.* (N.Y.), 2005, **127**(6), P 2353-2363.
[22] Mikhaylov A.S., Mikhaylov V.S. Quantum and acoustic scattering on $\mathbb{R}_+$ and a representation of the scattering matrix. *Proceedings Days on Diffraction 2017*, IEEE, 2017, P. 237–240.

NANOSYSTEMS: PHYSICS, CHEMISTRY, MATHEMATICS, 2019, 10 (2), P. 124–130

Numerical solution for the Schrödinger equation with potential in graphene structures

L. A. Nhat[1,2]

[1]Peoples' Friendship University of Russia (RUDN University),
6 Miklukho-Maklaya str., 117198, Moscow, Russia

[2]Tan Trao University, 22227, Tuyen Quang, Vietnam

leanhnhat@mail.ru

DOI 10.17586/2220-8054-2019-10-2-124-130

This paper presents a different numerical solution to compute eigenvalues of the Schrödinger equation with the potentials in graphene structures [1]. The research subjects include the Schrödinger equation and the exchange-correlation energy of the graphene structures in Grachev's article. Specifically, we used the pseudospectral method basing on the Chebyshev-Gauss-Lobatto grid to determine the approximate numerical results of the problem. The results are the discrete energy spectra and the corresponding eigenfunctions of the nonlinear spin waves in the graphene structure. Additionally, these results can be applied to create the nonlinear spin waves in the graphene structures.

Keywords: graphene, kinks, breathers, spin, pseudospectral method, Schrödinger equation, Chebyshev, eigenvalue problems, nonlinear models.

Received: 12 April 2019

Revised: 17 April 2019

1. Introduction

In 2010, D. D. Grachev and L. A. Sevastyanov invented the method for generating spin waves [2, 3]. This method formed the quantum collective excitations of spin density and magnetization density in graphene films. It may be used in quantum nanoelectronics, spintronics, for creating spin-processors, memory cells, physical field sensors, other devices and systems for processing and storing information of terahertz (and higher) range that have nanometric dimensions and work in a broad temperature range with minimum energy consumption.

Since the publication of this invention, the authors studied, built and perfected the theory of the method for generating spin waves. In particular, Grachev constructed the quantum field model to adequately describe ferromagnetic properties in graphene structures to match the results of physical and numerical experiments. This model described properties of monoatomic graphene layers, which connected with the presence of a nontrivial function of the distribution of the spin density, formed as a result of the spontaneous breakdown of the spin symmetry of valence electrons in atoms of carbon [4]; in [5], the authors provided the nonlinear field model to describe of the spin density distribution of the valence electrons in graphene films. This model describes experimentally observable ferromagnetic properties of such films; prior work [6] claimed that the offered variant of the nonlinear field model, in which carriers of spin density are not fermions (electrons), but bosons (spinons), is quite adequate for describing the magnetic properties of graphene structures. The authors proposed in two articles [1, 7] the desirability of a nonlinear model that describes a possible mechanism of ferromagnetism in graphene structures, resulting from electron-electron interaction and spontaneous breaking of spin symmetry of valence electrons. We investigated such spatially localized nonlinear spin of the valence electron density on the graphene surface such as kinks, and their interactions, as well as quasibound metastable states of the interacting kinks and antikinks, that are breathers [8].

In addition, many scientists have also studied how to spin waves in graphene, and they have gained certain achievements such as the excitations with spin reversal such as spin-flip and spin-wave excitations were studied in [9]. They showed that these excitations were correctly accounted for in the time-dependent Hartree-Fock and strong magnetic field approximations; F. J. Culchac investigated spin excitations and electronic properties of graphene nanoribbon devices with zigzag edges [10,11]. Those studies showed that a central point of a finite zigzag nanoribbon, when spin excitations are damped at all finite energies, their energy dispersion at small wave vector is dominated by antiferromagnetic correlations between the ribbons edges, in accordance with previous calculations. A. Matthew studied the collective excitations of doped graphene in the presence of in-plane magnetic fields and calculated the dispersions of charge and spin plasmons using time-dependent density-functional methods within a standard tight-binding approach [12].

Evidently, in the articles [1,4–8], it is shown that the density of spin symmetry was broken by the spontaneous breaking, which obeyed a nonlinear equation, and the offered nonlinear models with the limits will exist exact and

approximate solutions for the distribution of the spin density and magnetization on the surface of the graphene structures, as the method of the scattering matrix [5]; the finite element method (FEM) and the Ritz method [1, 7]; the Ritz method using Hermitian functions as coordinate functions [8].

Based on the density functional theory and the perturbation methods, in [1] proposed a physically reasonable nonlinear model of interacting massless Dirac fermions in graphene structures for practical applications. This model described the spin density (s) distribution of the valence electrons of the carbon atoms in graphene structures. This corresponds to the equation of the well-known nonlinear model $(\lambda\phi^4)$:

$$s'' = \lambda(s^2 - s_0^2)s, \tag{1}$$

where s_0 – the zero-order local spin density, λ – the self-interaction constant.

To illustrate this, consider the simplest nonlinear model $\lambda\phi^4$ when the envelopes depend on one spatial coordinate. It is well known that the Hamiltonian density of the model has the form:

$$H[s] = (\partial_\nu s \partial^\nu s)/2 + \lambda(s^2 - s_0^2)/4, \quad \nu = 0, 1, 2.$$

In this case, equation (1) was known to have two stable vacuum solutions: $s_\pm = \pm s_0$ and the kink-antikink solutions:

$$s_\pm = \pm s_0 th\left(\sqrt{\frac{\lambda s_0^2}{2}}x\right). \tag{2}$$

Due to the non-linearity of equation (1), for qualitative estimates, the author determined approximate solutions of equation (1) by choosing the field function of interacting kinkantikink pair in such simple form:

$$\Phi(x, a) = s_+(x + a) + s_-(x - a) - s_0 \tag{3}$$

where a is the parameter, and the function (3) has the following asymptotic behavior:

$$\begin{cases} \Phi(x, +\infty) = +s_0, \\ \Phi(+\infty, a) = \Phi(-\infty, a) = -s_0 \\ \Phi'_x(+\infty, a) = \Phi'_x(-\infty, a) = 0 \\ \Phi(x, -\infty) = -3s_0; \end{cases} \tag{4}$$

or

$$\begin{cases} \Phi(x, +\infty) = +s_0, \\ \Phi(+\infty, a) = \Phi(-\infty, a) = -s_0 \\ \Phi'_x(+\infty, a) = \Phi'_x(-\infty, a) = 0 \\ \Phi(x, 0) = -s_0; \end{cases} \tag{5}$$

It can easily be seen that there are two models. We call the conditions (4) – model A, and the conditions (5) – model B.

We can write a system of the Hamiltonian with the field function in the form (3) that satisfies the equation of the type (1) [1, 7]:

$$H\{\Phi, a\} = \frac{1}{2}\int_{-\infty}^{\infty} dx \left\{[\Phi'_x(x, a)]^2 + \frac{\lambda}{2}[\Phi(x, a)^2 - s_0^2]^2\right\}. \tag{6}$$

Similarly, we can write the energy density of the kink [7]:

$$E[s] = \int_{-\infty}^{\infty} dx \left\{\frac{s'^2_x}{2} + \frac{\lambda}{2}[s^2 - s_0^2]^2\right\}. \tag{7}$$

Combining (7) and (2) gives the result:

$$E[s] = \frac{2\sqrt{2\lambda}}{3}s_0^3. \tag{8}$$

Then, the sum of the mass-energy equivalent of free kink and antikink equals the potential energy of the breather depending on a with $U\{\Phi, a\}$ computed from (6) and the function $H\{\Phi, a\}$ possesses a minimum. We have the mass of the breather:

$$m[\lambda, s_0] = \frac{4\sqrt{2\lambda}}{3}s_0^3. \tag{9}$$

The Schrödinger equation for the quantum-mechanical wave function $\psi(a)$ of a stationary breather state with corresponding eigenenergy E has the form:

$$-\frac{\hbar^2}{2\widetilde{m}\,\{\lambda, s_0\}}\frac{\mathrm{d}^2}{\mathrm{d}a^2}\psi(a) + U(\Phi, a)\psi(a) = E\psi(a), \tag{10}$$

here $\widetilde{m}\,\{\lambda, s_0\} = m\{\lambda, s_0\}/c^2$ is the effective mass of the breather, c is the speed of light, $U(\Phi, a)$ is the potential energy, $\psi(a)$ is the wave function and E is the energy of the system.

Grachev's articles used the finite element method (FEM) and the conventional Ritz method to determine the eigenvalues and eigenfunctions of the Schrödinger equation (10) for the quantum-mechanical wave.

In this paper, we study the numerical solution to compute eigenvalues of the Schrödinger equation (10) with the energies of the system in graphene structures. That is the pseudospectral method basing on the Chebyshev polynomials of the first kind and using the Chebyshev-Gauss-Lobatto grid in the integration interval $[-1, 1]$.

2. Chebyshev differentiation matrix (CDM)

A grid function $v(x)$ is defined on the Chebyshev-Gauss-Lobatto points $x = \{x_0, x_1, \ldots, x_n\}$ such that $x_k = \cos(k\pi/n)$, $k = \overline{0, n}$. They are the extrema of the n-th order in the Chebyshev polynomial $T_n(x) = \cos(n\cos^{-1}x)$. The function $v(x)$ is interpolated by constructing the n-th order interpolation polynomial $g_j(x)$ such that $g_j(x_k) = \delta_{j,k}$,

$$p(x) = \sum_{j=0}^{n} p_j g_j(x), \tag{11}$$

where $p(x)$ is the unique polynomial of degree n and $p_j = v(x_j)$, $j = \overline{0, n}$. The following can be shown:

$$g_j(x) = \frac{(-1)^{j+1}(1-x^2)T_n'(x)}{c_j n^2 (x - x_j)}, \quad j = \overline{0, n}, \tag{12}$$

where

$$c_j = \begin{cases} 2, & j = 0 \text{ or } n, \\ 1, & \text{otherwise.} \end{cases} \tag{13}$$

As we know the values of $p(x)$ at $n+1$ points, we would like to find approximately the values of the derivative of $p(x)$ at those points $p'(x) = \dfrac{d}{dx}p(x)$. We can write the same in the matrix form:

$$p' = Dp \tag{14}$$

where $D = \left\{d_{i,j}^{(1)}\right\}$ is an $(n+1)\times(n+1)$ differentiation matrix.

Evidently, the derivative of $p(x_j)$ becomes:

$$p'(x_j) = \sum_{k=0}^{n} D_{j,k}\, p(x_k), \quad j = \overline{0, n}. \tag{15}$$

We have the entries $d_{i,j}^{(1)} = g_i'(x_j)$ which are [13, 14]

$$\begin{aligned} d_{0,0}^{(1)} &= -d_{n,n}^{(1)} = \frac{2n^2+1}{6}, \\ d_{i,i}^{(1)} &= -\frac{x_i}{2(1-x_i^2)}, \quad i = \overline{1, n-1}, \\ d_{i,j}^{(1)} &= \frac{c_i}{c_j}\frac{(-1)^{i+j}}{x_i - x_j}, \quad i \neq j, \quad i, j = \overline{1, n-1}, \end{aligned} \tag{16}$$

where c_k is determined by the formula (13).

Similarly, $p'(x)$ is a polynomial of degree $n-1$; it exists the second differentiation matrix D^2,

$$p'' = D^2 p, \tag{17}$$

and

$$p''(x_j) = \sum_{k=0}^{n} D_{j,k}^2\, p(x_k), \quad j = \overline{0, n}. \tag{18}$$

3. Pseudospectral method using the CDM for the Schrödinger equation

Suppose the Schrödinger equation has simple form as the following:

$$-\frac{d^2}{dx^2}u(x)+q(x)u(x)+\lambda u(x)=0,\quad u(-1)=u(1)=0 \tag{19}$$

and collocation points x_i such that $1=x_0>x_1>...>x_n=-1$.

We know that:

$$\frac{d^2}{dx^2}u_n(x_i)=\sum_{k=0}^{n}D_{i,k}^2u_n(x_k). \tag{20}$$

Thus, equation (19) takes the following form:

$$-\sum_{k=0}^{n}D_{i,k}^2u_n(x_k)+q(x_i)u(x_i)=-\lambda u(x_i),\quad i=\overline{1,\ n-1} \tag{21}$$

with $u_n(x_n)=0$ and $u_n(x_0)=0$.

Alternately, we partition the matrix D into matrices [13, 15]:

$$\begin{gathered}\widetilde{E}^{(1)}=\begin{pmatrix} d_{1,1}^{(1)} & d_{1,2}^{(1)} & \cdots & d_{1,n-1}^{(1)} \\ d_{2,1}^{(1)} & d_{2,2}^{(1)} & \cdots & d_{2,n-1}^{(1)} \\ \vdots & \vdots & \ddots & \vdots \\ d_{n-1,1}^{(1)} & d_{n-1,2}^{(1)} & \cdots & d_{n-1,n-1}^{(1)} \end{pmatrix}, \\ \widetilde{e}_0^{(1)}=\begin{pmatrix} d_{1,0}^{(1)} \\ d_{2,0}^{(1)} \\ \vdots \\ d_{n-1,0}^{(1)} \end{pmatrix}, \widetilde{e}_n^{(1)}=\begin{pmatrix} d_{1,n}^{(1)} \\ d_{2,n}^{(1)} \\ \vdots \\ d_{n-1,n}^{(1)} \end{pmatrix}.\end{gathered} \tag{22}$$

We can rewrite in the matrix form: $\widetilde{e}_0^{(1)}=\{d_{i,0}^{(1)}\}$, $\widetilde{E}^{(1)}=\{d_{i,j}^{(1)}\}$, $\widetilde{e}_n^{(1)}=\{d_{i,n}^{(1)}\}$, here $i,j=\overline{1,n-1}$.

Similarly, we partition matrix D^2 into matrices $\widetilde{e}_0^{(2)}$, $\widetilde{E}^{(2)}$, $\widetilde{e}_n^{(2)}$. So, (21) can then be written in the matrix form:

$$-\left(u_n(x_0)\widetilde{e}_0^{(2)}+\widetilde{E}^{(2)}u+u_n(x_n)\widetilde{e}_n^{(2)}\right)+Qu=-\lambda u. \tag{23}$$

Since $u_n(x_0)=0$ and $u_n(x_n)=0$, we have derived the following:

$$\left(-\widetilde{E}^{(2)}+Q\right)u=-\lambda u, \tag{24}$$

where u denotes the vectors with elements $\{u_n(x_i)\}$, while Q denotes the diagonal matrix with elements $\{g(x_i)\}, i=\overline{1,n-1}$.

4. Numerical solutions and results

In our research, the program has used the Mathematica 10.4 language [16]. Our numerical results are computed by the pseudospectral method using the CDM (CPSM), as shown in the CPSM columns. These numerical results as per Grachev's article have been included in the columns FEM for the sake of completeness.

The potential energy $U(\Phi,a)$ in nonlinear spin waves in graphene structures has been calculated; it had the analytic form [1, 7]:

$$U\{\Phi,a\}=\frac{4\sqrt{2\lambda}}{3}s_0^3\left(1-\frac{6}{t}+\frac{36\sqrt{2\lambda}s_0a-24}{t^2}+\frac{48\sqrt{2\lambda}s_0a}{t^3}\right), \tag{25}$$

where

$$t=\begin{cases} e^{2\sqrt{2\lambda}s_0a}-1 & \text{for model A,} \\ e^{2\sqrt{2\lambda}s_0|a|}-1 & \text{for model B.}\end{cases}$$

From section 4 of the article [1], we can deduce the following: if the vicinity of $a = 0$ and $|a| < 1/(5s_0\sqrt{2\lambda})$, this potential has the following asymptotic form of a power series:

$$U(\Phi, a) = 8s_0^5\lambda\sqrt{2\lambda}a^2(\frac{2}{5} - \frac{4s_0\sqrt{2\lambda}}{15} + \frac{s_0^2\lambda a^2(4 + 7s_0\sqrt{2\lambda}a)}{105} - \frac{16s_0^4\lambda^2a^4}{525} - \frac{32s_0^5\lambda^2\sqrt{2\lambda}a^5}{1575} + \frac{416s_0^6\lambda^3a^6}{3465} + \frac{32s_0^7\lambda^3\sqrt{2\lambda}a^7)}{6237}); \quad (26)$$

if $a \to +\infty$ then $U_{max} = U(\Phi, +\infty) = 4\sqrt{2\lambda}s_0^3)/3$; for model A, at $a \to -\infty$ then potential $U(\Phi, -\infty) = 4\sqrt{2\lambda}s_0^3(6|a| - 17)/3$. With $s_0 = 2$ and $\lambda = 1$, we have graphs of potential energy $U(\Phi, a)$ in the cases model A (denoted by U_A) and model B (denoted by U_B) as depicted in Fig. 1.

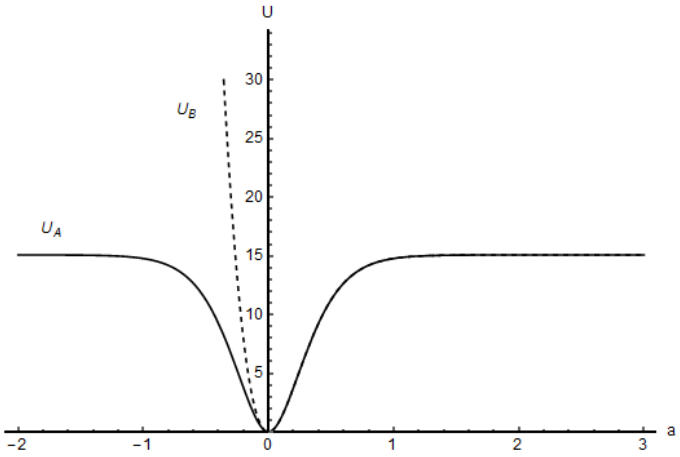

FIG. 1. Two cases model A and B of the potential energy $U(\Phi, a)$ in nonlinear spin waves in graphene structures with $s_0 = 2$ and $\lambda = 1$

Now, we consider the Schrödinger equation (10) in the case $\hbar = c = 1$:

$$-\frac{\mathrm{d}^2}{\mathrm{d}a^2}\psi(a) + 2\overline{U}(\Phi, a)\psi(a) = 2\overline{E}\psi(a), \quad (27)$$

here

$$2\overline{U}(\Phi, a) = 2m\{\lambda, s_0\}U(\Phi, a) = \frac{8\sqrt{2\lambda}s_0^3}{3}U(\Phi, a)$$

and

$$2\overline{E} = 2m\{\lambda, s_0\}E = \frac{8\sqrt{2\lambda}s_0^3}{3}E.$$

We apply the section 3 for the equation (27), we can thus rewrite in the matrix form:

$$\left(-\widetilde{E}^{(2)} + G\right)\psi = 2\overline{E}\psi. \quad (28)$$

where G is the diagonal matrix of order $n - 1$, with the elements:

$$\left\{\frac{8\sqrt{2\lambda}s_0^3}{3}U(\Phi, a_i)\right\}, \quad i = \overline{1, n-1}.$$

Thus, to find the energy $2\overline{E}$ of the system (27) and find eigenvalues $2\overline{E}$ in the equation (28) are equivalent, we have to deduce the eigenvalues of matrix $-\widetilde{E}^{(2)} + G$ and the total energy $E = \dfrac{3\overline{E}}{4s_0^3\sqrt{2\lambda}}$ as is shown in the Tab.1 for the two case models A (denoted by E^A) and B (denoted by E^B), with $\lambda = 1 and$ and $s_0 = 2$. Therefore, we have the graphics illustrating the first four eigenfunctions of the breather states of models A (denoted by $\psi^A(a)$) – Fig. 2 and B (denoted by $\psi^B(a)$) – Fig. 3.

Remarks: From the numerical results in Table 1, we see that: the numerical results of CPSM and FEM are equivalent. In addition, it provides many arbitrary numerical results based on practical applications. It is clear that this numerical solution is reliable and very accurate when $k < 2n/\pi$ [17]. Hence, it may become our calculation

TABLE 1. First ten eigenvalues of the total energy E^A and E^B in the cases model A and B with $\lambda = 1$ and $s_0 = 2$.

	CPSM		**FEM**	
k	E^A	E^B	E^A	E^B
1	2.118495	1.870306	2.11	1.87
2	6.063236	5.232607	6.06	5.23
3	9.495058	7.990805	9.49	7.99
4	12.300544	10.277019	12.29	10.27
5	14.375397	12.113396	14.28	12.11
6	16.168130	13.535662		13.51
7	18.343813	14.647713		14.48
8	20.916405	15.694926		15.00
9	23.816396	16.893204		
10	27.002109	18.303307		

tool for future studies. Furthermore, we contend that the offered nonlinear model existence of metastable kink-antikink bound states for the function of spin density on a two-dimensional graphene surface is possible. Finally, the numerical calculations show that the interval change between the next levels generally decreases with the energy growth, and since some value of energy, the spectrum becomes continuous.

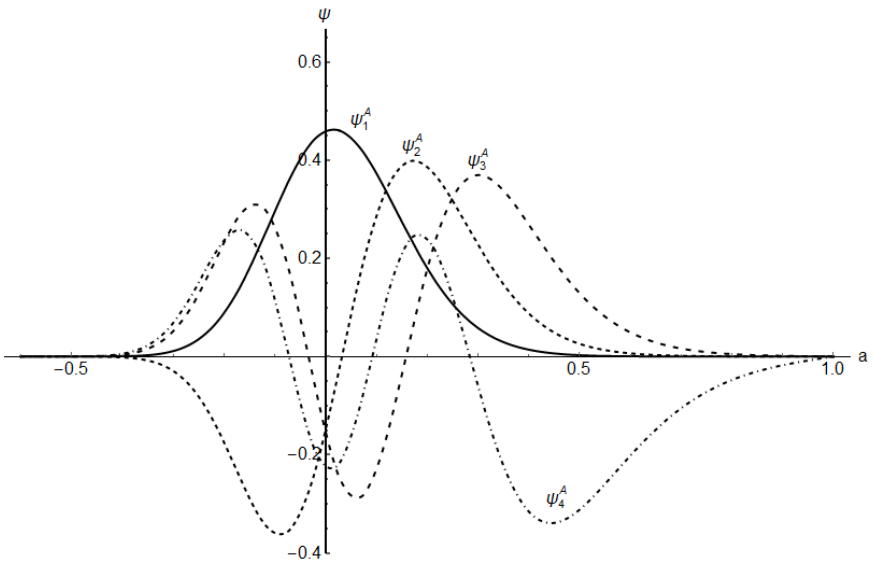

FIG. 2. First four eigenfunctions of model A with $s_0 = 2$ and $\lambda = 1$

5. Conclusion

We proposed a reasonable numerical model which offered approximate solutions for the spin density's distribution of the stationary pseudo-spin waves on the surface of the graphene monoatomic film. We have obtained the discrete energy spectra and the corresponding eigenfunctions of nonlinear spin waves in the graphene structure.

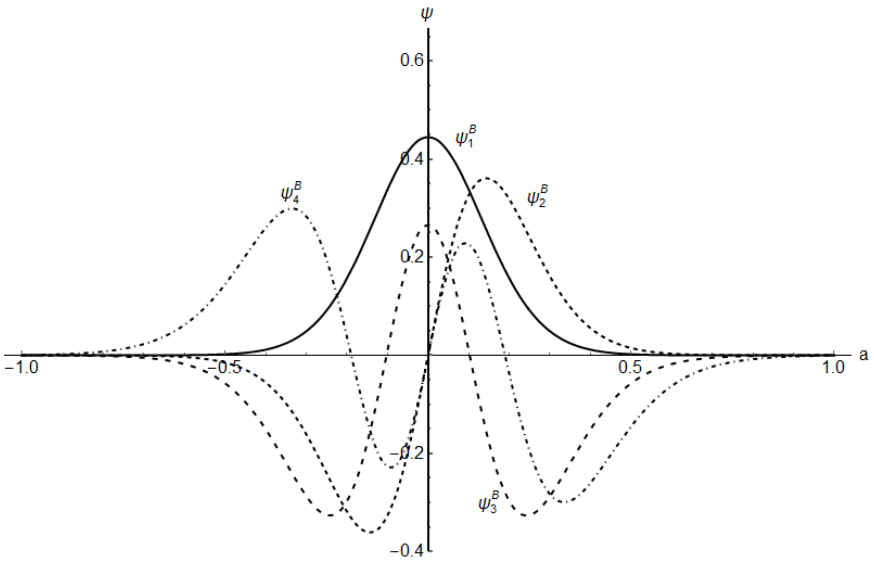

FIG. 3. First four eigenfunctions of model B with $s_0 = 2$ and $\lambda = 1$

More complete numerical results may be obtained by the Chebyshev pseudospectral method. These results may be applied to create the nonlinear spin waves in the graphene structures.

Acknowledgements

The author is greatly indebted to Prof. D. S. Kulaybov and to K. P. Lovetskiy for suggesting the problem and for many stimulating conversations.

The publication was prepared with the support of the *RUDN University Program 5-100*.

References

[1] Grachev D.D., Sevastianov L.A., Lovetskiy K.P. Nonlinear spin waves in graphene structures. *SPIN*, 2014, **4**(3), P. 1–13.
[2] Grachev D.D., Sevastianov L.A. Method of spin wave formation. Patent of Russia No. 2477907, 2010, 7 pp.
[3] Grachev D.D., Sevastianov L.A. Method for generating spin waves. Patent of United States No. US8,779,765 B2, 2014, 6 pp.
[4] Grachev D.D., Rybakov Y.P., Sevastianov L.A., Sheka E.F. Ferromagnetism in graphen and fulleren nanostructures. Theory, modelling, experiment. *RUDN J. of MIPh*, 2010, **1**, P. 20–27.
[5] Grachev D.D., Sevastianov L.A. Quantum field approach to the ferromagnetic properties of the graphene films. *Nanostuctures. Math. phys. Model.*, 2011, **4**(1), P. 5–15.
[6] Arzumanyan G.M., Ayrjan E.A., Grachev D.D., Sevastianov L.A. Quantum field model for graphene magnetism, modern trends in nanoscience. In book Balasoiu M., Arzumanyan G. M. *Modern trends in nanoscience*, Editura Academiei Romane, 2013, 236 pp.
[7] Grachev D.D., Sevastianov L.A., Lovetskiy K.P., Gusev A.A., Vinitsky S.I., Derbov V.L. Model for spin waves and lasing in monolayer graphene films. *Proc. of the SPIE*, 2015, **9448**, ID. 94481W, 14 pp.
[8] Kulyabov D.S., Lovetskiy K.P., Nhat L.A. Simple model of nonlinear spin waves in graphene structures. *RUDN J. of MIPh.*, 2018, **26**(3), P. 244–251.
[9] Roldan R., Fuchs J.-N., Goerbig M.O. Spin-flip excitations, spin waves, and magneto-excitons in graphene Landau levels at integer filling factors. *Phys. Rev. B*, 2010, **82**, ID 205418, 13 pp.
[10] Culchac F.J., Latge A., Costa A.T. Spin waves in graphene nanoribbon devices. *Phys. Rev. B*, 2012, **86** ID: 115407, 11 pp.
[11] Culchac F.J., Latge A., Costa A. T. Spin waves in zigzag graphene nanoribbons and the stability of edge ferromagnetism. *New J. Phys.*, 2011, **13**, ID: 033028, 5 pp.
[12] Matthew A., Carsten U. Collective charge and spin excitations in graphene with in-plane magnetic fields. In Abstracts of the Conference APS March Meeting, New Orleans - Louisiana, March 13, 2017, **64**(4), Abstract ID: BAPS.2017.MAR.P42.9, P. 1024.
[13] Mason J.C., Handscomb D.C. *Chebyshev polynomials*. CRC Press LLC, 2003, 335 pp.
[14] Don W.S., Solomonoff A. Accuracy and speed in computing the Chebyshev collocation derivative. *SIAM J. Sci. Comput.*, 1991, **16**(6), P. 1253–1268.
[15] Nhat L.A. Pseudospectral methods for nonlinear pendulum equations. *Zh. Sib. Fed. Univ. Mat. Fiz.*, 2019, **12**(1), P. 79–84.
[16] Martha L.A., James P.B. *Differential equations with mathematica*, ed. 3rd. Elsevier Inc, 2004, 893 pp.
[17] Weideman J.A.C., Trefethen L.N. The eigenvalues of second-order spectral differentiation matrices. *SIAM J. Numer. Analys.*, 1988, **25**(6), P. 1279–1298.

NANOSYSTEMS: PHYSICS, CHEMISTRY, MATHEMATICS, 2019, 10 (2), P. 131–140

A model of an electron in a quantum graph interacting with a two-level system

A. A. Boitsev, I. Y. Popov

ITMO University, Kronverkskiy, 49, St. Petersburg, 197101, Russia

boitsevanton@gmail.com, popov1955@gmail.com

PACS 03.65.Nk, 73.23.Ad **DOI 10.17586/2220-8054-2019-10-2-131-140**

A model of an electron in a quantum graph interacting with a two-level system is considered. The operator describing the model has the form of sum of tensor products. Self-adjoint extensions and a scattering matrix are written in terms of a boundary triplet, corresponding to the considered symmetric operator. Diagrams of reflection are calculated and numerical results are discussed .

Keywords: Aharonov-Bohm ring, nanostructure, quantum graph, scattering, solvable model.

Received: 1 March 2019

Revised: 30 March 2019

1. Introduction

Electron transport in nanostructures under the action of a magnetic field attracts great attention during last decades. The reason is observation of many interesting effects found applications in nanoelectronics. One of such intriguing problems is that of Aharonov-Bohm oscillations in quantum transport [1–3]. Several models were suggested to describe the phenomenon. One of the most effective in the field is the quantum graph model (see, e.g., [4–7]). An excellent review of the state of the art in quantum graph theory is presented in [8].

We are interested in the case when the system (quantum graph) with an Aharonov-Bohm ring interacts with another system having two energy levels. In this case, the operator of the whole system has the form of a sum of tensor products:

$$S := A_{\mathfrak{H}} \otimes I_{\mathfrak{T}} + I_{\mathfrak{H}} \otimes T_{\mathfrak{T}},$$

where self-adjoint operators A and T act in Hilbert spaces $\mathfrak{H}$ and $\mathfrak{T}$, respectively. It is well known that such operators describe the interaction of two quantum systems. Extension technique for such operators is widely discussed in [9]. We introduce a model for an electron in a quantum graph interacting with a two-level system. Such an operator also preserves a tensor structure described above. The first operator A stands for the quantum graph and the second operator T, which is, actually, a 2×2 matrix, describes the two-level system.

In the following, we investigate the considered operator using boundary triplets approach and the results from [9]. Scattering matrix is obtained and the diagrams of the argument of the reflection coefficient (scattering phase) are constructed. The scattering has a resonance character.

2. Preliminaries

2.1. Linear relations

A linear relation Θ in $\mathcal{H}$ is a closed linear subspace of $\mathcal{H} \oplus \mathcal{H}$. The set of all linear relations in $\mathcal{H}$ is denoted by $\widetilde{\mathcal{C}}(\mathcal{H})$. We denote also by $\mathcal{C}(\mathcal{H})$ the set of all closed linear (not necessarily densely defined) operators in $\mathcal{H}$. Identifying each operator $T \in \mathcal{C}(\mathcal{H})$ with its graph $\mathrm{gr}\,(T)$, we regard $\mathcal{C}(\mathcal{H})$ as a subset of $\widetilde{\mathcal{C}}(\mathcal{H})$.

The role of the set $\widetilde{\mathcal{C}}(\mathcal{H})$ in extension theory becomes clear from Proposition 2.3. However, its role in the operator theory is substantially motivated by the following circumstances: in contrast to $\mathcal{C}(\mathcal{H})$, the set $\widetilde{\mathcal{C}}(\mathcal{H})$ is closed with respect to taking inverse and adjoint relations Θ^{-1} and Θ^*. The latter is given by: $\Theta^{-1} = \{\{g, f\} : \{f, g\} \in \Theta\}$ and

$$\Theta^* = \left\{ \begin{pmatrix} k \\ k' \end{pmatrix} : (h', k) = (h, k') \text{ for all } \begin{pmatrix} h \\ h' \end{pmatrix} \in \Theta \right\}. \tag{1}$$

A linear relation Θ is called symmetric if $\Theta \subset \Theta^*$ and self-adjoint if $\Theta = \Theta^*$.

2.2. Boundary triplets and proper extensions

Let us briefly recall some basic facts regarding boundary triplets. Let S be a densely defined closed symmetric operator with equal deficiency indices $n_{\pm}(S) := \dim(\mathfrak{N}_{\pm i})$, $\mathfrak{N}_z := \ker(S^* - z)$, $z \in \mathbb{C}_{\pm}$, acting on some separable Hilbert space $\mathfrak{H}$.

Definition 2.1.
(i) *A closed extension $\widetilde{S}$ of S is called proper if* $\mathrm{dom}(S) \subset \mathrm{dom}(\widetilde{S}) \subset \mathrm{dom}(S^*)$.
(ii) *Two proper extensions $\widetilde{S}'$, $\widetilde{S}$ are called disjoint if* $\mathrm{dom}(\widetilde{S}') \cap \mathrm{dom}(\widetilde{S}) = \mathrm{dom}(S)$ *and transversal if in addition* $\mathrm{dom}(\widetilde{S}') + \mathrm{dom}(\widetilde{S}) = \mathrm{dom}(S^*)$.

We denote by $\mathrm{Ext}_{\mathrm{S}}$ the set of all proper extensions of S completed by the non-proper extensions S and S^* is denoted. For instance, any self-adjoint or maximal dissipative (accumulative) extension is proper.

Definition 2.2 ([10])**.** A triplet $\Pi = \{\mathcal{H}, \Gamma_0, \Gamma_1\}$, where $\mathcal{H}$ is an auxiliary Hilbert space and $\Gamma_0, \Gamma_1 : \mathrm{dom}(S^*) \to \mathcal{H}$ are linear mappings, is called a boundary triplet for S^* if the "abstract Green's identity":

$$(S^* f, g) - (f, S^* g) = (\Gamma_1 f, \Gamma_0 g) - (\Gamma_0 f, \Gamma_1 g), \;\; f, g \in \mathrm{dom}(S^*). \tag{2}$$

is satisfied and the mapping $\Gamma := (\Gamma_0, \Gamma_1)^\top : \mathrm{dom}(S^*) \to \mathcal{H} \oplus \mathcal{H}$ is surjective, i.e. $\mathrm{ran}(\Gamma) = \mathcal{H} \oplus \mathcal{H}$.

A boundary triplet $\Pi = \{\mathcal{H}, \Gamma_0, \Gamma_1\}$ for S^* always exists whenever $n_+(S) = n_-(S)$. Note also that $n_{\pm}(S) = \dim(\mathcal{H})$ and $\ker(\Gamma_0) \cap \ker(\Gamma_1) = \mathrm{dom}(S)$.

With any boundary triplet Π, one associates two canonical self-adjoint extensions $S_j := S^* \restriction \ker(\Gamma_j)$, $j \in \{0, 1\}$. Conversely, for any extension $S_0 = S_0^* \in \mathrm{Ext}_{\mathrm{S}}$ there exists a (non-unique) boundary triplet $\Pi = \{\mathcal{H}, \Gamma_0, \Gamma_1\}$ for S^* such that $S_0 := S^* \restriction \ker(\Gamma_0)$.

Using the concept of boundary triplets one can parameterize all proper extensions of A in the following way.

Proposition 2.3 ([11, 12])**.** *Let $\Pi = \{\mathcal{H}, \Gamma_0, \Gamma_1\}$ be a boundary triplet for S^*. Then the mapping:*

$$\mathrm{Ext}_{\mathrm{S}} \ni \widetilde{\mathrm{S}} \to \Gamma \mathrm{dom}\,(\widetilde{\mathrm{S}}) = \{(\Gamma_0 \mathrm{f}, \Gamma_1 \mathrm{f})^\top : \; \mathrm{f} \in \mathrm{dom}\,(\widetilde{\mathrm{S}})\} =: \Theta \in \widetilde{\mathcal{C}}(\mathcal{H}) \tag{3}$$

establishes a bijective correspondence between the sets $\mathrm{Ext}_{\mathrm{S}}$ *and $\widetilde{\mathcal{C}}(\mathcal{H})$. We write $\widetilde{S} = S_\Theta$ if $\widetilde{S}$ corresponds to Θ by* (3)*. Moreover, the following holds:*
(i) *$S_\Theta^* = S_{\Theta^*}$, in particular, $S_\Theta^* = S_\Theta$ if and only if $\Theta^* = \Theta$.*
(ii) *S_Θ is symmetric (self-adjoint) if and only if Θ is symmetric (self-adjoint).*
(iii) *The extensions S_Θ and S_0 are disjoint (transversal) if and only if there is a closed (bounded) operator B such that $\Theta = \mathrm{gr}(B)$. In this case* (3) *takes the form:*

$$S_\Theta := S_{\mathrm{gr}(B)} = S^* \restriction \ker(\Gamma_1 - B\Gamma_0). \tag{4}$$

In particular, $S_j := S^* \restriction \ker(\Gamma_j) = S_{\Theta_j}$, $j \in \{0, 1\}$, where $\Theta_0 := \begin{pmatrix} \{0\} \\ \mathcal{H} \end{pmatrix}$ and $\Theta_1 := \begin{pmatrix} \mathcal{H} \\ \{0\} \end{pmatrix} = \mathrm{gr}(\mathbb{O})$ where $\mathbb{O}$ denotes the zero operator in $\mathcal{H}$. Note also that $\widetilde{\mathcal{C}}(\mathcal{H})$ contains the trivial linear relations $\{0\} \times \{0\}$ and $\mathcal{H} \times \mathcal{H}$ parameterizing the extensions S and S^*, respectively, for any boundary triplet Π.

2.3. Gamma field and Weyl function

It is well known that Weyl function is an important tool in the direct and inverse spectral theory of Sturm-Liouville operators. In [11, 12] the concept of Weyl function was generalized to the case of an arbitrary symmetric operator S with $n_+(S) = n_-(S) \leqslant \infty$. Following [11] we briefly recall basic facts on Weyl functions and γ-fields associated with a boundary triplet Π.

Definition 2.4 ([11, 12])**.** Let $\Pi = \{\mathcal{H}, \Gamma_0, \Gamma_1\}$ be a boundary triplet for S^* and $S_0 = S^* \restriction \ker(\Gamma_0)$. The operator valued functions $\gamma(\cdot) : \rho(S_0) \to [\mathcal{H}, \mathcal{H}]$ and $M(\cdot) : \; \rho(S_0) \to [\mathcal{H}]$ defined by:

$$\gamma(z) := \left(\Gamma_0 \restriction \mathfrak{N}_z\right)^{-1} \qquad M(z) := \Gamma_1 \gamma(z), \quad z \in \rho(S_0), \tag{5}$$

are called the γ-field and the Weyl function, respectively, corresponding to the boundary triplet Π.

Clearly, the Weyl function can equivalently be defined by:

$$M(z)\Gamma_0 f_z = \Gamma_1 f_z, \qquad f_z \in \mathfrak{N}_z, \quad z \in \rho(S_0). \tag{6}$$

The γ-field $\gamma(\cdot)$ and the Weyl function $M(\cdot)$ in (5) are well defined. Moreover, both $\gamma(\cdot)$ and $M(\cdot)$ are holomorphic on $\rho(S_0)$ and the following relations:

$$\gamma(z) = \big(I + (z-\zeta)(S_0 - z)^{-1}\big)\gamma(\zeta),\ z, \zeta \in \rho(S_0), \tag{7}$$

and

$$M(z) - M(\zeta)^* = (z - \overline{\zeta})\gamma(\zeta)^*\gamma(z),\ z, \zeta \in \rho(S_0), \tag{8}$$

hold. Identity (8) yields that $M(\cdot)$ is $[\mathcal{H}]$-valued Nevanlinna function ($M(\cdot) \in R[\mathcal{H}]$), i.e. $M(\cdot)$ is $[\mathcal{H}]$-valued holomorphic function on $\mathbb{C}_\pm$ satisfying:

$$M(z) = M(\overline{z})^* \qquad \text{and} \qquad \frac{\operatorname{Im}(M(z))}{\operatorname{Im}(z)} \geqslant 0,\ z \in \mathbb{C}_+ \cup \mathbb{C}_-. \tag{9}$$

It also follows from (8) that $0 \in \rho(\operatorname{Im}(M(z)))$ for all $z \in \mathbb{C}_\pm$.

2.4. Krein-type formula for resolvents

Let $\Pi = \{\mathcal{H}, \Gamma_0, \Gamma_1\}$ be a boundary triplet for S^*, $M(\cdot)$ and $\gamma(\cdot)$ the corresponding Weyl function and γ-field, respectively. For any proper (not necessarily self-adjoint) extension $\widetilde{S}_\Theta \in \operatorname{Ext}_S$ with non-empty resolvent set $\rho(\widetilde{S}_\Theta)$ the following Krein-type formula holds (cf. [11, 12]):

$$(S_\Theta - z)^{-1} - (S_0 - z)^{-1} = \gamma(z)(\Theta - M(z))^{-1}\gamma^*(\overline{z}),\ z \in \rho(S_0) \cap \rho(S_\Theta). \tag{10}$$

Formula (10) extends the known Krein formula for canonical resolvents to the case of any $S_\Theta \in \operatorname{Ext}_S$ with $\rho(S_\Theta) \neq \emptyset$. Moreover, due to relations (3), (4) and (5) formula (10) is related to the boundary triplet Π. We emphasize, that this relation makes it possible to apply the Krein-type formula (10) to boundary value problems (see, e.g., [13, 14]).

2.5. Scattering

Let S be a densely defined closed symmetric operator with finite equal deficiency indices $n_\pm(S)$ and $\Pi = \{\mathcal{H}, \Gamma_0, \Gamma_1\}$ is a boundary triplet for S^*, Let $S_0 = S^* \restriction \ker\Gamma_0$ and S_Θ is a self-adjoint extension corresponding to $\Theta \in \tilde{C}(\mathcal{H})$. As $\dim\mathcal{H}$ is finite, by 10

$$(S_\Theta - z)^{-1} - (S_0 - z)^{-1}, \tag{11}$$

is a finite rank operator and the system $\{S_\Theta, S_0\}$ is a so-called complete scattering system, i.e. the wave operators:

$$W_\pm(S_\Theta, S_0) = s - \lim_{t \to \pm\infty} e^{itS_\Theta} e^{-itS_0} P^{ac}(S_0) \tag{12}$$

exists and they are complete, i.e. their ranges coincide with the absolutely continuous subspace $\mathfrak{H}^{ac}(S_\Theta)$ of S_Θ (see, e.g. [17], [15], [16]). By $P^{ac}(S_0)$ we denote the orthogonal projection on absolutely continuous subspace $\mathfrak{H}^{ac}(S_0)$ of S_0. The scattering operator $S(S_\Theta, S_0)$ of a scattering system $\{S_\Theta, S_0\}$ is defined as:

$$S(S_\Theta, S_0) = W_+(S_\Theta, S_0)^* W_-(S_\Theta, S_0). \tag{13}$$

If we regard the scattering operator as an operator in $\mathfrak{H}^{ac}(S_0)$ then it becomes unitary and commutes with absolutely continuous part:

$$S_0^{ac} = S_0 \restriction \mathfrak{H}^{ac}(S_0) \cap \operatorname{dom}(S_0). \tag{14}$$

of S_0 and thus it is unitarily equivalent to a multiplication operator induced by a family $\{S_\Theta(z)\}$ of unitary operators in a spectral representation of S_0^{ac} ([17], Proposition 9.57). Tis family is called a scattering matrix of a scattering system $S(S_\Theta, S_0)$.

Since the dimension $\dim\mathcal{H}$ is finite then the Weyl function $M(\cdot)$ corresponding to boundary triplet $\Pi = \{\mathfrak{H}, \Gamma_0, \Gamma_1\}$ is a matrix-valued Nevanlinna function. By Fatous theorem ([18]), the limit:

$$M(\lambda + i0) = \lim_{\varepsilon \to 0+0} M(\lambda + i\varepsilon) \tag{15}$$

exists for almost all $\lambda \in \mathbb{R}$. We denote the set of real point where the limit exists by Σ^M. We will use the notation:

$$\mathcal{H}_{M(\lambda)} = \operatorname{ran}(M(\lambda)), \quad \lambda \in \Sigma^M. \tag{16}$$

By $P_{M(\lambda)}$ we will denote the orthogonal projection on $\mathcal{H}_{M(\lambda)}$.

We will also use the notation:

$$N_\Theta(z) = (\Theta - M(z))^{-1}, \quad z \in \mathbb{C} \setminus \mathbb{R}, \tag{17}$$

where $\Theta \in \tilde{C}(\mathcal{H})$ is a self-adjoint relation corresponding to S_Θ. This function is well defined and the limit:

$$N_\Theta(\lambda + i0) = (\Theta - M(\lambda + i0))^{-1}, \tag{18}$$

exists almost for every $\lambda \in \mathbb{R}$. This set we will denote as Σ^N.

Theorem 2.5. *([14]) Let S be a densely defined symmetric operator with finite deficiency indices in separable Hilbert space $\mathfrak{H}$, let Π be a boundary triplet corresponding to S^* with corresponding Weyl function $M(\cdot)$, S_Θ is a self-adjoint extension of S, $S_0 = S^* \restriction \ker \Gamma_0$, $\Theta \in \tilde{C}(\mathcal{H})$, then in $L^2(\mathbb{R}, d\lambda, \mathcal{H}_{M(\lambda)})$ the scattering matrix of the complete scattering system $\{S_\Theta, S_0\}$ is given by:*

$$\mathfrak{S}_\Theta(\lambda) = I_{\mathcal{H}_{M(\lambda)}} + 2i\sqrt{\Im(M(\lambda+i0))}N_\theta(\lambda+i0)\sqrt{\Im(M(\lambda+i0))}, \tag{19}$$

for $\lambda \in \Sigma^M \cap \Sigma^N$.

3. Model construction

3.1. An electron in quantum graph

Let us consider a Hilbert space $\mathfrak{H}_1 = L^2(C_r \cup [-1,0])$, $r > 0$, where:

$$C_r := \{x \in \mathbb{R}^2 : \ \rho(x, -1-r) = r\}, \tag{20}$$

so that our Hilbert space is a union of a line segment $[-1,1]$ and a ring with center at the point $(-1-r) \in \mathbb{R}$ of radius r. In a ring we consider an operator (x stands for the angle φ in polar coordinates):

$$A_R f := -\left(\frac{1}{r}\frac{d}{dx} + i\Phi\right)^2 f \tag{21}$$

with domain $\operatorname{dom} A_R = \{f \in W^{2,2}[0,2\pi] : f(0) = f(2\pi) = 0\}$. Let us show that the operator is self-adjoint. Integrating by parts, we have:

$$(A_R f, g) = -\int_0^{2\pi}\left(\frac{1}{r^2}f'' - \frac{2i}{r}\Phi f' - \Phi^2 f\right)\overline{g}dx = -\frac{1}{r^2}\int_0^{2\pi} f''\overline{g}dx + \frac{2i}{r}\Phi\int_0^{2\pi} f'\overline{g}dx - \Phi^2\int_0^{2\pi} f\overline{g}dx =$$

$$-\frac{1}{r^2}\left(f'(2\pi)\overline{g}(2\pi) - f'(0)\overline{g}(0) + f(0)\overline{g}'(0) - f(2\pi)\overline{g}'(2\pi) + \int_0^{2\pi} f\overline{g}''dx\right) +$$

$$\frac{2\Phi}{r}\left(i\left(f(2\pi)\overline{g}(2\pi) - f(0)\overline{g}(0)\right) + \int_0^{2\pi} f\overline{ig}dx\right) + \Phi^2\int_0^{2\pi} f\overline{g}dx =$$

$$-\frac{1}{r^2}\left(f'(2\pi)\overline{g}(2\pi) - f'(0)\overline{g}(0) + f(0)\overline{g}'(0) - f(2\pi)\overline{g}'(2\pi)\right) + \frac{2\Phi}{r}i\left(f(2\pi)\overline{g}(2\pi) - f(0)\overline{g}(0)\right) +$$

$$\int_0^{2\pi} f\overline{\left(-\frac{1}{r^2}g'' + \frac{2\Phi}{r}ig' + \Phi^2 g\right)}dx.$$

This proves the statement.

Now we introduce a self-adjoint operator $A_S := -\dfrac{d^2}{dx^2}$ in $L^2[-1,0]$ with domain $\operatorname{dom} A_S = \{f \in W^{2,2}[-1,0] : f(-1) = f(0) = 0\}$.

In compound system we consider an operator A_1 acting in $\mathfrak{H}_1$ as an operator A_R on a circle and A_S on a line segment. To make it symmetric, we restrict it on a set of functions with the conditions:

$$\begin{gathered} f_2(-1) = f_1(0) = f_1(2\pi) \\ f_2'(-1) + \left(\frac{d}{dx} + i\Phi\right)f_1(0) - \left(\frac{d}{dx} + i\Phi\right)f_1(2\pi) = 0 \end{gathered}, \tag{22}$$

where $f_1 \in \operatorname{dom} A_R$, $f_2 \in \operatorname{dom} A_S$. To find the deficiency elements of A_1 we firstly solve the equation $A_R f = zf$ and come to an algebraic equation:

$$-\left(\frac{1}{r}\lambda - i\Phi\right)^2 = z \Leftrightarrow \frac{1}{r}\lambda - i\Phi = \pm\sqrt{z} \tag{23}$$

or $\lambda = i\left(r\Phi \pm r\sqrt{z}\right)$. The deficiency elements (if we choose the branch $\Im\sqrt{z} > 0$) are $e^{irx(\Phi\pm\sqrt{z})}$. For the operator A_S deficiency elements are $e^{\pm i\sqrt{z}}$. To find the deficiency elements of the considered operator A_1, we solve the system of algebraic equations. We start by introducing:

$$f_1 := c_3 e^{irx(\Phi+\sqrt{z})} + c_4 e^{irx(\Phi-\sqrt{z})}, \quad f_2 := c_1 e^{i\sqrt{z}} + c_2 e^{-i\sqrt{z}}, \quad c_i \in \mathbb{C} \tag{24}$$

and for simplicity introduce the notation $a := e^{-i\sqrt{z}}$, $b := e^{i\sqrt{z}}$, $f := e^{2\pi ir(\Phi+\sqrt{z})}$, $d := e^{2\pi ir(\Phi-\sqrt{z})}$. Then, from the boundary conditions, we obtain:

$$\begin{cases} c_1 a + c_2 b = c_3 + c_4, \\ c_3 + c_4 = c_3 f + c_4 d, \\ c_1\sqrt{z}a - c_2\sqrt{z}b + c_3\left(r(\Phi+\sqrt{z})(1-f) + \Phi(1-f)\right) + c_4\left(r(\Phi-\sqrt{z})(1-d) + \Phi(1-d)\right) = 0. \end{cases}$$

Solving the system above, we obtain:

$$f_1 = c_4\frac{d-1}{1-f}e^{irx(\Phi+\sqrt{z})} + c_4 e^{irx(\Phi-\sqrt{z})}, \tag{25}$$

$$\begin{aligned} f_2 = \frac{c_4}{2a}\left(\frac{d-f-2rd+2rdf+2r-2rf}{1-f}\right)e^{i\sqrt{z}x} + \\ \frac{c_4}{2b}\left(\frac{d-f+2rd-2rdf-2r+2rf}{1-f}\right)e^{-i\sqrt{z}x}. \end{aligned} \tag{26}$$

So, the deficiency indices of the operator A_1 are equal to 1, i.e. $n_\pm(A_1) = 1$.

The boundary triplet for the operator A_1 is as follows:

$$\mathcal{H}^{A_1} := \mathbb{C}, \quad \Gamma_0^{A_1} := f(0), \quad \Gamma_1^{A_1} := -f'(0).$$

One immediately checks that the equation (2.2) is satisfied. For simplicity we put $c_4 = 2(1-f)$ in (25) and (26). Then,

$$\Gamma_0^{A_1} f_2 = \frac{1}{a}\left(d-f-2rd+2rdf+2r-2rf\right) + \frac{1}{b}\left(d-f+2rd-2rdf-2r+2rf\right). \tag{27}$$

Putting:

$$u := \frac{1}{a}\left(d-f-2rd+2rdf+2r-2rf\right), \tag{28}$$

$$v := \frac{1}{b}\left(d-f+2rd-2rdf-2r+2rf\right), \tag{29}$$

the γ-field $\gamma^{A_1}(z)$ has the form (in accordance with definition 2.4):

$$\gamma^{A_1}(z) := \frac{1}{u+v}\left(ue^{i\sqrt{z}x} + ve^{-i\sqrt{z}x}\right). \tag{30}$$

Then the Weyl function (in accordance with definition 2.4) is:

$$M^{A_1}(z) := \Gamma_1^{A_1}\gamma^{A_1}(z) = -\frac{i\sqrt{z}(u-v)}{u+v}. \tag{31}$$

To obtain the scattering matrix (19), we have to calculate the limit of the Weyl function (2.4) to the real axis from the upper half-plane. All the calculations with the final expressions are obtained in Appendix A.

3.2. Operator on a half-line

Let us consider an operator:

$$A_2 := -\frac{d^2}{dx^2}, \tag{32}$$

with the domain $\operatorname{dom} A_2 = W_{00}^{2,2} = \{f \in W^{2,2}(0,\infty) : f(0) = f'(0) = 0\}$ in $\mathfrak{H}_2 = L^2(0,\infty)$. It is symmetric and its deficiency indices are $n_\pm(A_3) = 1$. In accordance with [9], the Weyl function for this operator has the following form:

$$M^{A_3}(z) := i\sqrt{z}.$$

It is clear that:

$$\Im M^{A_3}(\lambda) = \Im\left(i\sqrt{\lambda}\right) = \sqrt{\lambda}, \quad \lambda \geqslant 0$$

and 0 otherwise.

3.3. The direct sum of the operators

We consider the Hilbert space $\mathfrak{H} = \mathfrak{H}_1 \oplus \mathfrak{H}_2$ where $\mathfrak{H}_1$ and $\mathfrak{H}_2$ are defined above. We define an operator A as the operator:

$$A := A_1 \oplus A_2. \tag{33}$$

The operator A is symmetric and has deficiency indices $n_{\pm}(A) = 2$. It's Weyl function is obviously given by the expression:

$$M^A(z) = \begin{pmatrix} M^{A_1}(z) & 0 \\ 0 & M^{A_2}(z) \end{pmatrix} = \begin{pmatrix} -\dfrac{i\sqrt{z}(u-v)}{u+v} & 0 \\ 0 & i\sqrt{z} \end{pmatrix}. \tag{34}$$

3.4. Coupling to the two-level system

Now let us couple the considered operator to an operator:

$$T := \begin{pmatrix} 1 & 0 \\ 0 & 2 \end{pmatrix} \tag{35}$$

acting on the Hilbert space $\mathfrak{T} = \mathbb{C}^2$. For this purpose we consider an operator

$$S = A_{\mathfrak{H}} \otimes I_{\mathfrak{T}} + I_{\mathfrak{H}} \otimes T_{\mathfrak{T}}. \tag{36}$$

In accordance with [9], we have:

$$M^S(z) = M^A(z-1) \otimes \begin{pmatrix} 1 & 0 \\ 0 & 0 \end{pmatrix} + M^A(z-2) \otimes \begin{pmatrix} 0 & 0 \\ 0 & 1 \end{pmatrix} = \tag{37}$$

$$\begin{pmatrix} M^{A_1}(z-1) & 0 & 0 & 0 \\ 0 & M^{A_1}(z-2) & 0 & 0 \\ 0 & 0 & M^{A_2}(z-1) & 0 \\ 0 & 0 & 0 & M^{A_2}(z-2) \end{pmatrix}. \tag{38}$$

To find the scattering matrix, we need to calculate the limit of the Weyl function to the real axis which is, obviously:

$$M^S(\lambda) = M^S(\lambda + i0) = \begin{pmatrix} M^{A_1}(\lambda-1) & 0 & 0 & 0 \\ 0 & M^{A_1}(\lambda-2) & 0 & 0 \\ 0 & 0 & M^{A_2}(\lambda-1) & 0 \\ 0 & 0 & 0 & M^{A_2}(\lambda-2) \end{pmatrix}. \tag{39}$$

Now we need to calculate the imaginary part of the obtained limit. This gives us

$$\sqrt{\Im M^S(\lambda)} = \begin{pmatrix} \sqrt{\Im M^{A_1}(\lambda-1)} & 0 & 0 & 0 \\ 0 & \sqrt{\Im M^{A_1}(\lambda-2)} & 0 & 0 \\ 0 & 0 & \sqrt{\Im M^{A_2}(\lambda-1)} & 0 \\ 0 & 0 & 0 & \sqrt{\Im M^{A_2}(\lambda-2)} \end{pmatrix}. \tag{40}$$

3.5. Scattering matrix

Let us take the matrix of parameters Θ in the form ($\alpha, \beta \in \mathbb{C}$):

$$\Theta = \begin{pmatrix} 0 & \alpha & 0 & 0 \\ \overline{\alpha} & 0 & \beta & 0 \\ 0 & \overline{\beta} & 0 & \alpha \\ 0 & 0 & \overline{\alpha} & 0 \end{pmatrix}. \tag{41}$$

Then:

$$N_\Theta(\lambda) = (\Theta - M^S(\lambda))^{-1} = \begin{pmatrix} -M^{A_1}(\lambda-1) & \alpha & 0 & 0 \\ \overline{\alpha} & -M^{A_1}(\lambda-2) & \beta & 0 \\ 0 & \overline{\beta} & -M^{A_2}(\lambda-1) & \alpha \\ 0 & 0 & \overline{\alpha} & -M^{A_2}(\lambda-2) \end{pmatrix}^{-1}. \tag{42}$$

We denote:

$$a_{11} = M^{A_1}(\lambda - 1), \quad a_{22} = M^{A_1}(\lambda - 2), \quad a_{33} = M^{A_2}(\lambda - 1), \quad a_{44} = M^{A_2}(\lambda - 2).$$

Then, one has:

$$N_\Theta = \frac{1}{a_{11}a_{22}a_{33}a_{44} - a_{11}a_{44}|\beta|^2 - a_{11}a_{22}|\alpha|^2 - a_{33}a_{44}|\alpha|^2 + |\alpha|^4}\cdot$$

$$\left(\begin{pmatrix} a_{44}(-a_{22}a_{33} + |\beta|^2) + |\alpha|^2 a_{22} & |\alpha|^2\alpha - \alpha a_{33}a_{44} & 0 & 0 \\ |\alpha|^2\overline{\alpha} - \overline{\alpha}a_{33}a_{44} & -a_{11}a_{33}a_{44} + |\alpha|^2 a_{11} & 0 & 0 \\ -\overline{\alpha}\overline{\beta}a_{44} & -\overline{\beta}a_{11}a_{44} & 0 & 0 \\ -\overline{\alpha}^2\overline{\beta} & -a_{11}\overline{\alpha}\overline{\beta} & 0 & 0 \end{pmatrix} + \right.$$

$$\left.\begin{pmatrix} 0 & 0 & -\alpha\beta a_{44} & -\alpha^2\beta \\ 0 & 0 & -\beta a_{11}a_{44} & -\alpha\beta a_{11} \\ 0 & 0 & -a_{11}a_{22}a_{44} + |\alpha|^2 a_{44} & |\alpha|^2\alpha - a_{11}a_{22}\alpha \\ 0 & 0 & |\alpha|^2\overline{\alpha} - a_{11}a_{22}\overline{\alpha} & -a_{33}(a_{11}a_{22} - |\alpha|^2) + a_{11}|\beta|^2 \end{pmatrix}\right).$$

Assuming:

$$\Delta := \frac{2i}{a_{11}a_{22}a_{33}a_{44} - a_{11}a_{44}|\beta|^2 - a_{11}a_{22}|\alpha|^2 - a_{33}a_{44}|\alpha|^2 + |\alpha|^4},$$

we, finally, obtain:

$$\mathfrak{S}_\Theta(\lambda) = I + \Delta\cdot$$

$$\left(\begin{pmatrix} \Im a_{11}\left(a_{44}(-a_{22}a_{33} + |\beta|^2) + |\alpha|^2 a_{22}\right) & \sqrt{\Im a_{11}\Im a_{22}}\left(|\alpha|^2\alpha - \alpha a_{33}a_{44}\right) & 0 & 0 \\ \sqrt{\Im a_{11}\Im a_{22}}\left(|\alpha|^2\overline{\alpha} - \overline{\alpha}a_{33}a_{44}\right) & \Im a_{22}\left(-a_{11}a_{33}a_{44} + |\alpha|^2 a_{11}\right) & 0 & 0 \\ -\sqrt{\Im a_{11}\Im a_{33}}\overline{\alpha}\overline{\beta}a_{44} & -\sqrt{\Im a_{22}\Im a_{33}}\overline{\beta}a_{11}a_{44} & 0 & 0 \\ -\sqrt{\Im a_{11}\Im a_{44}}\overline{\alpha}^2\overline{\beta} & -\sqrt{\Im a_{22}\Im a_{44}}a_{11}\overline{\alpha}\overline{\beta} & 0 & 0 \end{pmatrix} + \right.$$

$$\left.\begin{pmatrix} 0 & 0 & -\sqrt{\Im a_{11}\Im a_{33}}\alpha\beta a_{44} & -\sqrt{\Im a_{11}\Im a_{44}}\alpha^2\beta \\ 0 & 0 & -\sqrt{\Im a_{22}\Im a_{33}}\beta a_{11}a_{44} & -\sqrt{\Im a_{22}\Im a_{44}}\alpha\beta a_{11} \\ 0 & 0 & \Im a_{33}\left(-a_{11}a_{22}a_{44} + |\alpha|^2 a_{44}\right) & \sqrt{\Im a_{33}\Im a_{44}}\left(|\alpha|^2\alpha - a_{11}a_{22}\alpha\right) \\ 0 & 0 & \sqrt{\Im a_{33}\Im a_{44}}\left(|\alpha|^2\overline{\alpha} - a_{11}a_{22}\overline{\alpha}\right) & \Im a_{44}\left(-a_{33}(a_{11}a_{22} - |\alpha|^2) + a_{11}|\beta|^2\right) \end{pmatrix}\right).$$

Now, we have to take the projection onto the absolutely continuous part, we calculate:

$$\left(\begin{pmatrix} 1 & 0 \\ 0 & 1 \end{pmatrix} \otimes \begin{pmatrix} 1 & 0 \end{pmatrix}\right) \mathfrak{S}_\Theta(\lambda) \left(\begin{pmatrix} 1 & 0 \\ 0 & 1 \end{pmatrix} \otimes \begin{pmatrix} 1 \\ 0 \end{pmatrix}\right) +$$

$$\left(\begin{pmatrix} 1 & 0 \\ 0 & 1 \end{pmatrix} \otimes \begin{pmatrix} 0 & 1 \end{pmatrix}\right) \mathfrak{S}_\Theta(\lambda) \left(\begin{pmatrix} 1 & 0 \\ 0 & 1 \end{pmatrix} \otimes \begin{pmatrix} 0 \\ 1 \end{pmatrix}\right),$$

and obtain:

$$\begin{pmatrix} 2 + \Delta\Im a_{11}\left(a_{44}(-a_{22}a_{33} + |\beta|^2) + |\alpha|^2 a_{22}\right) + \Delta\Im a_{22}\left(-a_{11}a_{33}a_{44} + |\alpha|^2 a_{11}\right) & 0 \\ -\Delta\sqrt{\Im a_{11}\Im a_{33}}\overline{\alpha}\overline{\beta}a_{44} - \Delta\sqrt{\Im a_{22}\Im a_{44}}a_{11}\overline{\alpha}\overline{\beta} & 0 \end{pmatrix} +$$

$$\begin{pmatrix} 0 & -\Delta\sqrt{\Im a_{11}\Im a_{33}}\alpha\beta a_{44} - \Delta\sqrt{\Im a_{22}\Im a_{44}}\alpha\beta a_{11} \\ 0 & 2 + \Delta\Im a_{33}\left(-a_{11}a_{22}a_{44} + |\alpha|^2 a_{44}\right) + \Delta\Im a_{44}\left(-a_{33}(a_{11}a_{22} - |\alpha|^2) + a_{11}|\beta|^2\right) \end{pmatrix}.$$

We are interested in the argument of the coefficient:

$$r := 2 + \Delta\Im a_{33}\left(-a_{11}a_{22}a_{44} + |\alpha|^2 a_{44}\right) + \Delta\Im a_{44}\left(-a_{33}(a_{11}a_{22} - |\alpha|^2) + a_{11}|\beta|^2\right). \tag{43}$$

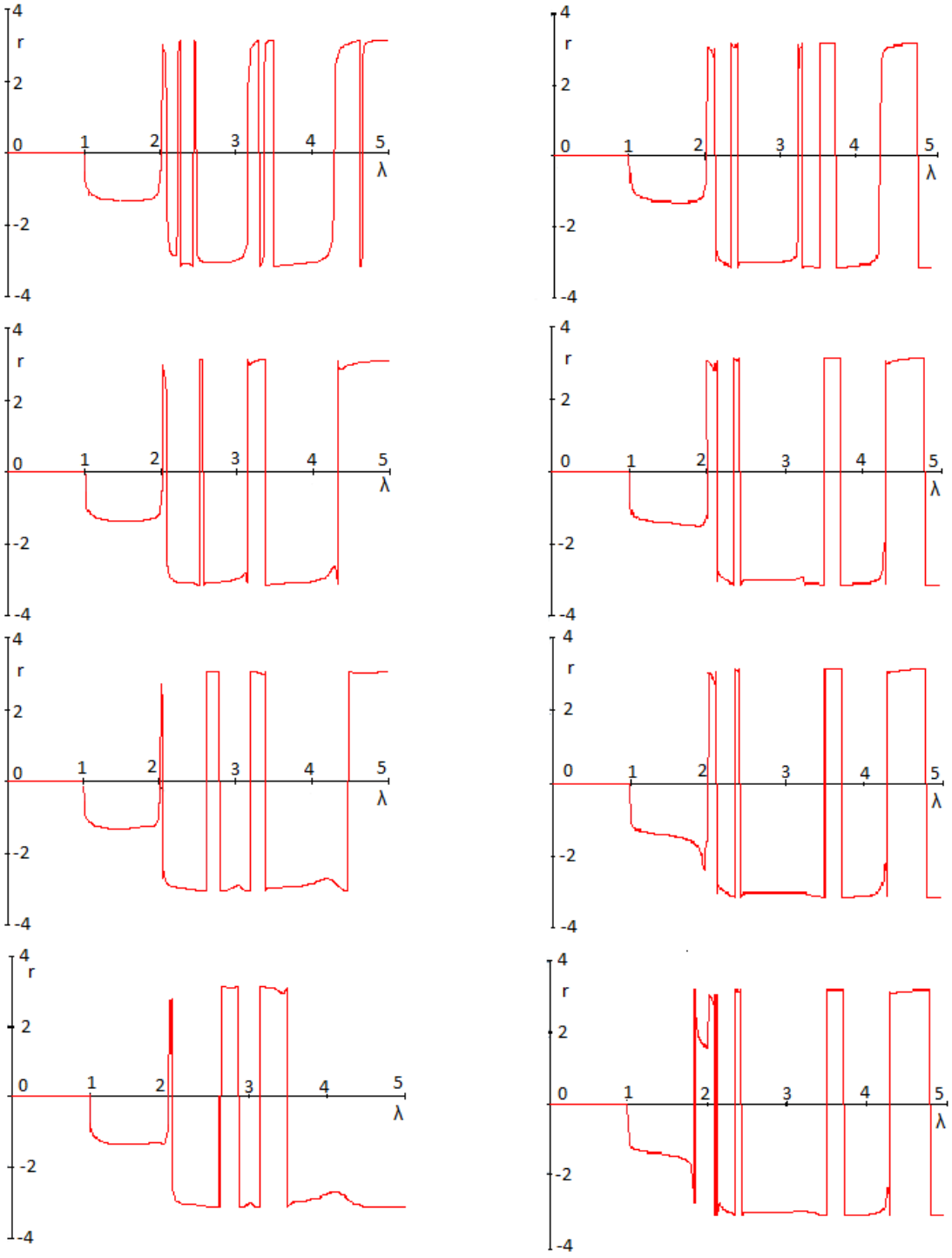

FIG. 1. Argument of the reflection coefficient $\arg r$ as a function of energy λ. Left column: $\alpha = \beta = 1/3$, values of Φ vary from top to bottom through, consequently, $1/4, 1/5, 1/8, 1/10$; right column: $\Phi = \beta = 1/3$, α vary from top to bottom through, consequently, $1/3, 1/5, 1/8, 1/12$ (arbitrary units)

3.6. Results and discussion

The dependence of the scattering phase $\arg r$ on the energy is shown in Fig. 1. Jumps of the phase correspond to resonances which positions depend on the magnetic field. One can observe this dependence looking through the left column of pictures. Naturally, for a weaker magnetic field, one has resonances closer to the corresponding eigenvalues of the operator for the ring without the magnetic field. As for influence of parameter α, it is shown in the left column of pictures in Fig. 1. Parameter α is responsible for the connection between the ring and the segment. Note that the coupling condition between the ring and the segment (22) depends on the magnetic field Φ (due to the "magnetic" derivatives the scattering phase changes). This explains the influence of α on the resonance position. As for β, which is responsible for the connection between the segment and the half-line, it does not influences on the resonance position essentially due to the absence of Φ in the coupling condition. Correspondingly, we did not present the pictures for different values of β (their variations are not essential).

Acknowledgements

This work was partially financially supported by the Government of the Russian Federation (grant 08-08), by grant 16-11-10330 of Russian Science Foundation.

References

[1] Dauber J., Oellers M., Venn F., Epping A., Watanabe K., Taniguchi T., Hassler F., Stampfer C. Aharonov-Bohm oscillations and magnetic focusing in ballistic graphene rings. *Phys. Rev. B*, 2017, **96**, P. 205407.
[2] Chakraborty T., Manaselyan A., Barseghyan M. Irregular Aharonov-Bohm effect for interacting electrons in a ZnO quantum ring. *J Phys Condens Matter*, 2017, **29**(7), P. 075605.
[3] Caudrelier V., Mintchev M., Ragoucy E. Exact scattering matrix of graphs in magnetic field and quantum noise. *J. Math. Phys.*, 2014, **55**, P. 083524.
[4] Exner P., Lotoreichik V., Perez-Obiol A. On the bound states of magnetic Laplacians on wedges. *Rep. Math. Phys*, 2018, **82**, P. 161–185.
[5] Kurasov P., Serio A. Topological damping of Aharonov-Bohm effect: quantum graphs and vertex conditions. *Nanosystems: Phys. Chem. Math.*, 2015, **6**(3), P. 309–319.
[6] Eremin D.A., Grishanov E.N., Nikiforov D.S., Popov I.Y. Wave dynamics on time-depending graph with Aharonov-Bohm ring. *Nanosystems: Phys. Chem. Math.*, 2018, **9**(4), P. 457–463.
[7] Chatterjee A., Smolkina M.O., Popov I.Y. Persistent current in a chain of two Holstein-Hubbard rings in the presence of Rashba spin-orbit interaction. *Nanosystems: Phys. Chem. Math.*, 2019, **10**(1), P. 50–62.
[8] G. Berkolaiko, P. Kuchment, *Introduction to Quantum Graphs*. AMS, Providence, 2012.
[9] Boitsev A.A., Brasche J., Malamud M., Neidhardt H., Popov I.Y. Boundary Triplets, Tensor Products and Point Contacts to Reservoirs Annales Henri Poincare, IET, 2018, **19**(9), P. 2783–2837.
[10] Derkach V. A., Malamud M. M., 1991, Generalized resolvents and the boundary value problems for Hermitian operators with gaps. *J. Funct. Anal.*, **95**(1), P. 1–95.
[11] Malamud M. M. Some classes of extensions of a Hermitian operator with lacunae, *Ukraïn. Mat. Zh.*, 1992, **44**(2), P. 215–233.
[12] Malamud M. M., 1992, Some classes of extensions of a Hermitian operator with lacunae, *Ukraïn. Mat. Zh.*, **44**(2), P. 215–233.
[13] Boitsev A. A., Brasche J., Neidhardt H., Popov I. Y., A model of electron transport through a boson cavity. *Nanosystems: Phys. Chem. Math.*, 2018, **9**, P. 171–178.
[14] Behrndt J., Malamud M.M., Neidhardt H. Scattering matrices and Weyl functions. *Proc. Lond. Math. Soc.*, 2008, **97**, P. 568–598.
[15] Kato T. *Perturbation Theory for Linear Operators, Die Grundlehren der mathematischen Wissenschaften*, Band 132, Springer-Verlag New York, Inc., New York 1966.
[16] Yafaev D.R. *Mathematical Scattering Theory: General Theory*, Translations of Mathematical Monographs, 105. American Mathematical Society, Providence, RI, 1992.
[17] Baumgartel H., Wollenberg M. *Mathematical Scattering Theory*, Akademie-Verlag, Berlin, 1983.
[18] Donoghue W.F. *Monotone Matrix Functions and Analytic Continuation*, Springer Verlag, Berlin and New York, 1974.

Appendix A: Limit of the Weyl function M^{A_1}

Let us investigate $M^{A_1}(\lambda)$, $\lambda \in \mathbb{R}$ and calculate it's imaginary part. We put $l = 2\pi r$ and calculate

$$u = -2\sin(l\sqrt{\lambda})\sin(l\Phi+\sqrt{\lambda}) - 4r\cos(l\sqrt{\lambda})\cos(\sqrt{\lambda}+l\Phi) + 2r\cos(2l\Phi+\sqrt{\lambda}) + 2r\cos\sqrt{\lambda} +$$
$$i\left(2\sin(l\sqrt{\lambda})\cos(l\Phi+\sqrt{\lambda}) - 4r\cos(l\sqrt{\lambda})\sin(\sqrt{\lambda}+l\Phi) + 2r\sin(2l\Phi+\sqrt{\lambda}) + 2r\sin\sqrt{\lambda}\right)$$

and

$$v = -2\sin(l\sqrt{\lambda})\sin(l\Phi-\sqrt{\lambda}) + 4r\cos(l\sqrt{\lambda})\cos(\sqrt{\lambda}-l\Phi) - 2r\cos(2l\Phi-\sqrt{\lambda}) - 2r\cos\sqrt{\lambda} +$$
$$i\left(2\sin(l\sqrt{\lambda})\cos(l\Phi-\sqrt{\lambda}) + 4r\cos(l\sqrt{\lambda})\sin(l\Phi-\sqrt{\lambda}) - 2r\sin(2l\Phi-\sqrt{\lambda}) + 2r\sin\sqrt{\lambda}\right).$$

Then,

$$u+v=-4\sin(l\sqrt{\lambda})\sin(l\Phi)\cos\sqrt{\lambda}+8r\cos(l\sqrt{\lambda})\sin\sqrt{\lambda}\sin(l\Phi)-4r\sin(2l\Phi)\sin\sqrt{\lambda}+$$
$$i\left(4\sin(l\sqrt{\lambda})\cos(l\Phi)\cos\sqrt{\lambda}-8r\cos(l\sqrt{\lambda})\sin\sqrt{\lambda}\cos(l\Phi)+4r\cos(2l\Phi)\sin\sqrt{\lambda}+4r\sin\sqrt{\lambda}\right).$$

If $\lambda<0$, then $\sqrt{\lambda}$ is purely complex, $\cos\sqrt{\lambda}\in\mathbb{R}$ and $\sin\sqrt{\lambda}$ are purely complex. Then for $\lambda\geqslant 0$ the lines above give real and imaginary part of $u+v$, i.e.

$$\Re(u+v)=$$
$$-4\sin(l\sqrt{\lambda})\sin(l\Phi)\cos\sqrt{\lambda}+8r\cos(l\sqrt{\lambda})\sin\sqrt{\lambda}\sin(l\Phi)-4r\sin(2l\Phi)\sin\sqrt{\lambda}$$
$$\Im(u+v)=$$
$$4\sin(l\sqrt{\lambda})\cos(l\Phi)\cos\sqrt{\lambda}-8r\cos(l\sqrt{\lambda})\sin\sqrt{\lambda}\cos(l\Phi)+4r\cos(2l\Phi)\sin\sqrt{\lambda}+4r\sin\sqrt{\lambda}$$

and for $\lambda<0$

$$\Re(u+v)=$$
$$i\left(4\sin(l\sqrt{\lambda})\cos(l\Phi)\cos\sqrt{\lambda}-8r\cos(l\sqrt{\lambda})\sin\sqrt{\lambda}\cos(l\Phi)+4r\cos(2l\Phi)\sin\sqrt{\lambda}+4r\sin\sqrt{\lambda}\right)$$
$$\Im(u+v)=$$
$$\frac{1}{i}\left(-4\sin(l\sqrt{\lambda})\sin(l\Phi)\cos\sqrt{\lambda}+8r\cos(l\sqrt{\lambda})\sin\sqrt{\lambda}\sin(l\Phi)-4r\sin(2l\Phi)\sin\sqrt{\lambda}\right)$$

In the same way we consider

$$u-v=$$
$$-4\sin(l\sqrt{\lambda})\cos(l\Phi)\sin\sqrt{\lambda}-8r\cos(l\sqrt{\lambda})\cos\sqrt{\lambda}\cos(l\Phi)+4r\cos(2l\Phi)\cos\sqrt{\lambda}+4r\cos\sqrt{\lambda}+$$
$$i\left(4\sin(l\sqrt{\lambda})\sin(l\Phi)\sin\sqrt{\lambda}-8r\cos(l\sqrt{\lambda})\cos\sqrt{\lambda}\sin(l\Phi)+4r\sin(2l\Phi)\cos\sqrt{\lambda}\right).$$

In this case for any $\lambda\in\mathbb{R}$ we have

$$\Re(u-v)=$$
$$-4\sin(l\sqrt{\lambda})\cos(l\Phi)\sin\sqrt{\lambda}-8r\cos(l\sqrt{\lambda})\cos\sqrt{\lambda}\cos(l\Phi)+4r\cos(2l\Phi)\cos\sqrt{\lambda}+4r\cos\sqrt{\lambda}$$
$$\Im(u-v)=$$
$$4\sin(l\sqrt{\lambda})\sin(l\Phi)\sin\sqrt{\lambda}-8r\cos(l\sqrt{\lambda})\cos\sqrt{\lambda}\sin(l\Phi)+4r\sin(2l\Phi)\cos\sqrt{\lambda}.$$

Then

$$M^A(\lambda)=-i\sqrt{\lambda}\frac{(\Re(u-v)+i\Im(u-v))\,(\Re(u+v)-i\Im(u+v))}{\Re^2(u+v)+\Im^2(u+v)}.$$

If $\lambda\geqslant 0$, then

$$\Im M^A(\lambda)=-\sqrt{\lambda}\frac{\Re(u+v)\Re(u-v)+\Im(u+v)\Im(u-v)}{\Re^2(u+v)+\Im^2(u+v)},$$

and if $\lambda<0$, then

$$\Im M^A(\lambda)=\sqrt{|\lambda|}\frac{\Im(u-v)\Re(u+v)-\Re(u-v)\Im(u+v)}{\Re^2(u+v)+\Im^2(u+v)}.$$

NANOSYSTEMS: PHYSICS, CHEMISTRY, MATHEMATICS, 2019, 10 (2), P. 141–146

Temperature dependence of quantum correlations in 1D macromolecular chains

A. V. Chizhov[1,2], D. Chevizovich[3], Z. Ivić[3], S. Galović[3]

[1]Bogoliubov Laboratory of Theoretical Physics, Joint Institute for Nuclear Research, Joliot-Curie, 6, Dubna, 141980, Russia

[2]Dubna State University, Universitetskaya, 19, Dubna, 141980, Russia

[3]Vinča Institute of Nuclear Sciences, 11001 Belgrade, Serbia

chizhov@theor.jinr.ru

PACS 05.60.Gg, 63.20.-e, 03.65.-w **DOI 10.17586/2220-8054-2019-10-2-141-146**

We investigate the problem of generating quantum correlations between different sites of a macromolecular chain by vibronic excitation depending on the temperature. The influence of temperature on the model dynamics is taken into account by employing the partial-dressing method based on the modified LangFirsov unitary transformation under the assumption that the chain collective oscillations are in the thermal equilibrium state. To describe quantum correlations between the chain sites in the case of the initial single-vibronic excitation, we use two-time correlation functions of the second order and the logarithmic negativity as the degree of entanglement. We find that at certain temperatures for various model parameters time-stable entanglement can occur in the chain.

Keywords: energy transport, vibron, small polaron, correlation functions, entanglement.

Received: 2 February 2019

Revised: 28 February 2019

1. Introduction

The study of macromolecular chains is important from the point of view of the large role they play in biology and technology. In particular, it is believed that protein molecules act as mediators in the mechanism providing energy for diverse biological processes such as photochemical reactions, crossmembrane ion transfer and signal transduction, muscle contraction, cellular mobility [1]. Macromolecular systems, due to their inherent miniature characteristics, are considered as very promising materials for the manufacture of microelectronic and optoelectronic devices [2–4]. Recently, DNA molecules and various polymers have been used for recording and storing information which is important for the development of molecular and quantum computers [5–8].

The first explanation of the problem of energy transport along a polypeptide chain based on the quantum mechanics was proposed by Davydov [9, 10]. Davydov's model supposed that, due to the exciton interaction with phonon modes, excitation forms a soliton that is more stable than the bare excitation. Nevertheless, due to the dipole-dipole coupling the life-time of the chain collective excitations appeared to be rather short. To overcome this problem, it was suggested that the energy losses may be prevented by the self-trapping mechanism caused by induced local distortion of the molecular chain. In this case, a vibronic excitation being surrounded by local lattice distortion may propagate in a polaron form along the chain with minimal energy losses for a long time [11, 12].

One of the main tasks for implementing a quantum computer is the problem of creating sustainable entanglement. In this article, based on the concept of partial dressing, we analyze the possibility of generating quantum correlations in the molecular chain by vibronic excitation, as well as the conditions for their stable existence in time. We focus on studying the question of the temperatures at which long-lived entanglement can arise for different regimes of the molecular chain that can be helpful for using macromolecular systems in quantum computing.

2. Model

We consider a 1D macromolecular periodic polymer chain, in which the transfer of vibronic excitation from one molecule to neighboring molecules occurs due to hopping mechanism because of the resonance interaction between the molecules.

Then the Hamiltonian of the vibron and phonon subsystem has the form [10]:

$$\begin{aligned}\hat{H} &= \Delta\sum_n \hat{A}_n^\dagger\hat{A}_n - \sum_n J_g\hat{A}_n^\dagger(\hat{A}_{n+g}+\hat{A}_{n-g}) + \sum_q \hbar\omega_q\hat{B}_q^\dagger\hat{B}_q \\ &+\frac{1}{\sqrt{N}}\sum_q\sum_n F_q \mathrm{e}^{iqnR_0}\hat{A}_n^\dagger\hat{A}_n(\hat{B}_q+\hat{B}_{-q}^\dagger). \qquad (1)\end{aligned}$$

$\hat{A}_n$ is the vibron annihilation operator on the n-th lattice site, $\hat{B}_q$ is the phonon annihilation operator with the frequency ω_q, Δ is the vibron excitation energy, J_g are hopping constants, R_0 is a distance between sites in the chain, and F_q is the vibron-phonon coupling parameter.

The transition to the polaron picture is achieved by applying the following unitary transformation operator (modified Lang-Firsov transformation) [13–15]:

$$\hat{U} = \exp\left\{-\frac{1}{\sqrt{N}}\sum_q\sum_n f_q \mathrm{e}^{-iqnR_0}\hat{A}_n^\dagger\hat{A}_n(\hat{B}_{-q}-\hat{B}_q^\dagger)\right\}. \tag{2}$$

Here $f_q = \delta\cdot F_q^*/(\hbar\omega_q)$, where $0\le\delta\le 1$ is variational parameter which measures the degree of the vibron dressing.

In terms of such an operator one can introduce operators of new quasiparticles: dressed vibrons $\hat{a}_n = \hat{U}\hat{A}_n\hat{U}^\dagger$ ($\hat{a}_n^\dagger = \hat{U}\hat{A}_n^\dagger\hat{U}^\dagger$), and new phonons $\hat{b}_q = \hat{U}\hat{B}_q\hat{U}^\dagger$ ($\hat{b}_q^\dagger = \hat{U}\hat{B}_q^\dagger\hat{U}^\dagger$).

Then the transformed Hamiltonian takes the form:

$$\begin{aligned}\hat{\tilde{H}} &= \hat{U}\hat{H}\hat{U}^\dagger \\ &= E\sum_n\hat{a}_n^\dagger\hat{a}_n - \sum_n J_g\hat{a}_n^\dagger(\hat{a}_{n+g}\hat{\Phi}_n(g)+\hat{a}_{n-g}\hat{\Phi}_n(-g)) + \sum_q\hbar\omega_q\hat{b}_q^\dagger\hat{b}_q \\ &+ \frac{1}{\sqrt{N}}\sum_q\sum_n(F_q-\hbar\omega_q f_q^*)\mathrm{e}^{iqnR_0}\hat{a}_n^\dagger\hat{a}_n(\hat{b}_q+\hat{b}_{-q}^\dagger) \\ &+ \frac{1}{N}\sum_q[\hbar\omega_q|f_q|^2 - F_q(f_q+f_{-q}^*)]\sum_{n\neq n'}\mathrm{e}^{iqR_0(n-n')}\hat{a}_n^\dagger\hat{a}_n\hat{a}_{n'}^\dagger\hat{a}_{n'},\end{aligned} \tag{3}$$

where

$$E = \Delta - \frac{1}{N}\sum_q[F_q(f_q+f_{-q}^*) - \hbar\omega_q|f_q|^2], \tag{4}$$

$$\hat{\Phi}_n(g) = \exp\left\{\frac{1}{\sqrt{N}}\sum_q f_q\mathrm{e}^{-iqnR_0}(\hat{b}_{-q}-\hat{b}_q^\dagger)(\mathrm{e}^{-iqR_0g}-1)\right\}. \tag{5}$$

In order to account for the influence of the thermal fluctuations on the properties of the autolocalized vibron, we apply the mean-field approach by averaging the transformed Hamiltonian over the phonon subsystem. Defining exciton states in the representation of wave vectors k, which take N discrete values, $k = 2\pi\nu$ ($\nu = 0, \pm1, \pm2\ldots$) in the interval $-\pi/R_0 < k \le \pi/R_0$, by:

$$\hat{a}_k = (1/\sqrt{N})\sum_n \mathrm{e}^{-iknR_0}\hat{a}_n, \tag{6}$$

an effective mean-field Hamiltonian reads:

$$\hat{H}_{\mathrm{MF}} = \sum_k E_{\mathrm{SP}}(k)\hat{a}_k^\dagger\hat{a}_k + \sum_q\hbar\omega_q\hat{b}_q^\dagger\hat{b}_q \tag{7}$$

with the energy of the small-polaron band state:

$$E_{\mathrm{SP}}(k) = \Delta - \frac{1}{N}\sum_q[F_q(f_q+f_{-q}^*) - \hbar\omega_q|f_q|^2] - 2J_g\mathrm{e}^{-W_g(T)}\cos(gkR_0), \tag{8}$$

where:

$$W_g(T) = \frac{1}{N}\sum_q|f_q|^2(2\langle n_q(T)\rangle+1)(1-\cos(gqR_0)) \tag{9}$$

is the vibron-band narrowing factor (which characterizes the enhancement of the polaron effective mass), and the phonon average number $\langle n_q(T)\rangle = 1/(\mathrm{e}^{\hbar\omega_q/k_\mathrm{B}T}-1)$.

Using Hamiltonian (7) and (inverse) transformation (6) we can determine the time evolution of the vibronic operators:

$$\hat{a}_n(t) = (1/\sqrt{N})\sum_k \mathrm{e}^{i[knR_0-\omega_k t]}\hat{a}_k(0) = \sum_m\hat{a}_m(0)\cdot(1/N)\sum_k\mathrm{e}^{i[k(n-m)R_0-\omega_k t]}, \tag{10}$$

where $\omega_k = E_{\mathrm{SP}}(k)/\hbar$.

In order to fix the variational parameter δ at temperature T with certain model parameters, we use the procedure of minimization of E_{SP}. In terms of adiabatic parameter $B = 2|J|/(\hbar\omega_C)$ and coupling constant $S = E_\mathrm{B}/(\hbar\omega_C)$

(where $E_{\rm B} = (1/N)\sum\limits_q \{|F_q|^2/(\hbar\omega_q)\}$ is the lattice deformation energy and Debye frequency ω_C) the problem of minimization of $E_{\rm SP}$ reduces effectively to minimization of the function:

$$\mathcal{E}(\tau) = -S(2-\delta)\delta - B{\rm e}^{-\delta^2 W_g(\tau,S)}, \tag{11}$$

where $\tau = k_{\rm B}T/(\hbar\omega_C)$ is the normalized temperature. Thus, the variational parameter δ at temperature T is found by the conditions $\partial\mathcal{E}(\tau)/\partial\delta = 0$ and $\partial^2\mathcal{E}(\tau)/\partial\delta^2 > 0$. This minimization procedure is similar to that used in refs. [16–18] for the study of polaron dressing in various systems of molecular chains.

The behavior of parameter δ for three different temperatures is shown in Fig. 1. It is important to note here that, along with the areas of smooth variation of the parameter, there is also an area of its sharp change. Since the variational parameter measures the degree of vibron dressing, such a sudden change of the value of δ may indicate an abrupt change of the degree of vibron dressing, i.e., a sudden change of its dynamical nature, which can be related to the phenomenon of the polaron crossover.

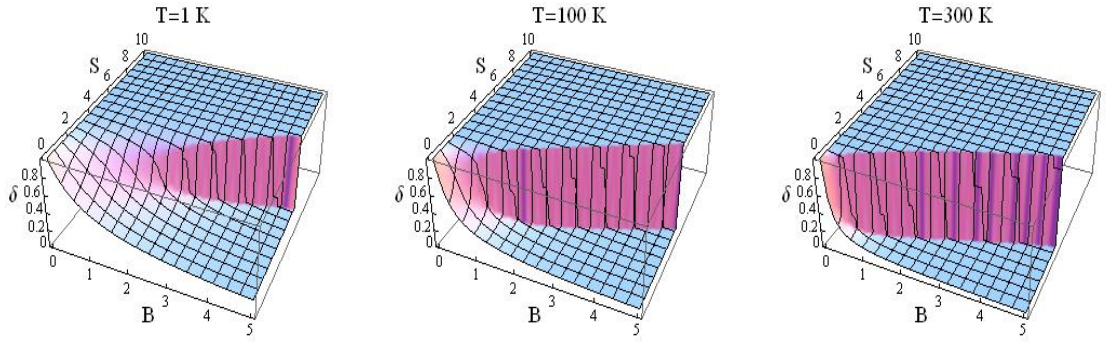

FIG. 1. Vibron dressing factor for $T = 1$ K, $T = 100$ K, and $T = 300$ K ($\omega_C = 10^{13}$ s^{-1})

The temperature dependence of the energy of a small polaron obtained in this way allows us to investigate quantum correlations that can occur between various sites of the molecular chain after the excitation of one of these sites.

3. Correlation functions

One of the methods for studying quantum correlations is to use correlation function [19]. In the case of single-vibronic excitation of the molecular chain, considered in this paper, full information on quantum correlations will be determined by the two-time correlation function of the second order which is defined as:

$$G^{(1,1)}(m,t_1;n,t_2) = {\rm Tr}\{\hat{\varrho}\hat{a}_m^\dagger(t_1)\hat{a}_n(t_2)\}, \tag{12}$$

where $\hat{\varrho}$ is the density matrix of the initial intramolecular excitation of the chain. This function determines the degree of the quantum (cross)correlation between the m-th and n-th sites of the chain, respectively, at times t_1 and t_2. In addition, the function $G^{(1,1)}(m,t_1;m,t_2)$ corresponds to the auto-correlation of the m-th site at times t_1 and t_2.

The initial density matrix of the chain in the case of a single-vibronic excitation can be determined in the basis of eigenstates of number operators corresponding to the chain sites $\hat{N}_n(0) = \hat{A}_n^\dagger(0)\hat{A}_n(0) = \hat{a}_n^\dagger(0)\hat{a}_n(0) = \hat{n}_n(0)$. If at the initial moment a single-vibration excitation has arisen, e.g., at the l-th site of the chain, then the density matrix can be represented in the form:

$$\hat{\varrho} = |1_l\rangle\langle 1_l| = \hat{a}_l^\dagger(0)|\{0\}\rangle\langle\{0\}|\hat{a}_l(0), \tag{13}$$

where $|\{0\}\rangle$ is the chain vacuum state when all sites are in unexcited (ground) states.

Then, taking into account Eqs. (10) and (13), the correlation function (12) is brought to the form:

$$\begin{aligned} G^{(1,1)}(m,t_1;n,t_2|1_l) &= \langle 1_l|\hat{a}_m^\dagger(t_1)\hat{a}_n(t_2)|1_l\rangle \\ &= \frac{1}{N}\sum_k \exp\{-i[kR_0(m-l)-\omega_k t_1]\}\cdot\frac{1}{N}\sum_{k'}\exp\{i[k'R_0(n-l)-\omega_{k'}t_2]\}. \end{aligned} \tag{14}$$

In macromolecules it is assumed that $N \gg 1$, so in the limit $N \to \infty$ one can use the following limiting relation

$$\frac{1}{N}\sum_k \ldots \to \frac{R_0}{2\pi}\int_{-\pi/R_0}^{\pi/R_0} dk \ldots . \tag{15}$$

It means that:

$$\begin{aligned}\frac{1}{N}\sum_k \mathrm{e}^{i[kR_0(m-n)-\omega_k t]} &\to \frac{R_0}{2\pi}\int_{-\pi/R_0}^{\pi/R_0} dk \exp\{i[kR_0(m-n)-\omega_k t]\} \\ &= i^{m-n}\,\mathrm{e}^{-i[\Delta/\hbar-\omega_C S(2-\delta)\delta]\cdot t}\, J_{m-n}(t\omega_C B\mathrm{e}^{-\delta^2 S\coth(1/2\tau)}) \equiv c_{mn}(t),\end{aligned} \tag{16}$$

where $J_n(x)$ is the Bessel function of the first kind of order n. Thus, the correlation function (14) can be given as:

$$G^{(1,1)}(m,t_1;n,t_2|1_l) = c^*_{ml}(t_1)c_{nl}(t_2). \tag{17}$$

4. Entanglement

As the measure of the degree of entanglement of bipartite states one can use the logarithmic negativity [20]:

$$E_{\mathcal{N}}(\hat{\varrho}) = \log_2 ||\hat{\varrho}^{T_2}|| \tag{18}$$

based on the trace norm:

$$||\hat{\varrho}^{T_2}|| = \mathrm{Tr}\sqrt{(\hat{\varrho}^{T_2})^\dagger \hat{\varrho}^{T_2}} \tag{19}$$

of the partial transpose of the density matrix of a bipartite state:

$$\langle i,j|\hat{\varrho}^{T_2}|k,l\rangle = \langle i,l|\hat{\varrho}|k,j\rangle. \tag{20}$$

For entangled states:

$$||\hat{\varrho}^{T_2}_{\mathrm{ent}}|| = 1 + 2|\sum_i \mu_i| \equiv 1 + 2\mathcal{N}(\hat{\varrho}) > 1, \tag{21}$$

where $\mu_i < 0$ are negative eigenvalues of $\hat{\varrho}^{T_2}_{\mathrm{ent}}$ so that

$$E_{\mathcal{N}}(\hat{\varrho}_{\mathrm{ent}}) > 0. \tag{22}$$

The partial transpose of the reduced density matrix for the sites m and n in the representation of the state vectors $(|10\rangle, |01\rangle, |00\rangle, |11\rangle)$ can be represented in the matrix form:

$$\hat{\varrho}^{T_n}_{\{mn\}}(t) = \begin{pmatrix} |c_{lm}(t)|^2 & 0 & 0 & 0 \\ 0 & |c_{ln}(t)|^2 & 0 & 0 \\ 0 & 0 & 1-|c_{lm}(t)|^2-|c_{ln}(t)|^2 & c^*_{ln}(t)c_{lm}(t) \\ 0 & 0 & c^*_{lm}(t)c_{ln}(t) & 0 \end{pmatrix} \tag{23}$$

which has only one negative eigenvalue:

$$\lambda_N = \frac{1}{2}\Big[1-|c_{lm}(t)|^2-|c_{ln}(t)|^2-\sqrt{(1-|c_{lm}(t)|^2-|c_{ln}(t)|^2)^2+4|c_{lm}(t)|^2|c_{ln}(t)|^2}\Big], \tag{24}$$

so that the logarithmic negativity:

$$\begin{aligned}E_{\mathcal{N}} &= \log_2[1+2|\lambda_N|] \\ &= \log_2\Big[|c_{lm}(t)|^2+|c_{ln}(t)|^2+\sqrt{(1-|c_{lm}(t)|^2-|c_{ln}(t)|^2)^2+4|c_{lm}(t)|^2|c_{ln}(t)|^2}\Big].\end{aligned} \tag{25}$$

5. Results

The behavior of two-site correlation functions and the logarithmic negativity as functions of time and temperature for various model parameters are shown in Figs. 2 and 3. These figures demonstrate the appearance of quantum correlations between chain sites in the processes of energy transfer along the macromolecular chain. Although both figures look similar, however, the scale of the logarithmic negativity amplitude corresponds to the measure of entanglement degree. It is worth noting that at certain temperatures two-site quantum correlations in the chain for various model parameters S and B can become long-lived in time. This is due to the fact that with such system parameters, the condition of full dressing of the vibron is ensured ($\delta \sim 1$) which effectively suppresses the parameter B in the time-dependent argument of the Bessel function in Eq. (16) due to the exponential multiplier. Such a temperature decreases with increasing the coupling constant S and decreasing the adiabatic parameter B. Thus, in the strong-coupling non-adiabatic regime ($S \gg 1$ and $B \ll 1$), time-stable quantum correlations in the chain can occur at low temperatures, while in the weak-coupling adiabatic regime, the entanglement state in

the chain can be maintained at high temperatures. This fact can be used to create optimal conditions for stable entanglement in such macromolecular systems.

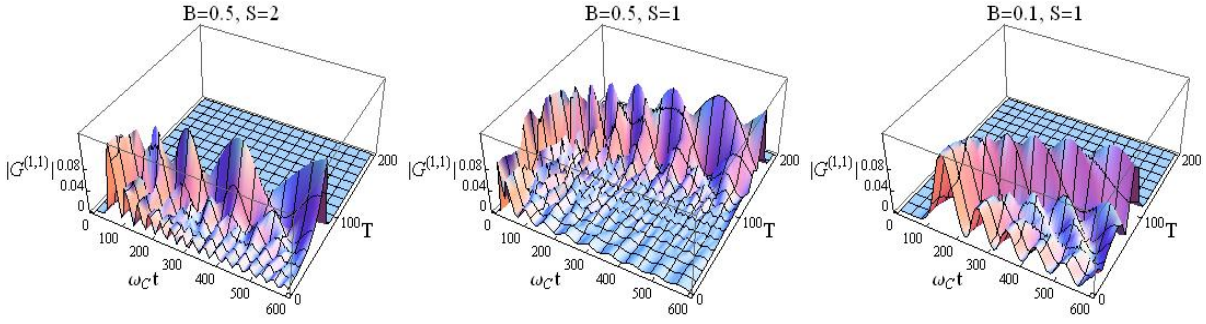

FIG. 2. Absolute value of the equal-time correlation function (17) for the sites $l-m=n-l=5$ depending on the scaled time ($\omega_C = 10^{13}$ s^{-1}) and temperature (in Kelvin) at various model parameters

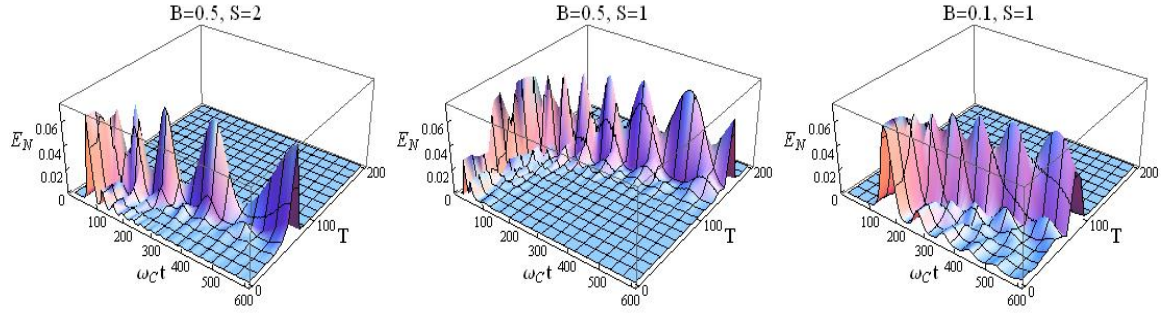

FIG. 3. The same as in Fig. 2 for the logarithmic negativity (25)

6. Conclusion

We analyzed the problem of generating quantum correlations between different chain sites depending on the temperature within the model of vibronic excitation transfer along a macromolecular chain. In order to take into account the effect of temperature on the model dynamics we used the partial-dressing method to treat the interaction problem of a vibron with chain collective oscillations being in the thermal equilibrium state. Based on two-time correlation functions of the second order and the logarithmic negativity as the degree of entanglement, in the case of the initial single-vibronic excitation we found occurrence of time-stable quantum correlations between the chain sites at certain temperatures for various model parameters. Such a temperature was shown to decrease with increasing the coupling constant and decreasing the adiabatic parameter that can be used to create required regimes for stable entanglement in macromolecular systems.

Acknowledgements

This work is partly supported by the bilateral project between the Serbian Ministry of Education and Science and "Theory of Condensed Matter" at JINR, Dubna, and by Serbian Ministry of Education and Science, under Contract Nos. III–45010 and III–45005.

References

[1] Davydov A. S. *Biology and quantum mechanics*. Naukova Dumka, Kiev, 1979, 142–216 (in Russian).
[2] Dekker C., Ratner M. A. Electronic properties of DNA. *Phys. World*, 2001, **14**(8), P. 29–33.
[3] Conwell E. Polarons and transport in DNA. *Topics in Current Chemistry*, 2004, **237**, P. 73–102.
[4] Mirkin C. A., Letsinger R. L., Mucic R. C., Storhoff J. J. A DNA-based method for rationally assembling nanoparticles into macroscopic materials. *Nature*, 1996, **382**(6592), P. 607–609.

[5] Adleman L. M. Molecular computation of solutions to combinatorial problems. *Science*, 1994, **266**(5187), P. 1021–1024.
[6] Kahan M., Gil B., Adar R., Shapiro E. Towards molecular computers that operate in a biological environment. *Physica D: Nonlinear Phenomena*, 2008, **237**(9), P. 1165–1172.
[7] Goldman N., Bertone P., Chen S., Dessimoz C., Leproust E. M., Sipos B., Birney E. Towards practical, high-capacity, low-maintenance information storage in synthesized DNA. *Nature*, 2013, **494**(7435), P. 77–80.
[8] Kumar S. N. A proper approach on DNA based computer. *American Journal of Nanomaterials*, 2015, **3**(1), P. 1–14.
[9] Davydov A. S. The theory of contraction of proteins under their excitation. *J. Theor. Biol*, 1973, **38**(3), P. 559–569.
[10] Davydov A. S. Solitons in molecular systems. *Phys. Scr.*, 1979, **20**(2), P. 387–394.
[11] Lang I. G., Firsov Yu. A. Kinetic theory of semiconductors with low mobility. *ZhETF*, 1962, **43**(5/11), P. 1843–1860.
[12] Yarkony D., Silbey R. Comments on exciton phonon coupling: Temperature dependence. *J. Chem. Phys.*, 1976, **65**(3), P. 1042–1052.
[13] Brown D. W., Ivić Z. Unification of polaron and soliton theories of exciton transport. *Phys. Rev. B*, 1989, **40**(14), P. 9876–9887.
[14] Čevizović D., Galović S., Ivić Z. Nature of the vibron self-trapped states in hydrogenbonded macromolecular chains. *Phys. Rev. E*, 2011, **84**(1), P. 011920-6.
[15] Čevizović D., Galović S., Reshetnyak A., Ivić Z. Vibron self-trapped states in biological macromolecules: Comparison of different theoretical approaches. *J. Phys.: Conf. Ser.*, 2012, **393**(1), P. 012033-8.
[16] Čevizović D., Galović S., Reshetnyak A., Ivić Z. The vibron dressing in α-helicoidal macromolecular chains. *Chin. Phys. B*, 2013, **22**(6), P. 060501-10.
[17] Čevizović D., Ivić Z, Galović S., Reshetnyak A., Chizhov A. On the vibron nature in the system of two parallel macromolecular chains: The influence of interchain coupling. *Physica B*, 2016, **490**, P. 9-15.
[18] Čevizović D., Chizhov A. V., Galović S. Vibron transport in macromolecular chains with squeezed phonons. *Nanosystems: Physics, Chemistry, Mathematics*, 2018, **9**(5), P. 597-602.
[19] Glauber R. J. The quantum theory of optical coherence. *Phys. Rev.*, 1963, **130**(6), P. 2529-2539.
[20] Vidal G., Werner R. F. Computable measure of entanglement. *Phys. Rev. A*, 2002, **65**(3), P. 032314-11.

NANOSYSTEMS: PHYSICS, CHEMISTRY, MATHEMATICS, 2019, 10 (2), P. 147–153

Numerical modeling of ion exchange waveguide for the tasks of quantum computations

V. Gerasimenko, N. Gerasimenko, F. Kiselev, E. Samsonov, S. Kozlov
ITMO University, Kronverkskiy, 49, Saint Petersburg, 197101, Russia
lyagacruz@gmail.com

DOI 10.17586/2220-8054-2019-10-2-147-153

This paper is devoted to the simulation of a single-mode ion-exchange waveguide and the 3dB directional coupler for quantum chips. We performed diffusion modeling of $Na^+ \leftrightarrow K^+$ ions in the $R_2O-SnO_2-SiO_2$ glass and optical modeling by the beam propagation method. A wavelength of 1064 nm was used corresponding to the requirements of the single-mode regime for our waveguide. Simulation of diffusion has shown that the profile of the refractive index of overlapping areas can be modeled by summing two separate profiles, which is crucial for optimizing performance. In the process of optical modeling it was possible to minimize losses on s-bends of changing the width of the bend and reducing the interaction length to zero. So we looked at many aspects of device optimization and performed a design, manufacture and characteristics simulation of a directional 3dB coupler. The overall transmittance of proposed device was evaluated as 0.96.

Keywords: directional coupler, integrated waveguide, quantum computation, integrated optics.

Received: 11 March 2018

Revised: 2 April 2019

1. Introduction

Integrated quantum photonics is a well-known physical platform for implementation of quantum computing. This technology uses principles of linear optics which were shown to be suitable for such tasks since a photon can exist in a superposition of two optical modes (spatial or polarization) and thus serve as a qubit. This approach is called dual-rail encoding and perfectly maps on photonic integrated circuits. Key elements of any linear optical quantum scheme are beamsplitters and phaseshifters.

Almost all modern devices of integrated quantum photonics are produced by lithography, growing on the surface of a crystal or etched semiconductor membranes [1–6]. All of these methods are extremely complicated and expensive, and in addition, all have significant drawbacks.

Etched semiconductor membranes are one of the most exotic quantum photonics materials, as crystals can be generated with the required dimensions. In addition its properties can be modified by doping [6]. At the same time, fabrication of membranes is a very complicated and expensive process, and, being non-coated, is very sensitive to environmental properties. Furthermore waveguides can be very fragile and easily damaged with the slightest manipulation.

Grown crystal waveguides are easier to manufacture and are less fragile then previous ones, but can be made with the same accuracy as membranes [5]. The main problem with these waveguides become apparent when one try to produce thermally or electromagnetically-controlled active elements. This is difficult because of the required optical insulation of these devices and waveguides.

Lithography is one of the most common processes for producing optical quantum computation devices [1, 4]. In comparison with etched membranes and grown crystal waveguides, lithographic ones are much rougher; for this technology, it is impossible to control the device's dimensions to nanometer-level specifications. However, this method is suitable for glasses with small refractive index contrast, so characteristic size of waveguide can be increased to micrometers, for which lithography error becomes negligible. In addition there are no problems with burying these waveguides, and the optical insulation task can be solved easily. Additionally, for a waveguide with sharp refractive index profile, one can determine the mode composition at a given wavelength using relatively simple calculations. On the other hand, for every optical quantum chip, it is crucial to ensure single mode propagation in an area where active element works, so sizes of waveguide and its border defects are close, this can be a source of relatively significant light scattering and losses.

The ion exchange process makes it even easier to obtain a buried waveguide chip, and this device would have specified parameters suitable for feeding through a fiber [7]. An Ion exchanged waveguide has a gradient refractive index profile, which has fewer losses and scattering problems, and thus don't impede proper device operation. Theoretically, it is possible to obtain single-mode gradient waveguide by ion exchange for wavelengths about 1.55 μm.

In this paper, we will consider the ion exchange of $Na^+ \leftrightarrow K^+$ in three-component glasses with the composition $R_2O-SnO_2-SiO_2$, since their optical properties shift [8] and parameters of the diffusion process [9] are known. At the same time, the sizes of the exchanged ions and the strengths of their fields are relatively similar, which allows one to ignore some effects specific for dissimilar ions [10].

This paper describes the numerical simulation of a single-mode ion-exchange waveguide and directional coupler for quantum chips.

2. Diffusion modeling

The first step in modeling of waveguides is the definition of its refractive index profile. This can be obtained via the modeling of the ion-exchange process. In this process, the longest stages are the diffusion of substituting ions into a glass and the displaced ones from a glass [8], so it is the first step to simulate these processes at the stage of production and burying of the waveguide.

Consider the case of ion exchange in thermally-stable glass, to which the mask is applied. In this case, the diffusion coefficient (D) can be considered constant and equal to the smaller of these coefficients for the exchanged ions. The source of substituting ions for creation of a waveguide is set by the boundary conditions: the concentration of these ions (C) on the non-masked part of the glass is constant and equal to the total concentration of alkaline ions in the studied glass. At the waveguide burying stage, the mask is removed, and the entire boundary is covered by the source of initial ions.

The diffusion equation takes the form:

$$\frac{\partial C}{\partial t} = D\nabla^2 C,$$

boundary conditions at the stage of obtaining the waveguide:

$$\begin{aligned} C &= 1, && \text{for non-masked area} \\ \frac{\partial C}{\partial t} &= 0, && \text{for masked area} \\ \frac{\partial C}{\partial t} &= DC, && \text{for inner boundaries} \end{aligned}$$

and at the stage of burying:

$$\begin{aligned} C &= 1, && \text{for melt-glass boundary} \\ \frac{\partial C}{\partial t} &= DC, && \text{for inner boundaries} \end{aligned}$$

Figure 1 describes simulated area graphically.

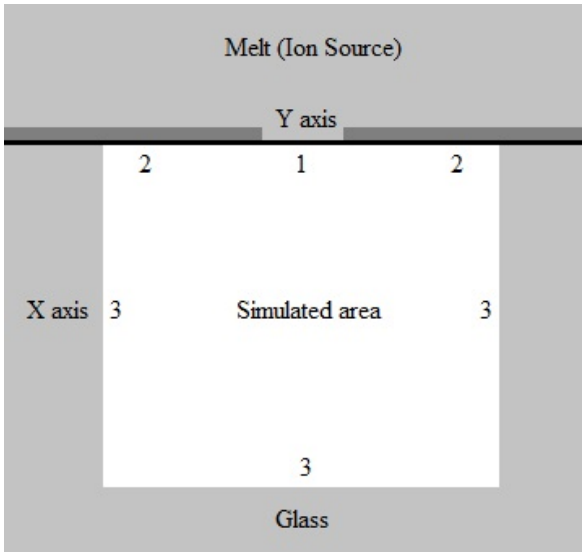

FIG. 1. Graphical description of simulated area. Space only inside white rectangle was modelled. 1 is a mark for non-masked area, 2 for masked one when waveguide is manufacturing. When it is burying both of the marks denote melt-glass boundary. 3 is a mark for inner boundaries (regardless of manufacturing stage)

For numerical simulation, we used the explicit finite difference method on rectangle grid with spatial step of 0.1 μm and time step of 0.25 ns.

After obtaining the distribution of the concentration of substituting ions, the next stage was to determine the profile of refractive index (n), which depends linearly on substituting ion concentration, as it was shown in some experimental works [7, 10]:

$$n = n_0 + \Delta n_{\max} C,$$

where $\Delta n_{\max}$ is the change in the refractive index at $C = 1$ (and $\Delta n = \Delta n_{\max} C$), n_0 is refractive index of the glass before ion exchange (at $C = 0$). Typical values can be found in catalogs and manuals [8].

With the ion exchange of $Na^+ \leftrightarrow K^+$ in three-component quartz glass R_2O–SnO_2-SiO_2 at a temperature of $T \approx 600$ °C, the diffusion coefficient is known $D \approx 3.4$ μms [10]. The calculations were done for the width of the non-mask area of 2 μm.

Simulation of ion exchange under such conditions gives the results shown in Fig. 2.

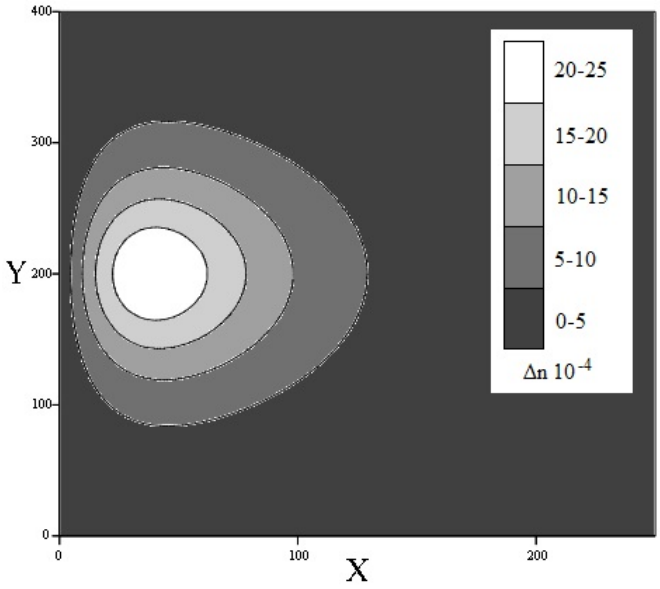

FIG. 2. The result of modeling the profile of refraction index. There was simulated a diffusion through 2 μm slit in mask. The step of counts on the axes is 0.1 μm

The calculation of ion concentrations for the transfer region in the directional coupler was also a subject of interest. Simulation, the results of which are presented in Fig. 3 and 4, showed that it is possible to use a simple summation of concentrations when the distance between non-masked areas is 14 μm, because the error in determining the refractive index does not exceed $5 - 7 \cdot 10^{-5}$. This fact makes it possible to exclude modeling of the merger and separation areas of the waveguides in the directional coupler.

3. Optical modeling

Since the refractive index difference between the core of the waveguide and the cladding is quite small, we used the beam propagation method [11] to simulate our device. First, we had to calculate field and an effective refractive index of the fundamental mode of this waveguide at 1064 nm wavelength (Fig. 5). This wavelength corresponds to an SPDC bi-photons source [12] and also fits the requirements of a single-mode regime for our waveguide.

In this section, we will refer to various parameters of the geometry of directional coupler. In general, this geometry can be represented by the geometry of the mask used to manufacture it (Fig. 6). An important characteristic about ion-exchanged glass waveguides is that their fundamental mode aligns well with the gradient of the refractive index profile. This causes an issue in the design process for the directional coupler. Since coupling between two modes depends on the value of the overlap integral, it becomes clear that coupling will be very weak if the waveguides' gradients don't intersect. This means that in order to achieve splitting of the power between two single-mode waveguides, we need to overlap our waveguides in the interaction region. This of course comes with a drawback, as we create wide and complex refractive index profile which might cause excitation of high

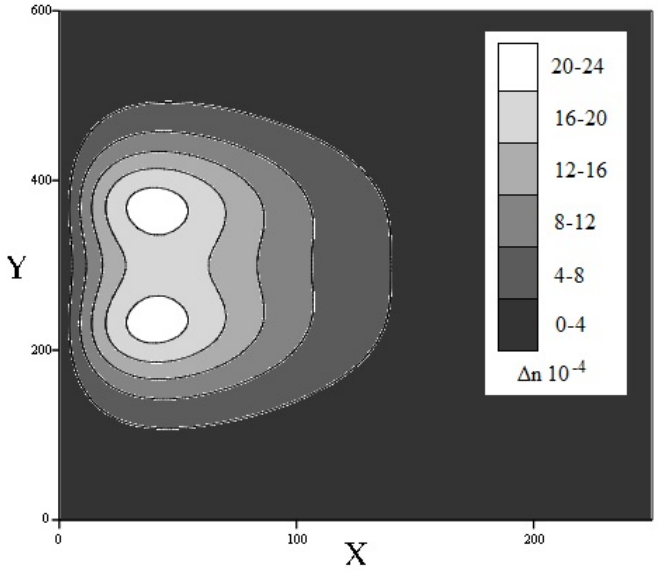

FIG. 3. The result of directional coupler modeling. Simulation was performed for two 2 μm slits with 14 μm of masked area between them. The step of counts on the axes is 0.1 μm

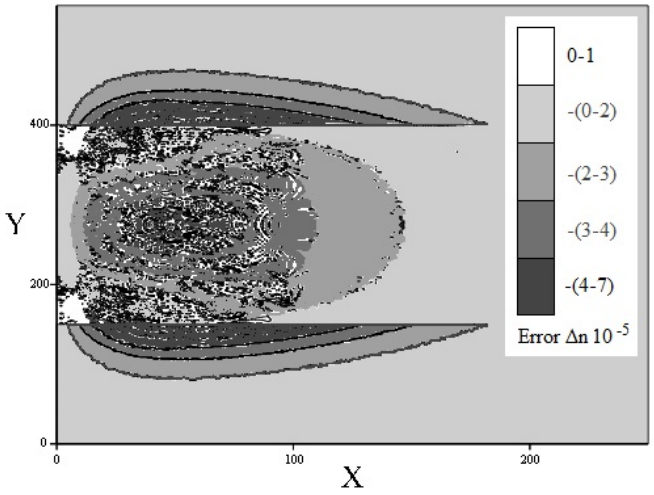

FIG. 4. A simple-summation error estimate for directional coupler. The step of counts on the axes is 0.1 μm. Maximum definition errors are $\Delta n = 0.00007$ (at sharp boundaries, after which one component of the sum remained) and $\Delta n = 0.00005$ (in the center)

order modes. Effectively, this could result in an additional loss of power (Fig. 7), as higher order modes of this region will have much less efficient coupling to single mode output waveguides.

Curvatures and leakage from the fundamental modes might occur at these bends (Fig. 8). In the optimization process, we decided to utilize the zero length for the so-called interaction region, meaning that very close overlap between the waveguide will remain only in one point. We observed that in this regime, we obtained fewer losses associated with the multi-mode regime of such overlap. In order to optimize the losses associated with s-bends, we decided to vary values for the initial separation and separation in the interaction region to determine whether we could reduce these losses while preserving overall length of the device and its splitting coefficient. Simulation of optimized design is shown on Fig. 9. One can see by the solid line on the value monitor that losses are significantly less than in cases shown on Fig. 7 and 8. The overall transmittance of the device is $\sim$0.96 with the length of 20 mm. We were able to achieve this with initial separation of 160 nm and separation in the interaction region of 15.82 μm. We want to note the importance of the analysis presented in the first section of this article. Showing

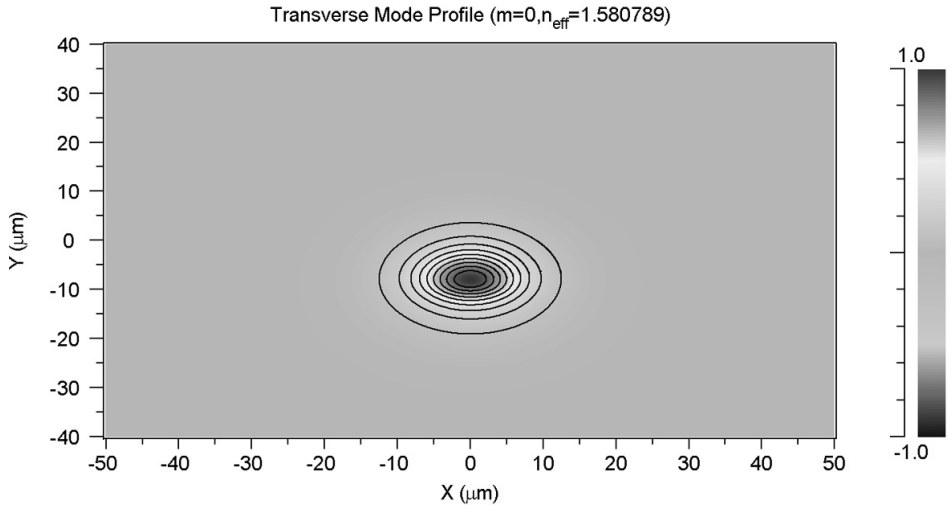

FIG. 5. Calculated fundamental mode of the ion-exchange glass waveguide with refractive index profile shown on Fig. 2

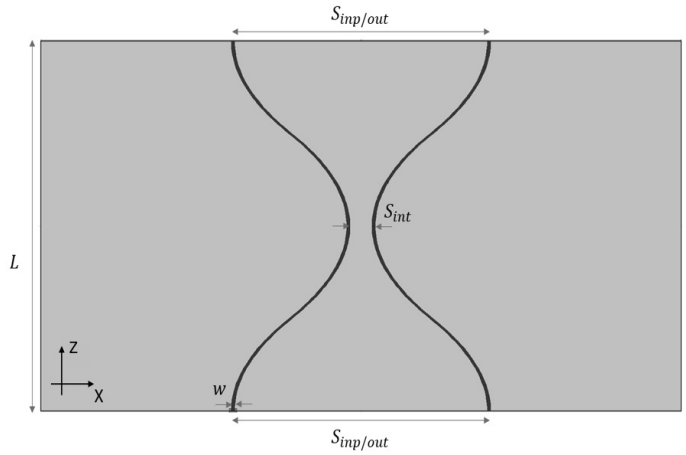

FIG. 6. Geometry of the mask for the 3dB directional coupler. $S_{inp/out}$ is initial and S_{int} is the interaction region separations, w is a width of slits in the mask which is 2 μm. Each of the two slits correspond to left and right optical channels of the device

that we can directly sum two displaced profiles instead of performing diffusion modeling for every separation in the interaction region allowed us to significantly expedite the optimization process.

4. Conclusion

In this paper, we performed design, fabrication and performance modeling of the 3dB directional coupler based on ion-exchanged glass waveguides. In the section dedicated to the optical modeling of the device, we showed important aspects of the design optimization. In particular, we showed how the problem of overlapping in the interaction region and its multi-mode regime can be mitigated by reducing the interaction length to zero and managing width of the s-bend. We also showed that the refractive index profile of overlapping regions can be simulated by directly summing two separated profile calculated from the modeling of diffusion process. This was extremely important in the optimization process of the device, as it saved a significant amount of time which would otherwise be spent on diffusion simulations. The proposed design of the device has length of 20 mm with maximum and minimum separation distances of 160 μm and 15.82 μm respectively. Its overall transmittance was evaluated as 0.96 which is different from ideal 1 due to light leakage from the s-bend.

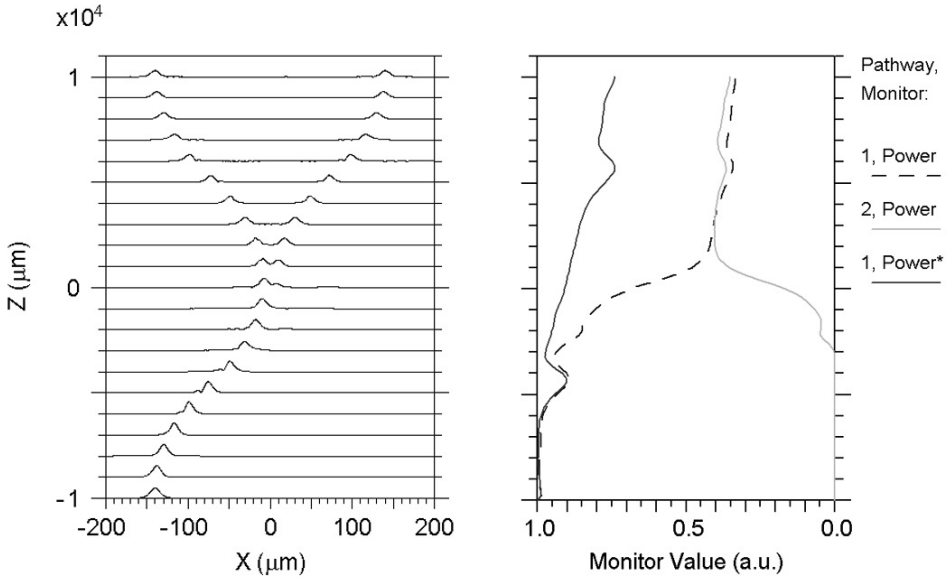

FIG. 7. Simulation of light propagation in the 3dB directional coupler with overlapped interaction region. The initial separation is 280 μm, separation in the interaction region is 16.5 μm, interaction length is 500 μm. Left is the field contour map along the device and right picture shows power in the left channel (dashed black), power in the right channel (solid grey) and overall power in the device (solid black)

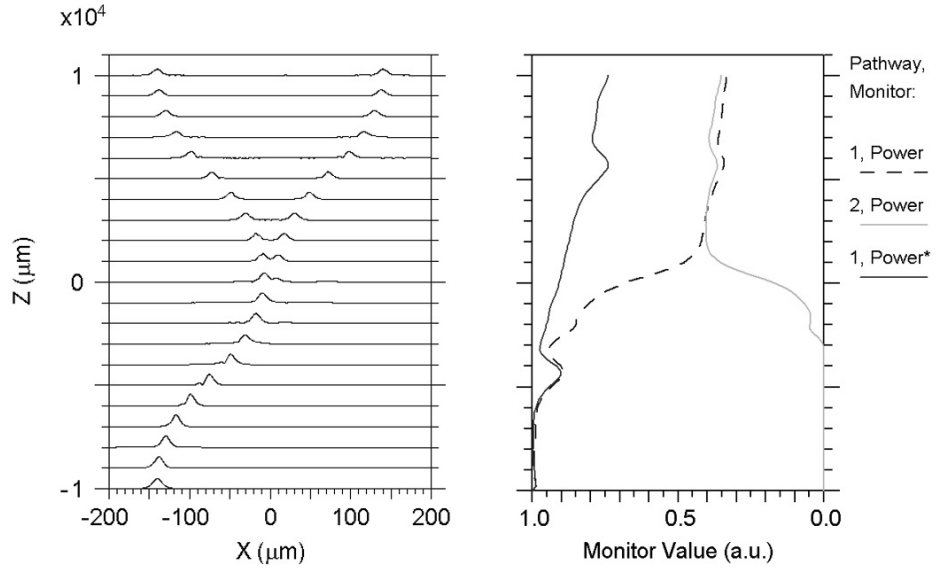

FIG. 8. Simulation 3dB directional coupler with coupling strength controlled by the curvatures of s-bends and separation of their inputs. Initial separation is 280 μm, separation in the interaction region is 14.5 μm, interaction length is 500 μm. The left is the field contour map along the device and right picture shows power in the left channel (dashed black), power in the right channel (solid grey) and overall power in the device (solid black)

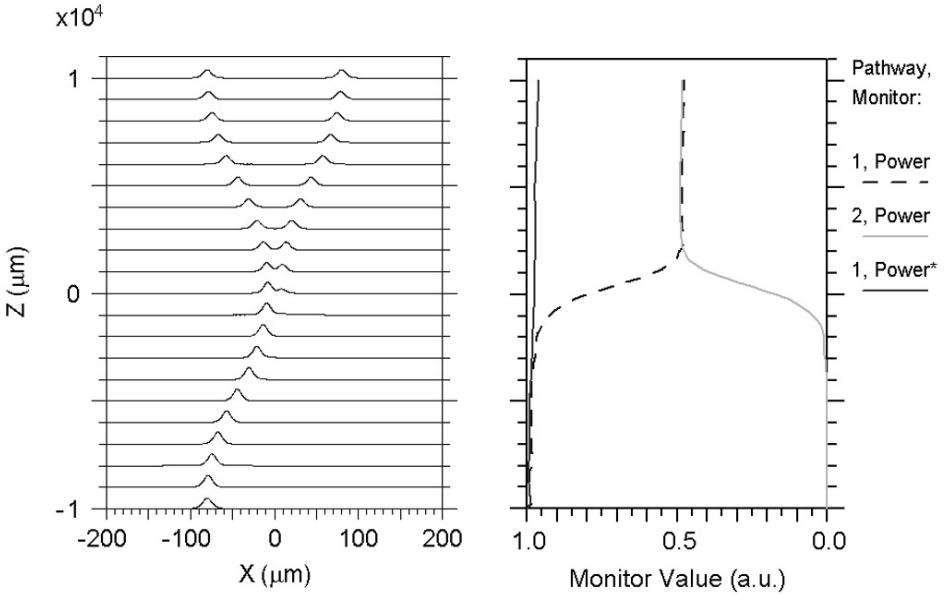

FIG. 9. Simulation of light propagation in of the optimized 3dB directional coupler. Initial separation is 160 μm, separation in the interaction region is 15.82 μm interaction length is 0 μm. Left is the field contour map along the device and right picture shows power in the left channel (dashed black), power in the right channel (solid grey) and overall power in the device (solid black)

References

[1] Matthews J.C.F., Politi A., Stefanov A., O'Brien J.L. Manipulation of multiphoton entanglement in waveguide quantum circuits. *Nature Photonics*, 2009, **3**(6), P. 346–350.

[2] Crespi A., Ramponi R., Osellame R., Sansoni L., Bongioanni I., Sciarrino F., Vallone G., Mataloni P. Integrated photonic quantum gates for polarization qubits. *Nature communications*, 2011, **2**, P. 566.

[3] Politi A., Matthews J.C.F., Thompson M.G., O'Brien J.L. Integrated quantum photonics. *IEEE Journal of Selected Topics in Quantum Electronics*, 2009, **15**(6), P. 1673–1684.

[4] Politi A., Cryan M.J., Rarity J.G., Yu S., O'Brien J.L. Silica-on-silicon waveguide quantum circuits. *Science*, 2008, **320**(5876), P. 646–649.

[5] Zhang Y., McKnight L., Engin E., Watson I.M., Cryan M.J., Gu E., Thompson M.G., Calvez S., O'Brien J.L., Dawson M.D. GaN directional couplers for integrated quantum photonics. *Applied Physics Letters*, 2011, **99**(16), P. 161119.

[6] Hallett D., Foster A.P., Hurst D.L., Royall B., Kok P., Clarke E., Itskevich I.E., Fox A.M., Skolnick M.S., Wilson L.R. Electrical control of nonlinear quantum optics in a nano-photonic waveguide. *Optica*, 2018, **5**(5), P. 644–650.

[7] West B.R., Madasamy P., Peyghambarian N., Honkanen S. Modeling of ion-exchanged glass waveguide structures. *Journal of Non-Crystalline Solids*, 2004, **347**(1-3), P. 18–26.

[8] Nikonorov N.V., Aseev V.A., Zhukov S.N., Ignatiev A.I., Kiselev S.S., Rokhmin A.S. *WAVEGUIDE PHOTONICS*. SPSU ITMO, St. Petersburg, 2008, 82 p.

[9] Zhabrev V.A. *Diffusion processes in a glassy coating layer*. Obtaining and applying protective coatings: proceedings of the 12-th All-Union Conference on Heat-Resistant Coatings, Leningrad April 16-18, 1985, Leningrad: Science, 1987, P. 14–18.

[10] Zhurikhina V.V., Petrov M.I., Sokolov K.S. and Shustova O.V. Ion-exchange characteristics of sodium-calcium-silicate glass: calculation from mode spectra. *Technical Physics*, 2010, **55**(10), P. 1447–1452.

[11] Yevick D., Hermansson B. Efficient beam propagation techniques. *J. Quantum Electron.*, 1990, **26**(1), P. 109–112.

[12] Magnitsky S., Frolovtsev D., Firsov V., Gostve P., Protsenko I., Saygin M. A SPDC-based source of entangled photons and its characterization. *Journal of Russian Laser Research*, 2015, **36**(6), P. 618–629

NANOSYSTEMS: PHYSICS, CHEMISTRY, MATHEMATICS, 2019, 10 (2), P. 154–157

Effect of anodizing voltage and pore widening time on the effective refractive index of anodic titanium oxide

N. A. Sapoletova[1], S. E. Kushnir[1,2]*, K. S. Napolskii[1,2]

[1]Department of Chemistry, Lomonosov Moscow State University, 119991, Moscow, Russia
[2]Department of Materials Science, Lomonosov Moscow State University, 119991, Moscow, Russia
*kushnir@elch.chem.msu.ru

PACS 42.25.Gy, 82.45.Aa, 82.45.Cc **DOI 10.17586/2220-8054-2019-10-2-154-157**

The unique optical properties of porous anodic titanium oxide (ATO) make it a promising material for solar energy conversion, sensorics, and opto-electronics. The optical path length and effective refractive index (n_{eff}) of ATO can be tuned by chemical etching of pore walls. However, precise control of these optical parameters is still challenging due to the lack of data on the effect of pore widening time on the n_{eff}. Here, a detailed study of the influence of anodizing voltage and pore widening time on the n_{eff} of the ATO films was performed. Analysis of reflectance spectra of ATO synthesized at 35 – 50 V shows that pore widening in 3 wt. % H_2O_2 aqueous solution allows one to control the n_{eff} at values ranging from 1.54 to 1.84. The data required for the prediction of the thickness, n_{eff}, and optical path length of the ATO films from anodizing and etching conditions are obtained.

Keywords: anodic titanium oxide, anodization, porous materials, film, refractive index, optical materials and properties.

Received: 5 April 2019

Revised: 15 April 2019

1. Introduction

Anodizing is one of the more promising methods for the production of porous TiO_2 films at room temperature [1]. Porous anodic titanium oxide (ATO) films demonstrate high efficiency in water photoelectrolysis [2], photocatalysis [3, 4], gas sensing [5], and can be used as carriers for controlled drug release [6–8]. In addition, ATO films have potential for application in dye-sensitized solar cells [9], refractive index sensors [10, 11], smart color windows, and electronic displays [12] owing to a high refractive index ($n_{TiO_2} = 2.6$ at $\lambda = 600$ nm [13]) and semiconductor properties of titanium oxide.

Optical path length of ATO films, the product of the film thickness and refractive index, is one of the key parameters that has great importance for optical applications. The thickness of ATO is directly proportional to charge density consumed during anodizing [14, 15], whereas control of the refractive index of ATO more challenging. Taking into account a small diameter of the pores in ATO films, which is much lower than the wavelength of visible light, the effective refractive index (n_{eff}) of ATO is a function of film porosity within a framework of the effective medium model. It is worth noting that the porosity and the n_{eff} values for anodic oxides change during the anodizing process due to chemical etching of the pore walls [16]. To the best of our knowledge, there are no systematic data on the n_{eff} of ATO as a function of anodizing voltage and the duration of chemical etching.

Here, we study the dependence of the thickness-to-charge density ratio and the n_{eff} of ATO films on anodizing voltage. Special attention is paid to the variation of the n_{eff} caused by chemical etching of pore walls in the anodizing electrolyte and aqueous H_2O_2 solution.

2. Materials and methods

Prior to anodizing, titanium foils (0.15 mm thick, 99.6 % purity) were electrochemically polished in a mixture of 99.5 wt. % acetic acid and 65 wt. % perchloric acid with a volume ratio of 9:1. Electrochemical polishing was performed over 4 min under square-wave applied voltage (40 V for 10 s and 60 V for 10 s) at a temperature below 25 °C as described elsewhere [15].

To prepare porous anodic titanium oxide films, Ti was anodized at a constant voltage between 30 – 60 V in an ethylene glycol electrolyte containing 0.3 wt. % NH_4F, 0.66 wt. % CH_3COONa, and 2 wt. % H_2O at 30 °C. The electrolyte solution was prepared by adding aqueous NH_4F to sodium acetate dissolved in ethylene glycol. The electrolyte was stirred at 480 RPM using an overhead stirrer. Experiments were performed in a two-electrode electrochemical cell with the distance of 2 cm between Ti electrodes. The anodized area and the total charge density consumed during anodizing of each sample was 1.13 cm^2 and 3.36 $C \cdot cm^{-2}$, respectively. To study pore

widening effect on the n_{eff} of the ATO in electrolyte, some of the prepared films were stored in electrolyte solution for 2 – 6 hours after anodizing. Finally, the ATO films were washed with ethanol and then air-dried. Some as-synthesized ATO films were aged in 3 wt. % H_2O_2 aqueous solution for 7.5 – 30 minutes under stirring.

Morphological characterization of the ATO films was performed by scanning electron microscopy (SEM) using LEO Supra 50 VP instrument. Perkin Elmer Lambda 950 spectrophotometer was used to record the reflectance spectra at incident angles of 8, 30, 45, 60, and 65° in a wavelength range of 650 – 890 nm.

3. Results and discussion

Optical reflectance spectra of the ATO films prepared at different anodizing voltages (U) are shown in Fig. 1a. In the case of the ATO obtained at $U = 35$ – 50 V, intense Fabry–Pérot oscillations of the reflectivity can be clearly seen in the spectra, resulting in high thickness uniformity for these samples at least across the irradiated area (4×4 mm^2). The Fabry–Pérot oscillations in the spectra of the samples, prepared at anodizing voltages outside the 35 – 50 V range, are weak or completely lacking, manifesting non-uniform thickness. Thus, the range of 35 – 50 V was chosen to study the dependence of the n_{eff} of the ATO films on the pore widening duration.

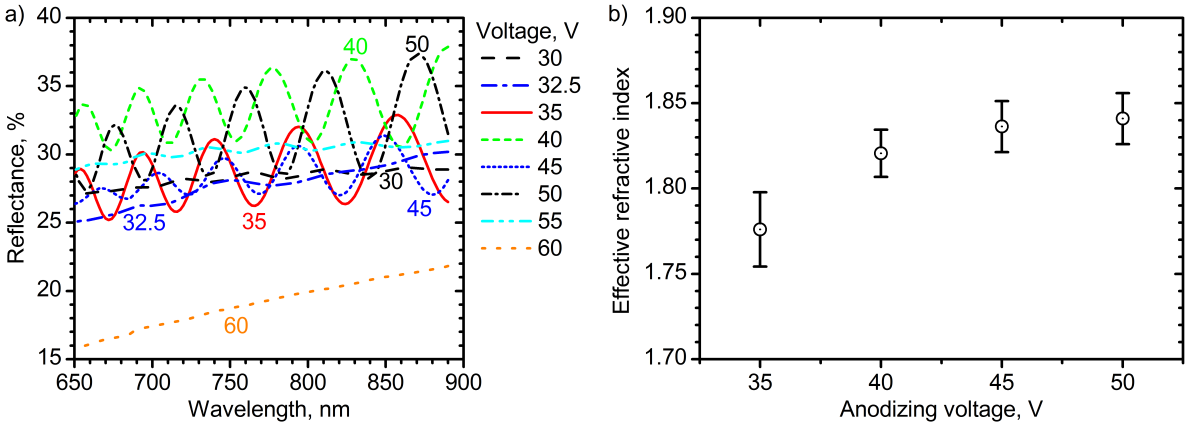

FIG. 1. Optical properties of ATO films prepared at various anodizing voltages. (a) Reflectance spectra recorded at incident angle of 8°. (b) The effective refractive index at 700 nm as a function of anodizing voltage

The positions of Fabry–Pérot oscillations in the spectra recorded at different incident angles were used for calculating the n_{eff} and sample thickness (h) using a protocol described previously [17]. The n_{eff} increases from 1.78 to 1.84 with growth of anodizing voltage from 35 to 50 V (Fig. 1b). Thickness-to-charge density ratio (h/q) lies in the range of 0.88 – 1.00 μm·cm^2·C^{-1}.

Typical SEM images of the ATO are shown in Fig. 2 on the example of the sample prepared at 35 V. ATO film consists of vertically aligned nanotubes contacting each other. The average distance between the centers of neighboring nanotubes (D_{int}) increases linearly from 79 to 111 nm with an increase in the anodizing voltage from 35 to 50 V; the proportionality constant D_{int}/U is 2.23 ± 0.03 nm V^{-1}, that is inside the range of corresponding value observed earlier for ethylene glycol based electrolytes (1.8 – 3.0) [14]. According to SEM data, the thickness of the samples prepared at $U = 35$ – 50 V is in the range of 2.9 – 3.2 μm, and thickness-to-charge density ratio lies in the range of 0.86 – 0.95 μm·cm^2·C^{-1}. It is worth noting that these values are in good agreement with spectral data.

The dependence of the effective refractive index of ATO films on the duration of chemical etching is shown in Fig. 3. Chemical etching of nanotube walls in F^--containing electrolyte solution leads to the growth of the porosity of the ATO, resulting in a decrease in the n_{eff} (Fig. 3a). The rate of pore widening in electrolyte solution is slow enough: change of the n_{eff} after several hours of etching is lower than 0.11 independently of anodizing voltage. A stronger (up to 0.28) decrease in the n_{eff} is observed in the aqueous H_2O_2 solution (Fig. 3b). The rate of pore widening is substantially faster only during the first 15 minutes of etching. Further etching leads to a minor change in the n_{eff} followed by the detaching of ATO film after 30 min. Pore widening in H_2O_2 solution increases the difference between the n_{eff} of the layers obtained at 35 and 50 V (Δn_{eff}) from 0.06 to 0.14. The trend of the Δn_{eff} increase during pore widening is in good agreement with one reported for the anodic alumina films prepared in oxalic [18] and sulfuric acid electrolytes [16]. Most likely, the decrease in etching rate (decreasing of the n_{eff}) after 7.5 min in H_2O_2 is caused by layered structure of ATO pore walls. The inner layer, contacting with

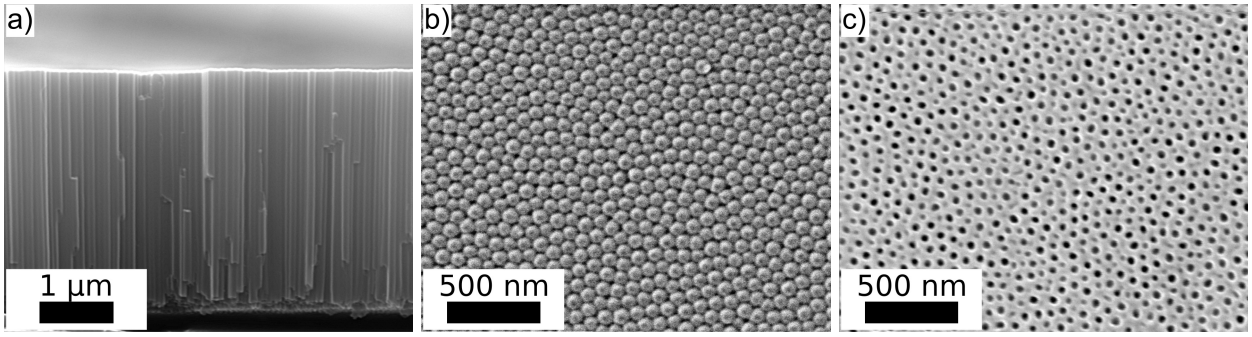

FIG. 2. SEM images of the ATO film prepared at $U = 35$ V: cross section (a), bottom (b) and top view (c)

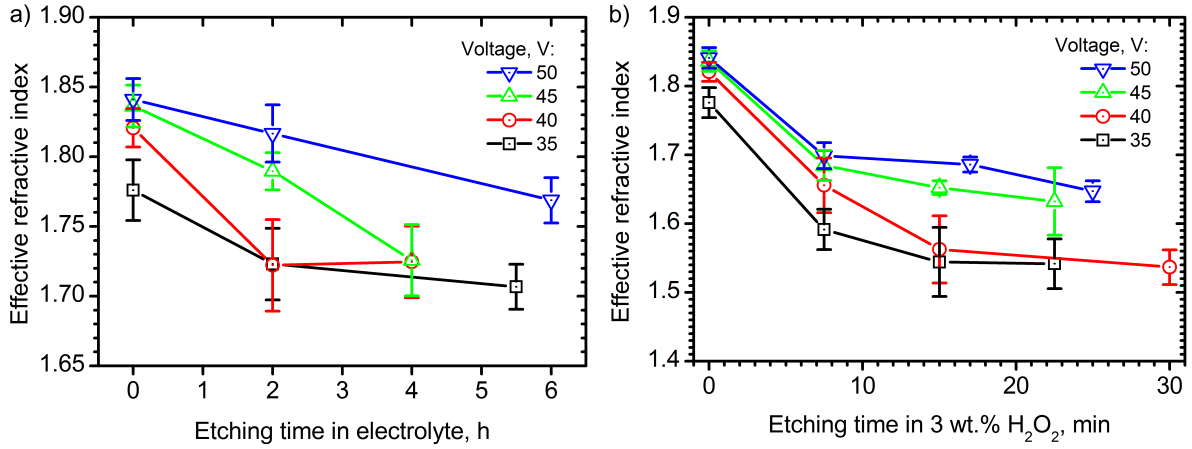

FIG. 3. Dependence of the effective refractive index at 700 nm on pore widening time for the ATO films prepared at 35 – 50 V: in the electrolyte (a) and in the 3 wt. % H_2O_2 aqueous solution (b)

electrolyte during anodizing, contains more impurities from electrolyte, that makes it less stable than the deeper layer consisting mainly of titania [19]. Obtained quantitative data on thickness and the n_{eff} of ATO will be in demand for the design of materials for antireflection coatings, memristive elements [20], photonic crystals [21], and solar cells.

4. Conclusions

High uniformity for the ATO film thickness was observed for the samples obtained in ethylene glycol electrolyte (0.3 wt. % NH_4F, 0.66 wt. % CH_3COONa, 2 wt. % H_2O) at anodizing voltages ranging from 35 to 50 V. The values of film thickness-to-charge density ratio vary from 0.86 to 1.00 $\mu m \cdot cm^2 \cdot C^{-1}$ according to analysis of the reflectance spectra and SEM images. The n_{eff} at 700 nm of the as-prepared ATO films is in the range of 1.78 – 1.84, which is higher than in the case of anodic alumina and bulk Al_2O_3. Pore widening in H_2O_2 solution allows one to achieve the lower bound of the n_{eff} of 1.54 and to increase the difference between the n_{eff} of the layers obtained at 35 and 50 V from 0.06 to 0.14. Chemical etching in aqueous H_2O_2 solution is an effective method for tuning the porosity of ATO films, saving their planarity and uniformity.

Acknowledgements

This work is supported by the Russian Science Foundation under grant No. 17-73-10471. Some experiments were carried out using the scientific equipment purchased by M. V. Lomonosov Moscow State University Program of Development.

References

[1] Regonini D., Bowen C.R., Jaroenworaluck A., Stevens R. A review of growth mechanism, structure and crystallinity of anodized TiO_2 nanotubes. *Materials Science and Engineering: R: Reports*, 2013, **74** (12), P. 377–406.

[2] Shankar K., Mor G.K., et al. Highly-ordered TiO_2 nanotube arrays up to 220 μm in length: use in water photoelectrolysis and dye-sensitized solar cells. *Nanotechnology*, 2007, **18** (6), 065707.
[3] Varghese O.K., Paulose M., LaTempa T.J., Grimes C.A. High-rate solar photocatalytic conversion of CO_2 and water vapor to hydrocarbon fuels. *Nano Letters*, 2009, **9** (2), P. 731–737.
[4] Arfanis M.K., Adamou P., et al. Photocatalytic degradation of salicylic acid and caffeine emerging contaminants using titania nanotubes. *Chemical Engineering Journal*, 2017, **310**, P. 525–536.
[5] Varghese O.K., Gong D., et al. Hydrogen sensing using titania nanotubes. *Sensors and Actuators B: Chemical*, 2003, **93** (1), P. 338–344.
[6] Song Y.-Y., Schmidt-Stein F., Bauer S., Schmuki P. Amphiphilic TiO_2 nanotube arrays: an actively controllable drug delivery system. *Journal of the American Chemical Society*, 2009, **131** (12), P. 4230–4232.
[7] Gulati K., Kant K., Findlay D., Losic D. Periodically tailored titania nanotubes for enhanced drug loading and releasing performances. *Journal of Materials Chemistry B*, 2015, **3** (12), P. 2553–2559.
[8] Wang Q., Huang J.-Y., et al. Recent advances on smart TiO_2 nanotube platforms for sustainable drug delivery applications. *International Journal of Nanomedicine*, 2016, **12**, P. 151–165.
[9] Kim D., Ghicov A., Albu S.P., Schmuki P. Bamboo-type TiO_2 nanotubes: improved conversion efficiency in dye-sensitized solar cells. *Journal of the American Chemical Society*, 2008, **130** (49), P. 16454–16455.
[10] Wang G., Wang J., An Y., Wang C. Anodization fabrication of 3D TiO_2 photonic crystals and their application for chemical sensors. *Superlattices and Microstructures*, 2016, **100**, P. 290–295.
[11] Kim W.-T., Choi W.-Y. Fabrication of TiO_2 photonic crystal by anodic oxidation and their optical sensing properties. *Sensors and Actuators A: Physical*, 2017, **260**, P. 178–184.
[12] Zheng L., Cheng H., et al. Porous TiO_2 photonic band gap materials by anodization. *The Journal of Physical Chemistry C*, 2012, **116** (9), P. 5509–5515.
[13] DeVore J.R. Refractive indices of rutile and sphalerite. *JOSA*, 1951, **41** (6), P. 416–419.
[14] Cortes F.J.Q., Arias-Monje P.J., Phillips J., Zea H. Empirical kinetics for the growth of titania nanotube arrays by potentiostatic anodization in ethylene glycol. *Materials & Design*, 2016, **96**, P. 80–89.
[15] Sapoletova N.A., Kushnir S.E., Napolskii K.S. Anodic titanium oxide photonic crystals prepared by novel cyclic anodizing with voltage versus charge modulation. *Electrochemistry Communications*, 2018, **91**, P. 5–9.
[16] Kushnir S.E., Pchelyakova T.Yu., Napolskii K.S. Anodizing with voltage versus optical path length modulation: a new tool for the preparation of photonic structures. *Journal of Materials Chemistry C*, 2018, **6** (45), P. 12192–12199.
[17] Kushnir S.E., Napolskii K.S. Thickness-dependent iridescence of one-dimensional photonic crystals based on anodic alumina. *Materials & Design*, 2018, **144**, P. 140–150.
[18] Rahman M.M., Garcia-Caurel E., et al. Effect of the anodization voltage on the pore-widening rate of nanoporous anodic alumina. *Nanoscale Research Letters*, 2012, **7** (1), 474.
[19] Dronov A., Gavrilin I., et al. Investigation of anodic TiO_2 nanotube composition with high spatial resolution AES and ToF SIMS. *Applied Surface Science*, 2018, **434**, P. 148–154.
[20] Morozova P.A., Petukhov D.I. Preparation of Au/TiO_2/Ti memristive elements via anodic oxidation. *Nanosystems: Physics, Chemistry, Mathematics*, 2017, **8** (6), P. 823–829.
[21] Ermolaev G.A., Kushnir S.E., Sapoletova N.A., Napolskii K.S. Titania photonic crystals with precise photonic band gap position via anodizing with voltage versus optical path length modulation. *Nanomaterials*, 2019, **9** (4), P. 651.

NANOSYSTEMS: PHYSICS, CHEMISTRY, MATHEMATICS, 2019, 10 (2), P. 158–163

Thermal expansion coefficients of $NaNO_2$ embedded into the nanoporous glasses

O. A. Alekseeva[1], A. A. Naberezhnov[2], D. Yu. Chernyshov[3], A. V. Fokin[2], A. A. Sysoeva[2], E. Rysiakiewicz-Pasek[4]

[1]Peter the Great St. Petersburg Polytechnic University, St. Petersburg, 195251 Russia
[2]Ioffe Institute, Russian Academy of Sciences, St. Petersburg, 194021 Russia
[3]European Synchrotron Radiation Facility, Grenoble Cedex 9, France
[4]Department of Experimental Physics, Faculty of Fundamental Problems of Technology, Wroclaw University of Science and Technology, Wybrzeże Wyspiańskiego 27, 50-370 Wroclaw, Poland

alekseevaolga0@gmail.com, alex.naberezhnov@mail.ioffe.ru, dmitry.chernyshov@esrf.fr, midbarzin@yandex.ru, annasysoeva07@mail.ru, Ewa.Rysiakiewicz-Pasek@pwr.edu.pl

PACS 61.05.C; 65.40.De; 68.65.-k; 67.30.ht **DOI 10.17586/2220-8054-2019-10-2-158-163**

The temperature evolution of the crystal structure of sodium nitrite nanoparticles has been studied with heating and cooling using synchrotron radiation diffraction. Nanocomposites have been prepared by embedding melted $NaNO_2$ into the pores of the glasses, average diameters of the pores were 20 nm and 46 nm. Analysis of obtained diffraction patterns has revealed significant difference of the coefficients of thermal expansion (contraction) on heating and on cooling between nanostructured and massive sodium nitrite in the temperature range corresponding to the paraelectric phase. It is confirmed that in these nanocomposites the phase transition from the ferroelectric to paraelectric phase remains the first-order phase transition. Temperature hysteresis of this phase transition is about 10 K.

Keywords: ferroelectrics, phase transitions, nanocomposite materials, synchrotron radiation diffraction.

Received: 11 February 2019

Revised: 21 February 2019

1. Introduction

The physical properties of systems consisting of ultra-small particles, phase transitions and critical phenomena occurring in them have been intensively studied in recent years, since nanocomposite materials, which exhibit unusual electronic, thermal, structural, optical and other properties determined by size and surface effects, are in demand. The main causes for differences in physical properties between nanocomposite and bulk materials are the proximity of lengths of the characteristic interactions and the nanoparticle sizes and the growth of effects of surface atoms on the physical properties of nanoobjects with reduction of their characteristic sizes. Local symmetry and interactions of surface atoms with an environment and matrix walls differ significantly from inherent internal atoms. In recent years, ferroelectric and dielectric nanomaterials attract the steadfast attention of researchers because of the potential of their use as materials for memory elements and/or storage media with high stability and reliability of operation (FeRAM), active optoelectronic devices (tunable photonic crystals), fiber optic communication lines.

One method for nanocomposite materials (NCM) production is intrusion or synthesis of substance into the nanoscale pores of pore matrixes. Porous glass, chrysotile asbestos, artificial opals, zeolites, mesoporous matrix MCM-41 and SBA-15 can be used [1–3] as host matrices for NCM creation. In this contribution, the nanocomposites based on porous glasses are considered. To produce our nanocomposite materials, we have used porous alkali borosilicate glasses. In alkali borosilicate glasses, after special heat treatment, a phase separation takes places on two components: the acid-resistant SiO_2-enriched phase (SiO_2 skeleton) and chemically reactive phase [4]. Selecting synthetic conditions, such as temperature and initial mixture composition, it is possible to form a system of two interpenetrating phases [4]. After chemical etching of these glasses, the 3D-structure forms. It can be defined as a continuous disordered structure of two interpenetrating percolating phases, namely a network of pores and solids. The pores in the glasses are connected to each other and their average diameter has a small spread ($\sim$ 5 – 10 %). Depending on preparation conditions the average pore diameter can vary from 30 to 500 Å. The typical example of porous silicate glass is Vycor industrial glass. The standard chemical composition is 96 % SiO_2, 3 % B_2O_3, 0.40 % Na_2O, $R_2O_3 \pm RO_2 < 1$ % (mainly Al_2O_3 and ZrO_2) [5].

$NaNO_2$ can be considered as a model object for study of crystal structure evolution and modification of macroscopic properties of nanocomposite materials. Ferroelectric properties of sodium nitrite have been studied very well, it can be easily embedded into the different natural and artificial porous matrices due to a good wetting ability. $NaNO_2$ undergoes the first order phase transition at $T_C \approx 437$ K. Between the ferroelectric and paraelectric phases there is an incommensurate phase observed over a very narrow (~ 1.5 K) temperature interval.

The dielectric properties of NCM "porous glasses+$NaNO_2$" have been previously studied [6–10] and the significant rapid growth of NCM dielectric permittivity (up to 10^8 at 100 Hz) above T_C has been observed [6–8] for ultra-dispersed sodium nitrite nanoparticles. It has also been shown that the volume pre-melted state characterized by significant values of thermal vibrations and ion mobilities is formed above T_C [11, 12]. The temperature dependencies of order parameters for $NaNO_2$ embedded into porous glasses with different average pore diameters (3, 7, 20, 46 and 320 nm) have been obtained [12]. It is shown that for nanoparticles with average size less than 50 nm there is a crossover of the phase transition from the first order to the second one.

The goal of this work was to study the peculiarities of thermal expansion and contraction of $NaNO_2$ nanoparticles with the average size larger than the critical size (> 50 nm) in a wide temperature interval including ferro- and paraelectric phases.

2. Experiment

The studies of structural evolution of NCMs with $NaNO_2$ were performed in the temperature interval 100 – 460 K (*i.e.* below and above Curie temperature T_C of bulk $NaNO_2$) using synchrotron radiation diffraction (BM01A station, ESRF, France) at $\lambda = 0.703434$ Å. The temperature step was 2 K in a vicinity of T_C and 5 K in other regions, temperature stability during the measurements was better than 1 K. The measurements were performed on heating and on cooling. The experimental results were treated by FullProf program. We have used two types of samples: NCM-20 corresponds to $NaNO_2$ embedded into porous glass with average pore size of 20 nm (PG20) and NCM-46 corresponds to sodium nitrite into porous glass with an average pore size of 46 nm (PG46). The diffraction patterns of bulk $NaNO_2$, empty PG20 and empty PG46 were measured in the same experimental conditions as the reference samples. In this case, the powder sodium nitrite was placed in a special thin quartz capillary.

Porous glasses PG20 were manufactured at Ioffe Institute, porous glasses PG46 – at Wroclaw University of Science and Technology. The glasses (plates with sizes of $10 \times 10 \times 0.5$ mm^3) were filled from a melt in vacuum at Ioffe Institute. After filling, the surfaces of the glasses were thoroughly cleaned from the remnants of bulk material and thin ($\sim 200 \times 200$ micron) parallelepipeds with ~ 10 mm in length were made from them. These samples were placed directly on the synchrotron radiation beam.

3. Results and discussion

The typical diffraction pattern for NCM PG46+$NaNO_2$ at $T = 330$ K and results of fitting procedure are shown in Fig. 1 All Bragg peaks correspond to $NaNO_2$ structure, and no admixtures were observed. The diffuse background is due to scattering on amorphous SiO_2, which forms the skeleton of porous glasses.

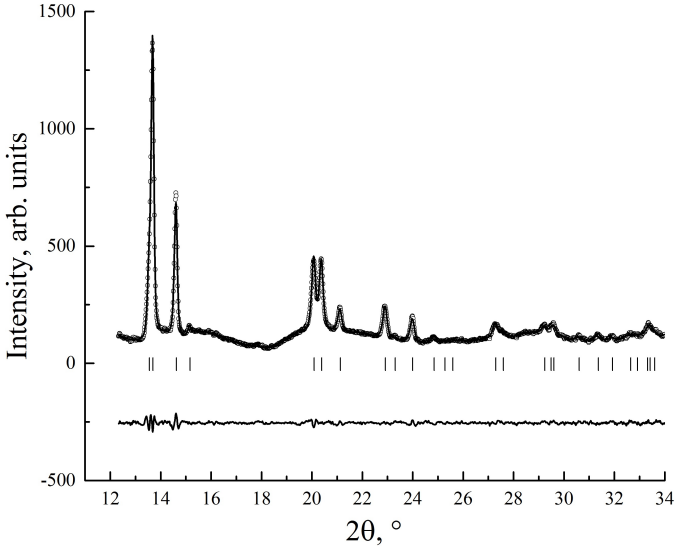

FIG. 1. Diffraction pattern for NCM-46 sample at 330 K. Solid line corresponds to calculated pattern, open circles – experimental data. Vertical bars – Bragg positions, the line in the bottom part is the difference between the experimental data and fitting

Bragg peaks are broadened due to size effect, the sizes of $NaNO_2$ nanoparticles were estimated from reflection widths at different temperatures. The values for NCM-20 are 72 (2) nm at room temperature and 54 (2) nm at 460 K in the paraelectric phase. The size for NCM-46 is 102 (2) nm in the ferroelectric phase and gradually decreases on heating (60 (2) nm at 460 K) [13].

As a result of fitting procedure we have obtained the temperature dependences of the lattice parameters (Fig. 2) for NCMs and for bulk sodium nitrite. It can be seen that temperature dependencies of a and b parameters practically coincide on heating for NCMs and for bulk $NaNO_2$ (for a throughout the measurement temperature interval, for b only in the ferroelectric phase below $T_C = 437$ K), but above T_C parameter b grows faster in NCMs than in bulk $NaNO_2$. On cooling $a(T)$ and $b(T)$ curves for NCMs lay significantly higher than in bulk material. Moreover one can note that the temperatures, where the dependences $a(T)$ and $b(T)$ change the slope due to ferroelectric phase transition, are much lower (~ 10 K) than in the bulk. It is necessary to note that the pronounced hysteresis loop in the temperature dependences of order parameter reported in our previous works [13] has the same value. A small hysteresis between heating and cooling curves have been observed for the bulk sodium nitrite but its value is noticeable smaller (~ 4 K) and can be explained by inertia of heating (cooling) of powder sample in a glass capillary.

Parameter c demonstrates the inverse behavior: for NCM $c(T)$ curves are close to the bulk one on cooling, but on heating these curves for NCM pass significantly higher than for the bulk $NaNO_2$.

Respectively we have observed the fast growth of the unit cell volume on heating above phase transition temperature in NCMs in comparison with bulk material (Fig. 2(b)).

Based on these results, the temperature dependences of the linear and volume thermal expansion coefficients (TEC) in $NaNO_2$ nanoparticles and bulk $NaNO_2$ have been calculated (Fig. 3).

Below Curie temperature and far from T_C, TECs exhibit a weak, close to linear growth on heating. Near the Curie temperature, the anomalies in the temperature dependences of TECs in the form of a characteristic peak are observed. One can note that the positions of TEC anomalies on heating and on cooling for $NaNO_2$ nanoparticles are significantly shifted against each other. This is in agreement with our data obtained for temperature dependences of order parameter [13], which also shows pronounced temperature hysteresis in these NCMs. It can be also seen that below the Curie temperature, TEC temperature dependences for NCMs and bulk $NaNO_2$ are quite similar, both on heating and on cooling. In the paraelectric phase, a noticeable difference of TEC values can be seen in the bulk material and in NCMs: upon heating in both NCMs TECs are larger than in the bulk, upon cooling we can see an opposite situation.

The temperature dependences of all parameters in the paraelectric phase of $NaNO_2$ were approximated by a linear dependence and the average TEC values in this temperature range were calculated. The obtained values are presented in Table 1.

It can be seen a significant difference in TEC values for $NaNO_2$ nanoparticles in both NCMs on heating and on cooling, which is not observed in the bulk material. This difference can be associated with a formation of specific pre-melted state above T_C, described in the papers for similar NCM on base of porous glasses with average pore diameter 7 nm [14] and for NCM on base of mesoporous sieves MCM-41 and SBA-15 [15]. This state takes place at temperatures significantly (about 100 degrees) below the melting point of $NaNO_2$ embedded into the porous glass and is characterized by anomalously large amplitudes of atomic thermal vibrations reaching the values exceeding Lindemann‘s criteria for melting. This causes a sharper growth of unit cell parameters and volume in $NaNO_2$ nanoparticles compared with the bulk material on heating and a significant difference between the corresponding TEC values on cooling.

4. Conclusion

The temperature evolution of crystal structure of $NaNO_2$ embedded in the porous glasses with average pore sizes 20 and 46 nm have been studied upon heating and cooling. It is shown that the linear and volume thermal expansion coefficients of $NaNO_2$ nanoparticles in the paraelectric phase differ essentially from these parameters that characterize bulk sodium nitrite. The pronounced thermal hysteresis of lattice parameters and TECs have been observed on heating and on cooling. The value of thermal hysteresis (~ 10 K) does not depends on nanoparticle sizes for these NCM and corresponds to the hysteresis observed in temperature dependences of order parameter for these NCM in the paper [13]. It confirms the statement that the phase transition from a ferroelectric to a paraelectric phase remains a first-order phase transition. The observed differences in TEC between NCM and bulk $NaNO_2$ in the paraelectric phase can be associated with formation of pre-melted state in nanostructured sodium nitrite above its Curie temperature.

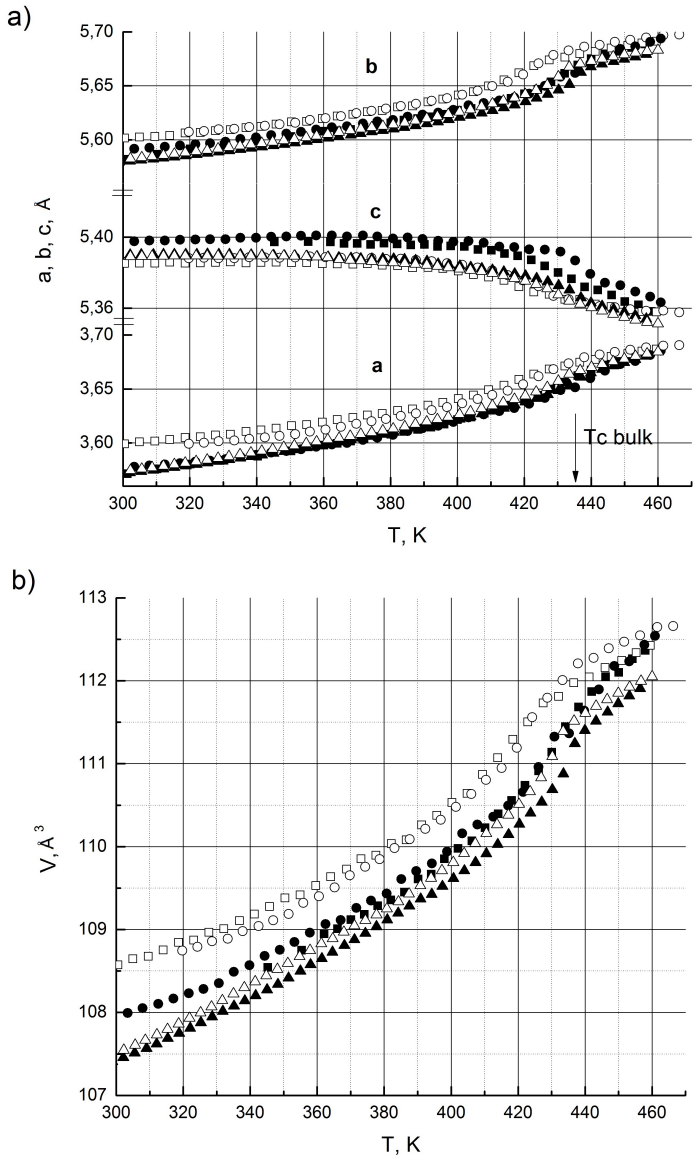

FIG. 2. Temperature dependencies of lattice parameters (a) and unit cell volume (b) for NCM-20 (circles), NCM-46 (squares) and the bulk $NaNO_2$ (triangles) on heating (filled symbols) and on cooling (open symbols)

Acknowledgements

This work was supported by the Russian Foundation for Basic Researches under Grant number 19-02-00760. In Peter the Great St. Petersburg Polytechnic University (SPbPU) the measurements were partly supported by RF Ministry of Education and Science (grant 3.1150.2017/4.6). The authors thank the staffers of BM01A (Swiss-Norwegian Beam Line, European Synchrotron Radiation Facility, Grenoble) for cooperation.

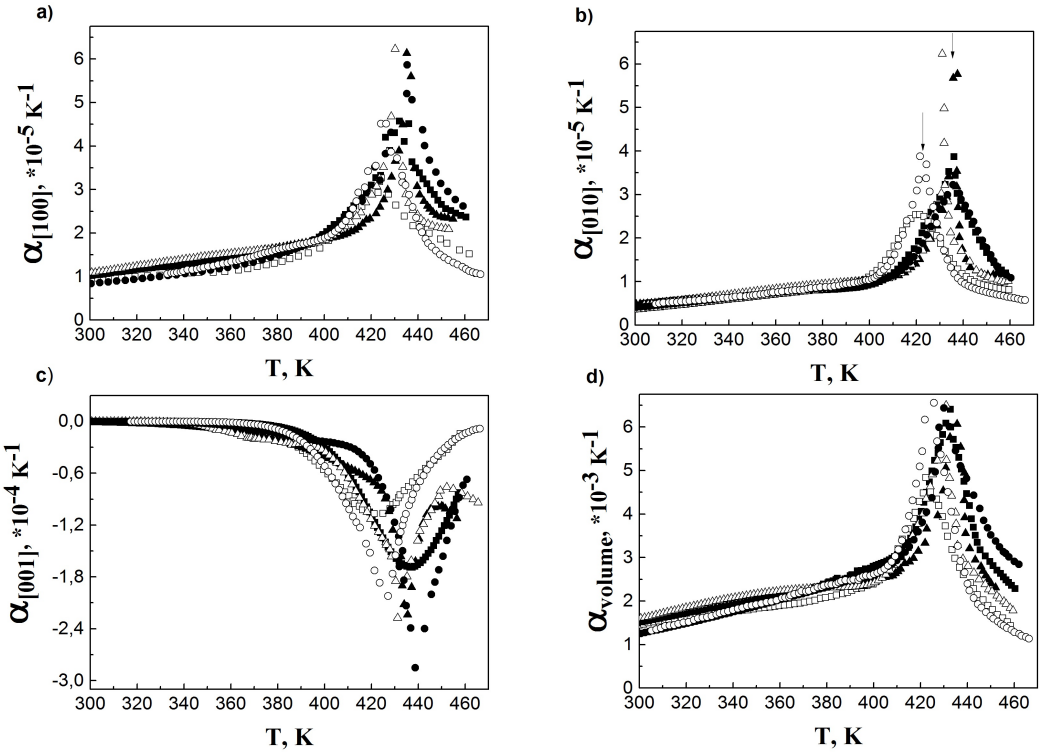

FIG. 3. Temperature dependences of the linear and volume thermal expansion coefficients (TEC) of $NaNO_2$ nanoparticles obtained by incorporation into the pore space of nanoporous glasses with an average pore diameter of 20 (circles) and 46 nm (squares), and of bulk $NaNO_2$ (triangles) on heating (filled symbols) and on cooling (open symbols). The arrows in Fig. 3(b) indicate T_C on heating and cooling obtained from temperature dependences of order parameter [13]. Errors do not exceed the symbol size

TABLE 1. The linear and volume thermal expansion (contraction) coefficients of $NaNO_2$ nanoparticles and of bulk $NaNO_2$ in the paraelectric phase

	TEC	10^{-5} K^{-1}	
		heating	cooling
bulk $NaNO_2$	α_a	26 ± 1	22 ± 1
	α_b	12 ± 1	10 ± 1
	α_c	-10 ± 1	-9 ± 1
	α_{vol}	28 ± 1	25 ± 1
NCM $NaNO_2$+PG46 nm	α_a	28 ± 1	16 ± 1
	α_b	15 ± 1	9 ± 1
	α_c	-13 ± 1	-6 ± 1
	α_{vol}	31 ± 1	19 ± 1
NCM $NaNO_2$+PG20 nm	α_a	32 ± 1	14 ± 1
	α_b	20 ± 1	8 ± 1
	α_c	-15 ± 1	-5 ± 1
	α_{vol}	38 ± 1	18 ± 1

References

[1] Levitz P., Ehret G., Sinha S.K., Drake J.M. Porous vycor glass – the microstructure as probed by electron-microscopy, direct energy-transfer, small-angle scattering and molecular adsorption. *J. Chem. Phys.*, 1991, **95** (8), P. 6151–6161.
[2] Pundsack F.L. The pore structure of chrysotile asbestos. *J. Phys. Chem.*, 1961, **65**, P. 30–33.
[3] Breck D.W. *Zeolite molecular sieves: Structure, Chemistry and Use.* A Willey – Interscience Publication Jonh Willey&Sons, New-York, 1974, 771 pp.
[4] Janowski F., Heyer W. *Poröse Gläser. Herstellung, Eigenschaften und Anwendung*, Deutscher Verlag für Grundstoffindustrie, Leipzig, 1982, 274 pp.
[5] Huang X. Manufacture of porous glass. *J. Non-Cryst. Solids*, 1989, **112**, P. 58–63.
[6] Pan'kova S.V., Poborchii V.V., Solov'ev V.G. The giant dielectric constant of opal containing sodium nitrate nanoparticles. *J. Phys.: Condens. Matter*, 1996, **8**, L203–206.
[7] Colla E.V., Koroleva E.Y., Kumzerov Yu.A., Savenko B.N. Ferroelectric phase transitions in materials embedded in porous media. *Ferroelectr., Lett.*, 1996, **20**, P. 143–147.
[8] Kinka M., Banys J., Naberezhnov A. Dielectric properties of sodium nitrite confined in porous glass. *Ferroelectrics*, 2007, **348**, P. 67–74.
[9] Rysiakiewicz-Pasek E., Poprawski R., Urbanowicz A., Maczka M. Porous glasses with sodium nitrite impregnations. *Optica Applicata*, 2005, **35** (4), P. 769–774.
[10] Rysiakiewicz-Pasek E., Poprawski R., et al. Properties of porous glasses with embedded ferroelectric materials *Jour. of Non-Cryst. Solids*, 2006, **352** (40–41), P. 4309–4314.
[11] Vakhrushev S.B., Kumzerov Yu.A., et al. 23Na spin-lattice relaxation of sodium nitrite in confined geometry. *Phys. Rev. B*, 2004, **70**, 132102 (3 pp).
[12] Naberezhnov A., Fokin A., et al. Structure and properties of confined sodium nitrite. *Eur. Phys. J. E.*, 2003, **12**, s21–s24.
[13] Naberezhnov A.A., Alekseeva O.A., et al. Order-Parameter Temperature Dependences in Nanocomposites of Porous Glass–Sodium Nitrite. *Bulletin of the Russian Academy of Sciences: Physics*, 2018, **82** (3), P. 238–241.
[14] Beskrovny A., Golosovsky I., et al. Structure evolution and formation of a pre-melted state in $NaNO_2$ confined within porous glass *Appl. Phys. A (Suppl.)*, 2002, **74**, s1001–s1003.
[15] Tien C., Charnaya E.V., et al. Coexistence of melted and ferroelectric states in sodium nitrite within mesoporous sieves *Phys. Rev. B*, 2005, **72**, 104105 (6 pp.)

NANOSYSTEMS: PHYSICS, CHEMISTRY, MATHEMATICS, 2019, 10 (2), P. 164–175

The influence of chemical prehistory on the structure, photoluminescent properties, surface and biological characteristics of $Zr_{0.98}Eu_{0.02}O_{1.99}$ nanophosphors

A. N. Bugrov[1,2], R. Yu. Smyslov[1,3], A. Yu. Zavialova[2,4], G. P. Kopitsa[5,6]

[1]Institute of Macromolecular Compounds of RAS, Bolshoy pr. 31, 199004 St. Petersburg, Russia
[2]St. Petersburg Electrotechnical University "LETI", ul. Professora Popova 5, 197376 St. Petersburg, Russia
[3]Peter the Great St. Petersburg Polytechnic University, Polytechnicheskaya 29, 195251 St. Petersburg, Russia
[4]St. Petersburg State Institute of Technology (Technical University), Moskovsky prospect 26, St. Petersburg, 190013, Russia
[5]St. Petersburg Nuclear Physics Institute, NRC KI, Orlova roscha mcr. 1, Gatchina, Leningrad region, 188300, Russia
[6]Grebenshchikov Institute of Silicate Chemistry RAS, Makarova nab. 2., letter B, 199034 St. Petersburg, Russia

alexander.n.bugrov@gmail.com, urs1968@gmail.com, zavialova.a.y@gmail.com, kopitsa_gp@pnpi.nrcki.ru

PACS 78.67. n; 78.67.Bf **DOI 10.17586/2220-8054-2019-10-2-164-175**

ZrO_2 nanoparticles doped with 2 mol.% of $EuO_{1.5}$ were obtained from solutions of inorganic salts, zirconium alkoxide and chelating compounds under hydro and solvothermal conditions. The phase compositions of the synthesized nanophosphors were determined using the methods of X-ray diffraction, photoluminescence and Raman spectroscopy. The changes in a particle size, the value of the specific surface area and its charge depending on the conditions of preparation (the type of solvent, isothermal exposure time) and the precursor nature used in the synthesis were considered. It was found that $Zr_{0.98}Eu_{0.02}O_{1.99}$ nanoparticles with a high content of the monoclinic phase, synthesized from zirconium and europium acetylacetonates, have the highest luminescence efficiency. At the same time, the maximum photoluminescence lifetime and the least cytotoxicity were characteristic of crystal phosphors with a more symmetrical crystal lattice of the host matrix, as well as a high surface area/volume ratio.

Keywords: solvothermal synthesis, zirconia, europium, phase transitions, nanoparticles, photoluminescence, fluorescence lifetime, quantum yield, cytotoxicity.

Received: 27 March 2019

Revised: 10 April 2019

1. Introduction

The rapid development of solid-state lighting technology has led to an increased demand for high-performance alternative luminescent sources of radiation [1]. It is known that Ln^{3+}-doped wide-bandgap semiconductor oxides can exhibit unique optical properties such as single or multicolor radiation, large Stokes shift, narrow spectral transition bands, long lifetime, and high photoluminescence quantum yield [2, 3]. The optical properties of oxide nanoparticles doped with Ln^{3+} largely depend on the type and structure of the host matrix [4,5]. Therefore, the correct selection of the absorption oscillator is significant for achieving the desired photoluminescence characteristics of lanthanide ions. Nanocrystalline zirconia is the most suitable host matrix for the creation of high-performance solid-state light-emitting devices based on Ln^{3+} ions due to its high refractive index, the band gap in the range from 4 to 6 eV, transparency in the visible and infrared spectral regions, as well as low frequency of phonons (470 cm^{-1}) [6, 7]. To date, nanophosphors based on ZrO_2 have been used in LEDs [8], fuel cells [9], solar panels [10], gas sensors [11], and photocatalytic systems [12,13]. The photostability and high lifetime of Ln^{3+} (the range of milliseconds) ion radiation in the ZrO_2 biologically-inert matrix made it possible to use such luminescent markers for medical purposes for detecting, visualizing, diagnosing and treating diseases [14–17].

For increasing the luminescence efficiency of lanthanide ions, as a rule, uniformity of their distribution in the ZrO_2 crystal lattice is required [18]. From this point of view, the methods of "soft chemistry" such as hydro and solvothermal synthesis are preferred [19–21]. They make it possible to control the processes of nucleation and crystallite growth by changing the treatment parameters, which leads to the formation of weakly aggregated particles of a given morphology with a narrow size distribution [22–24]. In turn, the different nature of the precursor and the composition of the reaction medium (e.g. water, an organic solvent, surfactant, mineralizer) predetermine the presence of the required functional groups on the surface of the nanoparticles being synthesized, which can then be used for conjugation with biomolecules [16, 25].

Selectivity for the excitation wavelength, energy transfer efficiency, lifetime and quantum yield of photoluminescence are determined mainly by the structure and size of ZrO_2 crystals, as well as the concentration and localization of Ln^{3+} active centers in them [26–29]. The distribution of trivalent lanthanide ions between the amorphous, monoclinic and more symmetrical tetragonal and cubic phases of ZrO_2 can be adequately distinguished using Eu3+ as a probe. Luminescent properties of europium ions are susceptible to changes in the first coordination sphere, which is manifested in the emission/excitation spectra and the dynamics of the excited state of ZrO_2:Ln^{3+} nanoparticles [26, 30].

In this connection, this work aimed to study the influence of chemical prehistory on the structure of $Zr_{0.98}Eu_{0.02}O_{1.99}$ nanoparticles, formed in the conditions of hydrothermal and solvothermal synthesis, using the europium ions as local probes. In addition, we sought to determine the interrelation of structural and dimensional parameters with the efficiency of luminescence of the obtained crystalline phosphors, as well as the analysis of their cytotoxicity depending on the evolution of surface characteristics concerning dermal fibroblasts to establish the possibility of their further biomedical application.

2. Experimental methods

2.1. Materials

The following reagents were used in the hydro and solvothermal synthesis of luminescent nanoparticles studied in this work: zirconium (IV) oxychloride octahydrate (98.5 %, Neva-Reactive, Saint Petersburg, Russia, CAS: 7699-43-6); zirconium (IV) acetylacetonate ($Zr(acac)_4$; 97 %, Vecton, Saint Petersburg, Russia, CAS: 17501-44-9); zirconium (IV) n-butoxide solution ($Zr(OBu^n)_4$; 80 wt.% in 1-butanol, Sigma-Aldrich, St. Louis, MO, USA, CAS: 1071-76-7); europium (III) chloride hexahydrate (99.9 % trace metals basis, Sigma-Aldrich, St. Louis, MO, USA, CAS: 13759-92-7); europium (III) acetylacetonate hydrate ($Eu(acac)_3 \times nH_2O$; 99.9 % trace metals basis, Sigma-Aldrich, St. Louis, MO, USA, CAS: 62667-64-5); ammonium hydroxide solution (25 %, Neva-Reactive, Saint Petersburg, Russia, CAS: 1336-21-6); ethanol (95 %, Vecton, Saint Petersburg, Russia, CAS: 64-17-5). Toluene (99.5 %, Vecton, Saint Petersburg, Russia, CAS: 108-88-3) was distilled before use.

2.2. Hydrothermal synthesis of nanoparticles

ZrO_2 nanoparticles containing 2 mol.% of $EuO_{1.5}$ were obtained by co-precipitating zirconium and europium hydroxides from 0.5 M solutions of their chlorides at pH = 9, using ammonia water (25 %). The precipitate was washed with distilled water until a negative reaction to chloride ions by repeated stirring with followed decantation and then dried in air at 100 °C. The obtained $ZrO(OH)_2$–$Eu(OH)_3$ powder was redispersed in distilled water (pH = 4 – 5), placed in a steel autoclave and treated under hydrothermal conditions during 4 hours at 250 °C.

2.3. Solvothermal synthesis of nanoparticles

The $Eu(acac)_3 \times nH_2O$ with a mass of 0.04 g was previously dissolved in anhydrous toluene for 3 hours with constant stirring. Zirconium acetylacetonate or butoxide in the amount of 1.87 g and 1.35 ml, respectively, were added to the obtained solutions. The resulting reaction mixtures were then magnetically stirred for 24 hours. The thermal treatment of solutions of organometallic compounds in toluene with pH = 4 – 5 was carried out in steel autoclaves at a temperature of 250 °C for 72 hours. The obtained powders of $Zr_{0.98}Eu_{0.02}O_{1.99}$ nanoparticles were repeatedly washed in ethanol, followed by centrifugation to remove organic impurities. After that, they were dried at 100 °C to constant weight and annealed in air at 500 °C for 2 hours.

2.4. Characterization techniques

The elemental composition of the $Zr_{1-x}Eu_xO_{2-0.5x}$ nanopowders obtained in the study was determined using energy-dispersive X-ray spectroscopy (EDX; SUPRA 55VP Carl Zeiss AG with an INCA microanalysis system, Germany) and X-ray fluorescence analysis (XRF; Spectroscan Max-GF2E spectrometer Spectron, Russia Q5). ZrO_2 nanoparticles doped with 2 mol.% Eu^{3+} ions were characterized using an X-ray diffraction method (XRD; Rigaku SmartLab diffractometer) with CuKα radiation (40 kV and 40 mA), scan rate of 0.5°/min in a range of 2θ angles from 10 to 80°. The PD-Win 4.0 [31] and ReX [32] software complexes, as well as ASTM and COD databases, were used to determine the phase composition and calculate the unit cell parameters of the nanoparticles. Transmission electron microscopy (TEM; JEOL JEM-2100F) with an accelerating voltage of 200 kV was used to determine the shape and size of the $Zr_{0.98}Eu_{0.02}O_{1.99}$ nanoparticles. The phase composition of the synthesized nanophosphors was analyzed using Raman spectroscopy (RS; LabRAM HR800, Horiba Jobin-Yvon) at room temperature with 488 nm of Ar^+ laser. A specific surface area (SBET) and porosity of synthesized nanopowders were determined by low-temperature nitrogen adsorption (QuantaChrome Nova 4200B analyzer,

Quantachrome Instruments, USA). Zeta potential was determined using an electrophoretic light scattering method (Malvern Zetasizer Nano ZS laser analyzer, Malvern Instruments, UK) at 25 °C, pH value of 6.4 with a background electrolyte concentration (NaCl) of 10^{-3} M. The optical band gap of nanocrystals based on zirconia was determined using diffuse reflectance spectra (Shimadzu UV-2550 spectrophotometer equipped with an ISR-2200 integrating sphere). MTT assay of ZrO_2-2 mol.% $EuO_{1.5}$ nanoparticles were carried out on dermal fibroblasts in accordance with the procedure described in detail in [33]. The photoluminescence (PL) quantum yield of nanophosphors was measured by the modified de Mello's method using a Fluorolog-3 fluorescence spectrometer equipped with a Quanta-j integrating sphere [34]. The excitation and emission spectra of nanoparticle powders were studied using a luminescence spectrophotometer LS-100 (PTI®, Canada). The luminescence lifetimes of $Zr_{0.98}Eu_{0.02}O_{1.99}$ nanoparticles were determined from the emission intensity decay using a pulse xenon lamp.

3. Results and discussion

The effects of the chemical prehistory of ZrO_2-2 mol.% $EuO_{1.5}$ nanoparticles on their phase composition, specific surface area, porosity, electrokinetic potential, photoluminescence, and biological activity were considered.

The elemental analysis of $Zr_{1-x}Eu_xO_{2-0.5x}$ nanoparticle samples is carried out under the conditions of hydro and solvothermal treatment corresponded to the 98 mol.% ZrO_2/2 mol.% $EuO_{1.5}$ ratio, according to the EDX and XRF methods (Table 1). The data obtained coincide within the error with the composition preset by the synthesis.

TABLE 1. Elemental analysis of synthesized nanoparticles based on ZrO_2 doped with $EuO_{1.5}$

Chemical prehistory	Data of fluorescence analysis calculated as oxides, mol.%		Data of EDX-analysis calculated as oxides, mol.%	
	ZrO_2	$EuO_{1.5}$	ZrO_2	$EuO_{1.5}$
$ZrOCl_2 \times 8H_2O/EuCl_3 \times 6H_2O$	97.8 ± 2.9	2.2 ± 0.1	97.1 ± 4.9	2.9 ± 0.2
$Zr(acac)_4/Eu(acac)_3 \times nH_2O$	98.2 ± 3.0	1.8 ± 0.1	98.1 ± 4.9	1.9 ± 0.1
$Zr(OBu^n)_4/Eu(acac)_3 \times nH_2O$	98.1 ± 2.9	1.9 ± 0.1	97.7 ± 4.9	2.3 ± 0.1

The PD-Win 4.0 and ReX software complexes, along with ASTM and COD databases [35–37] were used to determine the phase composition, calculate the average size of coherent scattering regions, as well as the lattice parameters for the unit cell of $Zr_{0.98}Eu_{0.02}O_{1.99}$ nanoparticles. Nanophosphors obtained from 0.5 M solutions of $ZrOCl_2 \times 8H_2O$ and $EuCl_3 \times 6H_2O$ by coprecipitating with following hydrothermal treatment are a mixture of tetragonal (t), cubic (c) and monoclinic (m) zirconia phases in the 74.8/12.2/13 ratio (Fig. 1, pattern *1*). The phase composition of nanoparticles synthesized by the treatment of toluene solutions of $Zr(acac)_4$ and $Eu(acac)_3 \times nH_2O$ at an elevated temperature and pressure includes 46.9 vol.% tetragonal, 23.5 vol.% cubic and 29.6 vol.% monoclinic zirconia (Fig. 1, pattern *2*), according to results of XRD pattern analysis. A monoclinic phase is not observed in the sample, but t- and c-ZrO_2 are present in the ratio 33.8/66.2 if $Zr(OBu^n)_4$ is used as a precursor (Fig. 1, pattern *3*, and Table 2). The parameters and the volume of the unit cell in the $Cl^- \rightarrow C_5H_7O_2^- \rightarrow C_4H_9O^-$ series decrease for t-ZrO_2, and grow for its cubic phase. For nanopowders obtained from precursors of different nature, the average sizes of coherent scattering regions calculated by the Debye–Scherrer formula are comparable with the particle diameter fixed by the TEM (Table 2, Fig. 2). According to microphotographs, the average diameter of $Zr_{0.98}Eu_{0.02}O_{1.99}$ quasi-spherical particles obtained by the solvothermal synthesis from zirconium and europium acetylacetonates was 8 nm, and in the case of a mixture of $Zr(OBu^n)_4/Eu(acac)_3 \times nH_2O$ – 4 nm (Fig. 2, micrograph *2* and *3*). The dehydration under hydrothermal conditions of $ZrO(OH)_2$–$Eu(OH)_3$ mixture co-precipitated from inorganic salts leads to the crystallization of nanophosphors larger size of about 15 nm (Fig. 2, micrograph *1*).

In the Raman spectra of the nanoparticles obtained from precursors of different nature, there are apparent differences in the phase composition (Fig. 3). The use of zirconium and europium acetylacetonates as the starting materials in the synthesis of ZrO_2-2 mol.% $EuO_{1.5}$ nanoparticles leads to a significant increase in the content of the monoclonal phase (peaks at 183, 335, 533, 556, 613 cm^{-1}) and a decrease in the volume fraction of the

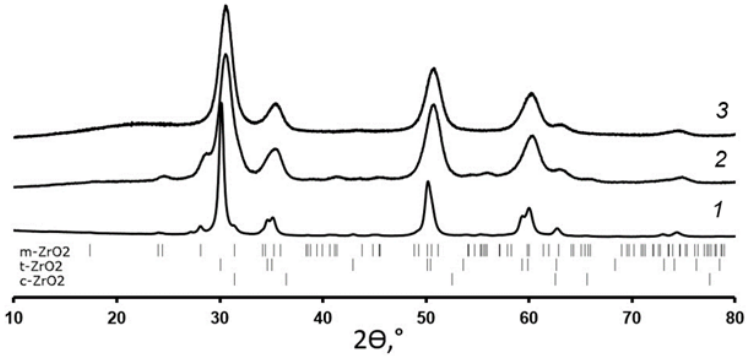

FIG. 1. X-ray diffraction patterns of $Zr_{0.98}Eu_{0.02}O_{1.99}$ nanoparticles synthesized from $ZrOCl_2$ and $EuCl_3$ crystalline hydrates (*1*), $Zr(acac)_4$ and $Eu(acac)_3 \times nH_2O$ (*2*), as well as $Zr(OBu^n)_4$ and $Eu(acac)_3 \times nH_2O$ (*3*)

TABLE 2. Structural parameters of $Zr_{0.98}Eu_{0.02}O_{1.99}$ nanoparticles synthesized in hydro- and solvothermal conditions from inorganic salts, metal alkoxide and chelating agents

Chemical prehistory	Phase composition	Unit cell parameters	Average crystallite size (XRD), nm
$ZrOCl_2 \times 8H_2O$/ $EuCl_3 \times 6H_2O$	13 vol.% m-ZrO_2	$a = 5.1783$; $b = 5.2099$; $c = 5.3171$; $\alpha = \gamma = 90$ °; $\beta = 99.25$ °; $V = 141.6$ Å^3	15 ± 3
	74.8 vol.% t-ZrO_2	$a = b = 3.6032$; $c = 5.1827$; $\alpha = \beta = \gamma = 90$ °; $V = 67.3$ Å^3	15 ± 3
	12.2 vol.% c-ZrO_2	$a = b = c = 5.1272$; $\alpha = \beta = \gamma = 90$ °; $V = 134.8$ Å^3	15 ± 3
$Zr(acac)_4$/ $Eu(acac)_3 \times nH_2O$	23.5 vol.% m-ZrO_2	$a = 5.1578$; $b = 5.1975$; $c = 5.3194$; $\alpha = \gamma = 90$ °; $\beta = 99.14$ °; $V = 140.8$ Å^3	8 ± 2
	46.9 vol.% t-ZrO_2	$a = b = 3.5964$; $c = 5.1872$; $\alpha = \beta = \gamma = 90$ °; $V = 67.1$ Å^3	6 ± 2
	29.6 vol.% c-ZrO_2	$a = b = c = 5.1313$; $\alpha = \beta = \gamma = 90$ °; $V = 135.1$ Å^3	6 ± 2
$Zr(OBu^n)_4$/ $Eu(acac)_3 \times nH_2O$	33.8 vol.% t-ZrO_2	$a = b = 3.5885$; $c = 5.1552$; $\alpha = \beta = \gamma = 90$ °; $V = 66.4$ Å^3	4 ± 1
	66.2 vol.% c-ZrO_2	$a = b = c = 5.1567$; $\alpha = \beta = \gamma = 90$ °; $V = 137.1$ Å^3	4 ± 1

tetragonal polymorphic modification (peaks at 149, 224, 292, 324, 407, 456 and 636 cm^{-1}) in comparison with analogs obtained from solutions of chlorides. Solvothermal treatment of $Zr(OBu^n)_4$/$Eu(acac)_3 \times nH_2O$ mixture in toluene makes it possible to synthesize nanoparticles mainly with the c-ZrO_2 structure characterized by a wide band of 530 – 670 cm^{-1} in the Raman spectra, as well as a unique phonon band F2g of ca. 625 cm^{-1} [7]. RS data confirm the phase composition determined by XRD (Table 2).

Based on the diffuse reflectance spectra $R(\lambda)$ in the visible and ultraviolet range from 2.5 to 6 eV, one calculated the Schuster–Kubelka–Munk or remission function [38]:

$$F\left(R_\infty\left(\lambda\right)\right) = \frac{\left(1 - R_\infty(\lambda)\right)^2}{2R_\infty(\lambda)} = \frac{K}{S} = \frac{2.303\varepsilon C}{S}, \tag{1}$$

where $R_\infty\left(\lambda\right)$ is the value of reflectance when it is already not changed in increasing system thickness; K is the absorption coefficient (twice the Beer's law absorption coefficient); S is twice the scattering coefficient of the sample; ε is the absorptivity, and C is the analyte concentration.

Using the plot of $\left(F\left(R_\infty\right)h\nu\right)^{1/\eta}$ versus energy, $h\nu$, one can estimate the optical bandgap, E_g, between the conduction band and the valence one in $Zr_{0.98}Eu_{0.02}O_{1.99}$ nanoparticles (Fig. 4). In the region of the highest

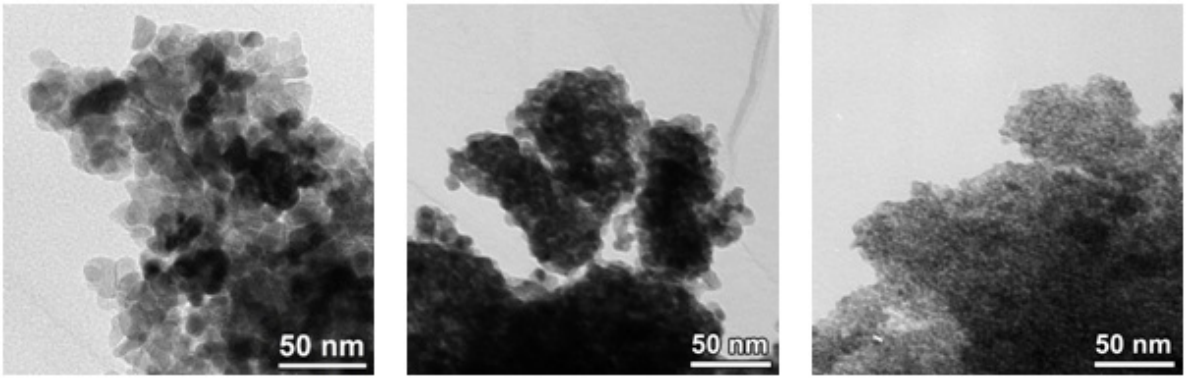

FIG. 2. TEM micrographs of $Zr_{0.98}Eu_{0.02}O_{1.99}$ nanoparticles synthesized from $ZrOCl_2$ and $EuCl_3$ crystalline hydrates (1), $Zr(acac)_4$ and $Eu(acac)_3 \times nH_2O$ (2), as well as $Zr(OBu^n)_4$ and $Eu(acac)_3 \times nH_2O$ (3)

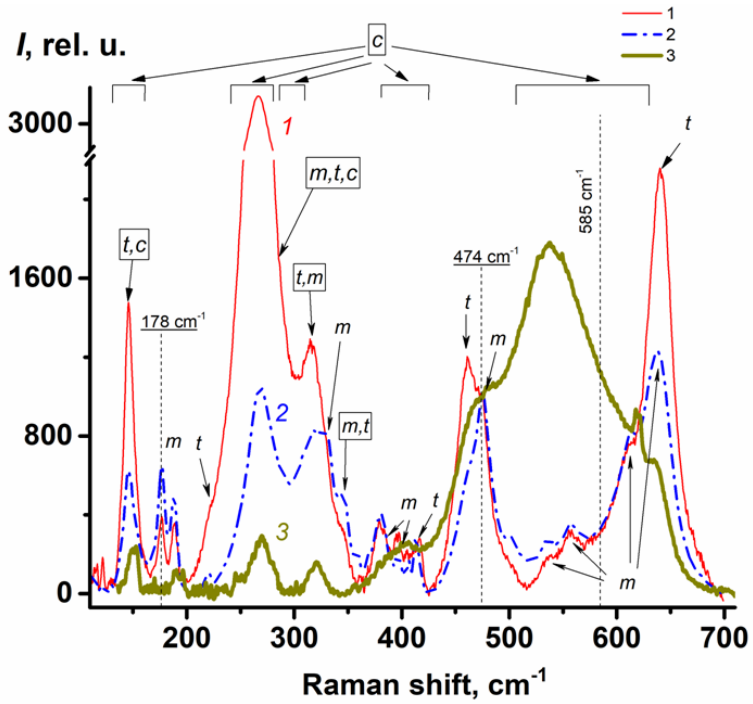

FIG. 3. Raman spectra of $Zr_{0.98}Eu_{0.02}O_{1.99}$ nanoparticles synthesized from $ZrOCl_2 \times 8H_2O$ and $EuCl_3 \times 6H_2O$ (1), $Zr(acac)_4$ and $Eu(acac)_3 \times nH_2O$ (2), as well as $Zr(OBu^n)_4$ and $Eu(acac)_3 \times nH_2O$ (3). Spectra were normalized at 474 cm^{-1}

obtained energy of 5 – 6 eV, the allowed indirect absorption transitions turned out to manifest themselves because there are linear approximations at $\eta = 2$ for all the cases under investigation [39]. At that, the E_g values of the studied nanoparticles are limited from 4 to 6 eV, which is consistent with prior research [6]. The bandgap of ZrO_2-2 mol.% $EuO_{1.5}$ nanoparticles synthesized from inorganic salts (E_{g1}) in comparison with $E_{g1'}$ of undoped zirconia increases from 4.85 to 5.12 eV. The introduction of 2 mol.% of $EuO_{1.5}$ into zirconia crystal lattice leads to decreasing the value of $(F(R_\infty)h\nu)^{1/2}$ as opposed to it (Note curves 1 and 1'). This result can mean the higher absorption ability of m-ZrO_2, which lessens in doping zirconia by Eu^{3+}, relative to one of t/c-phases in the region of 4 – 5.3 eV. For nanoparticles obtained from $Zr(OBu^n)_4$ and $Zr(acac)_4$, one observed the shifts from 4.85 eV of $E_{g1'}$ to 4.72 and 4.6 eV, respectively (Fig. 4). It was found that in the region of 3 – 4 eV absorption is less

for $Zr_{0.98}Eu_{0.02}O_{1.99}$ nanoparticles formed from $Zr(OBu^n)_4$ and $Zr(acac)_4$ as compared to those obtained from $ZrOCl_2 \times 8H_2O$. Here, the influence of t-phase is already reflected; the absorption ability of nanoparticles could decrease with the lower content of it. Moreover, the c-phase happens to be the least light-absorbing (Note curve 3, Fig. 4). It should be noted that the smaller additional E_g values for the systems synthesized from $ZrOCl_2 \times 8H_2O$ with 74.8 vol.% of t-ZrO_2, from $Zr(acac)_4$ with 23.5 vol.% of m-ZrO_2, and from $Zr(OBu^n)_4$ with 66.2 vol.% of c-ZrO_2 are determined from the plot in Fig. 4, as well. They are equal to 4.5, 3.6, and 3.5 eV, respectively. These data are consistent with the theoretical minimum E_g values obtained by the DFT method for the three different ZrO_2 modifications: 4.0 eV for t-ZrO_2, 3.6 eV for m-ZrO_2, and 3.3 eV for c-ZrO_2 [40]. Moreover, the shoulder in the range of 3.5 – 3.9 eV (curve 1, Fig. 4) may be attributed to intersitial oxygen states or oxygen vacancy states [40].

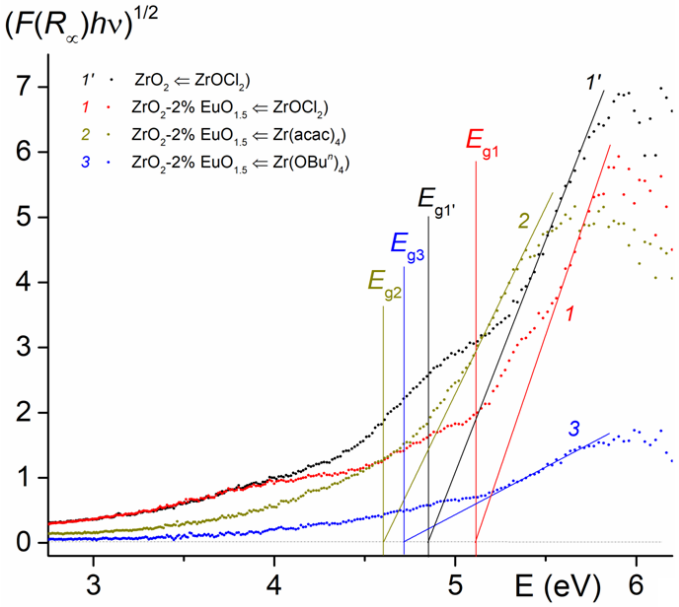

FIG. 4. Absorption spectra of $Zr_{0.98}Eu_{0.02}O_{1.99}$ phosphors synthesized from $ZrOCl_2$ and $EuCl_3$ crystalline hydrates (1), $Zr(acac)_4$ and $Eu(acac)_3 \times nH_2O$ (2), $Zr(OBu^n)_4$ and $Eu(acac)_3 \times nH_2O$ (3), as well as pure ZrO_2 nanoparticles prepared from $ZrOCl_2 \times 8H_2O$ (1')

The influence of the precursor nature on the photoluminescence of ZrO_2-2 mol.% $EuO_{1.5}$ nanoparticles synthesized by hydro- and solvothermal synthesis was also studied (Fig. 5). Peaks observed at 591, 607, 614, 628, 634, 653, 659, 702 and 749 nm, as well as the shoulder at 580 nm can be compared with the spectral terms of the Stark splitting for Eu^{3+} and the radiative transitions in the Dieke diagram for the $4f^n$ configuration of Eu^{3+} $^7F_J \leftarrow {}^5D_0$ ($J = 0 - 5$) [41,42]. The excitation spectra (Fig. 6) for these nanoparticles cover the range of intraconfiguration $4f^n$—$4f^n$ transitions in the region of 270 – 490 nm. In addition, the peaks at 227, 240, 256, and 265 nm are correlated with the interconfiguration $4f^n$—$5d^n$ transitions and charge transfer states. According to the excitation spectra, ones used the PL excitation wavelength of 255, 270, and 397 nm.

At the excitation of 247 – 255 nm in PL spectra (Fig. 5a) one observed a weak shoulder or a small peak at 614 nm. At this wavelength, the m-ZrO_2 polymorph manifests itself in photoluminescence. Thus, the contribution of the m-ZrO_2 increases in the series of $Zr(OBu^n)_4$/ $Eu(acac)_3 \times nH_2O$ (3) → $ZrOCl_2 \times 8H_2O$ /$EuCl_3 \times 6H_2O$ (1) → $Zr(acac)_4$/$Eu(acac)_3 \times nH_2O$ (2). The latter fact is reflected in the XRD and RS data (Table 2, Fig. 3) as the growth of the monoclinic phase. To that end, the ratio between the magnetic dipole transfer contribution and the electric dipole transfer one decreases, which indicates the lessening of crystal field symmetry around Eu^{3+}. It means that the pseudocubic (c/t) phase is lowered in the series. Also, it was found out that upon excitation at 270 and 397 nm of the $4f^n$—$4f^n$ transitions (Fig. 5b and c), the contribution of the c-ZrO_2 in the PL spectra (bands at 606 and 633 nm) of ZrO_2-2 mol.% $EuO_{1.5}$ nanoparticles increases in the series $ZrOCl_2 \times 8H_2O$/$EuCl_3 \times 6H_2O$ (1) → $Zr(acac)_4$/$Eu(acac_2)_3 \times nH_2O$ (2) → $Zr(OBu^n)_4$/$Eu(acac)_3 \times nH_2O$ (3), again consistent with the XRD data (Table 2, Fig. 3). Thus, there is the PL sensitivity of different ZrO_2-polymorph modifications to the excitation wavelengths [26]; in a short-wavelength region, the m-ZrO_2 determines luminescence, while in the long-wavelength region, the cubic phase is decisive.

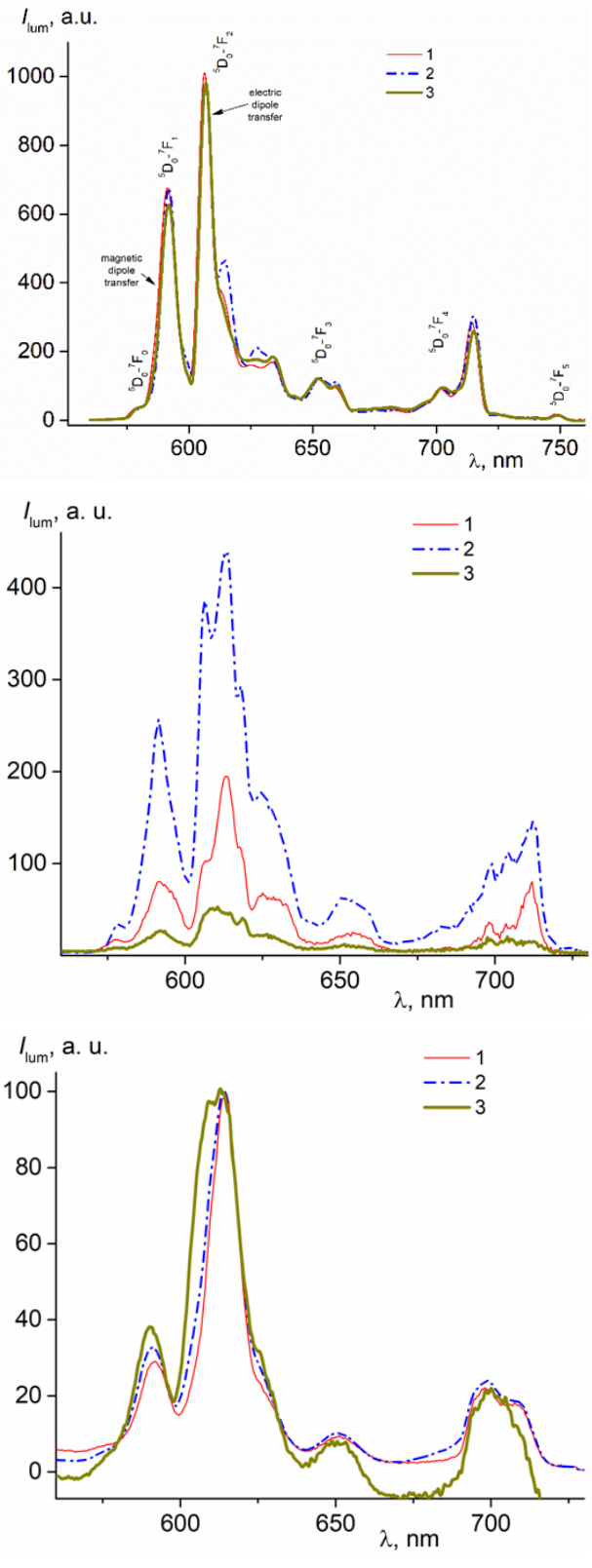

FIG. 5. The luminescence spectra (a – c), normalized at 606 (a) and 614 nm (c), for $Zr_{0.98}Eu_{0.02}O_{1.99}$ nanoparticles obtained by hydro and solvothermal synthesis from different precursors: $ZrOCl_2$ and $EuCl_3$ crystalline hydrates (1), $Zr(acac)_4$ and $Eu(acac)_3 \times nH_2O$ (2), $Zr(OBu^n)_4$ and $Eu(acac)_3 \times nH_2O$ (3). Excitation at 247 – 255 (a), 270 (b) and 397 nm (c)

TABLE 3. Photoluminescence lifetimes[1)] of $Zr_{0.98}Eu_{0.02}O_{1.99}$ nanoparticles formed from different precursors

Chemical prehistory	A_1	τ_{PL1}, ms	$A_2 = 1 - A_1$	τ_{PL2}, ms	χ^2_{red}
$ZrOCl_2 \times 8H_2O/EuCl_3 \times 6H_2O$	0.687	0.865	0.313	2.21	0.751
$Zr(acac)_4/Eu(acac)_3 \times nH_2O$	0.628	0.768	0.372	2.02	1.518
$Zr(OBu^n)_4/Eu(acac)_3 \times nH_2O$	0.436	1.160	0.564	3.22	2.668

[1)]PL lifetimes were fitted on the basis of the dual exponent decay (see Eq. 2) in minimizing a reduced χ^2_{red}-statistics.

[2)]Note the mean-weighted PL lifetimes, τ_{PLw}, calculated upon Eq. 3 and shown in Fig. 7.

The decay of PL intensity ($I_{lum}(t)$) for nanoparticles can be approximated by a model of the dual exponential function:

$$I_{lum}(t) = A_1 \exp(-t/\tau_{PL1}) + A_2 \exp(-t/\tau_{PL2}) + B, \tag{2}$$

where τ_{PL1} and τ_{PL2} are the PL lifetime for the first and second emission processes; A_1 and A_2 are the first and second pre-exponential factors. Term B is a background contribution. Based on the obtained τ_{PL} and their contributions in the two-exponential approximation (Table 3), the weighted-average luminescence lifetimes, τ_{PLw}, are calculated according to the expression (Fig. 6):

$$\tau_{PLw} = \frac{\sum_{i=1}^{2} A_i \tau_{PLi}^2}{\sum_{i=1}^{2} A_i \tau_{PLi}}. \tag{3}$$

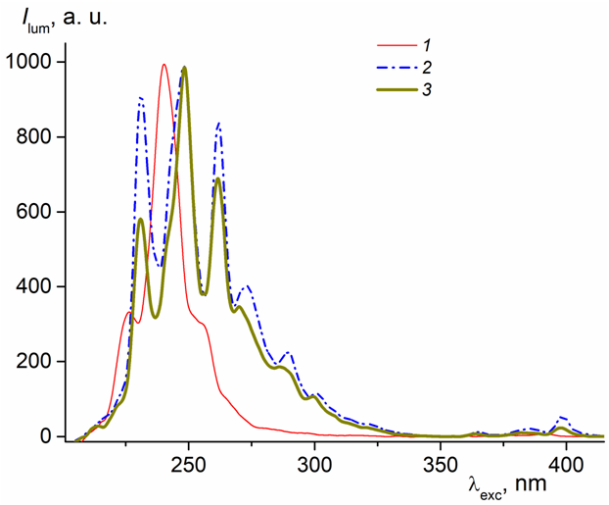

FIG. 6. The normalized excitation spectra of the luminescence of $Zr_{0.98}Eu_{0.02}O_{1.99}$ nanoparticles, obtained by hydro and solvothermal synthesis from different precursors: $ZrOCl_2$ and $EuCl_3$ crystalline hydrates (1), $Zr(acac)_4$ and $Eu(acac)_3 \times nH_2O$ (2), $Zr(OBu^n)_4$ and $Eu(acac)_3 \times nH_2O$ (3). Luminescence was observed at 606 nm (1) and 613 nm (2,3). The spectra are normalized at 240 nm (1) and 248 nm (2, 3)

According to the data shown in Fig. 7, PL lifetimes decrease from 2.8 to 1.5 ms upon increasing the m-ZrO_2content. As a result, the quantum yield rises to 2.3 %, as it was fixed in [43].

The results of low-temperature nitrogen adsorption show that ZrO_2-2 mol.% $EuO_{1.5}$ nanoparticles synthesized from $ZrOCl_2 \times 8H_2O/EuCl_3 \times 6H_2O$, $Zr(acac)_4/Eu(acac)_3 \times nH_2O$ and $Zr(OBu^n)_4/Eu(acac)_3 \times nH_2O$ are characterized by SBET values of 80.2, 91.6 and 96.6 m^2/g, respectively (Table 4). Sorption isotherms for these nanoparticles

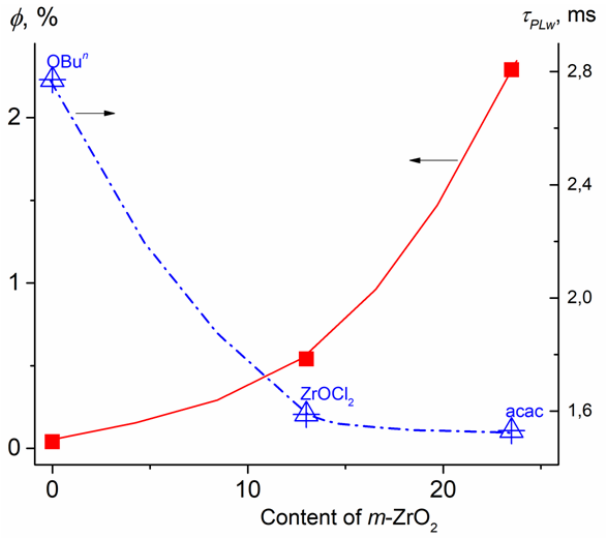

FIG. 7. Dependence of the lifetime and photoluminescence quantum yields of $Zr_{0.98}Eu_{0.02}O_{1.99}$ nanoparticles on the chemical prehistory $ZrOCl_2 \times 8H_2O$, $Zr(acac)_3$, and $Zr(OBu^n)_4$. Excitation was at 262 nm. Observation was at 614 nm

depend significantly on the method of their preparation (Fig. 8). The isotherms presented for nanopowders obtained from acetylacetonate solutions of zirconium and europium, as well as their chlorides, clearly belong to the IV type characteristic of mesoporous materials. Capillary condensation of the adsorbent can occur in the pores of these materials, which in turn leads to the appearance of hysteresis between adsorption and desorption isotherms (Fig. 8a). The course of the capillary-condensation hysteresis loop for these nanopowders according to IUPAC classification can be attributed to the H2 type, which indicates the presence of bottle-shaped mesopores in it. At the same time, for ZrO_2-2 mol.% $EuO_{1.5}$ nanoparticles obtained from zirconium (IV) butoxide solution and europium acetylacetonate hydrate, the sorption isotherm is close to the I type, which is inherent mainly to microporous samples. However, the observed hysteresis between the adsorption and desorption branches makes it possible to classify them also as an IV type.

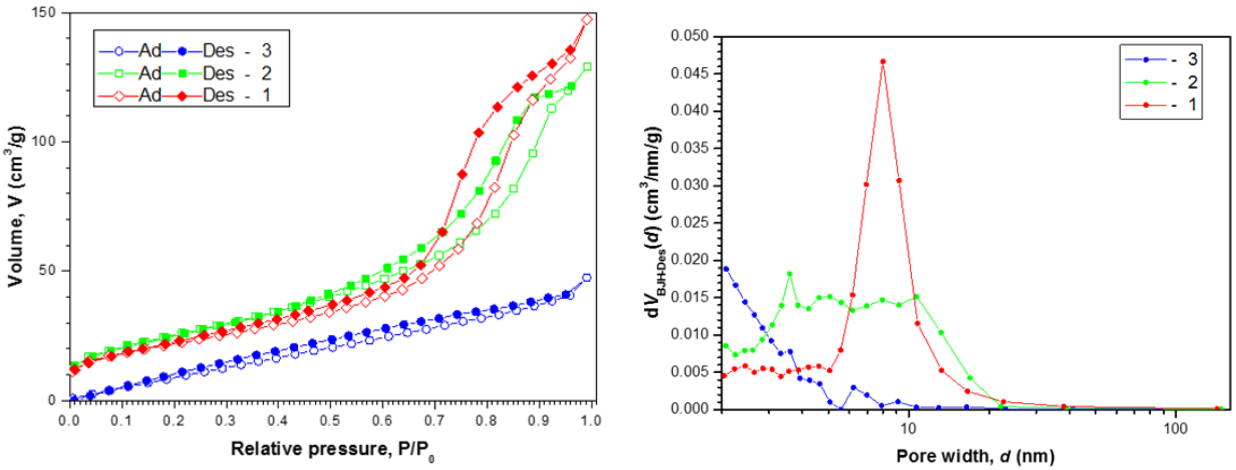

(a) (b)

FIG. 8. Adsorption-desorption isotherms (a) and BJH distributions of pore size (b) $Zr_{0.98}Eu_{0.02}O_{1.99}$ nanoparticles synthesized from $ZrOCl_2 \times 8H_2O$ and $EuCl_3 \times 6H_2O$ (1), $Zr(acac)_4$ and $Eu(acac)_3 \times nH_2O$ (2), as well as $Zr(OBu^n)_4$ and $Eu(acac)_3 \times nH_2O$ (3)

TABLE 4. The surface properties of $Zr_{0.98}Eu_{0.02}O_{1.99}$ nanoparticles with a different chemical prehistory, measured by the method of low-temperature nitrogen adsorption and electrophoretic light scattering

Chemical prehistory	S_{BET}, m^2/g	D_{pore}, nm	V_{pore}*, cm^3/g	ζ-potential, mV
$ZrOCl_2 \times 8H_2O/EuCl_3 \times 6H_2O$	80.2 ± 2.4	8	0.24	-8.7
$Zr(acac)_4/Eu(acac)_3 \times nH_2O$	91.6 ± 1.8	—	0.20	-4.2
$Zr(OBu^n)_4/Eu(acac)_3 \times nH_2O$	96.6 ± 3.9	—	0.05	15.3

*The specific volume of pores is determined by the limiting filling ($P/P_0 = 0.99$).

The pore size distribution in $Zr_{0.98}Eu_{0.02}O_{1.99}$ nanopowders, obtained from different precursors, was calculated for the desorption branch according to the BJH algorithm and is presented in Fig. 8b. The nanoparticle powder obtained from a toluene solution of $Zr(OBu^n)_4/Eu(acac)_3 \times nH_2O$ is characterized by a gradual pore size decrease in the range from 2 to 10 nm, which confirms the presence of both micro- and mesopores in it. A wide trapezoidal distribution of mesopores is observed in sizes ranging from *ca.* 3 to 20 nm, with a small number of micropores in the case of a sample synthesized from acetylacetonate hydrates of zirconium and europium. Moreover, only nanoparticles obtained by hydrothermal treatment of the $ZrO(OH)_2$–$Eu(OH)_3$ composition is characterized by a lognormal distribution of mesopores in the range from 5 to 20 nm with a maximum at *ca.* 8 nm.

In a series of $Zr_{0.98}Eu_{0.02}O_{1.99}$ nanoparticles obtained from different precursors, the highest survival of fibroblast cells was observed in a suspension of phosphors with the largest specific surface area and positive values of the zeta potential (Table 4). Moreover, the degree of cell culture survival in aqueous dispersions of ZrO_2-2 mol.% $EuO_{1.5}$ nanoparticles, obtained from $Zr(OBu^n)_4/Eu(acac)_3 \times nH_2O$, in the concentration range of 5 – 500 μg/ml varies quite weakly compared with other phosphors synthesized in this study (Fig. 9). Thus, the stabilization of the cubic zirconia modification by selecting of zirconium alkoxide as initial material in the synthesis allows the production of nanoparticles with a more developed surface and smallest cytotoxicity.

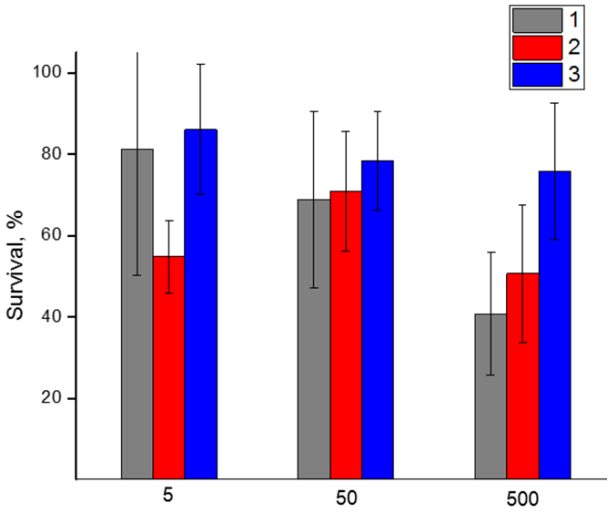

FIG. 9. MTT-test on human dermal fibroblasts in the dispersions of ZrO_2-2 mol.% $EuO_{1.5}$ nanoparticles obtained from different precursors: $ZrOCl_2 \times 8H_2O/EuCl_3 \times 6H_2O$ (1), $Zr(acac)_4/Eu(acac)_3 \times nH_2O$ (2), $Zr(OBu^n)_4/Eu(acac)_3 \times nH_2O$ (3)

4. Conclusion

As a result of the performed studies it is established that at the same content of Eu (III) in a reaction mixture crystallization of three polymorphic forms is observed, as in case of $ZrO(OH)_2$–$Eu(OH)_3$ dehydration under hydrothermal conditions, and for solvothermal treatment of zirconium and europium chelating compounds. In the latter case, the content of monoclinic and cubic phases of ZrO_2 is higher. It has been noted that the solvothermal treatment of zirconium butoxide and europium acetylacetonate hydrate under similar conditions leads mainly to the crystallization of nanoparticles with the structure of ZrO_2 metastable phases. It was possible based on measurements of quantum yields to connect the luminescence efficiency with the presence of monoclinic phase in the series of $Zr(OBu^n)_4$/$Eu(acac)_3 \times nH_2O \rightarrow ZrOCl_2 \times 8H_2O$/ $EuCl_3 \times 6H_2O \rightarrow Zr(acac)_4$/ $Eu(acac)_3 \times nH_2O$ for $Zr_{0.98}Eu_{0.02}O_{1.99}$ nanoparticles. It has been revealed that the more $Zr_{0.98}Eu_{0.02}O_{1.99}$ crystallites with monoclinic structure are formed in hydrothermal and solvothermal conditions of synthesis, the higher the quantum yield of Eu^{3+} luminescence is, and the shorter emission times are fixed. According to MTT-test, the metabolic activity of cells is preserved after three days of human fibroblast incubation in an aqueous dispersion of ZrO_2-2 mol.% $EuO_{1.5}$ nanoparticles, which indicates that they practically no cytotoxicity. Stabilization of more symmetrical t, c-ZrO_2 modifications in the process of solvothermal synthesis by selecting $Zr(OBu^n)_4$ and $Eu(acac)_3 \times nH_2O$ as precursors made it possible to obtain nanoparticles with a high surface/volume ratio and a positive zeta potential value, whose dispersions showed the highest survival rate of fibroblasts cells. Thus, the selection of synthesis conditions (nature of the precursor, type of solvent, and isothermal holding time) allows for varying the phase composition of the formed $Zr_{1-x}Eu_xO_{2-0.5x}$ nanoparticles. Moreover, the combination of the most effective monoclinic modification for luminescence with the least cytotoxic cubic phase of zirconia makes it possible to obtain phosphors with the required quantum yield and extinction coefficients, which have potential for application in biophotonics and medicine.

Acknowledgements

Alexander N. Bugrov acknowledges the Russian Foundation for Basic Research (grant No. 16-33-60227) for the financial support. The experimental work was facilitated by the Engineering Center equipment of the St. Petersburg State Technological Institute (Technical University). The quantum yield and Raman spectroscopy measurements were determined at the Center for Optical and Laser Materials Research, St. Petersburg State University. TEM studies were performed using equipment of the Federal Joint Research Center "Material science and characterization in advanced technology" supported by the Ministry of Education and Science of the Russian Federation (id RFMEFI62117X0018). The authors are grateful to Kirilenko D. A. from the Ioffe Institute for the study of samples obtained in this article by TEM. The authors are also appreciative to Kryukov A. E. from Institute of Macromolecular Compounds RAS for cytotoxicity studies and Rodionov I. A. from Institute of Chemistry, St. Petersburg State University for bandgap measurements.

References

[1] Di Bartolo B., Collins J., Silvestri L. *Nano-Optics: Principles enabling basic research and applications*, NATO Science for Peace and Security Series B: Physics and Biophysics, Springer Netherlands, 2017, 584 p.

[2] Gai S., Li C., Yang P., Lin, J. Recent progress in rare earth micro/nanocrystals: Soft chemical synthesis, luminescent properties, and biomedical applications. *Chem. Rev.*, 2014, **114** (4), P. 2343–2389.

[3] Luo W., Liu Y., Chen X. Lanthanide-doped semiconductor nanocrystals: electronic structures and optical properties. *Science China Materials*, 2015, **58** (10), P. 819–850.

[4] Chakraborty A., Debnath G.H., et al. Identifying the correct host – guest combination to sensitize trivalent lanthanide (guest) luminescence: Titanium dioxide nanoparticles as a model host system. *J. Phys. Chem. C*, 2016, **120** (41), P. 23870–23882.

[5] Raj A.K.V., Rao P.P., Sreena T.S., Thara T.R.A. Influence of local structure on photoluminescence properties of Eu^{3+} doped CeO_2 red phosphors through induced oxygen vacancies by contrasting rare earth substitutions. *Phys. Chem. Chem. Phys.*, 2017, **19**, P. 20110–20120.

[6] Gallino F., Di Valentin C., Pacchioni G. Band gap engineering of bulk ZrO_2 by Ti doping. *Phys. Chem. Chem. Phys.*, 2011, **13**, P. 17667.

[7] Basahel S.N., Ali T.T., Mokhtar M., Narasimharao K. Influence of crystal structure of nanosized ZrO_2 on photocatalytic degradation of methyl orange. *Nanoscale Research Letters*, 2015, **10** (1), P. 73.

[8] Lovisa L.X., Andres J., et al. Photoluminescent properties of ZrO_2: Tm^{3+}, Tb^{3+}, Eu^{3+} powders – Acombined experimental and theoretical study. *Journal of Alloys and Compounds*, 2017, **695**, P. 3094–3103.

[9] Yamamoto O., Arachi Y., et al. Zirconia based oxide ion conductors for solid oxide fuel cells. *Ionics*, 1998, **4** (5–6), P. 403–408.

[10] Sinhamahapatra A., Jeon J.-P., et al. Oxygen-deficient zirconia (ZrO_{2-x}): A new material for solar light absorption. *Sci. Rep.*, 2016, **6**, P. 27218.

[11] Martin L.P., Glass R.S. Hydrogen sensor based on yttria-stabilized zirconia electrolyte and tin-doped indium oxide sensing electrode. *Journal of the Electrochemical Society*, 2004, P. 22.

[12] Hernández S., Gionco C., et al. Insights into the sunlight-driven water oxidation by Ce and Er-doped ZrO_2. *Front. Chem.*, 2018, **6**, P. 368.

[13] Bugrov A.N., Rodionov I.A., et al. Photocatalytic activity and luminescent properties of Y, Eu, Tb, Sm and Er-doped ZrO_2 nanoparticles obtained by hydrothermal method. *Int. J. Nanotechnology*, 2016, **13** (1/2/3), P. 147–157

[14] Garnweitner G. Zirconia nanomaterials: Synthesis and biomedical application. *Nanotechnologies for the Life Sciences*, 2010, **8**, P. 245–285.
[15] Almjasheva O.V., Garabadzhiu A.V., et al. Biological effect of zirconium dioxide-based nanoparticles. *Nanosystems: physics, chemistry and mathematics*, 2017, **8** (3), P. 391–396.
[16] Ceja-Fdez A., López-Luke T., et al. Labeling of HeLa cells using ZrO_2:Yb^{3+}–Er^{3+} nanoparticles with upconversion emission. *Journal of Biomedical Optics*, 2015, **20** (4), P. 046006.
[17] Liu Y., Zhou S., et al. Amine-functionalized lanthanide-doped zirconia nanoparticles: Optical spectroscopy, time-resolved fluorescence resonance energy transfer biodetection, and targeted imaging. *J. Am. Chem. Soc.*, 2012, **134**, P. 15083–15090.
[18] Escribano P., Julian-Lopez B., et al. Photonic and nanobiophotonic properties of luminescent lanthanide-doped hybrid organic–inorganic materials. *J. Mater. Chem.*, 2008, **18**, P. 23–40.
[19] Dunne P.W., Munn A.S., et al. Continuous-flow hydrothermal synthesis for the production of inorganic nanomaterials. *Phil. Trans. R. Soc. A*, 2015, **373**, P. 20150015.
[20] Almjasheva O.V., Smirnov A.V., et al. Structural features of ZrO_2–Y_2O_3 and ZrO_2–Gd_2O_3 nanoparticles formed under hydrothermal conditions. *Russian Journal of General Chemistry*, 2014, **84** (5), P. 804–809.
[21] Moon B.K., Kwon I.M., et al. Synthesis and luminescence characteristics of Eu^{3+}-doped ZrO_2 nanoparticles. *Journal of Luminescence*, 2007, **122–123**, P. 855–857.
[22] Almjasheva O.V., Denisova T A. Water state in nanocrystals of zirconium dioxide prepared under hydrothermal conditions and its influence on structural transformations. *Russian Journal of General Chemistry*, 2017, **87** (1), P. 1–7.
[23] Dudnik E.V. Modern methods for hydrothermal synthesis of ZrO_2-based nanocrystalline powder. *Powder Metallurgy and Metal Ceramics*, 2009, **48** (3–4), P. 146–158.
[24] Bugrov A.N., Almjasheva O.V. Effect of hydrothermal synthesis conditions on the morpholgy of ZrO_2 nanoparticles. *Nanosystems: physics, chemistry and mathematics*, 2013, **4** (6), P. 810–815.
[25] Hobbs H., Briddon S., Lester E. The synthesis and fluorescent properties of nanoparticulate ZrO_2 doped with Eu using continuous hydrothermal synthesis. *Green Chem.*, 2009, **11**, P. 484–491.
[26] Tiseanu C., Cojocaru B., et al. Order and disorder effects in nano-ZrO_2 investigated by micro-Raman and spectrally and temporarily resolved photoluminescence. *Phys. Chem. Chem. Phys.*, 2012, **14**, P. 12970–12981.
[27] Smits K., Olsteins D., et al. Doped zirconia phase and luminescence dependence on the nature of charge compensation. *Scientific Reports*, **7**, P. 44453.
[28] Bugrov A.N., Smyslov R.Yu., et al. Phase composition and photoluminescence correlations in nanocrystalline ZrO_2:Eu^{3+} phosphors synthesized under hydrothermal conditions. *Nanosystems: physics, chemistry and mathematics*, 2018, **9** (3), P. 378–388.
[29] Meetei S.D., Singh S.D. Effects of crystal size, structure and quenching on the photoluminescence emission intensity, lifetime and quantum yield of ZrO:Eu nanocrystals. *Journal of Luminescence*, 2014, **147**, P. 328–335.
[30] Bugrov A.N., Smyslov R.Yu., et al. Soluble and insoluble polymer-inorganic systems based on poly(methyl methacrylate), modified with ZrO_2–$LnO_{1.5}$ (Ln = Eu, Tb) nanoparticles: Comparison of their photoluminescence. *Journal of Luminescence*, **2019**, *207*, P. 157–168.
[31] Melekh N.V., Frolova S.V., Aleshina L.A. X-Ray analysis of powdered celluloses obtained with the use of Lewis acids. *Polymer Science, Ser. A*, 2014, **56**, P. 129–136.
[32] Bortolotti M., Lutterotti L., Lonardelli I. ReX: a computer program for structural analysis using powder diffraction data. *J. Appl. Cryst.*, 2009, **42** (3), P. 538–539.
[33] Bugrov A.N., Zavialova A.Yu., et al. Luminescence of Eu^{3+} ions in hybrid polymer-inorganic composites based on poly(methyl methacrylate) and zirconia nanoparticles. *Luminescence*, 2018, P. 1–13.
[34] DeMello J.C., Wittmann H.F., Friend R.H. An improved experimental determination of external photoluminescence quantum efficiency. *Advanced Materials*, 1997, **9**, P. 230–232.
[35] Smith D.K., Newkirk H.W. The crystal structure of baddeleyite (monoclinic ZrO_2) and its relation to the polymorphism of ZrO_2. *Acta Crystallographica*, 1965, **18**, P. 983–991.
[36] Igawa N., Ishii Y. Crystal structure of metastable tetragonal zirconia up to 1473 K. *J. Am. Ceram. Soc.*, 2001, **84** (5), P. 1169–1171.
[37] Martin U., Boysen H., Frey F. Neutron powder investigation of tetragonal and cubic stabilized zirconia, TZP and CSZ, at temperatures up to 1400 K. *Acta Crystallographica Section B*, 1993, **49** (3), P. 403–413.
[38] Hecht H.G. The interpretation of diffuse reflectance spectra. *Journal of Research of the National Bureau of Standards – A. Physics and Chemistry*, 1976, **80** (4), 567.
[39] Heine C., Girgsdies F., et al. The model oxidation catalyst α-V_2O_5: insights from contactless in situ microwave permittivity and conductivity measurements. *Appl. Phys. A*, 2013, **112** (2), P. 289–296.
[40] Garcia J.C., Scolfaro L.M.R., et al. Structural, electronic, and optical properties of ZrO_2 from ab initio calculations, 2012, ArXiv:1204.2886v1 [cond-mat.mtrl-sci].
[41] Bunzli J.-C. G. On the design of highly luminescent lanthanide complexes. *Coordination Chemistry Reviews*, 2015, **293–294**, P. 19–47.
[42] Tamrakar R.K., Bisen D.P., Upadhyay K., Tiwari S. Synthesis and thermoluminescence behavior of ZrO_2:Eu^{3+} with variable concentration of Eu^{3+} doped phosphor. *Journal of Radiation Research and Applied Sciences*, 2014, **7**, P. 486–490.
[43] Ahemen I., Dejene F.B. Effect of Eu^{3+} ion concentration on phase transition, site symmetry and quantum efficiency of ZrO_2 nanocrystal rods. *Journal of Nanoscience and Nanotechnology*, 2018, **18**, P. 2429–2440.

NANOSYSTEMS: PHYSICS, CHEMISTRY, MATHEMATICS, 2019, 10 (2), P. 176–183

Influence of hexylamine and alcohols as cosurfactants on microemulsion phase behavior and solubilization

Hüsnüye Durmaz[1], Mehmet İşcan[2]

[1]Trakya University, Faculty of Education, 22030 Edirne, Turkey
[2]Trakya University, Faculty of Science, Department of Chemistry, 22030 Edirne, Turkey
husniyedurmaz@trakya.edu.tr, miscan22@gmail.com

DOI 10.17586/2220-8054-2019-10-2-176-183

This study investigated the influence of cosurfactants on the phase behavior and solubilization capacity of microemulsions. Firstly, we determined the influence of alcohol chain length on the microemulsion solubilization capacity in microemulsion systems containing sodium dodecyl sulfate (SDS), heptane, and water; utilizing n-butanol, n-hexanol, n-octanol and hexylamine as cosurfactants. Then, we compared the effect of the cosurfactant on the solubilization capacity of the microemulsion with SDS. Based on the results, we suggest that hexylamine is a good candidate to produce microemulsions since hexylamine behaved as a cationic surfactant. Secondly, keeping constant the rate of surfactant/cosurfactant and varying the rate of alcohol to hexylamine as cosurfactant, we explain the cosurfactant effect in systems with SDS, alcohol, methylene chloride, and sodium molybdate using the spectrophotometric method. Results showed that the absorbance (ABS) values increased continuously in the systems of n-octanol and n-decanol with increasing amounts of hexylamine. The change in ABS values is considered to be related to microemulsion structure inversion.

Keywords: microemulsion, cosurfactant, microstructure, phase behavior, solubilization.

Received: 18 April 2019

Revised: 21 April 2019

1. Introduction

There is growing interest in investigating phase behavior and the solubilization capacity of microemulsions due to their common use in industrial applications, pharmaceuticals, enhanced oil recovery, consumer products, and drug delivery systems [1–4]. Ever since their introduction, microemulsions have been studied theoretically as well as experimentally by various researchers [5–8]. Understanding the phase behavior and solubilization capacity of microemulsions plays a vital role in designing and developing specific applications.

Microemulsions are thermodynamically stable and optically isotropic mixtures containing water or brine, surfactant, organic solvent, and often a cosurfactant. A microemulsion system comprises four or five components, namely, water, organic solvent, surfactant, cosurfactant, and electrolyte [9]. Structurally, depending on the proportion of the components, they have been classified as either distribution of oil-in-water (O/W) or water-in-oil (W/O) [7, 9–11]. The phase behavior of microemulsion systems is very important, and is shown in the Gibbs triangle diagram [12].

Part of the research on microemulsions is related to the maximum solubility of the organic solvent and/or water with a low amount of surfactant [13, 14]. The use of a cosurfactant, usually a medium-chain-length alkyl alcohol such as n-butanol, increases the stability of the microemulsion [14]. It has been reported that several factors such as the nature of hydrocarbons and alcohols as cosurfactant, concentration of surfactant, temperature and electrolyte influence the properties of the microemulsions, such as solubilization and phase behavior [1, 3, 8, 14–17]. For example, when hydrocarbon levels exceed 50 % or increase the alkyl chain length of the oil, the solubilizing capacity of water decreases in the microemulsion systems, consisting of oil, water, single-surfactant, cosurfactant (alcohol) and electrolyte [18]. Therefore, Li, Wang and Wang suggested that mixed anionic-cationic surfactants were more beneficial for forming W/O microemulsions with low surfactant content than a single surfactant, due to the synergistic effect resulting from strong Coulombic interactions between the cationic and anionic surfactants. They studied the effect of oil and alcohol chain length on the water solubilization and phase behaviors of W/O microemulsions with mixed-surfactant systems containing SDS as an anionic surfactant and tetradecyl trimethyl ammonium bromide (CTAB) as a cationic surfactant. According to their conclusions, the water solubilization capacity in the studied systems: (1) Increases when the cationic surfactant (CTAB) amount is increased in mixed surfactant systems with SDS as a major anionic surfactant, (2) Decreases by increasing the oil chain length at constant ratios of alcohol to the surfactant and anionic to the cationic surfactant, and (3) Increases with an increasing alcohol chain length in the order of n-butanol $<$ n-pentanol $<$ n-hexanol, and as the alcohol concentration increases [18].

Another important argument is that using hexylamine instead of medium-chain-length alcohols as cosurfactant reduces problems with the solubilization of water at high hydrocarbon levels. As cited by Wormuth and Kaler "*the first reference to the use of amines as cosurfactants is by Winsor*" in 1948 [17]. Venable, Elders and Fang indicate that hexylamine is a good candidate to produce microemulsions. Based on previous studies [19], Wormuth and Kaler report that "*pseudoternary-phase diagrams of various amines combined with anionic and cationic surfactants show large one-phase regions and high solubility of water in oil-rich regions*" [17]. Most previous studies on the influence of cosurfactant have been concerned with alcohols. As mentioned above, the selection of cosurfactant is of vital importance. For example, since short-chain alcohols are volatile and flammable substances, medium-chain-length alcohols such as pentanol and hexanol are not suitable for pharmaceuticals due to their high irritation potential, and using long-chain-length alcohols may cause the formation of lamellar liquid crystalline phases instead of microemulsion phases [4, 20]. Therefore, there is a need to better understand the role of hexylamine as a cosurfactant in the behavior of microemulsions. To select the appropriate cosurfactant is crucial to the solubilization capacity of microemulsions, as well as their formation.

Based on the application potential of microemulsions, this study had two aims. Initially, the aim was to investigate the effect of cosurfactants on microemulsion systems with SDS, heptane and water by using n-butanol, n-hexanol, n-octanol and hexylamine as cosurfactant, and then comparing the microemulsion regions in the phase diagrams. The second aim of the study was to explain the structural changes in microemulsions using mixed hexylamine plus alcohol as a cosurfactant with the spectrophotometric method, since the mixtures combining n-alkanol and amine show a variety of different behaviors [21]. Although use of different techniques such as dynamic light scattering (DLS), static light scattering (SLS), and FT-IR, pulse-gradient NMR, and X-ray scattering (SANS, SAXS) [22, 23] give more detailed knowledge of the microemulsion structure, we can also interpret the microemulsion structure by looking at changes in their basic ABS values.

2. Experiment procedure

2.1. Materials

Sodium dodecylsulfate (SDS, Merck, 98 %) was recrystallised twice from hot 99 % ethanol. It was dried in a vacuum oven at 50 °C and stored in a desicator. Sodium molybdate dihydrate ($Na_2MoO_4 \cdot 2H_2O$, 99 %), and rubrene 1 (5, 6, 11, 12 tetraphenylnaphthacene, 98 %) were purchased from Aldrich Chemie and were used as received. n-Heptane (Merck, 99 %), n-butanol (Merck, $>$ 99 %), n-hexanol (Merck, 99 %), n-octanol (Aldrich, $>$ 99 %), hexylamine (Merck, $>$ 98 %), methylene chloride (Merck, $>$ 99.5 %), and hydrogen peroxide (Merck, 30 %) were used without further purification. The water was distilled twice.

2.2. Apparatus

A Vortex-Genie 2 Mixer was used for all mixing treatments. The spectra and absorbance measurements were recorded on a Shimadzu UV-1601 spectrophotometer over wavelength ranges of 400 – 600 nm.

2.3. Methods

SDS and heptane were selected as the anionic surfactant and the organic solvent in all systems. We utilized n-butanol, n-hexanol, n-octanol and n-hexylamine as cosurfactants and prepared microemulsion systems of SDS/Heptane/Water at constant pressure and temperature, as previously described [11, 13, 24]. All experiments were carried out at room temperature. A series mixture was prepared consisting of various amounts of surfactant, cosurfactant and organic solvent in 10 mL screw-cap centrifuge tubes. In these microemulsion systems, the weight ratio surfactant/cosurfactant was held constant at 0.5. The contents of the tubes were blended by vortex mixing for several minutes to equilibrate at room temperature. The slurries obtained were titrated with twice-distilled water from a 1 mL micro-burette. After each drop of water was added, the tubes were vigorously stirred in the vortex mixer. The blurred emulsion spontaneously transformed into a clear single-phase environment, indicating the beginning of the microemulsion phase. Then, the titration process continued until permanent turbidity or phase separation was seen visually. Furthermore, samples were equilibrated for at least several days in a thermostatic bath to control the turbidity or phase separation. The procedure used for ternary and quaternary phase diagram determination followed the method introduced by Ezrahi, Aserin, Garti and Berkovic [25]. The surfactant + cosurfactant were considered to be a single component for the ternary phase diagram.

We followed the spectrophotometric method described by Aubry and Bouttemy [26] to investigate the microemulsions' structure with SDS/hexylamine+alcohol/methylene chloride/sodium molybdate (0.2 M). In this part of the experiment, initially, a water-in-oil (W/O) microemulsion with SDS/n-butanol/methylene chloride/sodium molybdate system was adapted from the study of Nardello, Marti, Pierlot and Aubry [27].

3. Results and discussion

3.1. Phase Behavior of SDS/Heptane/Water Systems

We investigated the effects of the cosurfactant on the phase behavior and solubilization capacity of the microemulsions with SDS. The pseudoternary phase diagrams were drawn up at 0.5 of the weight ratio surfactant / cosurfactant, and are presented in Fig. 1. When the systems in which n-butanol, n-hexanol and n-octanol were used as cosurfactant are compared (Fig. 1), it can be seen that the microemulsion region was reduced with increasing alcohol chain length. The interaction energy between the alcohol and oil molecules increases as the alcohol chain length is increased, and hence water solubilization capacity decreases due to the increasing alcohol carbon number [28–30]. As known, phase behavior is correlated with the oil/water interfacial tension, the size of dispersed particles and the solubilization of oil and water in the microemulsion [31]. Depending on the length of the alcohol chain, the distribution of alcohol in the oil and water phases affects microstructure and the extension of microemulsion area. As pointed out by Miyata, Miyamoto and Yonese [32], the second effect of the alcohol is to compete with surfactant for interfacial adsorption by entering the interfacial area and by pulling apart the surfactant molecules, which is caused to decrease of the interfacial surfactant concentration per unit area. The presence of alcohol decreases both the polar head group interaction and the hydrocarbon chain interactions of the surfactant molecules by causing of mutual solubility change of hydrophilic and hydrophobic components.

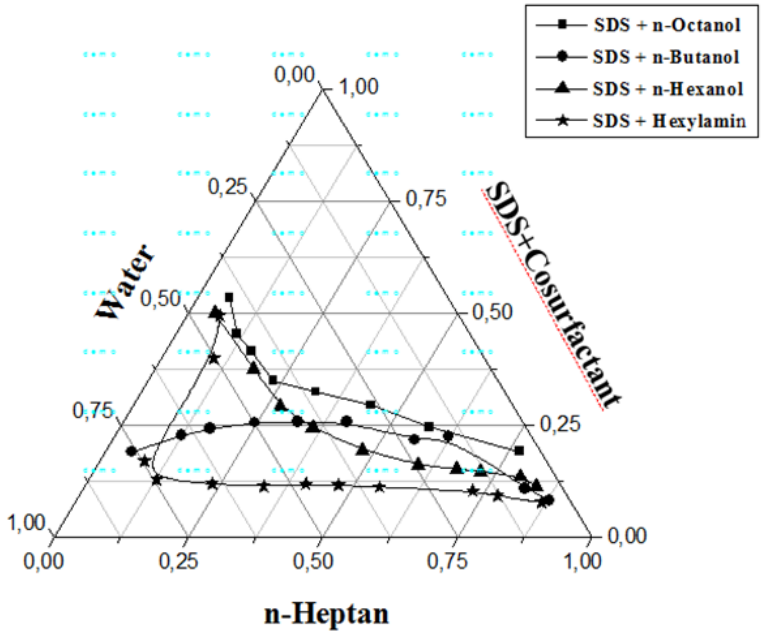

FIG. 1. Pseudoternary phase diagram of the SDS/Cosurfactant/n-Heptan/Water at room temperature. [SDS/Cosurfactant = 0.5 (weight)]

When the phase diagrams (Fig. 1) are examined, it is seen that the microemulsion region in the system with hexylamine as cosurfactant is larger than the others. As can be seen from Fig. 1, hexylamine is an effective cosurfactant for microemulsions, giving rise to high solubilization of heptane and water at the weight ratio surfactant/cosurfactant of 0.5. As pointed out by Venable and Viox [33], medium chain length alkyl amines are more effective cosurfactants for microemulsion formation than are medium chain length alcohols with sodium doecyl sulfate as the surfactant. This observation correlates with the good solubility of water in hexylamine and poor solubility of hexylamine in water [34]. It can also be explained in terms of the hydrophile-lipophile balance (HLB), due to reduction of the strong hydrophilicity of SDS by the amine interaction. This means that the SDS becomes less hydrophilic when hexylamine is added as cosurfactant to the system. A specific ionic interaction between the amine and anionic surfactant occurs in the surfactant-rich interfacial region [17]. The repulsive force in these microemulsions is, in fact, like that in an ionic micelle, resulting from coulombic repulsion between the NH2+ group of the hexylamine head group; which, being directly attached to the alkyl chain, would have to be located close to the hydrophobic core [35].

It is worth noting that hexylamine acts as if positively charged under experimental conditions, thus becoming a cationic surfactant in itself. Due to the role of hexylamine as a cationic cosurfactant, this microemulsion system

can be depicted as a mixture of anionic and cationic surfactants. Mixed anionic-cationic surfactant systems often have synergistic effects [2]. As reviewed by Doan, Acosta, Scamehorn and Sabatini, while adding alcohol is not preferred in certain environmental and consumer product formulations, the addition of alcohol is generally necessary to avoid liquid crystal formation in mixed anionic-cationic surfactant systems [2]. Venable, Elders and Fang observed that hexylamine was effective as a cosurfactant with both the aliphatic hydrocarbon heptane and the aromatic hydrocarbon toluene. Similarly, they mention that the superiority of "*hexylamine would be explained with the concept of the hydrophile-lipophile balance (HLB) of surfactant systems, as put forth by Shinoda et al. (1984)*" [19].

3.2. Phase Behavior of SDS/hexylamine + alcohol/methylene chloride/sodium molybdate (0.2 M)

New SDS/methylene chloride/sodium molybdate (aq) systems were prepared to investigate the cosurfactant's effect on structural changes using the spectrophotometric method. In preparation of these systems, the surfactant/cosurfactant ratio was fixed at 0.5 by weight in all of the systems, and combinations of alcohol and hexylamine were used as cosurfactant by changing the ratio of alcohol to hexylamine at 75/25, 50/50, 25/75 by weight. In these media, the resulting microemulsion systems in which both sodium molybdate as an ionic compound and rubrene-1 as an organic compound were dissolved simultaneously were compared. The sodium cations of sodium molybdate decrease repulsion between the negatively-charged head groups of SDS and hence favor the formation of reverse micelles. The water-in-oil microemulsions (W/O) used in the present study are described as roughly spherical water microdroplets coated with an interfacial film of SDS; n-butanol being dispersed in a continuous phase of methylene chloride, as shown by Aubry and Bouttemy [26]. One important feature of these media is their ability to dissolve simultaneously considerable amounts of hydrophilic compounds that are confined in aqueous droplets and hydrophobic organic molecules localized in the continuous organic phase. Structural changes to the microemulsions are interpreted as based on changes to the absorbance. The wavelength (λ) – absorbance (ABS) changes of microemulsions with SDS, alcohol, hexylamine, methylene chloride and sodium molybdate solution are shown in Figs. 2, 3, 4, and 5.

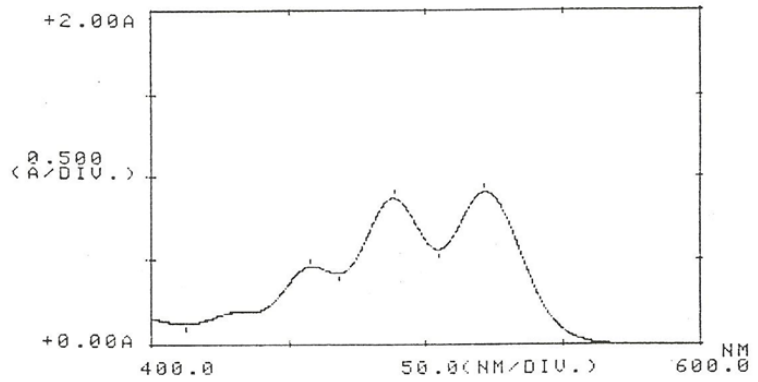

FIG. 2. The wavelength-absorbance change of the system with SDS/Hexylamine/Methylene chloride/Sodium molybdate (aq). SDS/Hexylamine = 0.5

As is seen from Figures 2, 3, 4, and 5, the 0.914 ABS value at 521.8 nm wavelength indicates that hexylamine is also an effective cosurfactant in the SDS/methylene chloride/sodium molybdate (aq) system.

Next, we investigated the more complex effects of changing the ratio of alcohol to hexylamine as cosurfactant by including n-butanol, n-octanol and n-decanol. Alteration in the alcohol-to-hexylamine weight ratio may cause the formation of a wide variety of structures of differing geometry and topology; ranging from oil-in-water spherical droplets, elongated aggregates and bicontinuous systems to water-in-oil droplets [8].

From Figs. 3, 4, and 5 it can be concluded that when the amount of hexylamine is increased in the mixed alcohol plus hexylamine, the solubilization capacity of the microemulsions may increase, decrease, or maximise depending on the structure of the alcohol used. When n-butanol, n-octanol and n-decanol were used, the ABS values increased. Therefore, it was considered that an increase had occurred in the interfacial region; and in each system, the size of water droplets increased relative to the solubility of water in hexylamine on increasing the amount of hexylamine. When the ratio of alcohol to hexylamine was decreased, fading of the red solution was not noticed visually. Thus, we can say that the structure of the microemulsions must have changed from W/O to O/W.

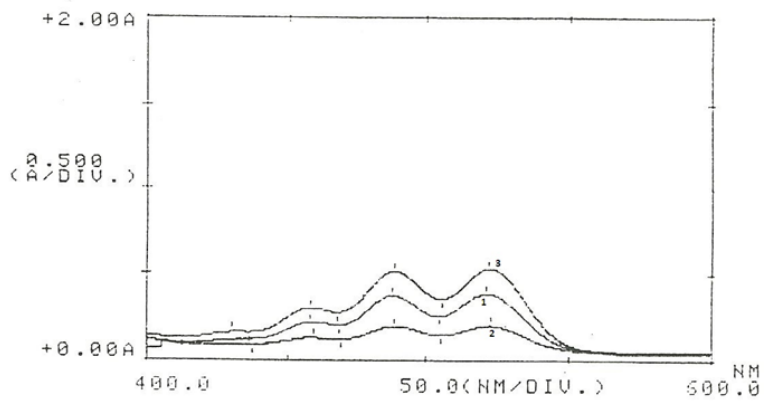

FIG. 3. The wavelength-absorbance change of the system with SDS/n-Butanol + Hexylamine/Methylene chloride/Sodium molybdate (aq). [SDS/(n-Butanol + Hexylamine)] = 0.5

1. n-Butanol + Hexylamine = 75/25 (weight)
2. n-Butanol + Hexylamine = 50/50 (weight)
3. n-Butanol + Hexylamine = 25/75 (weight)

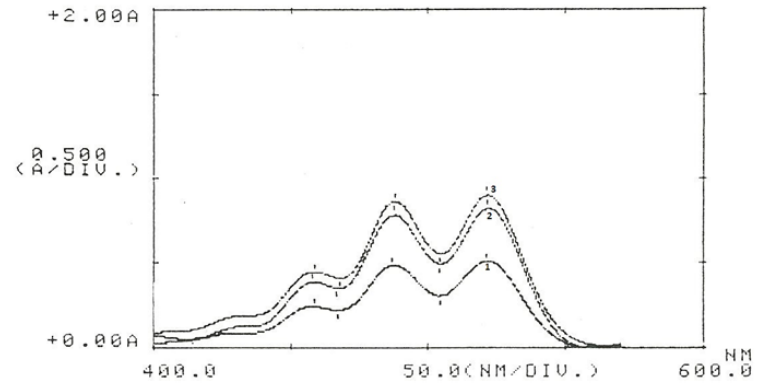

FIG. 4. The wavelength-absorbance change of the system with SDS/n-Octanol + Hexylamine/Methylene chloride/Sodium molybdate (aq). [SDS/(n-Octanol + Hexylamine)] = 0.5

1. n-Octanol + Hexylamine = 75/25 (weight)
2. n-Octanol + Hexylamine = 50/50 (weight)
3. n-Octanol + Hexylamine = 25/75 (weight)

To explain the structural changes, we should consider the cohesive interactions. These interactions are included in the denominator of a modified form of the R-ratio [36, 37]:

$$R = \frac{(A_{C_1O} + A_{C_2O}) - A_{OO} - (A_{L_1L_1} + A_{L_1L_2} + A_{L_2L_2})}{(A_{C_1W} + A_{C_2W}) - A_{WW} - (A_{H_1H_1} + A_{H_1H_2} + A_{H_2H_2})},$$

where C_1 is the surfactant and C_2 is the alcohol (cosurfactant). The parameters A stand for cohesive energies per unit area of interface. H and L denote hydrophilic and lipophilic interactions, respectively. Thus, A_{C_1O} (or A_{C_1W}) is the cohesive energy between the lipophilic (or hydrophilic) portions of surfactant molecules and the oil (or water); A_{C_2O} (or A_{C_2W}) is a similar term for the interaction between alcohol and oil (or water) molecules; $A_{L_1L_1}$ (or $A_{H_2H_2}$) are the cohesive energies between the lipophilic (or hydrophilic) moieties of the surfactant and alcohol molecules, respectively; and $A_{L_1L_2}$ (or $A_{H_1H_2}$) denotes the hydrophobic (or hydrophilic) interaction between the surfactant and alcohol. All negative terms promote segregation of the components as separate phases. By definition, A_{C_2O} increases with NA (the alcohol carbon number), tending to increase the R-ratio, and the water solubilization diminishes as NA increases [36, 37].

If $R > 1$, the corresponding characteristic system is type II (W/O). If $R < 1$, the characteristic system is type I (O/W). It then follows that there is a correspondence between type III behavior and $R = 1$ [36, 37].

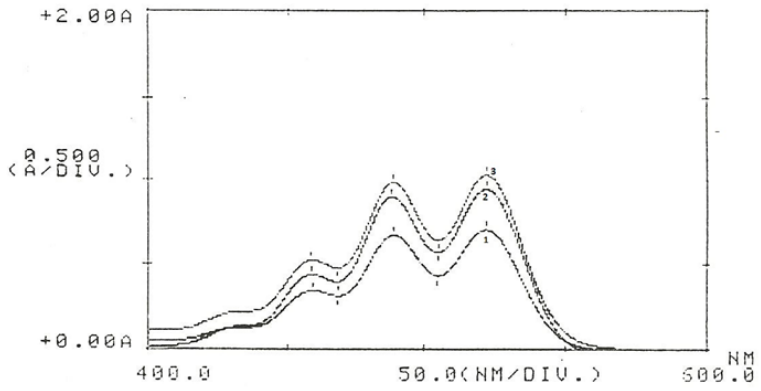

FIG. 5. The wavelength-absorbance change of the system with SDS/n-Decanol + Hexylamine/Methylene chloride/Sodium molybdate (aq). [SDS/(n-Decanol + Hexylamine)] = 0.5

1. n-Decanol + Hexylamine = 75/25 (weight)
2. n-Decanol + Hexylamine = 50/50 (weight)
3. n-Decanol + Hexylamine = 25/75 (weight)

It might be expected that the presence of hexylamine in the aqueous phase would tend to increase the solubility of the surfactants. Thus, with the addition of a low molecular weight alcohol, a microemulsion phase is expected to enrich the proportion of the aqueous phase in the microemulsion. By increasing the amount of hexylamine, which increases the interaction between water molecules and amine groups, it was thought that an increase would occur at A_{CW} and A_{HH}. However, a decrease transpired at A_{CO} and A_{LL}. As the weight ratio of n-butanol/hexylamine was equal (50/50) in the system of n-butanol plus hexylamine, a decrease occurred in the ABS value at 521.8 nm wavelength. The behavior was equally complex compared to that of n-octanol and n-decanol. To explain this disparity, it has been suggested that a breakdown in aggregate structure occurred in the typical microemulsion system. A typical microemulsion system contains neither oil-in-water nor water-in-oil microemulsion particles, but, rapid changes or fluctuations in aggregate size and shape take place. On the other hand, this decrease in the ABS value may be interpreted such that, to a certain extent, the alcohol from the oil phase can partition into the interface to stabilize the additional interfacial area. However, as the alcohol in the oil phase is depleted, further growth of water droplets would increase the interfacial tension at the O/W interface due to an increase in the area per molecule and thus destabilize the microemulsion, and hence prevent further solubilization of water [15]. When the weight ratio of n-butanol/hexylamine was equal to 25/75 in the same system, an increase was observed in the highest hexylamine concentration, as in the other systems. Adding alcohol and hexylamine to the surfactant/water/oil system entails a change in the interaction of energy per unit area of the interface of C layer with the O and W regions. This change is dependent on the nature of the alcohol, the amount of hexylamine, and their interfacial concentrations.

Both from W/O to O/W and from O/W to W/O, trends have been reported in the literature for anionic surfactants [16, 37]. In our study, an inversion from W/O to O/W occurred in the highest additive hexylamine (alcohol/hexylamine = 25/75 (weight)). When the surfactant, alcohol and hexylamine concentrations are decreased by keeping the ratio of surfactant to cosurfactant constant, the interfacial alcohol and hexylamine concentration decreases. The balance of interactions of C with O and W becomes more favorable to W. This tends to in turn microemulsion structure. A_{CW} probably increases due to intermolecular hydrogen bonding, which increases the ability of the -NH_2 group to form hydrogen bonds with water molecules. Finally, the lateral interaction between the surfactant molecules obviously increased. It can be asserted that with addition hexylamine to system with alcohol as a cosurfactant, the change in the cohesion energies accompanying the hydrophilic and hydrophobic interaction between the alcohol, hexylamine and the surfactant (A_{LL} and A_{HH} in the R ratio used as the criterion for the determination of the type of microemulsion) might cause change in the structure of microemulsion. Additionally, it can be suggested that the transition between microemulsion types is mainly caused by changing the HLB values of the water-oil interfacial layer including surfactant and cosurfactant components. It can be stated that n-butanol plus hexylamine equilibrates the interfacial interaction balance of SDS which is a very hydrophilic surfactant.

For further studies, we recommend the use of different techniques such as dynamic light scattering (DLS), static light scattering (SLS), FT-IR *etc.* techniques to design, characterization of microemulsion systems and to

examine the effects of cosurfactants on the structure of microemulsion systems as performed in several studies (for example [22, 38]).

4. Conclusion

In the first part of the present study, we investigated the effect of hexylamine and three different alcohols as cosurfactants with a SDS/Heptane/Water system on phase behavior and solubilization of microemulsions. According to our results, it can be suggested that hexylamine performed better as a cationic surfactant in the SDS/Heptane/Water system than n-butanol, n-hexanol and n-octanol under experimental conditions. In the second part of the study, we compared the effects of hexylamine only and mixed-cosurfactants (hexylamine+alcohol) with SDS, methylene chloride, and sodium molybdate (0.2 M) systems on the microemulsion structure, based on change in ABS values using the spectroscopic method.

In conclusion, it can be said that the type of cosurfactant used and the ratio of hexylamine to alcohol as cosurfactant have an impact on microemulsion structure due to interactions between the surfactant and organic solvent. This behavior of hexylamine plus alcohol as a cosurfactant may be important for researchers when investigating the appropriate microemulsion medium for industrial applications, pharmaceutical applications, consumer products, and drug delivery systems.

References

[1] Bera A., Mandal A., Ojha K., Kumar T. Water solubilization capacity and conductance behaviors of anionic and cationic microemulsion systems. *Journal of Chemical and Engineering Data,* 2011, **56** (12), P. 4422-4429.
[2] Doan T., Acosta E., Scamehorn J.F., Sabatini D.A. Formulating middle-phase microemulsions using mixed anionic and cationic surfactant systems. *Journal of Surfactants and Detergents*, 2003, **6** (3), P. 215–224.
[3] Liu H., Zhang X., et al. Phase behavior of sodium dodecyl sulfate-n-butanol-kerosene-water microemulsion system. *Chinese Journal of Chemical Engineering*, 2014, **22** (6), P. 699–705.
[4] Surabhi K., OP K., Atul N., Arun G. Microemulsions: Developmental aspects. *Research Journal of Pharmaceutical, Biological and Chemical Sciences*, 2010, **1** (4), P. 683–706.
[5] Nagarajan R., Ruckenstein E. Molecular theory of microemulsions, *Langmuir*, 2000, **16** (16), P. 6400–6415.
[6] Ruckenstein E. Thermodynamic approaches to microemulsions. *Journal of Colloid and Interface Science*, 1998, **204** (1), P. 143–150.
[7] Schwuger M-J., Stickdorn K., Schomacker R. Microemulsions in technical processes. *Chemical Reviews*, 1995, **95** (4), P. 849–864.
[8] Zana R. Aqueous surfactant-alcohol systems: A review. *Advances in Colloid and Interface Science*, 1995, **57**, P. 1–64.
[9] Leung R., Shah D.O. Solubilization and phase equilibria of water-in-oil microemulsions. *Journal of Colloid and Interface Science*, 1987, **120** (2), P. 320–329.
[10] Binks B.P., Fletcher P.D.I., Taylor D.J.F. Temperature insensitive microemulsions. *Langmuir*, 1997, **13** (26), P. 7030–7038.
[11] Chew C.H., Gan L.M. Monohexyl ether of ethylene glycol and diethylene glycol as microemulsion cosurfactants. *Journal of Dispersion Science and Technology*, 1990, **11** (1), P. 49–68.
[12] Bellocq A-M., Biasis J., et al. Three dimensional phase diagram of the brine-toluene-butanol-sodium dodecyl sulphate system. *Journal of Colloid Interface Science*, 1980, **74** (2), P. 311–321.
[13] Chew C.H., Gan L.M., Koh L.L., Wong M.K. Microemulsion systems with monobutyl ether of ethylene glycol or diethylene glycol or diethylene glycol as cosurfactant. *Journal of Dispersion Science and Technology*, 1988, **9** (1), P. 17–31.
[14] Li X., Kunieda H. Catanionic surfactants: Microemulsion formation and solubilization. *Current Opinion in Colloid and Interface Science*, 2003, **8**(4–5), P. 327–336.
[15] Bansal V.K., Shah D.O., O'Connell J.P. Influence of alkyl chain length compatibility on microemulsion structure and solubilization. *Journal of Colloid and Interface Science*, 1980, **75** (2), P. 462–475.
[16] Baviere M., Schechter R., Wade W. The influence of alcohols on microemulsion composition. *Journal of Colloid and Interface Science*, 1981, **81** (1), P. 266–279.
[17] Wormuth K.R., Kaler E.W. Amines as microemulsion cosurfactants. *The Journal of Physical Chemistry*, 1987, **91** (3), P. 611–617.
[18] Li X., Wang J., Wang J. Effects of mixed anioniccationic surfactants and alcohol on solubilization of water-in-oil microemulsions. *Journal of Dispersion Science and Technology*, 1999, **20** (3), P. 993–1007.
[19] Venable R.L, Elders K.L., Fang J. Microemulsions with high water solubilizing capacity at high hydrocarbon levels and very low surfactant concentrations. *Journal of Colloid and Interface Science*, 1986, **109** (2), P. 330–335.
[20] Upadhyaya A., Acosta E.J., Scamehorn J.F., Sabatini D.A. Microemulsion phase behavior of anionic-cationic surfactant mixtures: Effect of tail branching. *Journal of Surfactants and Detergents*, 2006, **9** (2), P. 169–179.
[21] Hevia F., Gonzalez J.A., et al. Thermodynamics of mixtures with strongly negative deviations from Raoult's law. XV. Permittivities and refractive indices for 1-alkanol + n-hexylamine systems at (293.15 – 303.15) K. Application of the Kirkwood–Frohlich model. *Fluid Phase Equilibria*, 2018, **468**, P. 18–28.
[22] Cuenca V.E., Falcone R.D., Silber J.J., Correa N.M. How the type of cosurfactant impacts strongly on the size and interfacial composition in gemini 12-2-12 RMs explored by DLS, SLS, and FTIR techniques. *The Journal of Physical Chemistry B*, 2016, **120**, P. 467–476.
[23] Khan F.K., Singh M.K., Sen S. Measuring size, size distribution, and polydispersity of water-in-oil microemulsion droplets using fluorescence correlation spectroscopy: Comparison to dynamic light scattering. *The Journal of Physical Chemistry B*, 2016, **120** (5), P. 1008–1020.
[24] Waysbort D., Ezrahi S., et al. 1H NMR Study of a U-Type nonionic microemulsion. *Journal of Colloid and Interface Science*, 1997, **188** (2), P. 282–295.

[25] Ezrahi S., Aserin A., Garti N., Berkovic G. An Excursion into phase tetrahedra-where physical chemistry and geometry meet. *Journal of Chemical Education*, 1998, **75** (12), P. 1648–1652.
[26] Aubry J-M., Bouttemy S. Preparative oxidation of organic compounds in microemulsions with singlet oxygen generated chemically the sodium molybdate/hydrogen peroxide system. *Journal of the American Chemical Society*, 1997, **119** (23), P. 5286–5294.
[27] Nardello V., Marti M.J., Pierlot C., Aubry J-M. Photochemistry without Light: Oxidation of Rubrene in a Microemulsion with a Chemical Source of Singlet Molecular Oxygen. *Journal of Chemical Education*, 1999, **76** (9), P. 1285–1288.
[28] Almgren M., Swarup S. Size of sodium dodecyl sulfate micelles in the presence of additives. *Journal of Colloid and Interface Science*, 1983, **91** (1), P. 256–266.
[29] Bury R., Treiner C. Heats of solution of aliphatic and aromatic, linear, branched, and cyclic alcohols in aqueous sodium dodecyl sulfate micelles at 298 °K. *Journal of Colloid and Interface Science*, 1985, **103** (1), P. 1–10.
[30] Zhou M., Rhue R.D. Effect of interfacial alcohol concentrations on oil solubilization by sodium dodecyl sulfate micelles. *Journal of Colloid and Interface Science*, 2000, **228** (1), P. 18–23.
[31] Balcan M., Mihaÿilescu F-C., et al. Microemulsion systems containing diesel and colza oil as alternative fuels: Phase studies, interfacial tension and solubilization. *Fuel*, 2014, **117**, 251–258.
[32] Miyata I., Miyamoto H., Yonese M. Effect of chain lengths n-alcohol on the formation of single-phase microemulsions n-heptan/n-alcohol/sodium dodecyl sulfate/water systems. *Chem. Pharm. Bull*, 1996, **44** (5), 1049–1055.
[33] Venable R.L., Viox D.H. A microemulsion cosurfactant with excellent water stabilization at high oil content. *Journal of Dispersion Science and Technology*, 1984, **5** (1), P. 73–80.
[34] Fang J., Venable R.L. Conductivity study of the microemulsion system sodium dodecyl sulfate-hexylamine- heptane-water. *Journal of Colloid and Interface Science*, 1987, **116** (1), P. 269–277.
[35] Tanford C. Micelle shape and size. *The Journal of Physical Chemistry*, 1972, **76** (21), P. 3019–3024.
[36] Garti N., Aserin A., Ezrahi S., Wachtel E. Water solubilization and chain length compatibility in nonionic microemulsions. *Journal of Colloid and Interface Science*, 1995, **169** (2), P. 428–436.
[37] Bourrel M., Schechter R.S. *Microemulsions and Releated System: Formulation, Solvency, and Physical Properties*. Surfactant Science Series, 1988, **30**, Marcel Dekker, Inc., New York.
[38] Sharifi S., Amirkhani M., et al. Light scattering and SAXS study of AOT microemulsion at low size droplet. *Soft Nanoscience Letters*, 2012, **2**, P. 8–12.

NANOSYSTEMS: PHYSICS, CHEMISTRY, MATHEMATICS, 2019, 10 (2), P. 184–189

Humic acid-stabilized superparamagnetic maghemite nanoparticles: surface charge and embryotoxicity evaluation

A. E. Goldt[1], A. Yu. Polyakov[2]*, T. A. Sorkina[3], A. L. Dubov[4,5], G. A. Davidova[6], I. I. Selezneva[6], Y. V. Maximov[7], I. A. Presnyakov[5], N. Yu. Polyakova[8], E. A. Goodilin[2,4,5], I. V. Perminova[5]

[1]Skolkovo Institute of Science and Technology, Moscow, Russia
[2]Kurnakov Institute of General and Inorganic Chemistry, Russian Academy of Sciences, Moscow 119991, Russia
[3]Science & Technology Department, Management Company RUSNANO, LLC, Moscow, Russia
[4]Department of Materials Science, Lomonosov Moscow State University, Moscow 119991, Russia
[5]Department of Chemistry, Lomonosov Moscow State University, Moscow 119991, Russia
[6]Institute of Theoretical & Experimental Biophysics of Russian Academy of Sciences, Pushchino 142290, Russia
[7]Semenov Institute of Chemical Physics of Russian Academy of Sciences, Moscow 119991, Russia
[8]I. M. Sechenov First Moscow State Medical University of the Ministry of Health of the Russian Federation (Sechenov University), Moscow, Russia

*a.yu.polyakov@gmail.com

PACS 75.47.Lx, 82.70.Dd **DOI 10.17586/2220-8054-2019-10-2-184-189**

Superparamagnetic iron oxide γ-Fe_2O_3 (maghemite) nanoparticles (SPION) encapsulated into water-soluble microspheres of rock salt were synthesized via a new aerosol spray pyrolysis procedure. Humic acids (HA) were employed to stabilize the aqueous suspensions of γ-Fe_2O_3 nanoparticles released upon dissolution of the NaCl matrix. The effect of HA on the surface charge of maghemite-based colloids was studied in pH range of 3 – 10. Humic polyanions compensate positive charges on a hydrated γ-Fe_2O_3 surface resulting in strongly negative ζ-potential (< -40 mV) of colloid even in acidic environment. In neutral and alkaline environment, ζ-potential of maghemite-based colloid drops below -55 mV; thus, HA should effectively stabilize the nanoparticle colloid over the whole pH range studied. Meanwhile, bare maghemite SPION at pH 3 – 6 have ζ-potential in the $+20$ mV to -20 mV range (isoelectric point at pH 4.35), which is insufficient for electrostatic stabilization of the suspensions. The absence of embryotoxicity of HA-stabilized nanoparticles was demonstrated.

Keywords: small superparamagnetic iron oxide nanoparticles (SPION), humic acids, magnetic fluids, colloidal properties, embryotoxicity, biomedicine.

Received: 20 January 2019

Revised: 31 January 2019

1. Introduction

Superparamagnetic iron oxide nanoparticles (SPIONs) with a size less than 5 nm have attracted growing attention as emerging nanomaterials for biomedical applications, including magnetic resonance imaging (MRI), drug delivery and theranostics, due to their high biocompatibility, chemical stability, tunable surface features, prolonged blood circulation time due to the reduced phagocytosis by macrophages and T_1-shortening effect (unlike larger iron oxide nanoparticles) in MRI [1–4].

To achieve enhanced colloidal stability and versatility of biomedical applications, numerous approaches have been developed for the surface modification of SPIONs employing the specifically designed synthetic ligands [1, 5]. Meanwhile, the cheap and effective natural stabilizers for the SPIONs are still of high demand. It was previously demonstrated that the humic acids (HA), i.e. the natural organic matter originating from biochemical and microbiological transformations of organic materials under environmental conditions, can efficiently stabilize iron oxide nanoparticles due to the numerous highly developed branches with irregularly located organic functional groups [6–11]. However, the colloidal stability of the resulting core-shell organic-inorganic nanomaterials at different pH values was not characterized, while it is crucial for biomedical applications of the stabilized SPIONs. Additionally, the toxicity of these nanomaterials were evaluated on NCTC clone L929 cells [6], but never studied on the embryos, while the absence of embryotoxicity is an important criterion applicable to the new biomedical agents.

Here, we report the effect of humic acids on the surface charge of water-dispersed ultrasmall superparamagnetic γ-Fe_2O_3 nanoparticles at different pH values, as well as embryotoxicity evaluation of these stabilized SPIONs.

2. Experimental section

2.1. Synthesis

$Fe(NO_3)_3 \cdot 9H_2O$, NaCl and urea of analytical purity grade were purchased from Sigma-Aldrich. Leonardite humic acids (HA) were isolated from the commercially available potassium humate (Powhumus, Humintech Ltd., Germany) [12]. To prepare 100 mg/l HA solution, a weight of the solid sample was dissolved first in a few ml of 1.0 M NaOH upon sonication for 20 min at room temperature, diluted by deionized water (Milli-Q, Millipore), and adjusted to pH 7.0 using 0.1 M HCl.

Maghemite nanoparticles incorporated into the NaCl microspheres were synthesized according to the aerosol spray pyrolysis (ASP) procedure described elsewhere [13]. In brief, dry NaCl was added to 0.25 M aqueous $Fe(NO_3)_3$ to achieve final molar ratio of γ-Fe_2O_3 to NaCl of 1:10. Urea was also added to the solution to enhance the combustion in the hot zone and yield finer nanoparticles. The obtained solution was atomized using an ultrasonic nebulizer (resonant frequency of 1.7 MHz, 0.5 – 5 micron solution droplets). The aerosol stream was injected into a horizontal quartz reactor (20 mm inner diameter, 900 mm length) pre-heated to 650 °C. The flow rate of air used as a carrier gas was 10 L/min, resulting in a transfer of the spray through the hot zone during ca. 5 sec. The resulting powders were collected at a surface of a microporous glass fiber filter after the aerosol has been transported and transformed in the hot zone.

To prepare a magnetic fluid, the obtained microspheres were dispersed in 100 mg/l HA solution followed by ultrasonic treatment for 20 min. Concentration of iron oxide was 43 mg/l (30 mg/l Fe(III)), which corresponds to 200 mg/l of salt-maghemite composite. The salt from the composite also provides 157 mg/l (2.7 mmol/l) NaCl concentration in the resulting colloid. For the further transmission electron microscopy and Mössbauer spectroscopy studies, the suspension of HA-stabilized SPIONs was sedimented by 10 min centrifugation at 7000 rpm and dried in ambient air.

2.2. Physicochemical characterization

Scanning electron microscopy (SEM) images were obtained using a Leo Supra 50 VP microscope (Carl Zeiss) at accelerating voltage of 5 kV. Transmission electron microscopy (TEM) images were obtained using a Hitachi H-8100 transmission electron microscope (accelerating voltage of 200 kV) to investigate morphology and size of nanoparticles.

Mössbauer spectroscopy was used to study SPIONs at 77 and 300 K using a constant-acceleration WissEl spectrometer (Germany) equipped with a krypton proportional detector, a γ-radiation source of ^{57}Co in a rhodium matrix, and a Janis helium cryostat (model CCS-850). Chemical shifts were referred to metallic α-iron. The spectra were fitted using the least square minimization procedure by the standard software.

ζ-Potential values were determined using Zetasizer Nano ZS (Malvern Instruments) at 25 °C. Standard folded capillary ζ-cells were employed. The pH of the nanoparticle colloids was adjusted using 0.1 M HCl and 0.1 M NaOH to study the changes of ζ-potential in the pH range of 3 – 10 (starting from pH 3 and going to the higher pHs).

2.3. Embryotoxicity

The embryotoxicity of the obtained SPIONs was assessed using in vitro mice embryo growth tests. To culture the embryos, 16 cultural liquid (Sigma, pH 7.0 – 7.3, 37 °C, 5 % CO_2) was used. In total, 40 mice embryos were tested in this study. γ-Fe_2O_3 and HA-stabilized γ-Fe_2O_3 were added to the embryos-containing liquid at the ratio of 1:10. Growing embryos were monitored up to the blastocyst stage in the control group using optical microscopy (Axiovert 200, Zeiss, Germany) for counting a number of blastocysts and characterization of their anomalies.

3. Results and discussion

ASP is a known effective technique for continuous and scalable synthesis of iron oxide nanoparticles and allows successful preparation of the metastable superparamagnetic phases, like γ-Fe_2O_3 [13]. The morphology of the composite obtained by ASP is known to be dependent on the concentration of the sprayed precursor solution, flow velocity (i.e. the duration of the spray transfer through the hot zone) and the furnace temperature [13]. The particles obtained in this work upon 5 s transfer of ultrasonic fog through a hot zone (650 °C) consisted of hollow 0.5 – 2 μm NaCl microspheres formed from submicron solution droplets loaded with ultrasmall iron oxide nanoparticles (Fig. 1a). Dissolution of the obtained microspheres in aqueous humic acid solution results in a stable sol of iron oxide nanoparticles. To disaggregate the SPIONs more effectively, an ultrasonic treatment has been applied resulting in separate 2 – 5 nm nanoparticles (Fig. 1c), as observed by TEM of the centrifuged SPION-HA colloid (Fig. 1b). Note that the nanoparticle sizes calculated from TEM images (2 – 5 nm; 3.5 $\pm$ 0.8 nm mean

size) are significantly below the hydrodynamic diameter (145 ± 60 nm) reported for the same SPION-HA colloids elsewhere [6]. This supports the previous hypothesis that SPIONs not only adsorb the humic substances but also penetrate into the branched structure of the conglomerates of humic acid molecules and become assembled there [6, 7]. A simplified illustration of this process is given on Fig. 2. It should be noted that a similar assembling effect was found for the synthetic dendrimers and Fe_3O_4 nanoparticles [14].

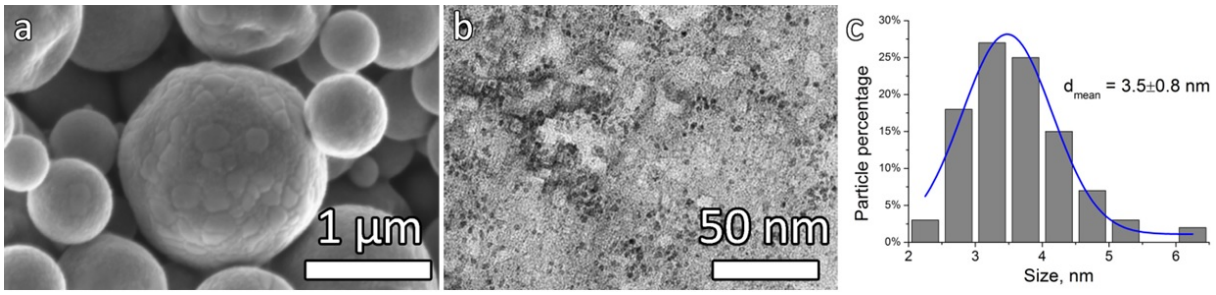

FIG. 1. (a) SEM image of the SPION-NaCl microspheres obtained by the ASP method at 650 °C. (b) TEM image of the SPION sol obtained by dispersion/dissolution of SPION-NaCl microspheres in the aqueous humic acid solution and sedimented by 10 min centrifugation at 7000 rpm. Note the amorphous HA mass in which the SPIONs are distributed. (c) Size distribution of the SPIONs in suspension as observed by TEM

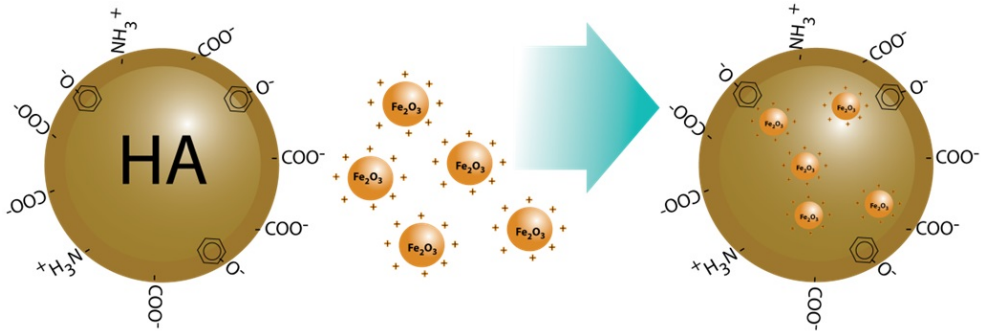

FIG. 2. A simplified scheme for stabilization of γ-Fe_2O_3 nanoparticles by conglomerates (possibly, micelles) of humic acid molecules

The superparamagnetic behavior of dried HA-stabilized γ-Fe_2O_3 nanoparticles was confirmed using Mössbauer spectroscopy at 300 K and 77 K, which is also a powerful tool to study the iron oxide speciation [8, 15]. The characteristic paramagnetic signal (doublet) observed at room temperature (Fig. 3a) switches to hyperfine structure lines, which were fitted by 3 sextet components (Fig. 3b, Table 1).

The Mossbauer spectrum of maghemite nanoparticles at 77 K is known to be rather complicated and is usually fitted by multiple components [16], ascribed to the different Fe^{+3} positions in the $(Fe^{+3}{}_8)_A[Fe^{+3}{}_{40/3}\square_{8/3}]_B O_{32}$ spinel phase ($\square$ represents the vacancies of the octahedral sites), impact of the surface states [17], etc. In our

TABLE 1. Mössbauer parameters of γ-Fe_2O_3 particles stabilized by HA at 77 K [δ is the isomer shift relative to α-Fe, ε is the quadrupole splitting, Γ is the line width, and H_{in} is the internal magnetic field (T)]

Component	δ	ε	Γ	H_{in},	Relative content (%),
	±0.03 mm/s			±0.5T	±1 %
γ-Fe_2O_3 –1	0.41	0.00	0.78	45.4	33
γ-Fe_2O_3 –2	0.42	0.00	0.78	48.7	46
γ-Fe_2O_3 –3	0.43	0.00	0.78	39.9	21

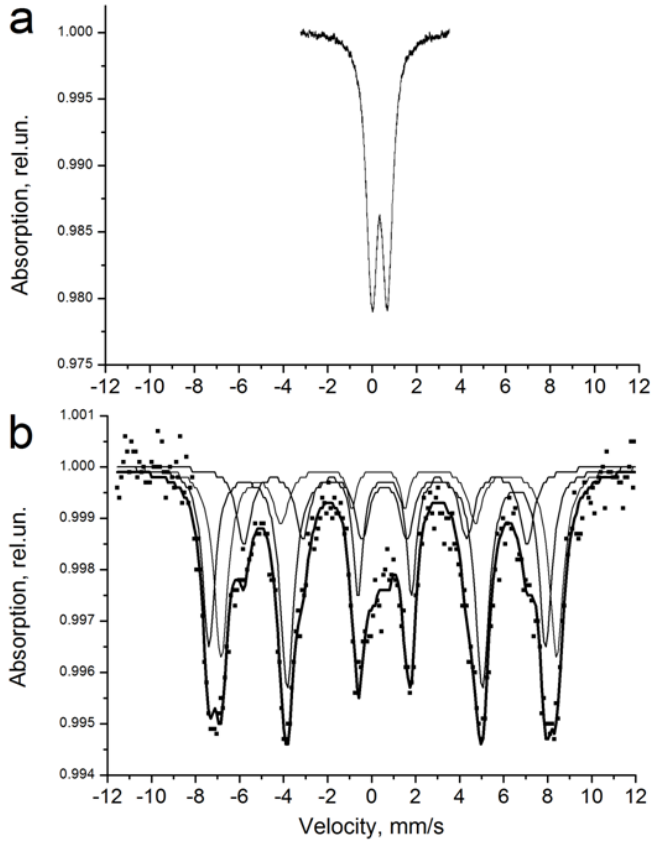

FIG. 3. ^{57}Fe Mössbauer spectra of the dried SPION-HA suspension at 300 K (a) and 77 K (b)

previous Mössbauer study, the low temperature (63 – 90 K) spectra of the dry γ-Fe_2O_3–NaCl nanocomposite were fitted by two sextets with the internal magnetic fields (H_{in}) of 43 – 50 T [13]. Therefore, the additional component with the lower H_{in} ($\delta = 0.43 \pm 0.03$ mm/s, $\varepsilon = 0.00 \pm 0.03$ mm/s and $H_{in} = 39.9 \pm 0.5T$) can be related to the interaction of HA with the surface of magnetic phase.

When dispersed in aqueous medium, iron oxide nanoparticles are hydrated and their surface is enriched with Fe–OH sites demonstrating an amphoteric behavior, i.e. reacting with H^+ or OH^- ions from dissolved acids and bases (depending on pH value) and producing the positive (Fe–OH_2^+) or negative (Fe–O^-) charges, respectively [9]. The changes of the surface charge affect the electrostatic repulsion between the nanoparticles and thus, the overall stability of the colloid according to the DLVO theory [9, 18, 19]. Here, we employed ζ-potential measurements to characterize the surface charge of γ-Fe_2O_3 nanoparticles and their conglomerates with HA at pH range of 3 – 10 (Fig. 4). At pH 3, the ζ-potential of the bare SPIONs (released upon dissolution of NaCl component of the ASP-produced microspheres) is $+18.5$ mV and decreases monotonically with the pH growth over the whole studied range. The nanoparticles remain positively charged below pH 4.35 and have negative charges at higher pH values. The pH 4.35 at which the surface charge of γ-Fe_2O_3 switch from positive (predominance of Fe–OH_2^+ groups) to negative (predominance of Fe–O^- groups) can be considered as the isoelectric point (IEP) for the obtained maghemite nanoparticles. The observed IEP for the ASP-synthesized γ-Fe_2O_3 is significantly lower than that reported for the maghemite nanoparticles synthesized by co-precipitation (pH_{IEP} = 6.6 [20]). Generally, the particles with a ζ-potential higher than $+30$ mV or lower than -30 mV are considered to be electrostatically stable in colloids; at lower ζ-potential values, the particles are prone to agglomeration [21, 22]. Note that the ζ-potential of non-stabilized ASP-synthesized γ-Fe_2O_3 nanoparticles is below these threshold values in acidic medium.

The presence of 100 mg/L HA drastically changes the surface charge of the SPION colloid. Even at low pH values ζ-potential becomes strongly negative (-40 mV at pH 3) and drops below -55 mV at pH > 7. It seems that a high amount of the carboxylate-rich humic polyanions adsorbed on the surface of the SPIONs (and entrapping them as discussed above) leads to neutralization (Fe–OH_2^+ + Hum–COO^- $\leftrightarrow$ Fe–OOC–Hum + H_2O) and then compensation of positive charges on the iron oxide surface even in acidic medium. A similar effect of humic and fulvic acids on the iron oxide surface charge was previously reported for the magnetite [9] and hematite [23–25]

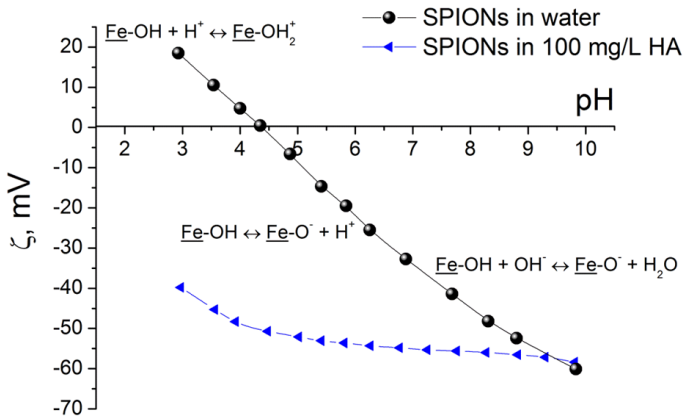

FIG. 4. ζ-potential of SPIONs as a function of pH in the absence and in the presence of 100 mg/L HA solution at room temperature. The concentration of SPION-NaCl composite is 200 mg/L, which corresponds to 30 mg/L on Fe(III) basis

particles. The repulsion of the strong negative charges provided by humic polyanions leads to stabilization of the SPION sol over the whole pH range studied.

The influence of nanoparticles on the development of embryos seems to be quite important to avoid embryotoxic effects of new medical agents [26–28]. Our analysis has evidently demonstrated (Fig. 5) that HA-coated γ-Fe_2O_3 has no negative effects on *in vitro* growth of mice embryos. Moreover, SPION-added embryos gave about 10 % surplus of healthy blastocysts with respect to the control group. These data support our previous cytotoxicity study, which demonstrated no toxicity of the same HA-stabilized γ-Fe_2O_3 nanoparticles with respect to the NCTC clone L929 cells [6], and provide additional justification for a future possibility of HA-coated SPION applications in biomedicine.

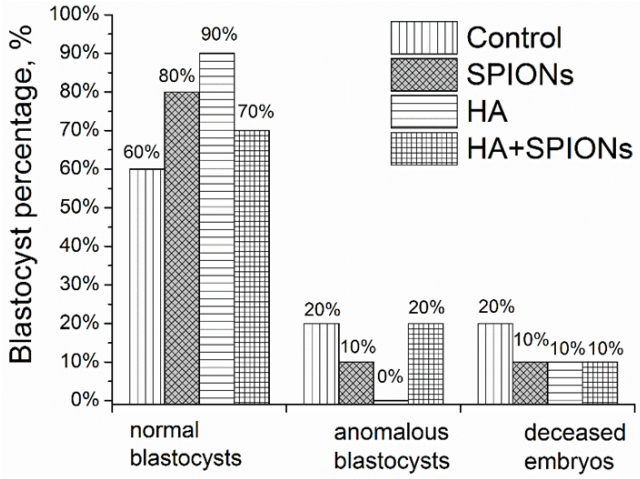

FIG. 5. *In vitro* influence of nude and HA-stabilized SPIONs (released from the γ-Fe_2O_3–NaCl nanocomposite) on the viability of mice 2-cell embryos

4. Conclusions

Humic acids show a significant effect on the surface charge of ASP-synthesized ultrasmall (2 – 5 nm) superparamagnetic γ-Fe_2O_3 nanoparticles in aqueous suspensions. While non-modified γ-Fe_2O_3 nanoparticles have ζ-potential within $+20$ mV to -20 mV range at pH 3 – 6 (isoelectric point at pH 4.35), humic substances shift the ζ-potential towards much lower values (< -40 mV) required for the effective electrostatic stabilization of the colloids. Importantly, the in vitro studies revealed no embryotoxic effect of the designed HA-stabilized sols against the mice 2-cell embryos. These data strengthen the role of HA as an effective biocompatible stabilizing agent for magnetic fluids in possible biomedical applications.

Acknowledgements

The work was carried out within the State Assignment on Fundamental Research to the Kurnakov Institute of General and Inorganic Chemistry.

References

[1] Song C., Sun W., Xiao Y., Shi X. Ultrasmall iron oxide nanoparticles: synthesis, surface modification, assembly, and biomedical applications. *Drug Discov. Today*, 2019, **24** (3), P. 835–844.
[2] Weissleder R., Elizondo G., et al. Ultrasmall superparamagnetic iron oxide: characterization of a new class of contrast agents for MR imaging. *Radiology*, 1990, **175** (2), P. 489–493.
[3] Rui Y.-P., Liang B., et al. Ultra-large-scale production of ultrasmall superparamagnetic iron oxide nanoparticles for T_1-weighted MRI. *RSC Adv.*, 2016, **6** (27), P. 22575–22585.
[4] Emashova N.A., Kudryashov V.E., et al. Quo vadis, worldwide nanoindustry. *Nanotechnologies Russ.*, 2016, **11** (3–4), P. 117–127.
[5] Dimarco M., Guilbert I., et al. Colloidal stability of ultrasmall superparamagnetic iron oxide (USPIO) particles with different coatings. *Int. J. Pharm.*, 2007, **331** (2), P. 197–203.
[6] Chekanova A.E., Sorkina T.A., et al. New environmental nontoxic agents for the preparation of core-shell magnetic nanoparticles. *Mendeleev Commun.*, 2009, **19** (2), P. 72–74.
[7] Polyakov A.Y., Goldt A.E., et al. Constrained growth of anisotropic magnetic δ-FeOOH nanoparticles in the presence of humic substances. *CrystEngComm*, 2012, **14** (23), P. 8097–8102.
[8] Polyakov A.Y., Sorkina T.A., et al. Mössbauer spectroscopy of frozen solutions as a stepwise control tool in preparation of biocompatible humic-stabilized feroxyhyte nanoparticles. *Hyperfine Interact.*, 2013, **219** (1–3), P. 113–120.
[9] Illés E., Tombácz E. The effect of humic acid adsorption on pH-dependent surface charging and aggregation of magnetite nanoparticles. *J. Colloid Interface Sci.*, 2006, **295** (1), P. 115–123.
[10] Demangeat E., Pédrot M., et al. Colloidal and chemical stabilities of iron oxide nanoparticles in aqueous solutions: the interplay of structural, chemical and environmental drivers. *Environ. Sci. Nano*, 2018, **5** (4), P. 992–1001.
[11] Kulikova N.A., Polyakov A.Y., et al. Key Roles of Size and Crystallinity of Nanosized Iron Hydr(oxides) Stabilized by Humic Substances in Iron Bioavailability to Plants. *J. Agric. Food Chem.*, 2017, **65** (51), P. 11157–11169.
[12] Perminova I.V., Kovalenko A.N., et al. Design of Quinonoid-Enriched Humic Materials with Enhanced Redox Properties. *Environ. Sci. Technol.*, 2005, **39** (21), P. 8518–8524.
[13] Chekanova A.E., Dubov A.L., et al. Soluble microcapsules for non-toxic magnetic fluids. *Mendeleev Commun.*, 2009, **19** (1), P. 4–6.
[14] Yang J., Luo Y., et al. Conjugation of Iron Oxide Nanoparticles with RGD-Modified Dendrimers for Targeted Tumor MR Imaging. *ACS Appl. Mater. Interfaces*, 2015, **7** (9), P. 5420–5428.
[15] Kirillova S.A., Almjasheva O.V., Panchuk V.V., Semenov V.G. Solid-phase interaction in ZrO_2–Fe_2O_3 nanocrystalline system. *Nanosyst. Phys. Chem. Math.*, 2018, **9** (6), P. 763–769.
[16] Ramos Guivar J.A., Bustamante A., et al. Mössbauer study of intermediate superparamagnetic relaxation of maghemite (γ-Fe_2O_3) nanoparticles. *Hyperfine Interact.*, 2014, **224** (1–3), P. 89–97.
[17] Zakharova I.N., Shipilin M.A., Alekseev V.P., Shipilin A.M. Mössbauer study of maghemite nanoparticles. *Tech. Phys. Lett.*, 2012, **38** (1), P. 55–58.
[18] Polyakov A.Y., Lebedev V.A., et al. Non-classical growth of water-redispersible spheroidal gold nanoparticles assisted by leonardite humate. *CrystEngComm*, 2017, **19** (5), P. 876–886.
[19] Israelachvili J. *Intermolecular and Surface Forces*. Academic Press, Elsevier, Burlington, 2011, 710 p.
[20] Nurdin I., Syarofi R., Satrianananda. The Effect of pH and Time on The Stability of Superparamagnetic Maghemite Nanoparticle Suspensions. *MATEC Web Conf.*, 2016, **39**, 01001, DOI: 10.1051/matecconf/20163901001.
[21] Sikora A., Bartczak D., et al. A systematic comparison of different techniques to determine the zeta potential of silica nanoparticles in biological medium. *Anal. Methods*, 2015, **7** (23), P. 9835–9843.
[22] Večeř M., Pospíšil J. Stability and Rheology of Aqueous Suspensions. *Procedia Eng.*, 2012, **42**, P. 1720–1725.
[23] Amal R., Raper J.A., Waite T.D. Effect of fulvic acid adsorption on the aggregation kinetics and structure of hematite particles. *J. Colloid Interface Sci.*, 1992, **151** (1), P. 244–257.
[24] Verrall K.E., Warwick P., Fairhurst A.J. Application of the Schulze–Hardy rule to haematite and haematite/humate colloid stability. *Colloids Surfaces A Physicochem. Eng. Asp.*, 1999, **150** (1–3), P. 261–273.
[25] Ramos-Tejada M.M., Ontiveros A., Viota J.L., Durán J.D.G. Interfacial and rheological properties of humic acid/hematite suspensions. *J. Colloid Interface Sci.*, 2003, **268** (1), P. 85–95.
[26] Peng G., He Y., et al. Differential effects of metal oxide nanoparticles on zebrafish embryos and developing larvae. *Environ. Sci. Nano*, 2018, **5** (5), P. 1200–1207.
[27] Patel S., Jana S., et al. Toxicity evaluation of magnetic iron oxide nanoparticles reveals neuronal loss in chicken embryo. *Drug Chem. Toxicol.*, 2019, **42** (1), P. 1–8.
[28] Magro M., De Liguoro M., et al. The surface reactivity of iron oxide nanoparticles as a potential hazard for aquatic environments: A study on *Daphnia magna* adults and embryos. *Sci. Rep.*, 2018, **8** (1), 13017.

NANOSYSTEMS: PHYSICS, CHEMISTRY, MATHEMATICS, 2019, 10 (2), P. 190–198

Synthesis and down-conversion luminescence of $Ba_4Y_3F_{17}$:Yb:Pr solid solutions for photonics

S. V. Kuznetsov[1], A. S. Nizamutdinov[2], M. N. Mayakova[1], V. V. Voronov[1], E. I. Madirov[2], A. R. Khadiev[2], D. A. Spassky[3], I. A. Kamenskikh[4], A. D. Yapryntsev[5], V. K. Ivanov[5], M. A. Marisov[2], V. V. Semashko[2], P. P. Fedorov[1]

[1]Prokhorov General Physics Institute of the Russian Academy of Sciences, 38 Vavilov str., Moscow, 119991 Russia

[2]Kazan Federal University, 18 Kremljovskaya, Kazan, 420008 Russia

[3]Skobeltsyn Institute of Nuclear Physics, Lomonosov Moscow State University, Leninskie Gory, Moscow 119991, Russia

[4]Physics Faculty of Lomonosov Moscow State University, Leninskie Gory, Moscow 119991, Russia

[5]Kurnakov Institute of General and Inorganic Chemistry of the Russian Academy of Sciences, 31 Leninsky pr., Moscow,119991 Russia

kouznetzovsv@gmail.com

PACS 42.70.-a, 81.20.Fw **DOI 10.17586/2220-8054-2019-10-2-190-198**

Single-phase powders of $Ba_4Y_3F_{17}$:Yb:Pr solid solutions with an average agglomerate size of 400 nm were synthesized by co-precipitation from aqueous solutions. It was shown that the down-conversion mechanism in the investigated samples was quantum cutting, with one photon absorbed by Pr^{3+} ions resulting in two photons emitted by Yb^{3+} ions. At first, overall the external quantum yield of down-conversion luminescence measured appeared to be relatively high, with a maximum value of 2.9 % for the $Ba_4Y_3F_{17}$:Pr(0.1 %):Yb(10 %) sample. It makes this compound promising for Si-based solar cells efficiency enhancement.

Keywords: synthesis, down-conversion, luminescence, solid solutions, photonics, fluorides.

Received: 2 March 2019

Revised: 8 April 2019

1. Introduction

The forecast for the development of renewable energy [1], conducted by Fraunhofer ISE, showed that by 2030, humanity will reach the terawatt power generation capacity through photovoltaic devices. About 95 percent of this power will be generated by silicon solar panels. The cost of generating 1 kilowatt hour (kWh) of energy will be no higher than the cost of generating energy from fossils and nuclear power. One of the most significant drawbacks of Si-based solar cells is the low efficiency of power generation due to the limited range of high spectral susceptibility of crystalline silicon to sunlight. There are various options to increase the efficiency [2–8], including additional layers based on up-conversion (UC) [6, 7] and down-conversion [8] luminophores. These methods result in energy transfer from non-sensitive regions of the spectrum to crystalline silicon photosensitive range. The most efficient UC material excited at 980 nm is β-$NaYF_4$:21.4%Yb:2.2%Er with a reported photoluminescence quantum yield (PLQY) 10.5 % at pump power density P=35 W/cm^2 [9]. Other efficient UC materials described in the literature include BaY_2ZnO_5:7%Yb:3%Er with PLQY=5 % at P=2.2 W/cm^2 [10], La_2O_2S:9%Yb:1%Er with PLQY=5.8 % at P=13 W/cm^2 [11] and SrF_2:Yb(2 mol.%):Er(2 mol%) with PLQY=2.8 % at 10 W/cm^2 [7]. The phenomenon of quantum cutting is one of the down-conversion mechanisms, which allows one to transform the blue pump radiation to near infrared with an efficiency of more than 100 %. It was previously shown, that one of the most promising from the point of view of high quantum energy transfer efficiency is the ytterbium-praseodymium doping pair [12–17]. Previously, we studied solid solutions based on calcium fluoride and strontium fluoride doped with praseodymium and ytterbium [18, 19]. The best result was achieved for a solid solution based on SrF_2, which demonstrated an energy transfer coefficient of more than 100 % and a quantum yield of 1.1 % [18]. Usually, the luminescence efficiency increases with the transition to heavier matrices and with reduced symmetry. In this connection, it was logical to proceed to the study of fluorite solid solutions based on barium fluoride. It was previously shown that it was impossible to synthesize single-phase solid solutions $Ba_{1-x}R_xF_{2+x}$ (R – rare earth elements) by co-precipitation technique [20–22], since two-phase samples were synthesized. It is possible to synthesize $Ba_{1-x}R_xF_{2+x}$ solid solutions by high temperature melting technique, while fluorite-related trigonal

distorted $Ba_4Y_3F_{17}$ single-phases are synthesized from aqueous solutions [20–23]. The aim of this work was to study the synthesis and spectral-luminescent characteristics of $Ba_4Y_3F_{17}$ solid solutions.

2. Experimental

$Ba_4(Y,Yb,Pr)_3F_{17}$ samples were synthesized by co-precipitation from aqueous solutions as reported elsewhere [21, 24]. We used 99.99 wt% pure ytterbium, yttrium and praseodymium nitrate hexahydrates, barium nitrate (all reagents were manufactured by LANHIT, Russia), 99.99 wt% pure dihydrate potassium fluoride (REACHEM, Russia) and double distilled water as starting materials without further purification. Preliminary, the potassium fluoride was dried at 350°C for 3 hours. 0.08 M aqueous solutions of barium nitrate and rare earth nitrate were added dropwise to potassium fluoride (0.16 M) with intense stirring. Potassium fluoride was taken with a 50 % excess from stoichiometry. The process was carried out according to the following reaction:

$$4\mathrm{Ba(NO_3)_2} + 3\mathrm{R(NO_3)_3} + 17\mathrm{KF} = \mathrm{Ba_4R_3F_{17}}\downarrow + 17\mathrm{KNO_3}, \quad \mathrm{R} = \mathrm{Y, Yb, Pr}.$$

The resulting precipitates were dried at 45°C and annealed at 600°C. As a result, single-phase powders of $Ba_4(Y,Yb,Pr)_3F_{17}$ solid solutions were synthesized.

The samples were analyzed by X-ray powder diffraction on a Bruker D8 Advance (CuKα radiation) diffractometer. The unit cell parameters were calculated by TOPAS software (R_{wp} <10). Particle size, morphology and composition of the samples were analyzed by a Carl Zeiss NVision 40 scanning electron microscope equipped with an EDX detector.

Diffuse reflection spectra were recorded by a Thorlabs IS200 integrating sphere and a StellarNet EPP2000 spectrometer equipped with deuterium and halogen lamps. Luminescence and luminescence excitation spectra were measured using specialized setup for luminescence spectroscopy. A 150 W Xe lamp combined with monochromator MDR-206 was used as the excitation source. Luminescence was detected using an Oriel MS257 spectrograph equipped with Marconi 30–11 CCD detector. Also the luminescence was recorded by a StellarNet spectrometer with a spectral resolution of 0.5 nm and excited with 445 nm continuous wave laser diode. Luminescence kinetics were recorded with the use of MDR-23 equipped with FEU-100 and FEU-62 photomultipliers as detectors for UV-visible and IR spectral ranges, respectively. The time scanning for luminescence kinetics registration was carried out by two digital oscilloscopes: a BORDO oscilloscope with a bandwidth of 200 MHz, dynamic range of 10 bits, and a Tektronix DPO7354 oscilloscope with a bandwidth of 3.5 GHz, dynamic range of 8 bits. Pulsed excitation was arranged from OPO system Lotis TII LT2211 with 7 ns pulse duration and 10 Hz pulse repetition rate. The quantum yield of down-conversion luminescence was measured directly using a Thorlabs IS200 integrating sphere with previously-reported methods [25]. The radiation from the integrating sphere was transferred to a StellarNet spectrometer by optical fiber. The spectral characteristics of the recording system were calibrated with the use of TRSh-2850 and DRGS-12 lamps. All measurements were performed at 300 K.

3. Samples characterization

X-ray powder diffraction patterns of 45°C-dried $Ba_4(Y,Yb,Pr)_3F_{17}$ solid solutions are presented in Fig. 1a. The synthesis was carried out by the co-precipitation from aqueous solutions, and as a result, the particles have physically and chemically adsorbed water on their surfaces. It leads to the quenching of luminescence. The effect of annealing on the increase in luminescence intensity was previously demonstrated for both up-conversion and down-conversion phosphors in [19]. Thermal treatment was performed in the platinum crucible under air at 600°C for 1 hour. Annealing has resulted in a significant narrowing of the XRD peaks in comparison to the samples dried at 45°C (Fig. 1b).

Sobolev and Tkachenko [26] constructed phase diagrams of the BaF_2–RF_3 systems from melting points to 800°C for R=Sm–Lu and up to 900°C for R=La–Nd. In all systems, extensive regions of $Ba_{1-x}R_xF_{2+x}$ solid solutions with fluorite structure (space group $Fm3m$) are formed. The maximum is x=0.50±0.02 for R=La–Nd and decreases with decreasing ionic radius of R^{3+}. Fluorite-related phases of variable composition $Ba_{4\pm x}R_{3\pm x}F_{17\pm x}$ with a structure derived from fluorite (hexagonal crystal symmetry, space group *R*-3), formed in a concentration range of 40–45 mol.% RF_3, detected in systems with R=Sm–Lu. These phases melt incongruently for R=Tb–Lu, Y and decay in the solid state for R=Sm–Gd. A detailed consideration of the crystal structure of such phases for R=Y, Yb was carried out in [27], where a hexagonal structure with the ideal formula $Ba_4Y_3F_{17}$ was confirmed for them. It is shown that this hexagonal structure is a distortion of the cubic lattice of barium fluoride. However, the degree of this distortion is small, and on the X-ray powder patterns, the corresponding cleavage of the main reflexes is very weak. In accordance with this, the Table 1 presents only the data for the cubic sub-cell. The unit cell parameters (*a*) and coherent scattering range (*D*) have been calculated for $Ba_4(Y,Yb,Pr)_3F_{17}$ solid solutions (Table 1). The size of the coherent scattering region of samples dried at 45°C was about 20 nm. After annealing

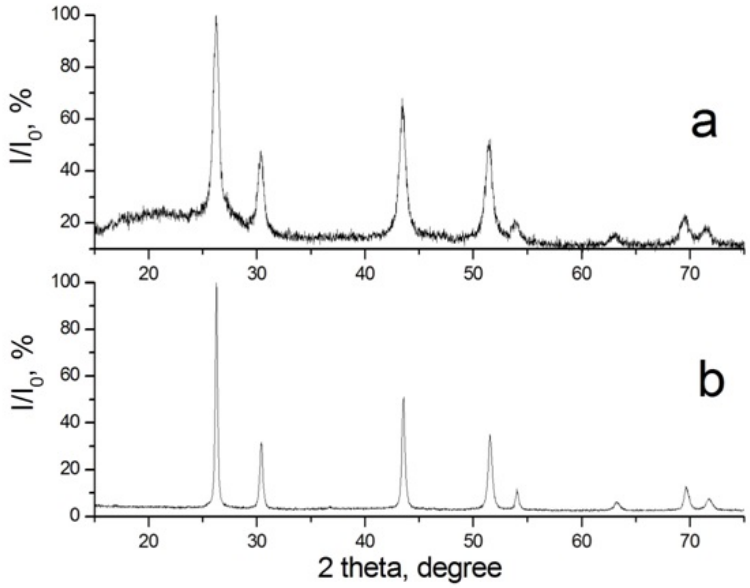

FIG. 1. X-ray powder diffraction patterns of $Ba_{0.5714}Y_{0.3282}Yb_{0.1}Pr_{0.0004}F_{2,4286}$ upon drying at 45°C (a) and annealing at 600°C (b)

at 600°C, this value was increased several-fold. It should be noted that there is a regular decrease in the unit cell parameters with increasing ytterbium content in the crystal lattice. It is due to the fact that the ionic radius of ytterbium is smaller than that of yttrium according to the Shannon system [28].

TABLE 1. Unit cell parameters of $Ba_4(Y,Yb,Pr)_3F_{17}$ solid solutions

Compositions of the initial aqueous solution	After drying at 45°C		After annealing at 600°C	
	a, Å	D, nm	a, Å	D, nm
$Ba_{0.5714}Y_{0.3982}Yb_{0.03}Pr_{0.0004}F_{2,4286}$	5.9175(5)	20±1	5.8978(4)	>100
$Ba_{0.5714}Y_{0.3282}Yb_{0.1}Pr_{0.0004}F_{2,4286}$	5.9021(7)	14±1	5.8851(2)	70±6
$Ba_{0.5714}Y_{0.2782}Yb_{0.15}Pr_{0.0004}F_{2,4286}$	5.8818(6)	25±1	5.8710(3)	90±8
$Ba_{0.5714}Y_{0.3976}Yb_{0.03}Pr_{0.001}F_{2,4286}$	5.9118(6)	19±1	5.8905(2)	71±6
$Ba_{0.5714}Y_{0.3276}Yb_{0.1}Pr_{0.001}F_{2,4286}$	5.8997(6)	23±1	5.8800(3)	>100
$Ba_{0.5714}Y_{0.2776}Yb_{0.15}Pr_{0.001}F_{2,4286}$	5.8843(8)	21±1	5.8684(6)	>100

The particles of $Ba_4(Y,Yb,Pr)_3F_{17}$ solid solutions are agglomerates with an average particle size of 400 nm (Fig. 2). The change in size depending on the content of ytterbium and praseodymium is not substantial.

The composition of the samples has been determined by energy-dispersive analysis (Table 2). Yb content is higher than in the initial aqueous solutions. The yttrium content is the same as in the initial aqueous solutions. The barium content decreases with increasing ytterbium content, which is confirmed by the corresponding distribution coefficient. The appearance of potassium in the crystal lattice of this solid solution arises from the fluorinating agent. The absence of potassium in a number of samples indicates that its amount is less than the detection limit.

4. Spectral-kinetic characteristics

The diffusion reflection spectrum of $Ba_4Y_3F_{17}$:Pr(0.1 %):Yb(1.00 %) sample is shown in Fig. 3. The characteristic Pr^{3+} ions transitions from $^3H_4$ manifold to ^3P_J and $^1D_2$ states appear in the blue and red spectral regions correspondingly. However, the reflection spectrum is dominated by the transition from $^2F_{7/2}$ to $^2F_{5/2}$ states of Yb^{3+} ions at ∼980 nm.

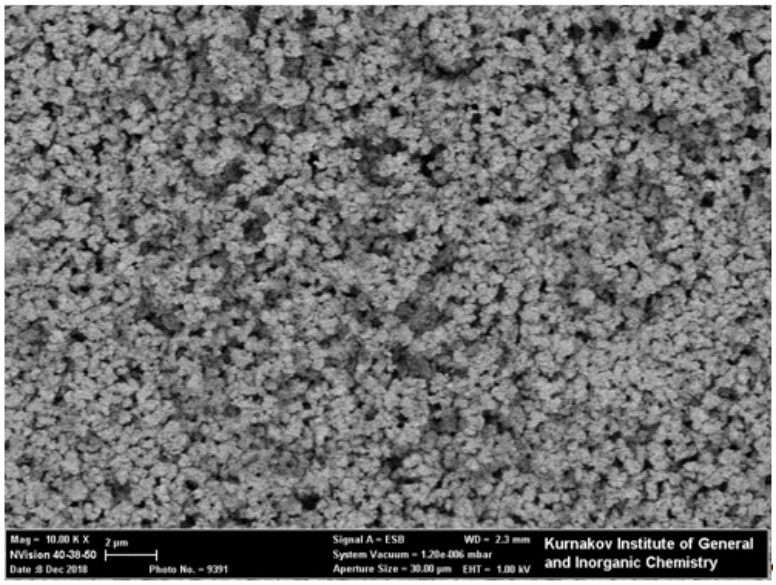

FIG. 2. SEM image of $Ba_4(Y,Yb,Pr)_3F_{17}$ powder annealed at 600°C

TABLE 2. The energy-dispersive analysis of $Ba_4(Y,Yb,Pr)_3F_{17}$ solid solutions

Compositions of the initial aqueous solution	Composition of the solid solutions as determined by EDX*	Barium, yttrium and ytterbium distribution coefficients (EDX composition / Initial composition)
$Ba_{0.5714}Y_{0.3982}Yb_{0.03}Pr_{0.0004}F_{2,4286}$	$Ba_{0.5624}Y_{0.4026}Yb_{0.0350}F_{2,4376}$	0.98/1.01/1.16
$Ba_{0.5714}Y_{0.3282}Yb_{0.1}Pr_{0.0004}F_{2,4286}$	$Ba_{0.5380}Y_{0.3440}Yb_{0.1180}F_{2,4620}$	0.94/1.05/1.18
$Ba_{0.5714}Y_{0.2782}Yb_{0.15}Pr_{0.0004}F_{2,4286}$	$Ba_{0.5100}K_{0.0131}Y_{0.2814}Yb_{0.1961}F_{2,4644}$	0.89/1.01/1.30
$Ba_{0.5714}Y_{0.3976}Yb_{0.03}Pr_{0.001}F_{2,4286}$	$Ba_{0.5490}Y_{0.4140}Yb_{0.0370}F_{2,4510}$	0.96/1.04/1.23
$Ba_{0.5714}Y_{0.3276}Yb_{0.1}Pr_{0.001}F_{2,4286}$	$Ba_{0.5340}K_{0.0110}Y_{0.3300}Yb_{0.1250}F_{2,4440}$	0.93/1.00/1.25
$Ba_{0.5714}Y_{0.2776}Yb_{0.15}Pr_{0.001}F_{2,4286}$	$Ba_{0.5140}K_{0.0140}Y_{0.2830}Yb_{0.1890}F_{2,45800}$	0.90/1.02/1.26

*The praseodymium content is below the EDX detection limit

The luminescence spectra of the samples were investigated under excitation by 445 nm light, which corresponds to the excitation of Pr^{3+} ions and lies within efficient solar spectrum. All samples have exhibited luminescence of both Pr^{3+} and Yb^{3+} ions. In Fig. 4, the luminescence spectra are shown for $Ba_4Y_3F_{17}$:Pr(0.1 %) samples co-doped with 10 % and 15 % Yb.

The ions pair Pr^{3+} and Yb^{3+} often exhibit a quantum cutting effect, which consists in emission of two photons of Yb^{3+} luminescence as a result of absorption of one photon to ^3P_J manifold of Pr^{3+} ions. It is clearly seen from the comparison in the spectral range 400–650 nm of excitation spectrum monitored at 980 nm and diffusion reflection spectrum of the sample (see Fig. 5).

Excitation to ^3P_J manifold of Pr^{3+} ions may lead to two excited Yb^{3+} ions whereas energy of excitation to $^1D_2$ manifold of Pr^{3+} is not enough to achieve quantum cutting effect. From Fig. 5, we see qualitatively that the ratio of areas under lines $^3P_J/^1D_2$ is higher for excitation spectrum than that for reflectance of those which is the evidence of quantum cutting effect [29].

It is worth noting that the excitation spectrum was not corrected for the spectral sensitivity function because of the absence of a reference sample with constant quantum yield in the region 500–600 nm. However, the intensity

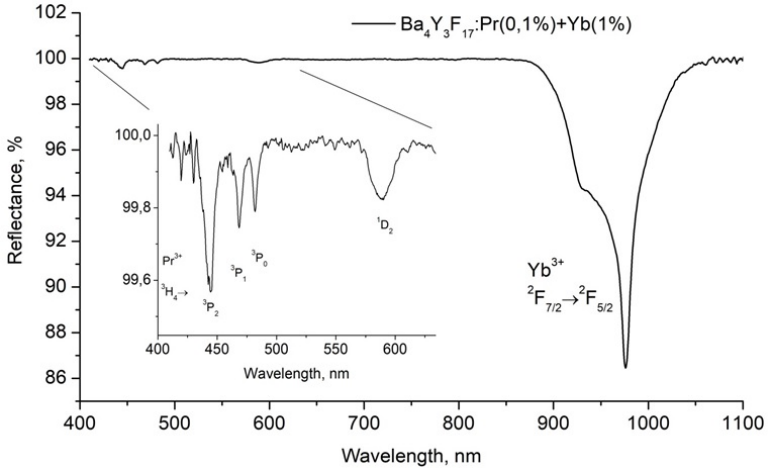

FIG. 3. Diffusion reflection spectrum of $Ba_4Y_3F_{17}$:Pr(0.1 %):Yb(1.0 %) powder sample. The inset shows the magnified visible spectral range reflection

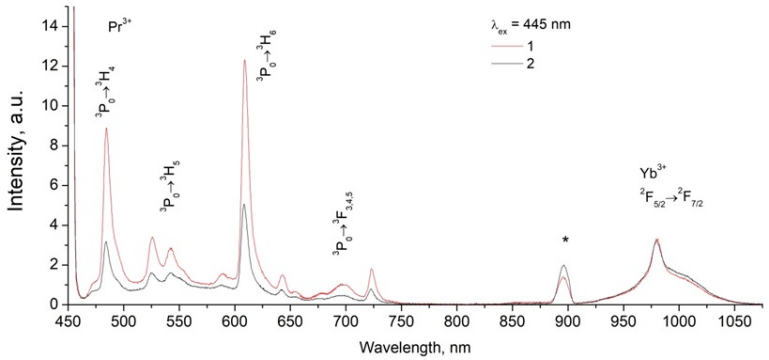

FIG. 4. Luminescence spectra of $Ba_4Y_3F_{17}$:Pr(0.1 %):Yb(10.00 %) (1) and $Ba_4Y_3F_{17}$:Pr(0.1 %):Yb(15.00 %) (2) powder samples excited by 445 nm CW laser light. The sign (*) indicates the second order observation of excitation light

of the excitation source at 590 nm is several times higher than that at 450 nm. Therefore, we expect even higher relative intensity for the group of lines in the region 440–500 nm after the correction. The presented spectra allow one to make a qualitative conclusion concerning the quantum cutting effect in the studied samples without any quantitative estimations on the efficiency of the process.

As a result, we clearly see the down-conversion luminescence of Yb^{3+} ions when samples are excited to $^3H_4$-$^3P_2$ transition of Pr^{3+} ions. The energy transfer features will inevitably appear in luminescence kinetics curves. The Pr^{3+} luminescence decays at 605 nm are shown in Fig. 6.

Curves in Fig. 6 indicate that the luminescence decay from ^3P_J manifold of Pr^{3+} ions is non-exponential, especially for the early stage of decay. We see that an increase in the Yb^{3+} ion concentration leads to quenching of Pr^{3+} luminescence, which speaks for non-radiative energy transfer. Due to the non-exponential character of decay, the average luminescence lifetimes were calculated with the use of formula (1):

$$t_{avg} = \frac{\int t^* I(t) dt}{\int I(t) dt}, \tag{1}$$

where $I(t)$ is the intensity of the decay curve, and t is time.

The results of calculation are presented in Table 3.

The luminescence lifetime values presented in Table 3 indicate the energy transfer from Pr^{3+} ions to Yb^{3+} ions. But also we see that there is some increase for Pr^{3+} luminescence lifetime with the increase of Pr^{3+} content. As this is seen in double doped samples this can be the evidence of certain cross-relaxation process resulting in energy back transfer from Yb^{3+} to Pr^{3+} as transitions $^2F_{7/2}$ to $^2F_{5/2}$ of Yb^{3+} ions and $^1G_4$-$^3P_0$ of Pr^{3+} ions are almost equal in energy. These peculiarities are also shown in Yb^{3+} luminescence kinetics.

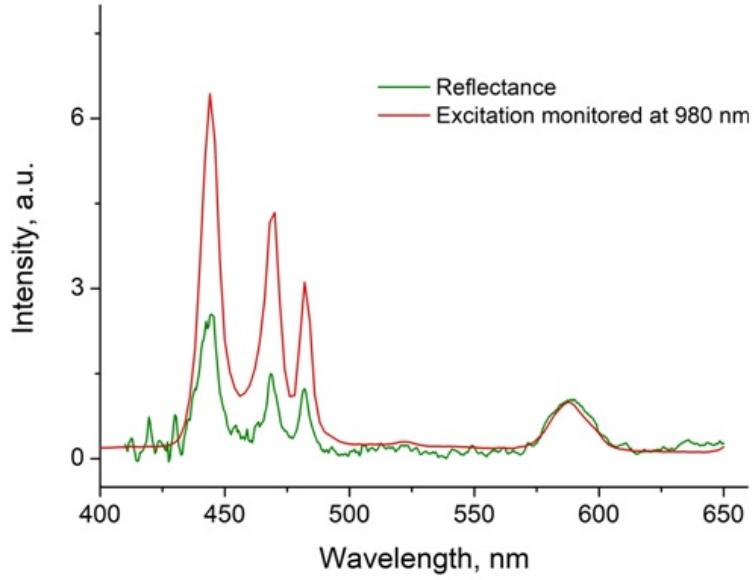

FIG. 5. Excitation spectrum monitored and 980 nm and diffusion reflection spectrum for $Ba_4Y_3F_{17}$:Pr(0.1 %):Yb(10.0 %) powder sample both normalized to the maximum of $^3H_4$-$^1D_2$ transition. Higher values of intensity of excitation lines correspondent to $^3H_4$-^3P_J transitions compared to normalized values of reflectance of those illustrate the quantum cutting effect

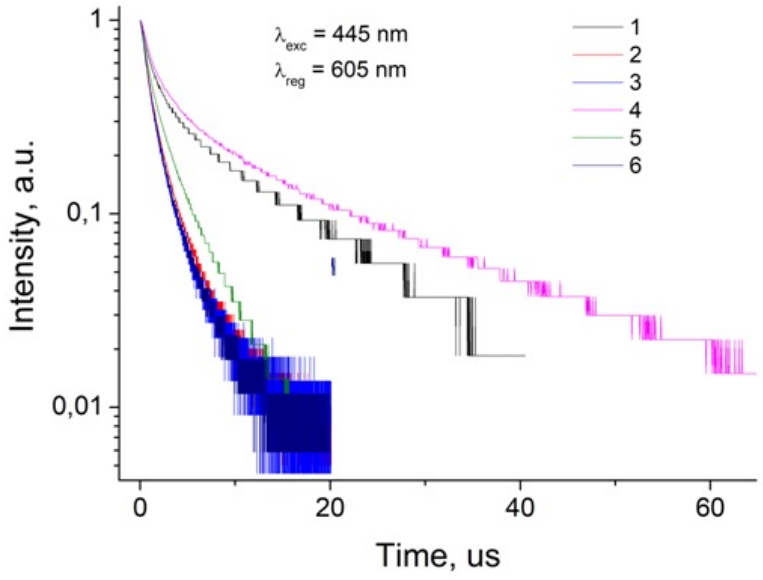

FIG. 6. Luminescence decay curves of $Ba_4Y_3F_{17}$:Pr(X %):Yb(Y %) samples excited at 445 nm registered at 605 nm. Here X/Y corresponds to 0.04/3.00 (1), 0.04/10.00 (2), 0.04/15.00 (3), 0.1/3.00 (4), 0.1/10.00 (5), 0.1/15.00 (6)

TABLE 3. Average luminescence lifetime of Pr^{3+} detected at 605 nm in $Ba_4Y_3F_{17}$:Pr:Yb powder under 445 nm excitation, μs

Yb and Pr content, mol.%	Yb (3.0 %)	Yb (10.0 %)	Yb (15.0 %)
Pr (0.04 %)	9.0	2.8	2.5
Pr (0.1 %)	15.9	3.0	2.3

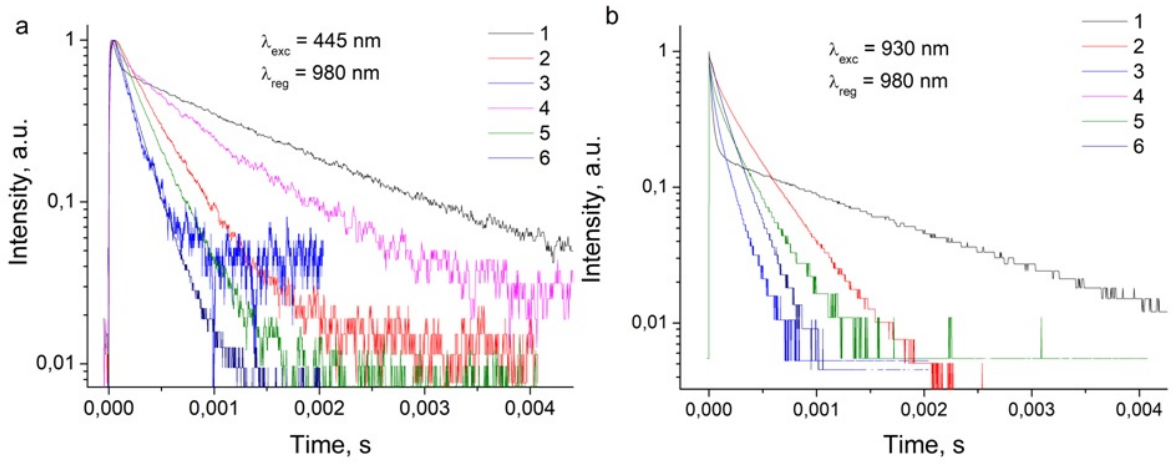

FIG. 7. Luminescence decay curves of $Ba_4Y_3F_{17}$:Pr(X %):Yb(Y %) samples registered at 980 nm excited at 445 nm (a) and 930 nm (b). Here X/Y corresponds to 0.04/3.00 (1), 0.04/10.00 (2), 0.04/15.00 (3), 0.1/3.00 (4), 0.1/10.00 (5), 0.1/15.00 (6)

The luminescence decays of Yb^{3+} ions both under 445 nm excitation (Fig. 7a) and 980 nm excitation (Fig. 7b) appear to be non-exponential due to non-radiative quenching and also due to sensitized character of excitation for the latter. The luminescence lifetime was estimated as the average lifetime by formula (1) also, the results are presented in Table 4.

TABLE 4. Average luminescence lifetime of Yb^{3+} detected at 980 nm in $Ba_4Y_3F_{17}$:Pr:Yb powder under 445 and 930 nm excitation

Avg. time, ms	Yb 3.0 %		Yb 10.0 %		Yb 15.0 %	
Excitation, nm	**445**	**930**	**445**	**930**	**445**	**930**
Pr 0.04 %	1.47	1.48	0.345	0.320	0.159	0.124
Pr 0.10 %	0.729	0.756	0.266	0.248	0.184	0.167

Results of calculation in Table 4 show that Yb^{3+} ions exhibit strong concentration quenching. Also, it is important to note that the increase of Pr^{3+} ions also leads to a decrease in Yb^{3+} luminescence lifetime, which is seen for high concentrations of Yb^{3+} ions. It is a known feature of Pr/Yb ions pair when Yb^{3+} ions transfer their excitation to $^1G_4$ manifold of Pr^{3+} ions [19, 29]. At the same time, the down-conversion mechanism results in a bit longer luminescence lifetime when excited at 445 nm. From Fig. 7a, we can see that the luminescence of Yb^{3+} under 445 nm pulse excitation exhibits some build-up which was not observed in kinetics with direct Yb^{3+} excitation (Fig. 7b). This build-up time is on the same order of magnitude with the $^3P_0$ manifold of Pr^{3+} lifetime, which speaks for a rate of energy transfer to Yb^{3+} as high as on the order of 10^6 s^{-1}.

The luminescence spectrum corrected for the spectral sensitivity of our detection system allows estimation of energy transfer efficiency [19]. Ratios of integral luminescence intensity of Yb^{3+} ions to the integral luminescence intensity of the whole emission spectrum of the sample can be the measure of energy transfer coefficient between sensitizer (Pr^{3+}) and activator (Yb^{3+}) ions together with their concentration quenching processes (2):

$$q^E = \frac{\int I^{Yb}(\lambda)d\lambda}{\int (I^{Yb}(\lambda) + I^{Pr}(\lambda))d\lambda}, \tag{2}$$

where $I^{Yb}(\lambda)$ is the Yb^{3+} ion luminescence intensity, $I^{Pr}(\lambda)$ is the Pr^{3+} ion luminescence intensity. The corresponding calculation results are presented in Table 5.

From Table 5, we see that the energy transfer efficiency from Pr^{3+} ions to Yb^{3+} ions reaches 74 % for $Ba_4Y_3F_{17}$:Pr(0.1 %):Yb(15.0 %) powder sample which is relatively large and speaks for high efficiency of the down-conversion system, since Yb^{3+} luminescence is not quenched at a high rate at this concentration.

TABLE 5. Energy transfer from Pr^{3+} to Yb^{3+} ions in $Ba_4Y_3F_{17}$ powder estimated from luminescence spectra, %

Yb and Pr content, mol.%	Yb (10.0 %)	Yb (15.0 %)
Pr (0.04 %)	54	58
Pr (0.10 %)	58	74

The external efficiency of down conversion was investigated for studied samples by means of measurement of quantum yield of Yb^{3+} ions luminescence excited at 445 nm in the integrating sphere attached to the spectrometer by the technique described in [25]. Results are presented in the Table 6.

TABLE 6. Estimated external quantum yield of down-conversion luminescence of Yb^{3+} ions of $Ba_4Y_3F_{17}$:Pr:Yb powder samples measured in integrating sphere, %

Yb and Pr content, mol.%	Yb (10.0 %)	Yb (15.0 %)
Pr (0.04 %)	0.8	0.8
Pr (0.1 %)	2.9	2.6

The results of external quantum yield measurement of down conversion luminescence in $Ba_4Y_3F_{17}$:Pr:Yb powder samples speak for the potential of the compound. Values of quantum yield above 2 % are relatively high compared to CaF_2:Pr:Yb and SrF_2:Pr:Yb solid solutions with its values lower than 1 [18, 19], or upconverter materials for solar cells (about 1 %) [30].

5. Conclusions

Single-phase powders of $Ba_4Y_3F_{17}$:Yb:Pr solid solutions with an average agglomerate size of 400 nm were synthesized by co-precipitation from aqueous solutions. The down-conversion luminescence was investigated in $Ba_4Y_3F_{17}$ co-doped with Pr^{3+} and Yb^{3+} ions. When excited to ^3P_J manifold of Pr^{3+} ions, the samples exhibited luminescence of both Pr^{3+} and Yb^{3+} ions. The energy transfer efficiency appeared to be 74 % for Pr^{3+} 0.1 % and Yb^{3+} 15.0 %, which appears to be efficient, since Yb^{3+} luminescence is still not strongly quenched at this concentration. It was shown that the down-conversion mechanism in the investigated samples is quantum cutting, when one photon absorbed by Pr^{3+} ions results in two photons emitted by Yb^{3+} ions. At the same time, the energy back transfer from Yb^{3+} to Pr^{3+} was observed apparently through resonant energy transfer involving $^2F_{7/2}$–$^2F_{5/2}$ of Yb^{3+} ions and $^1G_4$-$^3P_0$ of Pr^{3+} ions transitions. Overall, the external quantum yield of down-conversion luminescence measured in our study appeared to be relatively high, with a maximum value of 2.9 % for $Ba_4Y_3F_{17}$:Pr(0.1 %):Yb(10.0 %) sample, which makes this compound promising for Si-based solar cell efficiency enhancement.

Acknowledgements

The study was funded by the Russian Science Foundation (project # 17-73-20352). Authors thank E. V. Chernova for her assistance with the preparation of this manuscript.

References

[1] Weber E.R. Photovoltaics moving into the terawatt age. *Proc. SPIE* 10368, Next Generation Technologies for Solar Energy Conversion VIII, 1036803, 25 August 2017, DOI: 10.1117/12.2277978.

[2] Green M.A., Bremner S.P. Energy conversion approaches and materials for high-efficiency photovoltaics. *Nature Mater.*, 2017, **16**, P. 23–34.

[3] Han G., Zhang S., Boix P.P., Wong L.H., Sun L., Lien S.Y. Towards high efficiency thin film solar cells. *Progress in Materials Science*, 2017, **87**, P. 246–291.

[4] Engelhart P., Wendt J., Schulze A., Klenke C., Mohr A., Petter K., Stenzel F., Hörnlein S., Kauert M., Junghänel M., Barkenfelt B., Schmidt S., Rychtarik D., Fischer M., Müller J.W., Wawer P. R&D pilot line production of multi-crystalline Si solar cells exceeding cell efficiencies of 18 %. *Energy Procedia*, 2011, **8**, P. 313–317.

[5] Yang J., Myong S.Y., Lim K.S. Novel ultrathin LiF interlayers for efficient light harvesting in thin-film Si tandem solar cells. *Solar Energy*, 2015, **114**, P. 259–267.

[6] Fischer S., Ivaturi A., Jakob P., Krämer K.W., Martin-Rodriguez R., Meijerink A., Richards B., Goldschmidt J.Ch. Upconversion solar cell measurements under real sunlight. *Optical Materials*, 2018, **84**, P. 389–395.
[7] Kuznetsov S., Ermakova Yu., Voronov V., Fedorov P., Busko D., Howard I.A., Richards B.S., Turshatov A. Up-conversion Quantum Yield of SrF_2:Yb^{3+}, Er^{3+} Sub-micron Particles Prepared by Precipitation from Aqueous Solution. *J. Mater. Chem. C.*, 2018, **6**, P. 598–604.
[8] Huang X., Han S., Huang W., Liu X. Enhancing solar cell efficiency: the search for luminescent materials as spectral converters. *Chem. Soc. Rev.*, 2013, **42**, P. 173–201.
[9] Kaiser M., Wurth C., Kraft M., Hyppanen I., Soukka T., Resch-Genger U. Power-dependent upconversion quantum yield of $NaYF_4$:Yb^{3+},Er^{3+} nano- and micrometer-sized particles - measurements and simulations. *Nanoscale*, 2017, **9**, P. 10051–10058.
[10] Etchart I., Huignard A., Berard M., Nordin M.N., Hernandez I., Curry R.J., Gillin W.P., Cheetham A.K. Oxide phosphors for efficient light upconversion: Yb^{3+} and Er^{3+} co-doped Ln_2BaZnO_5 (Ln = Y, Gd). *J. Mater. Chem.*, 2010, **20**, P. 3989–3994.
[11] Pokhrel M., Kumar G.A., Sardar D.K. Highly efficient NIR to NIR and VIS upconversion in Er^{3+} and Yb^{3+} doped in M_2O_2S (M = Gd, La, Y). *J. Mater. Chem. A*, 2013, **1**, P. 11595–11606.
[12] Piper W.W., DeLuca J.A., Ham F.S. Cascade fluorescent decay in P^{3+}-doped fluorides: Achievement of a quantum yield greater than unity for emission of visible light. *J. Lumin.*, 1974, **8**, P. 344–348.
[13] Lee T.-J., Luo L.-Y., Cheng B.-M., Diau W.-G., Chen T.-M. Investigation of Pr^{3+} as a sensitizer in quantum-cutting fluoride phosphors. *Appl. Phys. Lett.*, 2008, **92**, P. 081106-1–081106-3.
[14] Van der Ende B.M., Aarts L., Meijerink A. Near-infrared quantum cutting for photovoltaics. *Adv. Mater.*, 2009, **21**, P. 3073–3077.
[15] Song P., Jiang C. Modeling of down converter based on Pr^{3+}–Yb^{3+} codoped fluoride glasses to improve sc-Si solar cells efficiency. *AIP Adv.*, 2012, **2**, P. 042130-1–042130-10.
[16] Zhang L., Xu J., Hu Y., Chen G., Wang Zh. Near-infrared quantum cutting in Pr^{3+}–Yb^{3+} co-doped oxyfluoride glass ceramics containing CaF_2 nanocrystals. *J. Wuhan University of Technology-Mater. Sci. Ed.*, 2013, P. 455–459.
[17] Shao W., Chen G., Ohulchanskyy T.Y., Yang Ch., Agren H., Prasad P.N. A core – multiple shell nanostructure enabling concurrent upconversion and quantum cutting for photon management. *Nanoscale*, 2017, **9**, P. 1934–1941.
[18] Kuznetsov S.V., Proydakova V.Yu., Morozov O.A., Gorieva V.G., Marisov M.A., Voronov V.V., Yapryntsev A.D., Ivanov V.K., Nizamutdinov A.S., Semashko V.V., Fedorov P.P. Synthesis and quantum yield investigations of the $Sr_{1-x-y}Pr_xYb_yF_{2+x+y}$ luminophores for photonics. *Nanosystems: physics, chemistry, mathematics*, 2018, **9**(5), P. 663–668.
[19] Kuznetsov S.V., Morozov O.A., Gorieva V.G., Mayakova M.N., Marisov M.A., Voronov V.V., Yapryntsev A.D., Ivanov V.K., Nizamutdinov A.S., Semashko V.V., Fedorov P.P. Synthesis and luminescence studies of CaF_2:Yb:Pr solid solutions powders for photonics. *J. Fluor. Chem.*, 2018, **211**, P. 70–75.
[20] Kuznetsov S.V., Fedorov P.P., Voronov V.V., Samarina K.S., Ermakov R.P., Osiko V.V. Synthesis of $Ba_4R_3F_{17}$ (R stands for Rare-Earth Elements) Powders and Transparent Compacts on Their Base. Russ. *J. Inorg. Chem.*, 2010, **55**(4), P. 484–493.
[21] Fedorov P.P., Mayakova M.N., Kuznetsov S.V., Voronov V.V., Ermakov R.P., Samarina K.S., Popov A.I., Osiko V.V. Co-precipitation of yttrium and barium fluorides from aqueous solutions. *Mater. Res. Bull.*, 2012, **47**, P. 1794–1799.
[22] M. Karbowiak, J. Cichos Does BaYF5 nanocrystals exist? - The BaF_2-YF_3 solid solution revisited using photoluminescence spectroscopy. *Journal of Alloys and Compounds*, 2016, **673**, P. 258–264.
[23] Li T., Li Y., Luo R., Ning Zh., Zhao Y., Liu M., Lai X., Zhong Ch., Wang Ch., Zhang J., Bi J., Gao D. Novel $Ba(Gd_{1-x}Y_x)_{0.78}F_5$: 20 mol% Yb^{3+}, 2 mol% Tm^{3+} ($0 \leq x \leq 1.0$) solid solution nanocrystals: A facile hydrothermal controlled synthesis, enhanced upconversion luminescent and paramagnetic properties. *J. Alloys Comp.*, 2018, **740**, P. 1204–1214.
[24] Fedorov P.P., Kuznetsov S.V., Mayakova M.N., Voronov V.V., Ermakov R.P., Baranchikov A.E., Osiko V.V. Coprecipitation from aqueous solutions to prepare binary fluorides. *Russ. J. Inorg. Chem.*, 2011, **56**(10), P. 1525–1531.
[25] Yasyrkina D.S., Kuznetsov S.V., Ryabova A.V., Pominova D.V., Voronov V.V., Ermakov R.P., Fedorov P.P. Dependence of quantum yield of up-conversion luminescence on the composition of fluorite-type solid solution $NaY_{1-x-y}Yb_xEr_yF_4$. *Nanosystems: physics, chemistry, mathematics*, 2013, **4**(5), P. 648–656.
[26] Sobolev B.P., Tkachenko N.L. Phase diagrams of BaF_2–(Y, Ln)F_3 systems. *J. Less. Common Met.*, 1982, **85**, P. 155–170.
[27] Maksimov B.A., Solans Kh., Dudka A.P., et al. The fluorite-matrix-based $Ba_4R_3F_{17}$ (R=Y,Yb) crystal structure. Ordering of cations and specific features of the anionic motif. *Crystallogr. Rep.*, 1996, **41**(1), P. 50.
[28] Shannon R.D. Revised Effective Ionic Radii and Systematic Studies of Interatomic Distances in Halides and Chalkogenides. *Acta Cryst.*, 1976, **A32**, P. 751–767.
[29] Aarts L., van der Ende B., Reid M., Meijerink A. Downconversion for Solar Cells in YF_3:Pr^{3+}, Yb^{3+}. *Spectroscopy Letters*, 2010, **43**, P. 373–381.
[30] de Wild J., Meijerink A., Rath J.K., van Sark W.G.J.H.M., Schropp R.E.I. Upconverter solar cells: materials and applications. *Energy Environ. Sci.*, 2011, **4**, P. 4835–4848.

NANOSYSTEMS: PHYSICS, CHEMISTRY, MATHEMATICS, 2019, 10 (2), P. 199–205

PVP-stabilized tungsten oxide nanoparticles (WO_3) nanoparticles cause hemolysis of human erythrocytes in a dose-dependent manner

A. L. Popov[1], I. V. Savintseva[1], N. R. Popova[1], T. O. Shekunova[2,3], O. S. Ivanova[3], A. B. Shcherbakov[4], D. A. Kozlov[2,3], V. K. Ivanov[2,3]*

[1]Institute of Theoretical and Experimental Biophysics, Russian Academy of Sciences, Pushchino, Moscow region, 142290, Russia
[2]Lomonosov Moscow State University, Moscow, 119991, Russia
[3]Kurnakov Institute of General and Inorganic Chemistry, Russian Academy of Sciences, Moscow, 119991, Russia
[4]Zabolotny Institute of Microbiology and Virology, National Academy of Sciences of Ukraine, Kyiv, D0368, Ukraine

antonpopovleonid@gmail.com, savintseva_irina@mail.ru, nellipopovaran@gmail.com, taisia.shekunova@yandex.ru, runetta05@mail.ru, carotene@igic.ras.ru, kozlov@inorg.chem.msu.ru, *van@igic.ras.ru

PACS 68.65.k, 81.20.n, 82.70.Dd, 87.17.Ee **DOI 10.17586/2220-8054-2019-10-2-199-205**

Tungsten oxide nanoparticles (WO_3 NPs) are increasingly being considered as a promising material for biomedical applications. However, toxicological information on their effect on red blood cells (RBCs) remains very scarce. In this study, we examined the toxicity of PVP-stabilized tungsten oxide nanoparticles against human RBCs. Optical microscopy and spectrophotometry data showed that WO_3 NPs induce hemolytic activity. This effect is probably attributed to the direct interaction of the nanoparticles with the RBCs, resulting in the oxidative stress, membrane injury, and subsequent hemolysis.

Keywords: tungsten oxide nanoparticles, human erythrocytes, hemolysis.

Received: 10 February 2019

Revised: 21 February 2019

1. Introduction

Tungsten oxide nanoparticles (WO_3 NPs) are considered as a promising nanomaterial for biomedical applications due to their multifunctionality and therapeutic importance. In recent years, WO_3 NPs have been employed in advanced biomedical applications as antibacterial coatings, contrast agents for X-ray computed tomography or biosensors [1–8]. However, a comprehensive multi-faceted study of their cytotoxicity, in particular hemotoxicity, is still missing. Meanwhile, hemolytic analysis is mandatory for all types of nanomaterials, since their hemolytic activity depends strongly on the size, shape and charge of the nanoparticles, as well as synthesis approaches. Earlier, Chen et al. examined the size-dependent cytotoxicity of silver nanoparticles (Ag NPs) against fish RBCs using three different preparations with characteristic size of nanoparticles of 15 nm, 50 nm, or 100 nm. Data obtained showed that Ag NPs exhibited size effect on their adsorption and uptake by RBCs: the smaller particles possess higher hemolytic activity than that of the larger particles [9]. Aisaka et al. demonstrated hemoglobin release from human erythrocytes upon incubation with TiO_2 nanoparticles. However, the hemolysis was abolished by plasma, and so physical (mechanical) factors are the most important in TiO_2-induced hemolysis [10]. Vinardell et al. compared the hemolytic behavior of bulk aluminum oxide and aluminum oxide nanoparticles on erythrocytes from humans, rats and rabbits. Aluminum oxide nanoparticles are less hemolytic than bulk aluminum oxide and aluminum oxide nanowires, and behave differently depending on the size and shape of the particles [11]. Babu et al. investigated the size-dependent interaction of zinc oxide nanoparticles (ZnO NPs) with RBCs, and their impact on cell viability, DNA damage, reactive oxygen species (ROS) generation. Results obtained showed that ZnO NPs exhibited a size dependent effect on RBCs and hemoglobin (Hb), particularly those NPs with size less than 50 nm [12].

Considering WO_3 nanoparticles as a promising contrast agent for X-ray computed tomography, one should analyze their effect on human blood cells. Here, we evaluated the hemolytic activity of PVP-stabilized WO_3 nanoparticles and suggested possible WO_3 nanoparticles cytotoxicity mechanisms.

2. Materials and methods

2.1. Synthesis and characterization of tungsten oxide nanoparticles (WO_3 NPs)

Ultrasmall hydrated tungsten oxide nanoparticles were synthesized by hydrothermal processing of tungstic acid in the presence of polyvinylpyrrolidone (PVP K-30, average mol. wt. 40,000) as template, stabilizer and growth regulator. Tungstic acid was prepared by ion-exchange method using sodium tungstate (Na_2WO_4) solution and strongly acidic cation exchange resin (Amberlite® IR120). Briefly, ion exchange resin (in a hydrogen form) was swelled in water and loaded into the glass column (filling volume 200 ml). Then, 100 ml of 0.05 M sodium tungstate solution was passed through the column dropwise; 4 g of PVP was added to the obtained eluent; solution was transferred to the flask and stirred for 4 h at reflux. During heating a clear sol of hydrated WO_3 was formed, as evidenced by the appearance of UV-absorption band at 325 nm and Tyndall cone. For cell experiments, sol obtained was diluted to prepare 0.1 – 25.0 mg/ml WO_3 colloid solutions.

In order to determine the possible influence of polyvinylpyrrolidone stabilizer (PVP) on RBCs, we also prepared individual PVP solutions in a similar way.

High-resolution transmission electron microscopy (HR-TEM) analysis was performed using a Libra 200 MC microscope (Zeiss, Germany). TEM images were recorded using a CCD camera (Gatan, USA) with a matrix size of 4096 $\times$ 4096 pixels.

X-ray diffraction (XRD) patterns were collected using a Rigaku D/MAX 2500 diffractometer (Bragg–Brentano reflection geometry) with a scintillation counter. All measurements were performed with CuK$\alpha_{1,2}$ radiation generated on a rotating Cu anode (50 kV, 250 mA) and monochromatized by a curved graphite [0 0 2] monochromator. XRD patterns were obtained in the 2θ range 5 – 80° at a 2θ step of 0.02° and a counting time at least of 10 s per step. Before the measurements the WO_3 sols were applied to an ITO substrate and dried.

The FTIR spectra of the samples were recorded on a Bruker ALPHA spectrometer, in a range of 400 – 4000 cm^{-1}, in attenuated total reflectance mode. To avoid solvent effect WO_3 sol and PVP solution were dried at 50 °C for 1 h.

2.2. Analysis of hemolytic activity

The analysis of hemolytic activity was performed on human blood collected from a healthy patient. The method for hemolysis assay was reported earlier [13]. Prior to WO_3 nanoparticles exposure, the absorbance spectrum of the positive control supernatant was checked and used only when the optical density was in the range of 0.50 – 0.55. Red blood cells (RBCs) were then incubated with WO_3 nanoparticles for 2 h and further centrifuged to isolate the cells. After that, 100 μL of supernatant for each sample was transferred to a 96-well plate. The absorbance values of the supernatant at 570 nm were determined by using a microplate reader. The percent hemolysis of RBCs was calculated according to the equation: percent hemolysis = ((sample absorbance – negative control absorbance)/(positive control absorbance – negative control absorbance)) $\times 100$.

2.3. Optical microscopy of RBCs

Optical microscopy images of RBCs incubated with WO_3 nanoparticles were taken using a Carl Zeiss Axiovert 200 fluorescence-light microscope and recorded by a Canon A620 digital camera.

2.4. Statistical analysis

The experiments were conducted in 3 – 4 repetitions, with analytical estimations done for each WO_3 NPs concentration in three repetitions. Experimental results were compared with the control. Statistical analysis was performed using the methods of variation statistics. We determined the mean values and the standard deviation of the mean. The significance of differences between the groups was determined by Student t-test. The obtained data were processed using GraphPad 6.0 and Microsoft Excel 2007 software.

3. Results and discussion

According to HR-TEM (Fig. 1), WO_3 nanoparticles are ultra small and about 1 nm in size. Obviously, the growth of WO_3 nanoparticles was effectively suppressed by the presence of PVP surfactant.

The XRD data are presented in Fig. 2. The XRD pattern of a dried PVP solution (Fig. 2(a)) contains two broad maxima at 12.1° and 19.9° 2θ which are characteristic for pure PVP. These data are in a good agreement with previously reported results [14, 15]. The sharp peaks are corresponding to ITO substrate signal. The XRD pattern of the dried WO_3 sol (Fig. 2(b)) is mostly X-ray amorphous and partially similar to PVP XRD pattern. A significant increase in intensity at $2\theta < 10°$ may be due to X-ray scattering on ultra small WO_3 nanoparticles.

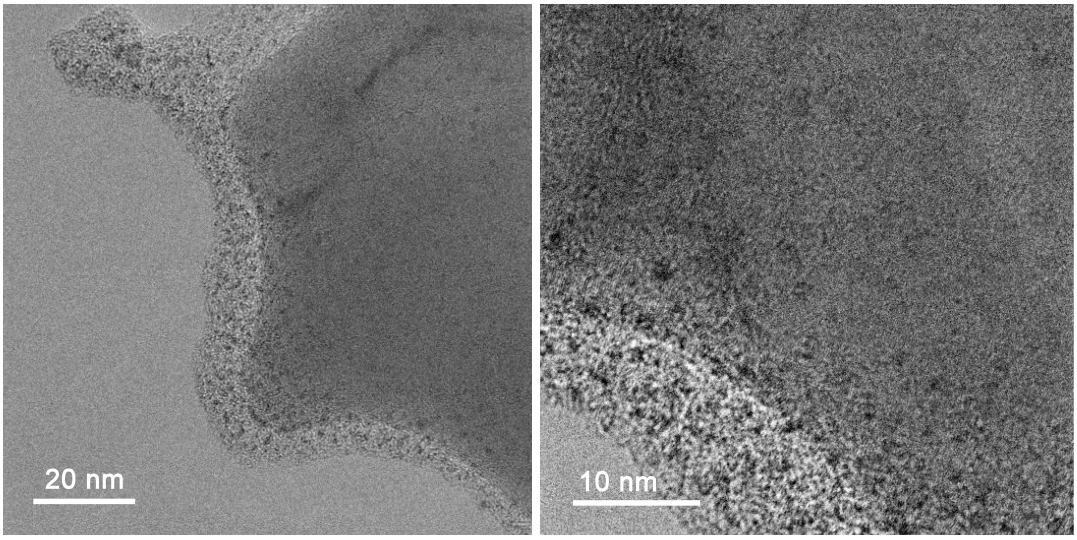

FIG. 1. HR-TEM image of PVP-stabilized WO_3 nanoparticles

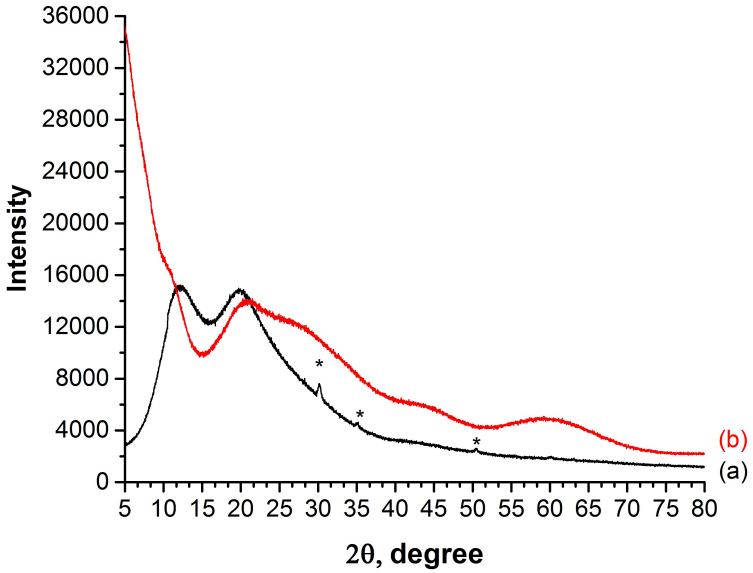

FIG. 2. X-ray diffraction patterns of dried PVP solution (a) and dried WO_3 sol (b). ITO substrate diffraction maxima are marked with *

The FTIR spectra of dried PVP solution and WO_3 sol are shown in Fig. 3. The spectrum for dried PVP solution is similar to the spectra of individual PVP given in literature [16–18]. The FTIR spectrum of dried WO_3 sol is identical to dried PVP solution excepting the ranges of 795 – 995 cm^{-1} and 420 – 435 cm^{-1}. Absorbance in these ranges is typical for tungsten oxide [19–22]. Note that FTIR spectrum of dried WO_3 sol after UV irradiation ($\lambda = 365$ nm, exposure time – 1 min) is similar to dried WO_3 sol kept in dark, while a slight difference in splitting of the absorption band at 430 cm^{-1} is observed. Such a difference can be caused by distortions of [WO_6] octahedra upon changes in tungsten oxidation state.

The appearance of the test tubes with RBCs upon exposure to WO_3 NPs for 2 h is shown in Fig. 4(a). It can be seen that hemolytic activity of WO_3 NPs is dose-dependent. High concentrations of WO_3 NPs lead to the aggregation of the particles, which increases hemolytic activity. It is also well known that tungsten oxide nanoparticles possess enormous redox activity, which can lead to oxidative damage of red blood cell membranes [6].

The results of the spectrophotometric analysis of supernatants confirm the trend revealed by the appearance of the RBCs (Fig. 4(b)). Optical microphotographs of RBCs without WO_3 NPs (Fig. 4(c)) showed cells with

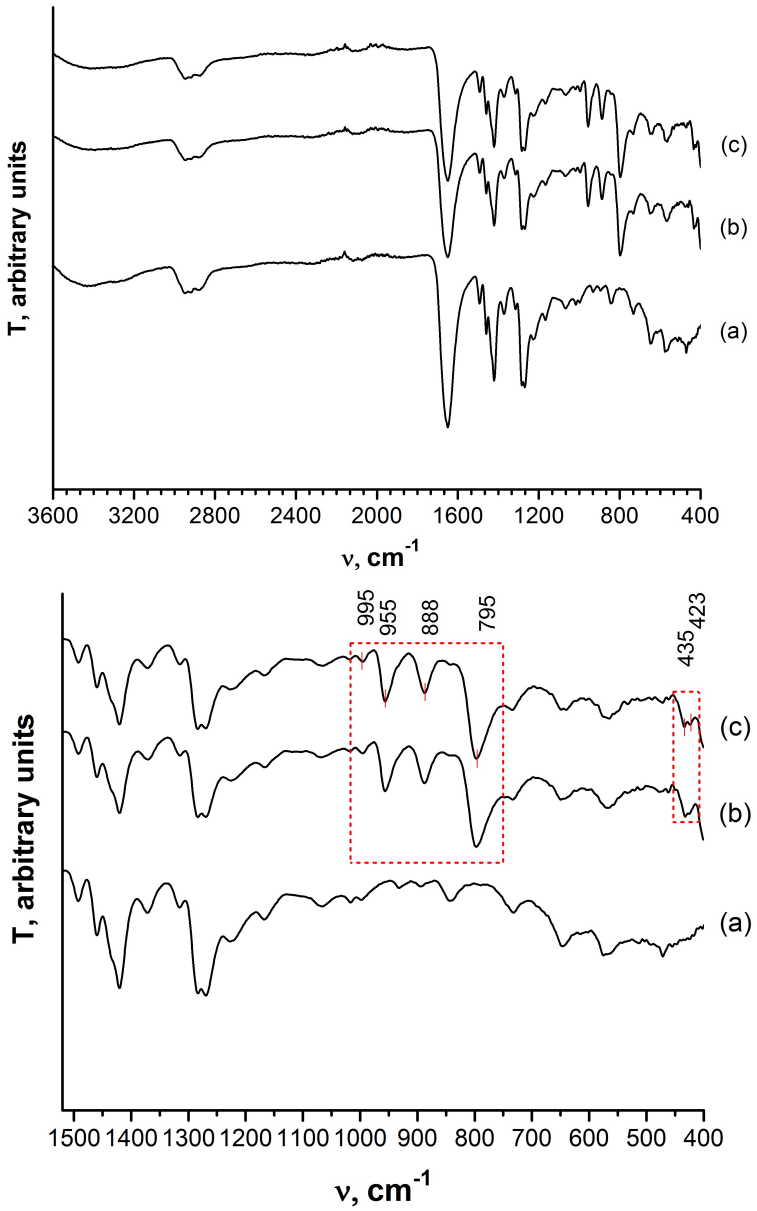

FIG. 3. Survey IR spectrum (above), and its fragment (below): dried PVP solution (a), dried WO_3 sol (b), dried WO_3 sol after UV irradiation (c)

undamaged membranes, however treatment with WO_3 NPs (12.5 mg/ml) for 2 h caused damage to 100 % of RBCs with hemoglobin release and cell lysis leading to formation erythrocyte membrane ghosts (Fig. 4(d)).

Surface functionality of nanoparticles is one of the key factors determining their possible uses in therapeutic applications, imparting functional properties and dictating their circulation profile in the blood stream [23, 24]. For example, the nanoparticles' surface hydrophobicity has a critical role in the cellular uptake, toxicity, and immune responses of nanomaterials [25–27]. Meanwhile, when entering the bloodstream, nanoparticles interact with blood proteins to form a protein corona, which changes their functional characteristics thus affecting final physiological effect [28–32]. It was previously shown that the preincubation of nanoparticles with plasma proteins can give rise to hemolytic activity of nanomaterials [33]. In our experiments, we also simulated the conditions of the microenvironment in the bloodstream by preincubating nanoparticles in a solution of serum albumin, the main protein of the blood plasma, and evaluated their hemolytic activity upon this treatment (Fig. 5).

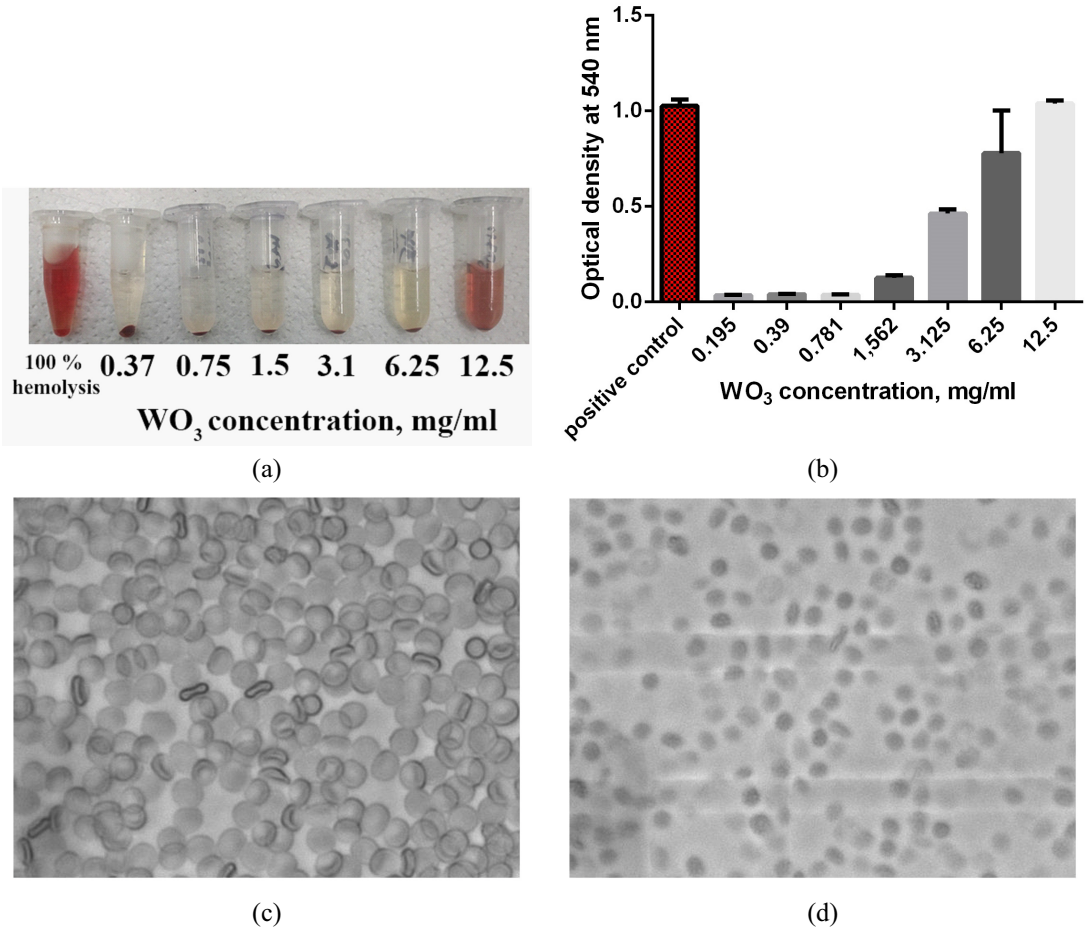

FIG. 4. Hemolysis of human red blood cells upon incubation with WO_3 nanoparticles. Appearance of the test tubes containing RBCs upon exposure to WO_3 NPs for 2 h (a). The hemolysis of WO_3 nanoparticles measured spectrophotometrically at 540 nm (b). Optical microscopy images of RBCs without WO_3 NPs (c) and RBCs exposed to WO_3 NPs (12.5 mg/ml) for 2 h (d)

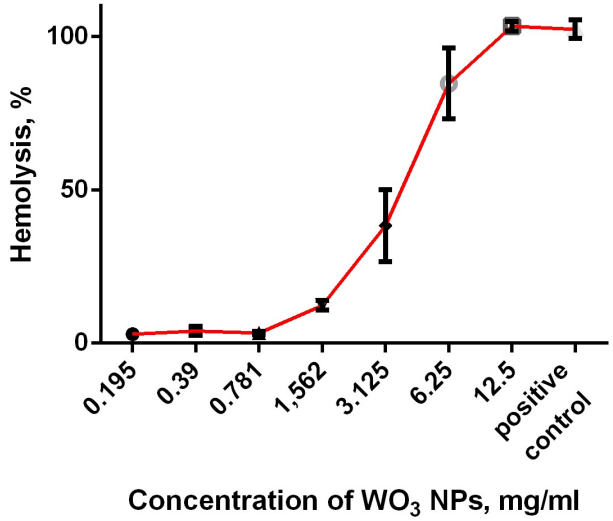

FIG. 5. Hemolytic activity of WO_3 NPs after preincubation with serum albumin. The rate of hemolysis was calculated using water (Milli Q) as the positive control. Error bars represent standard deviations ($n = 3$)

Meanwhile, no significant changes in hemolytic activity of WO_3 NPs were observed in the presence of serum albumin.

Thus, the toxic action of tungsten oxide nanoparticles on human blood cells is probably realized via molecular mechanisms. Further research is required to clarify the nature of this toxic action.

4. Conclusions

Ultra small tungsten oxide nanoparticles were synthesized using polyvinylpyrrolidone as the growth regulator. Tungsten oxide nanoparticles were comprehensively studied using HR-TEM, XRD and FTIR techniques.

PVP-stabilized tungsten oxide nanoparticles were shown to exhibit notable hemolytic activity in a dose-dependent manner. The reasons for WO_3 NPs' toxic action were clarified.

Acknowledgements

The work supported by Russian Science Foundation (project 18-73-10150).

References

[1] Hosseini F., Rasuli R., Jafarian V. Immobilized WO_3 nano-particles on graphene oxide as a photo-induced antibacterial agent against UV resistant Bacillus Pumilus. *J. Phys. D: Appl. Phys.*, 2018, **51** (14), 145403.

[2] Hariharan V., Radhakrishnan S., et al. Synthesis of polyethylene glycol (PEG) assisted tungsten oxide (WO_3) nanoparticles for L-dopa bio-sensing applications. *Talanta*, 2011, **85** (4), P. 2166–2174.

[3] Deng K., Hou Z., et al. Enhanced Antitumor Efficacy by 808 nm Laser-Induced Synergistic Photothermal and Photodynamic Therapy Based on a Indocyanine-Green-Attached $W_{18}O_{49}$ Nanostructure. *Adv. Funct. Mater.*, 2015, **25** (47),P. 7280–7290.

[4] Chen Z., Wang Q.,et al. Ultrathin PEGylated $W_{18}O_{49}$ nanowires as a new 980 nm-laser-driven photothermal agent for efficient ablation of cancer cells in vivo. *Adv Mater.*, 2013, **25** (14), P. 2095–2100.

[5] Sharker S.Md., Kim S.M., et al. Functionalized biocompatible WO_3 nanoparticles for triggered and targeted in vitro and in vivo photothermal therapy. *J. Control. Release*, 2015, **217**, P. 211–220.

[6] Zhou Z., Kong B., et al. Tungsten Oxide Nanorods: An Efficient Nanoplatform for Tumor CT Imaging and Photothermal Therapy. *Sci. Rep.*, 2014, **4**, 3653.

[7] Liu J., Han J., et al. *In vivo* near-infrared photothermal therapy and computed tomography imaging of cancer cells using novel tungsten-based theranostic probe. *Nanoscale*, 2014, **6** (11), P. 5770–5776.

[8] Liu P., Wang Y., et al. Ultrasmall $WO_{3-x}@\gamma$-poly-l-glutamic Acid Nanoparticles as a Photoacoustic Imaging and Effective Photothermal-Enhanced Chemodynamic Therapy Agent for Cancer. *ACS Appl. Mater. Interfaces*, 2018, **10** (45), P. 38833–38844.

[9] Chen L.Q., Fang L., et al. Nanotoxicity of silver nanoparticles to red blood cells: Size-dependent adsorption, uptake and hemolytic activity. *Chem. Res. Toxicol.*, 2015, **28** (3), P. 501–509.

[10] Aisaka Y., Kawaguchi R., Watanabe S. Hemolysis Caused by Titanium Dioxide Particles. *Inhalation Toxicol.*, 2008, **20**, P. 891–893.

[11] Vinardell M.P., Sordé A., et al. Comparative effects of macro-sized aluminum oxide and aluminum oxide nanoparticles on erythrocyte hemolysis: influence of cell source, temperature, and size. *J. Nanopart. Res.*, 2015, **17**, 80.

[12] Babu E.P., Subastri A., et al. Size Dependent Uptake and Hemolytic Effect of Zinc Oxide Nanoparticles on Erythrocytes and Biomedical Potential of ZnO-Ferulic acid Conjugates. *Sci. Rep.*, 2017, **7**, 4203.

[13] Dobrovolskaia M.A., Clogston J.D., et al. Method for analysis of nanoparticle hemolytic properties in vitro. *Nano Lett.*, 2018, **8**, P. 2180–2187.

[14] El Hotaby W., Sherif H.H.A., et al. Assessment of in situ-Prepared Polyvinylpyrrolidone-Silver Nanocomposite for Antimicrobial Applications. *Acta Phys. Pol. A*, 2017, **131** (6), P. 1554–1560.

[15] Li X.G., Kresse I., et al. Morphology and gas permselectivity of blend membranes of polyvinylpyridine with ethylcellulose. *Polymer*, 2001, **42** (16), P. 6859–6869.

[16] Liu H., Zhang B., et al. Hydrothermal synthesis of monodisperse Ag_2Se nanoparticles in the presence of PVP and KI and their application as oligonucleotide labels. *J. Mater. Chem.*, 2008, **18** (22), P. 2573–2580.

[17] Melnikova O.A., Samkova I.A., Melnikov M.Yu., Petrov A.Yu. IR-spektroskopic studies of chemical structure of polymeric complexes of medicinal substances on the basis of pollyvinilpirrolidon. *Advances in current natural sciences*, 2016, **8**, P. 42–49.

[18] Basha M.A.F. Magnetic and optical studies on polyvinylpyrrolidone thin films doped with rare earth metal salts. *Polym. J.*, 2010, **42**, P. 728–734.

[19] Balzer R., Drago V., Schreiner W.H., Probst L.F.D. Synthesis and Structure-Activity Relationship of a WO_3 Catalyst for the Total Oxidation of BTX. *J. Braz. Chem. Soc.*, 2014, **25** (11), P. 2026–2031.

[20] Prabhu N., Agilan S., et al. Effect of temperature on the structural and optical properties of WO_3 nanoparticles prepared by solvo thermal method. *Digest Journal of Nanomaterials and Biostructures*, 2013, **8** (4), P. 1483–1493.

[21] Kumar V.B., Mohanta D. Formation of nanoscale tungsten oxide structures and colouration characteristics. *Bull. Mater. Sci.*, 2011, **34** (3), P. 435–442.

[22] He G.H., Liang C.J., et al. Preparation of novel Sb_2O_3/WO_3 photocatalysts and their activities under visible light irradiation. *Mater. Res. Bull.*, 2013, **48** (6), P. 2244–2249.

[23] Saha K., Bajaj A., Duncan B., Rotello V.M. Beauty is skin deep: a surface monolayer perspective on nanoparticle interactions with cells and bio-macromolecules. *Small*, 2011, **7**, P. 1903–1918.

[24] Mout R., Moyano D.F., Rana S., Rotello V.M. Surface functionalization of nanoparticles for nanomedicine. *Chem. Soc. Rev.*, 2012, **41**, P. 2539–2544.

[25] Zhu Z.J., Posati T., et al. The Interplay of Monolayer Structure and Serum Protein Interactions on the Cellular Uptake of Gold Nanoparticles. *Small*, 2012, **8**, P. 2659–2663.
[26] Chompoosor A., Saha K., et al. The role of surface functionality on acute cytotoxicity, ROS generation and DNA damage by cationic gold nanoparticles. *Small*, 2010, **6**, P. 2246–2249.
[27] Moyano D.F., Goldsmith M., et al. Nanoparticle Hydrophobicity Dictates Immune Response. *J. Am. Chem. Soc.*, 2012, **134**, P. 3965–3967.
[28] Walkey C.D., Chan W.C.W. Understanding and controlling the interaction of nanomaterials with proteins in a physiological environment. *Chem. Soc. Rev.*, 2012, **41**, P. 2780–2799.
[29] Monopoli M.P., Aberg C., Salvati A., Dawson K.A. Biomolecular coronas provide the biological identity of nanosized materials. Nat. Nanotechnol., 2012, **7**, P. 779–786.
[30] Arvizo R.R., Giri K., et al. Identifying New Therapeutic Targets via Modulation of Protein Corona Formation by Engineered Nanoparticles. *PLoS One*, 2012, **7**, e33650.
[31] Salvador-Morales C., Flahaut E., et al. Complement activation and protein adsorption by carbon nanotubes. *Mol. Immunol.*, 2006, **43**, P. 193–201.
[32] Owens D.E., Peppas N.A. Opsonization, biodistribution, and pharmacokinetics of polymeric nanoparticles. *Int. J. Pharm.*, 2006, **307**, P. 93–102.
[33] Saha K., Moyano D.F., Rotello V.M. Protein coronas suppress the hemolytic activity of hydrophilic and hydrophobic nanoparticles. *Mater Horiz.*, 2014, **1**, P. 102–105.

NANOSYSTEMS: PHYSICS, CHEMISTRY, MATHEMATICS, 2019, 10 (2), P. 206–214

Formation of rhabdophane-structured lanthanum orthophosphate nanoparticles in an impinging-jets microreactor and rheological properties of sols based on them

O. V. Proskurina[1,2], E. V. Sivtsov[1], M. O. Enikeeva[1,2], A. A. Sirotkin[1], R. Sh. Abiev[1], V. V. Gusarov[2]

[1]Saint Petersburg State Institute of Technology, Moskovsky Pr., 26, Saint Petersburg, 190013, Russia

[2]Ioffe Institute, Politekhnicheskaya Saint 26, Saint Petersburg, 194021, Russia

proskurinaov@mail.ru, pjeka@yahoo.fr, abiev.rufat@gmail.com, victor.v.gusarov@gmail.com

DOI 10.17586/2220-8054-2019-10-2-206-214

A free impinging-jets microreactor was used for synthesizing rhabdophane-structured $LaPO_4$ sols. The rheological behavior was investigated for the sols obtained both by reagents mixing in a microreactor, and by pouring the initial solutions together and mixing them on a magnetic stirrer. Lanthanum phosphate sols obtained by two ways are structured systems characterized by deformation behavior accompanied by shear liquefaction. Some discovered anomalies were found to be associated with flow nonequilibrium at low shear rates, which indirectly indicates stronger binding of particles in the structure of samples obtained by the microreactor synthesis.

Keywords: $LaPO_4 \cdot nH_2O$, rhabdophane, nanorods, free impinging-jets microreactor, rheology.

Received: 2 March 2019

Revised: 19 March 2019

1. Introduction

When aqueous solutions of lanthanum salts interact with phosphoric acid or with solutions of phosphate salts at relatively low temperatures, usually there occurs crystallization of a lanthanum orthophosphate-based phase with a rhabdophane-type hexagonal structure, which contains some amount of $LaPO_4 \cdot nH_2O$ [1–5]. When precipitating in an acidic medium, the rhabdophane-structured nanoparticles are generally shaped as nanorods [6, 7].

The morphology, size and structure of nanoparticles, as well as the presence and amount of impurity phases in a nanopowder can significantly influence the mechanical and functional properties of the materials obtained from them [8, 9], including the properties of monazite ceramics obtained by sintering nanopowders based on the rhabdophane-structured phase [10–15]. The morphology and size of rhabdophane-structured lanthanum orthophosphate-based particles greatly determine the rheological properties of their dispersion in liquid media and, consequently, the possibility of using nanoparticles as liquid crystals, which, as was shown in [16–19], can be promising when doping $LaPO_4$ with Eu^{3+}, Tb^{3+} and other ions. The literature contains a limited number of works on the rheology of a dispersion based on the rhabdophane-structured lanthanum orthophosphate nanoparticles [20].

The mentioned reasons show the necessity to develop such methods for synthesizing lanthanum orthophosphate nanopowders that would ensure their morphological characteristics, dispersion and phase composition necessary for obtaining materials with high-level properties. There exist several methods for synthesizing lanthanum orthophosphate nanoparticles, for example, the sol-gel method [21–23], hydrothermal synthesis [24, 24, 25], and the microwave heating synthesis [26–28].

One of the burgeoning trends in chemical technology is the use of microreactors [29]. Impinging-jets microreactors have not yet been sufficiently studied, but have already proved to be promising in the synthesis of nanoparticles [30–34].

Impinging-jet microreactors allow the dissipation of a large amount of energy within a very small volume [35]. Under certain flow regimes of the colliding jets of reagent solutions, it leads to localization of the reaction zone in a confined space with dimensions on the order of hundreds of nanometers, with a uniform distribution of the initial components corresponding to a specified stoichiometry [36]. Under the conditions like used in [34], a nanoparticle of only one phase can be formed, and it will have a size comparable to that of the critical nucleus. As a result, the formation of by-products that differ compositionally from the stoichiometry of the target phase is almost completely excluded. These reasons indicate the promise of using impinging-jet microreactors for producing nanoparticles.

At the same time, the synthesis of lanthanum orthophosphate nanoparticles in a free impinging-jet microreactor (FIJMR) has a significant difference in contrast to the synthesis of cobalt ferrite and bismuth orthoferrite considered in [34]. During the synthesis of $CoFe_2O_4$ and $BiFeO_3$ nanoparticles, a jet of a solution of salts of the initial components, mixed in a specified proportion, collided in the microreactor with a jet containing a precipitant:

ammonia or sodium hydroxide solution. In this case, there was no need in a precise observance of the proportion between the content of a mixed salts solution and that of the alkali solution in the reaction zone. In the case of lanthanum orthophosphate synthesis in the free impinging-jets microreactor, even a slight deviation from the La:P = 1:1 ratio in the reaction zone can lead to the formation of impurity phases with another La:P ratio [37–39]. It may be much more difficult to ensure the necessary La: P ratio in the case of lanthanum orthophosphate synthesis in an impinging-jet microreactor, since in this case solutions containing a lanthanum salt and a phosphate salt (or phosphoric acid) will be supplied into the reaction zone as different jets, the flow rate of which may differ by a few percent.

The prospects of using the thus-synthesized nanoparticles for obtaining nanopowders or compact materials are largely determined by their morphological characteristics, chemical, phase and dispersion composition, as well as by the rheological properties of sols based on them. Recently, interest has emerged in the development and investigation of the different quasi-one-dimensional structures (nanorods, nanowires, nanofibers, nanotubes) is due to their remarkable functional properties [40–44].

These reasons show the urgency of studying the possibility of synthesizing lanthanum orthophosphate nanoparticles in the FIJMR, and of conducting a comparative analysis of characteristics of nanoparticles obtained in a microreactor and of the rheological behavior of sols based on them, compared to the properties of lanthanum orthophosphate nanoparticles obtained by one of the most common synthesis methods.

2. Experimental

2.1. $LaPO_4 \cdot nH_2O$ synthesis

The initial reagents used in this work were lanthanum nitrate (puriss. grade) and monosubstituted ammonium phosphate $NH_4H_2PO_4$ (pur. grade). The lanthanum phosphate particles were precipitated when pouring 100 ml of 0.064 M aqueous solution of $La(NO_3)_3$ into 100 ml of 0.064 M aqueous solution of $NH_4H_2PO_4$ and mixing them with a magnetic stirrer. This resulted in the formation of a white suspension, from which, after stirring for a few minutes, a semi-transparent sol was obtained.

Similar solutions were used for the synthesis of lanthanum phosphate particles in a FIJMR. The FIJMR described in [32] was used. The initial solutions were fed into the jet microreactor through two nozzles with a diameter of 0.44 mm and 0.46 mm. Lanthanum nitrate and ammonium phosphate solutions were supplied as thin jets with a fixed flow rate of 250 ml/min, colliding at a speed of about 23 m/s in a vertical plane at an angle of about 72°, at 22°C and atmospheric pressure. The mutual arrangement of the nozzles and the flow rate were set to make the collision of jets produce a liquid sheet with an average thickness of 10–15 μm, in which the initial component solutions contacted each other and mixed (Fig. 1). Co-precipitation of lanthanum phosphate in a jet microreactor occurred within 5–10 milliseconds.

The result was a suspension, which, at stirring, also transformed into a stable sol.

FIG. 1. Liquid sheet formation at the jets collision in the free impinging-jets microreactor

A centrifuge was used to precipitate and wash the obtained samples. The sols were centrifuged for 5 hours at 15 thousand rpm. After 5 cycles of centrifugation, washing with distilled water and using an ultrasonic bath for the dispersal, the obtained samples were dried at 105°C.

3. Characterization

X-ray diffractograms were recorded on a Rigaku SmartLab 3 powder diffractometer ($Cu_{K\alpha}$ emission) in the 2θ=20–60° angle range with a 0.01° step and a shooting speed of 0.1°/min. The samples' phase compositions were found using the ICSD PDF-2 database.

The average crystallite size was determined with the help of the SmartLab Studio II software package from Rigaku. Crystallite size distribution and distribution parameters were determined by the fundamental parameters method in approximation to the log-normal distribution model, using the SmartLab Studio II software package.

The morphology of the washed and dried samples, as well as the particle size and elemental composition of the samples were determined using a Tescan Vega 3 SBH scanning electron microscope with an Oxford Instruments X-ray microanalysis attachment.

Transmission electron microscopy (TEM) studies for determining samples microdiffraction were performed on a JEOL JEM-2100F microscope with the accelerating voltage of 200 kV.

The flow curves for the sols were obtained on the Anton Paar PHYSICA MCR302 rheometer, and the data processing was performed using the RHEOPLUS / 32 V.3.62 software. A cone-plane measuring system with a diameter of 25 mm was used; the minimum gap size was 0.051 mm. The time interval between successive measurements in constructing the flow curve was 2 s.

4. Results and discussion

The X-ray diffraction data for the samples are shown in Fig. 2a. Diffractograms of all samples correspond to those of the rhabdophane phase.

The X-ray microanalysis data for the samples show that the P: La ratio in the samples is in the range of (48±2): (52±2) at.%, which, within the limits of error, corresponding to the ratio specified for the synthesis, which corresponds to $LaPO_4$ stoichiometry. A small amount of nitrogen (around 1.8%) is present in the samples, which may indicate that the ammonium nitrate produced during the synthesis was not completely washed off from the sol particles.

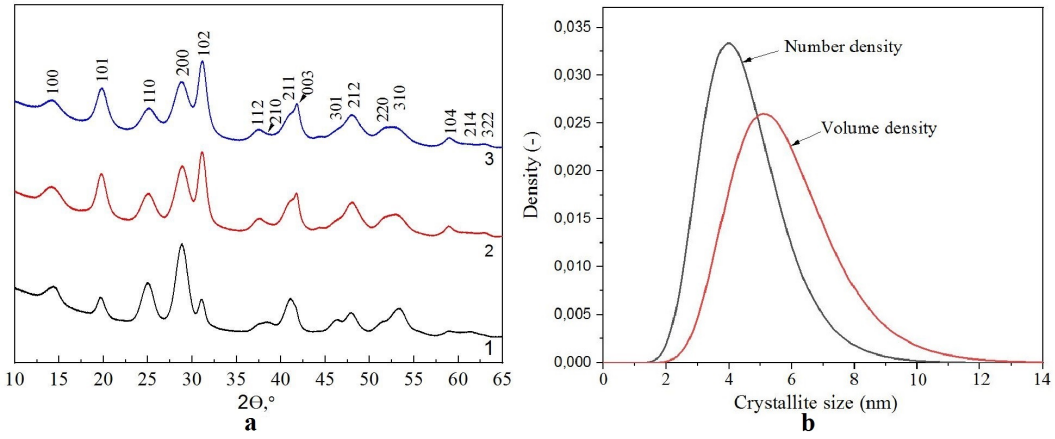

FIG. 2. (a) – X-ray diffraction data: 1 – sol, washed after FIJMR, non-dried, 2 – sol, washed and dried after FIJMR, 3 – sol, washed and dried after precipitation on magnetic stirrer; (b) – Distribution of the crystallites number and volume by size, determined from reflex (200) for sample 1

The TEM results presented in Fig. 3 show that individual nanorods are approximately 4–7 nm thick. This result correlates well with the data on the crystallite size distribution obtained from the analysis of the broadened (200) line in the X-ray diffractogram (Fig. 2b). The nanorod length starts from 25–30 nm and reaches several hundred nm. Fig. 3c demonstrates the oriented coalescence of three hexagonal nanorods along the edges.

Micrographs of samples taken with a scanning electron microscope are shown in Fig. 4. The samples are represented by rods with a thickness of about 20–40 nm and a length of up to 1 μm.

A comparison of the SEM particle size data with the TEM data and the results of the crystallites size distribution analysis allows a conclusion that $LaPO_4 \cdot nH_2O$ nanocrystals form aggregates consisting of crystallites that are fused together in the form of nanorods oriented along the 6th-order axis of the rhabdophane structure.

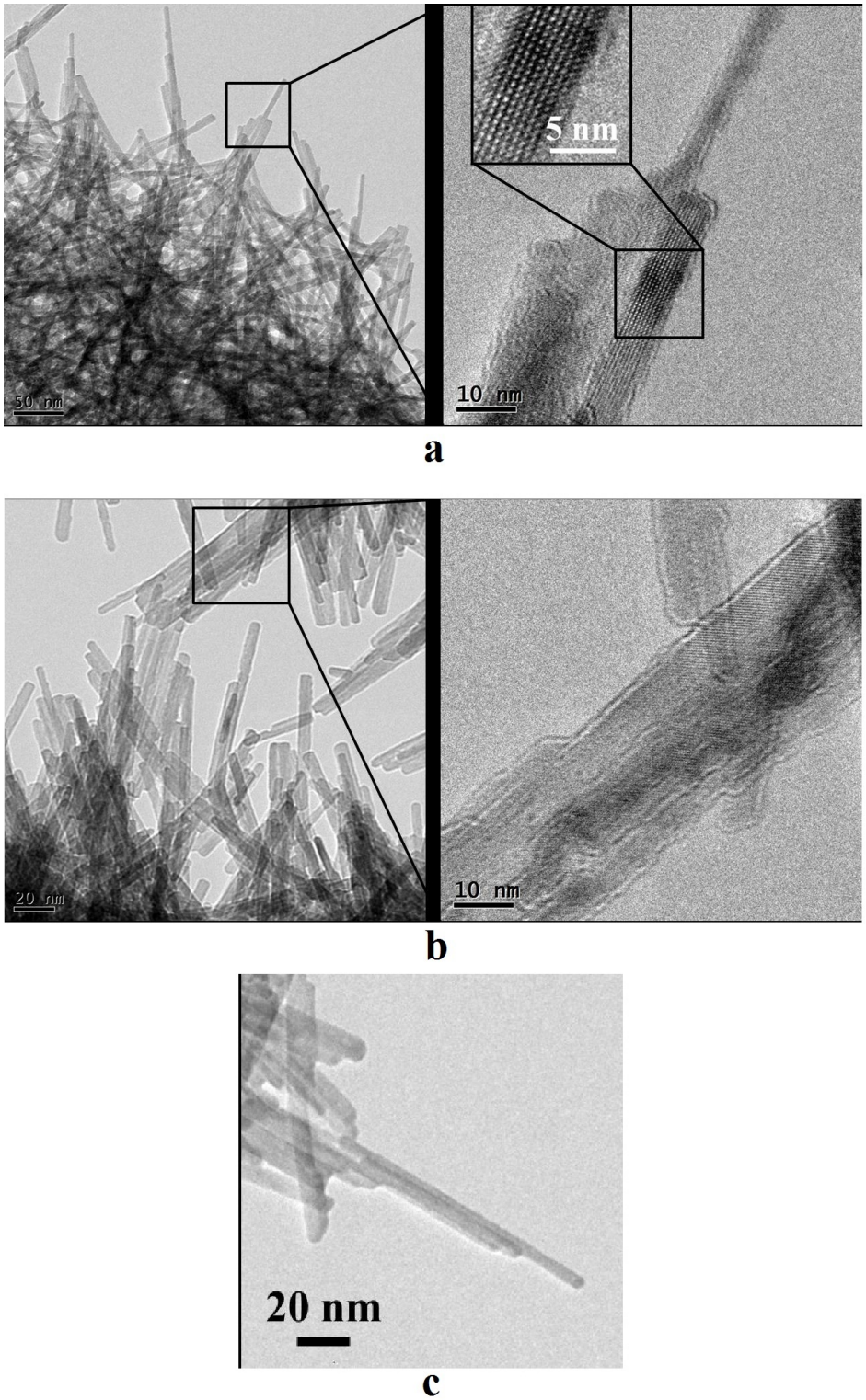

FIG. 3. TEM images for the sample obtained in FIJMR (a), and the sample obtained via precipitation on magnetic stirrer (b), (c)

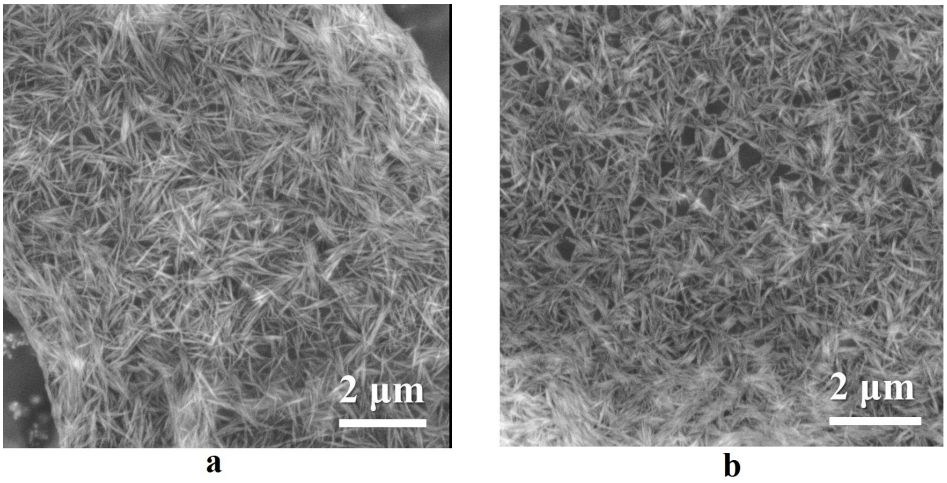

FIG. 4. SEM micrographs of the sample obtained in FIJMR (a), and the sample obtained via mixing on magnetic stirrer (b)

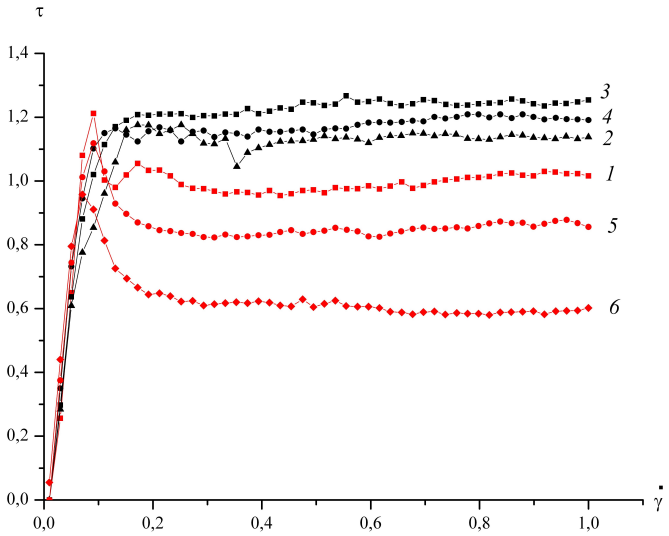

FIG. 5. τ(Pa) as a function of the shear rate γ (s^{-1}) for the sols obtained through the microreactor synthesis in the region of low shear rates. Time intervals between adjacent measurements: 1-2, 2-3, 3-4 – 3 min; 4-5 – 6 min, 5-6 – 3 min

The rheological behavior of lanthanum phosphate sols has been studied in two ranges of shear strain rates: at low rates from 0.01 to 1 s^{-1}, and in the range from 0.5 to 200 s^{-1} which is typical for similar studies. The flow curve was taken at least 4 times for each experiment. The curve numbers match the numbers of the experiments in this series.

The initial series of the flow curves for the sols obtained by microreactor synthesis is characterized by an anomaly, which is expressed in the constant shear stress plateau after a short region of the usual shear-thinning behavior (Fig. 5). Moreover, this change of the flow mode occurs in some cases through the maximum shear stress (Fig. 5, curves 1, 2, 5, 6). This is characteristic of the structured thixotropic systems in a non-equilibrium state during the experiment. As the shear rate increases (when its values are small), the aggregates do not have enough time to collapse to a size that is in equilibrium at a given shear rate, which leads to stress accumulation. At a certain moment, rapid fragmentation of the non-equilibrium aggregates begins and determines the behavior shown in Fig. 1. It is characteristic that a series of successive repetitions of the experiment with the minimum time interval between them leads to the unification of the flow curves (Fig. 5, curves 3, 4), which disappears again after a relatively long pause (Fig. 5, curves 5, 6).

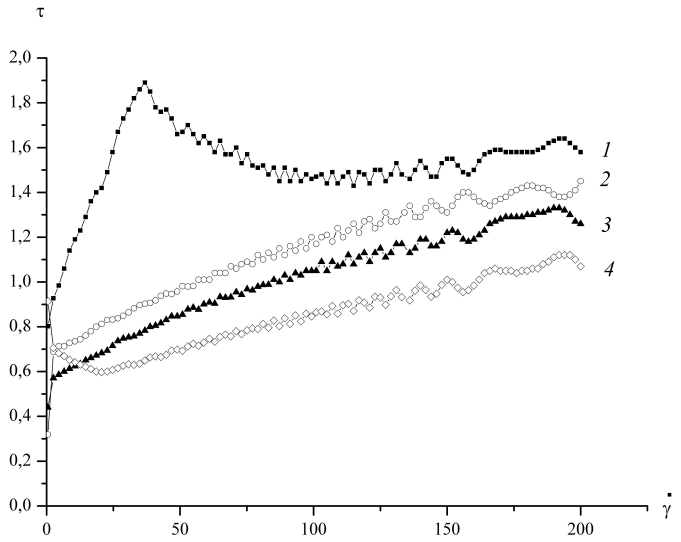

FIG. 6. τ(Pa) as a function of the shear rate γ (s^{-1}) for the sols obtained through the microreactor synthesis in a broad range of shear rates. The first curve starts 3 min after the last measurement in the previous series (Fig. 5). Time intervals between adjacent measurements: 1-2 – 4 min; 2-3 – 5 min; 3-4 – 6 min

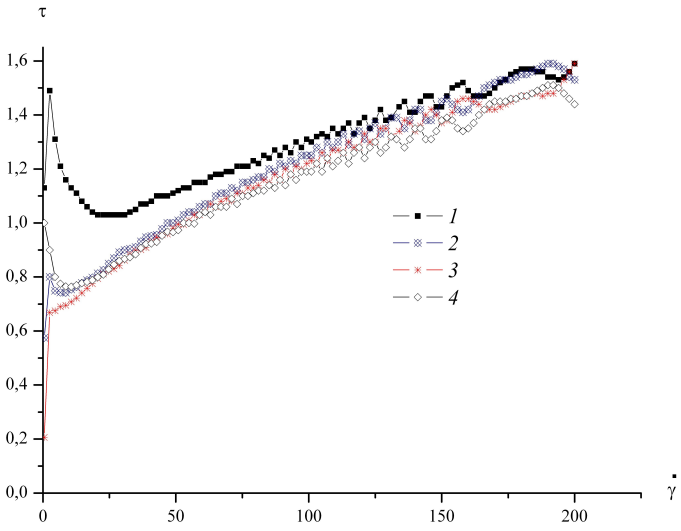

FIG. 7. τ(Pa) as a function of the shear rate γ (s^{-1}) for the sols obtained through the microreactor synthesis without deformation prehistory, in a broad range of shear rates. Time intervals between adjacent measurements: 5 min

Interestingly, the replacement of one sample with another that has no deformation prehistory does not lead to a change in the flow curves appearance (Fig. 7) and in the nature of their change in a series of successive measurements, but significantly shortens the time interval of the above-described anomaly manifestation to the values observed in the experiments at low shear rates (Fig. 5).

A similar anomaly is also manifested in the flow curves in a wide (0.5–200 s^{-1}) range of shear rates (Fig. 6). It occurs over a much longer time interval and can be easily seen when taking into account that the interval between adjacent points in the presented dependencies is 2 seconds. Already, during the second repetition of the experiment, the flow curves become unified (Fig. 6, curves 2, 3), which become typical for shear thinning and can be formally described, for example, by the classical Herschel-Bulkley equation [45]. Usually, such an experiment is not reproduced more than 2-3 times [46]. However, as it follows from the form of curve 4 in Fig. 6, the anomaly can reappear with an increase in the time interval between experiments.

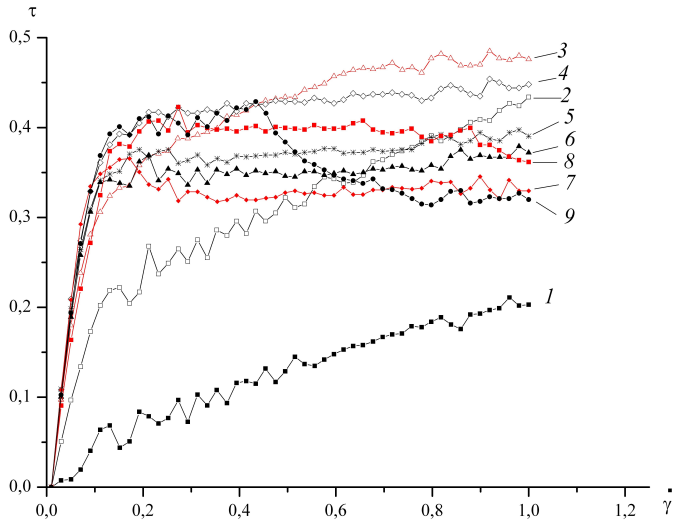

FIG. 8. τ(Pa) as a function of the shear rate γ (s^{-1}) for the sols obtained by precipitation in the region of low shear rates. Time intervals between adjacent measurements: 3 min

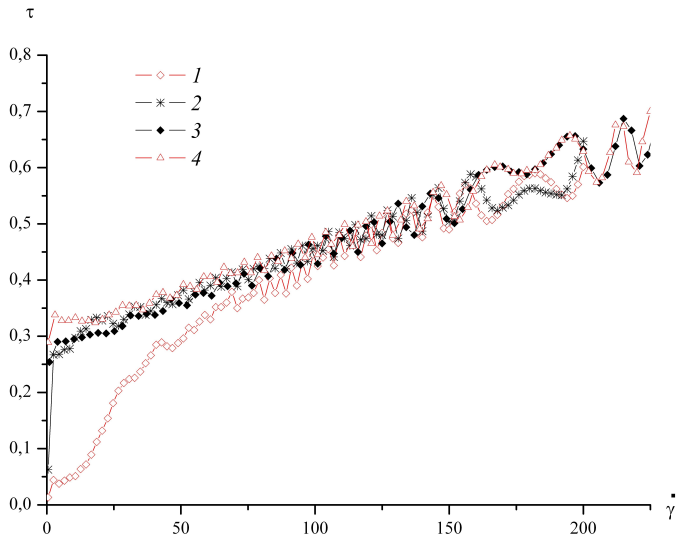

FIG. 9. τ(Pa) as a function of the shear rate γ (s^{-1}) for the sols obtained by precipitation in the broad range of shear rates. The first curve starts 7 min after the last measurement in the previous series (Fig. 8). Time intervals between adjacent measurements: 1-2 – 5 min; 2-3 – 4 min; 3-4 – 13 min

The behavior of the sols obtained by precipitation is completely different when mixing reagents in a glass and stirring on a magnetic stirrer. The corresponding flow curves are shown in Fig. 8. In the region of low shear rates (below 1 s^{-1}), the first three flow curves are typical for shear thinning (Fig. 8, curves 1-3). Then the constant shear stress plateau appears (Fig. 8, curves 4-6), followed by the maximum shear stress (Fig. 8, curves 7-9). Therefore, it can be concluded that the nonequilibrium character of the flow intensifies along with the experiment reproduction.

Another difference from the behavior of sols obtained by the microreactor synthesis is in the absence of the flow curve anomalies over a broad range of shear rates (Fig. 9). Their appearance becomes unified and characteristic of the plastic flow already starting from the second repetition. And even a relatively long pause before the last measurement (Fig. 9, curve 4) does not cause a pronounced anomaly to appear, as was observed for the samples obtained through the microreactor synthesis.

5. Conclusion

The presented data allow one to conclude that all the obtained lanthanum phosphate sols are structured systems, which are characterized by deformation behavior accompanied by shear thinning. The revealed anomalies associated with flow nonequilibrium at low shear rates indirectly indicate a stronger binding of particles in the structure of the samples obtained through the microreactor synthesis.

Acknowledgements

Rheological and X-ray diffraction studies, scanning electron microscopy and elemental analysis of samples were performed employing the equipment of the Engineering Center of the Saint Petersburg State Institute of Technology (Technical University). We thank our colleague D. P. Danilovich for his contribution to the project.

Structural characterization was made on the equipment of the Federal Joint Research Centre "Material science and characterization in advanced technology" (Ioffe Institute, Saint Petersburg, Russia). The authors would like to thank V. N. Nevedomsky for his assistance.

This work was supported by the Russian Foundation for Basic Research (project No 18-29-12119).

References

[1] Buissette V., Moreau M., Gacoin T., Boilot J.-P., Chane-Ching J.-Y., Le Mercier T. Colloidal Synthesis of Luminescent Rhabdophane $LaPO_4:Ln^{3+} \cdot xH_2O$ (Ln = Ce, Tb, Eu; x∼0.7) *Nanocrystals. Chem. Mater.*, 2004, **16**, P. 3767–3773.

[2] Fang Y.-P., Xu A.-W., Song R.-Q., Zhang H.-X., You L.-P., Yu J.C., Liu H.-Q. Systematic Synthesis and Characterization of Single-Crystal Lanthanide Orthophosphate Nanowires. *J. Am. Chem. Soc.*, 2003, **125**(51), P. 16025–16034.

[3] Glorieux B., Matecki M., Fayon F., Coutures J.P., Palau S., Douy A., Peraudeau G. Study of lanthanum orthophosphates polymorphism, in view of actinide conditioning. *Journal of Nuclear Materials*, 2004, **326**(2-3), P. 156–162.

[4] Neupane M.R., Garrett G.A., Rudin S., Andzelm J.W. Phase dependent structural and electronic properties of lanthanum orthophosphate ($LaPO_4$). *J. Phys. Condens. Matter.*, 2016, **28**(20), P. 205501.

[5] Gausse C., Szenknect S., Qin D.W., Mesbah A., Clavier N., Neumeier S., Bosbach D., Dacheux N. Determination of the Solubility of Rhabdophanes $LnPO_4 \cdot 0.667H_2O$ (Ln = La to Dy). *Eur. J. Inorg. Chem.*, 2016, **28**, P. 4615–4630.

[6] Osipov A.V., Mezentseva L.P., Drozdova I.A., Kuchaeva S.K., Ugolkov V.L., Gusarov V.V. Preparation and thermal transformations of nanocrystals in the $LaPO_4$-$LuPO_4$-H_2O system. *Glass Physics and Chemistry*, 2009, **35**(4), P. 431–435.

[7] Roncal-Herrero T., Rodríguez-Blanco J.D., Oelkers E.H., Benning L.G. The direct precipitation of rhabdophane ($REEPO_4 \cdot nH_2O$) nano-rods from acidic aqueous solutions at 5-100°C. *J. Nanopart. Res.*, 2011, **13**, P. 4049–4062.

[8] Boakye E.E., Hay R.S., Mogilevsky P. Spherical Rhabdophane Sols. II: Fiber Coating. *J. Am. Ceram. Soc.*, 2007, **90**(5), P. 1580–1588.

[9] Mogilevsky P., Hay R.S., Boakye E.E., Keller K.A. Evolution of Texture in Rhabdophane-Derived Monazite Coatings. *J. Am. Ceram. Soc.*, 2003, **86**(10), P. 1767–1772.

[10] Kenges K.M., Proskurina O.V., Danilovich D.P., Aldabergenov M.K., Gusarov V.V. Synthesis and Properties of Nanocrystalline Materials Based on $LaPO_4$. *Russian Journal of Applied Chemistry*, 2017, **90**(7), P. 1047–1054.

[11] Sujith S.S., Arun Kumar S.L., Mangalaraja R.V., Peer Mohamed A., Ananthakumar S. Porous to dense $LaPO_4$ sintered ceramics for advanced refractories. *Ceramics International*, 2014, **40**, P. 15121–15129.

[12] Arinicheva Y., Clavier N., Neumeier S., Podor R., Bukaemskiy A., Klinkenberg M., Roth G., Dacheux N., Bosbach D. Effect of powder morphology on sintering kinetics, microstructure and mechanical properties of monazite ceramics. *Journal of the European Ceramic Society*, 2018, **38**(1), P. 227–234.

[13] Colomer M.T., Díaz-Guillén J.A., Fuentes A. Nanometric Sr-Doped $LaPO_4$ Monazite: Synthesis by Mechanical Milling, Characterization, and Water Incorporation on its Structure. *Journal of the American Ceramic Society*, 2010, **93**(2), P. 393–398.

[14] Sankar S., Raj A.N., Jyothi C.K., Warrier K.G.K., Padmanabhan P.V.A. Room temperature synthesis of high temperature stable lanthanum phosphate-yttria nano composite. *Materials Research Bulletin*, 2012, **47**, P. 1835–1837.

[15] Shijina K., Sankar S., Midhun M., Firozkhan M., Nair B.N., Warrier K.G., Hareesh U.N.S. Very low thermal conductivity in lanthanum phosphate-zirconia ceramic nanocomposites processed using a precipitation-peptization synthetic approach. *New J. Chem.*, 2016, **40**, P. 5333–5337.

[16] Kim J., Cotte A., Deloncle R., Archambeau S., Biver C., Cano J.-P., Lahlil K., Boilot J.-P., Grelet E., Gacoin T. $LaPO_4$ Mineral Liquid Crystalline Suspensions with Outstanding Colloidal Stability for Electro-Optical Applications. *Adv. Funct. Mater.*, 2012, **22**(23), P. 4949–4956.

[17] Kim J., Martinelli L., Lahlil K., Boilot J.-P., Gacoin T., Peretti J. Optimized combination of intrinsic and form birefringence in oriented $LaPO_4$ nanorod assemblies. *Applied Physics Letters*, 2014, **105**(6), P. 061102.

[18] Kim J., Michelin S., Hilbers M., Martinelli L., Chaudan E., Amselem G., Fradet E., Boilot J.-P., Brouwer A.M., Baroud C.N., Peretti J., Gacoin T. Monitoring the orientation of rare-earth-doped nanorods for flow shear tomography. *Nature Nanotechnology*, 2017, **12**(9), P. 914–919.

[19] Riwotzki K., Meyssamy H., Kornowski A., Haase M. Liquid-Phase Synthesis of Doped Nanoparticles: Colloids of Luminescing $LaPO_4$:Eu and $CePO_4$:Tb Particles with a Narrow Particle Size Distribution. *J. Phys. Chem. B*, 2000, **104**(13), P. 2824–2828.

[20] Hay R.S., Boakye E.E., Mogilevsky P. Spherical Rhabdophane Sols. I: Rheology and Particle Morphology. *J. Am. Ceram. Soc.*, 2007, **90**(5), P. 1574–1579.

[21] Gavrichev K.S., Ryumin M.A., Tyurin A.V., Khoroshilov A.V., Mezentseva L.P., Osipov A.V., Ugolkov V.L., Gusarov V.V. Thermal behavior of $LaPO_4 \cdot nH_2O$ and $NdPO_4 \cdot nH_2O$ nanopowders. *Journal of Thermal Analysis and Calorimetry*, 2010, **102**, P. 809–811.

[22] Maslennikova T.P., Osipov A.V., Mezentseva L.P., Drozdova I.A., Kuchaeva S.K., Ugolkov V.L., Gusarov V.V. Synthesis, mutual solubility, and thermal behavior of nanocrystals in the $LaPO_4$-YPO_4-H_2O system. *Glass Physics and Chemistry*, 2010, **36**(3), P. 351–357.

[23] Sankar S., Prajeesh G.P.V., Anupama V.N., Krishnakumar B., Hareesh P., Nair B.N., Warrier K.G., Hareesh U.N.S. Bifunctional lanthanum phosphate substrates as novel adsorbents and biocatalyst supports for perchlorate. *Journal of Hazardous Materials*, 2014, **275**, P. 222–229.
[24] Bryukhanova K.I., Nikiforova G.E., Gavrichev K.S. Synthesis and study of anhydrous lanthanide orthophosphate (Ln = La, Pr, Nd, Sm) nanowhiskers. *Nanosystems: Phys. Chem. Math.*, 2016, **7**(3), P. 451–458.
[25] Byrappa K., Murukanahally Kempaiah Devaraju, Paramesh J.R., Basavalingu B., Soga K. Hydrothermal synthesis and characterization of $LaPO_4$ for bio-imaging phosphors. *Journal of Materials Science*, 2008, **43**(7), P. 2229–2233.
[26] Colomer M.T., Zur L., Ferrari M., Ortiz A.L. Structural-microstructural characterization and optical properties of Eu^{3+}, Tb^{3+}-codoped $LaPO_4 \cdot nH_2O$ and $LaPO_4$ nanorods hydrothermally synthesized with microwaves. *Ceramics International*, 2018, **44**, P. 11993–12001.
[27] Colomer M.T., Delgado I., Ortiz A.L., Farinas J.C. Microwave-assisted Hydrothermal Synthesis of Single-crystal Nanorods of Rhabdophane-type Sr-doped $LaPO_4 \cdot nH_2O$. *J. Am. Ceram. Soc.*, 2014, **97**(3), P. 750–758.
[28] Runowski M., Grzyb T., Zep A., Krzyczkowska P., Gorecka E., Giersig M., Lis S. Eu^{3+} and Tb^{3+} doped $LaPO_4$ nanorods, modified with a luminescent organic compound, exhibiting tunable multicolour emission. *RSC Adv.*, 2014, **4**, P. 46305–46312.
[29] Stankiewicz A.I., Moulijn J.A. Process intensification: Transforming chemical engineering. *Chem. Eng. Prog.*, 2000, **96**(1), P. 22–34.
[30] Marchisio D.L., Rivautella L., Barresi A.A. Design and Scale-Up of Chemical Reactors for Nanoparticle Precipitation. *AIChE Journal*, 2006, **52**(5), P. 1877–1887.
[31] Kumar R.D.V., Prasad B.L.V., Kulkarni A.A. Impinging Jet Micromixer for Flow Synthesis of Nanocrystalline MgO: Role of Mixing/Impingement Zone. *Ind. Eng. Chem. Res.*, 2013, **52**, P. 17376.
[32] Abiev R.Sh., Al'myasheva O.V., Gusarov V.V., Izotova S.G. Method of producing nanopowder of cobalt ferrite and microreactor to this end. RF Patent 2625981, Bull. N 20, 20.07.2017. https://patents.google.com/patent/RU2625981C1/en.
[33] Abiev R.S., Almyasheva O.V., Izotova S.G., Gusarov V.V. Synthesis of cobalt ferrite nanoparticles by means of confined impinging-jets reactors. *J. Chem. Tech. App.*, 2017, **1**(1), P. 7–13.
[34] Proskurina O.V., Nogovitsin I.V., Il'ina T.S., Danilovich D.P., Abiev R.Sh., Gusarov V.V. Formation of BiFeO3 Nanoparticles Using Impinging Jets Microreactor. *Russian Journal of General Chemistry*, 2018, **88**(10), P. 2139–2143.
[35] Johnson B.K., Prud'homme R.K. Chemical Processing and Micromixing in Confined Impinging Jets. *AIChE Journal*, 2003, **49**(9), P. 2264–2282.
[36] Ba-ldyga J., Jasińska M., Orciuch W. Barium Sulphate Agglomeration in a Pipe – An Experimental Study and CFD Modeling. *Chemical Engineering & Technology*, 2003, **26**(3), P. 334–340.
[37] Kenges K.M., Proskurina O.V., Danilovich D.P., Aldabergenov M.K., Gusarov V.V. Influence of the Conditions for Preparing $LaPO_4$-Based Materials with Inclusions of the LaP_3O_9 Phase on Their Thermal and Mechanical Properties. *Russian Journal of Applied Chemistry*, 2018, **91**(9), P. 1539–1548.
[38] Colomer M.T. Effect of Sr^{2+} doping on sintering behavior, microstructural development and electrical properties of $LaPO_4 \cdot nH_2O$ nanorods prepared by dry mechanical milling. *International Journal of Hydrogen Energy*, 2018, **43**(29), P. 13462–13474.
[39] Colomer M.T., Mosa J. Thermal Evolution, Second Phases, and Sintering Behavior of LaPO4nH2O Nanorods Prepared by Two Different Chemical Synthesis Routes. *Ceramics International*, 2015, **41**(6), P. 8080–8092.
[40] Podval'naya N.V., Zakharova G.S., Liu Y. Phase Formation in the System $Zn(VO_3)_2$-HCl-$VOCl_2$-H_2O. *Russian Journal of Inorganic Chemistry*, 2017, **62**(8), P. 1104–1110.
[41] Krasilin A.A., Gusarov V.V. Redistribution of Mg and Ni cations in crystal lattice of conical nanotube with chrysotile structure. *Nanosystems: Phys. Chem. Math.*, 2017, **8**(5), P. 620–627.
[42] Zhou G. Study of hydrothermally synthesized $LiFePO_4$ with different morphology. *Russian Journal of Applied Chemistry*, 2017, **90**(9), P. 1519–1523.
[43] Mashentseva A.A., Kozlovskiy A.L., Turapbay K.O., Temir A.M., Seytbaev A.S., Zdorovets M.V. Determination of Optimal Conditions for Electoless Synthesis of Copper Nanotubes in the Polymer Matrix. *Russian Journal of General Chemistry*, 2018, **88**(6), P. 1213–1218.
[44] Botman S.A., Leble S.B. Electrical conductivity model for quasi-one-dimensional structures. *Nanosystems: Phys. Chem. Math.*, 2017, **8**(2), P. 231–235.
[45] Herschel W.H., Bulkley R. Measurement of consistency as applied to rubber-benzene solutions. *Am. Soc. Test. Proc.*, 1926, **26**, P. 621–633.
[46] Schramm G. *A Practical Approach to Rheology and Rheometry*. 2-nd Ed. Gebrueder HAAKE GmbH, Karlsruhe, 2000, 291 p.

NANOSYSTEMS: PHYSICS, CHEMISTRY, MATHEMATICS, 2019, 10 (2), P. 215–226

Electron microscopy of biogenic minerals: structure and sizes of uranium dioxide nanoparticles with Mn^{2+} impurities

E. I. Suvorova

A. V. Shubnikov Institute of Crystallography, Federal Scientific Research Centre "Crystallography and Photonics" of Russian Academy of Sciences, Leninsky pr., 59, 19333 Moscow, Russia

suvorova@crys.ras.ru

PACS 61.46.Df, 68.37.Lp, 87.17.-d **DOI 10.17586/2220-8054-2019-10-2-215-226**

Methodological aspects of the extraction of structural and chemical information from transmission electron microscopy (TEM) of uranium dioxide (UO_2) biogenic nanoparticles are presented. Nanoparticles were formed via the bacterial reduction of water-soluble uranyl acetate with U (VI) in the presence of Mn^{2+} ions and cultures *Shewanella oneidensis* MR-1 in the medium. The particles of 1.2 – 3.5 nm in diameter and particle agglomerations were visualized in conventional TEM, high resolution TEM, scanning TEM modes. Their phase and chemical composition were investigated with electron diffraction, X-ray energy dispersive spectrometry and electron energy loss spectroscopy with high spatial resolution. Maintenance of the element balance helped to find the composition of the mixture of UO_2 and Mn acetates. The interpretation of TEM data and modeling allowed to propose the mechanism for the suppression of UO_2 particle growth and higher resistance to dissolution of smaller UO_2 particles with adsorbed Mn acetate compared to the larger pure particles.

Keywords: uranium dioxide nanoparticles, bacterial reduction, manganese impurity, transmission electron microscopy.

Received: 10 February 2019

Revised: 21 March 2019

1. Introduction

One of the primary reasons for investigating the biogenic minerals is to better understand the mechanism of interaction of living organisms and inorganic materials [1]. A direct involving of bacteria in the reduction of metals and metalloids (iron, chromium, uranium, selenium, tellurium and so on) is of considerable interest mainly because of the potential application in the treatment and bioremediation of uranium-contaminated groundwater. The basis of such treatment is the transformation of highly soluble U(VI) salts to sparingly soluble uranium (IV) oxide, uraninite. However, the strategy can be successful if the biogenic uraninite remains immobilized and does not easily oxidize [2]. Therefore, the structure and morphology of biogenic minerals, as well the impurity effect, have been and remain a subject of close attention with a view to addressing problems in fundamental and applied science and in technology.

The presence of different impurities has the potential to complicate the remediation process: change the rates of uranium transformations, influence the size and shapes of precipitated particles, enhance or inhibit dissolution and oxidation of the U(IV) oxide biogenic mineral. Manganese (Mn) is the 10th most abundant element in the Earth's crust and second only to iron as the most common heavy metal and Mn(II) is readily depleted from igneous and metamorphic rocks by interactions with surface water and groundwater being highly mobile in acidic aqueous systems [3]. Mn (II) presented in groundwater is considered a pollutant mainly because of their organoleptic properties [4]. Therefore, there is a request to develop environmentally friendly ways to remove Mn from water. In this regard, the combination of redox and adsorption processes is very attractive for removing two ions U(VI) and Mn(II) simultaneously.

Among all the methods available for the study of small particles, analytical transmission electron microscopy (TEM) offers possibilities for visualization in conventional TEM, high resolution TEM (HRTEM), scanning TEM (STEM) modes, investigation of phase (electron diffraction) and element composition (X-ray energy dispersive spectrometry, EDS), determination of chemical and oxidation state (electron energy loss spectroscopy, EELS) of individual particles of a few nm size, their agglomerations and mixtures of different phases with high spatial resolution. Severe requirements are imposed on thickness of TEM specimens. Clearly interpretable data can be obtained only for thin samples with a thickness of less than 50 nm and in some cases (for instance, using high-resolution methods) the thickness of the samples should not exceed 10 nm. The electron radiation effect on biogenic minerals can be a big issue. Small particles can change their shape and size, and such changes depend on both the time of irradiation and the intensity of the beam. The electron damage affects the structure and/or the chemistry of specimens when inelastic scattering (heating) breaks the chemical bonds (radiolysis) [5].

In this work, the particular interest was in identifying and characterizing the uranium-containing compound produced by metal-reducing bacteria in the presence of Mn impurities using TEM, electron diffraction, X-ray EDS and EELS. An additional objective is to provide insight methodological aspects, revisiting the TEM data coupling with electron diffraction simulation and structure modeling to propose the mechanism of higher resistance of smaller uraninite particles with adsorbed Mn acetate compared to the larger pure UO_2 particles.

2. Materials and methods

2.1. Cell cultures

Biogenic samples were prepared under anoxic conditions at École Polytechnique Fédérale de Lausanne (EPFL), Switzerland. All details of preparation of bacterial cultures (*Shewanella oneidensis* MR-1) for reduction of U(VI) and chemical experiments are given elsewhere [6–9].

2.2. Reduction of U(VI) in the presence of Mn impurities

A colony of *Shewanella oneidensis* MR-1 was grown in LB medium (water, peptide tryptone, yeast extract and NaCl). Reduction of U(VI) from uranyl acetate was carried out at pH 6.3 within 12 h for most of the conditions. The $MnCl_2$ solution was added to adjust to 0.1, 0.25, 0.5, 1.0, 2.5, 5.0 and 8.0 mM concentrations.

The cells and resulting nanoparticles were collected by centrifugation. The resulting pellet was washed with anoxic H_2O. Some part of samples was treated with 1 M NaOH to remove the biomass and 0.5 M $NaHCO_3$ to remove remaining adsorbed U(VI) as much as possible. Thus, the two main types of samples were investigated using TEM: samples containing cells and nanoparticles, and samples containing nanoparticles only. Mn^{2+} adsorbed on the particle surface and weakly bound to it was rinsed off using 25 ml of 20 mM MES (2-(N-morpholino) ethanesulfonic acid) buffer at pH 5. More details on specimen treatments and chemicals can be found elsewhere [7, 8].

2.3. Transmission electron microscopy

Samples for TEM study were prepared by drying the colloids of cells with particles on a carbon-coated copper grid (whole mount specimens) or as 50 – 80 nm slices of epoxy (Araldite, Epon or DER resin) with embedded cells and particles. In the latter case, bacterial specimens after reduction were fixed in 2.5 % glutaraldehyde and sequentially dehydrated in pure grade ethanol series (from 25 % to 100 %). The dehydrated cells with nanoparticles were collected by centrifugation and embedded in Araldite resin or Epon resin, then polymerized. The thin slices of polymerized resin were cut with an ultramicrotome using a diamond knife and then placed on copper grids with porous carbon films.

The structure and chemical composition of the particles were studied by conventional TEM, HRTEM, STEM, selected area electron diffraction (SAED), X-ray EDS and EELS in a CM300UT FEG (300 kV field emission gun, 0.65 nm spherical aberration, and 0.17 nm resolution at Scherzer defocus) and a Tecnai Osiris (200 kV high brightness XFEG, 0.24 nm point resolution, a-twin pole piece with Super-X EDX).

The TEM/HRTEM and EEL spectra images were processed with the Gatan Digital Micrograph software. The X-ray EDS microanalysis was performed in STEM mode and quantitative data were derived with the help of INCA (Oxford) and ESPRIT software (Bruker). Quantitative EDS analysis was carried out using the Cliff–Lorimer standard-less method at the nanoscale with thickness correction [5] and in this work were done assuming several possible thickness values from 0 to 60 nm.

The simulation and interpretation of SAED patterns and diffractograms (Fast Fourier transforms) of HRTEM images and structure modeling were performed with the JEMS software package [10] using the known crystal structures and atom positions, electron-optic parameters of the microscopes. The measurement errors in electron diffraction patterns and HRTEM images were about 5 % and 2 %, correspondingly.

3. Results and discussion

3.1. Imaging and composition of the biogenic minerals

The (S)TEM images showed cells coated by nanoparticles and nanoparticle agglomerations in the extracellular space (Figs. 1 and 2). The chemical and phase composition of biogenic minerals were derived from X-rays energy dispersive spectra (Fig. 1(b) and Fig. 2(c,d)) and SAED patterns (Fig. 1(d) and Fig. 2(b)) obtained from nanoparticles. The (S)TEM images in Fig. 1 obtained from the cells embedded in the resin show particles only in the extracellular space and the STEM image in the Fig. 2 taken from the whole mount sample demonstrates completely covered cells by U oxide particles together with the extracellular agglomerates.

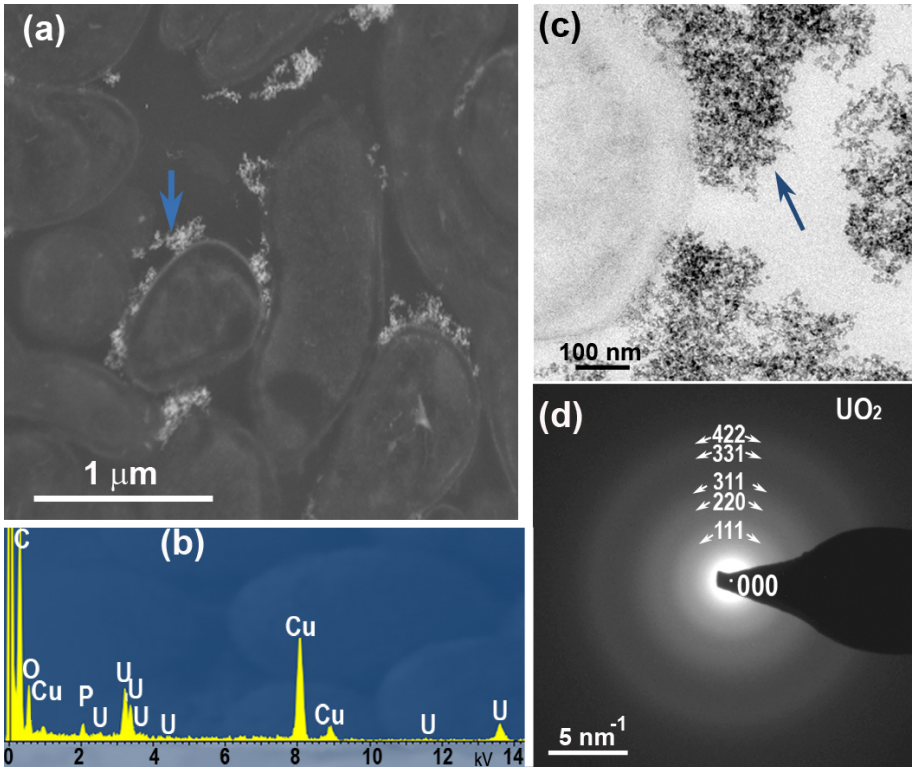

FIG. 1. STEM image of cells and UO_2 nanoparticles in an extracellular space embedded in araldite resin (a), X-ray EDS spectrum obtained from the particle agglomeration indicated by arrows (b), TEM image of one of cells and UO_2 nanoparticles (c) and the corresponding SAED pattern (d) obtained from the particle agglomeration indicated by an arrow in the TEM image.

The following elements were identified by X-ray EDS: U and O in the control sample without impurities (Fig. 1(b)), P comes from cells, C comes from cells and from the carbon support, Cu comes from the TEM grid. Chemical analysis of samples in which manganese chloride was added showed that manganese is mainly localized in agglomerates of UO_2 (Fig. 2(c, d)), where it is almost 10 times larger than on the surface of bacteria. The presence of chlorine from the $MnCl_2$ precursor was not detected in the dried samples because of complete washing out. Elements Fe, Co, Ni (from the microscope material) and Cu (from the supporting grid), which were not included in the samples were deconvoluted during quantitative microanalysis.

The phase composition of minerals is derived quite easily from the experimental SAED patterns which were compared with the simulated ones using JEMS for different U oxides (UO_3, U_3O_8, UO, UO_2 and U_4O_9). Crystallographic parameters for U oxides are listed in Table 1. Analysis showed that the simulated SAED patterns from the UO_2 phase with cubic structure (sp.gr. Fmm, $a = 0.544$ nm) had the best match with the experimental ones despite the broaden rings. The example of such matching is shown in Fig. 2(b). All other oxides (with the exception of UO) should have the reflections closer to the center of the SAED pattern in comparison with the UO_2 phase. However, no evidence has been obtained for the presence of reflections from other U oxides.

Quantitative data obtained from X-ray ED spectra showed a significant amount of oxygen which cannot be explained by the presence of UO_2 only. Thus, the EDS data led to the assumption that Mn oxides (MnO, MnO_2, Mn_3O_4 and Mn_2O_3) or other compounds containing Mn and O are formed. Simulation of ring diffraction patterns from the mixture of UO_2 and some Mn oxides (not presented here) with the crystal parameters listed in Table 1 showed that even for the low content of Mn oxides in mixture of nanoparticles the SAED patterns must contain some reflections closer to the central beam. However the background of experimental SAED pattern corresponded only to the UO_2 ring pattern as well Mn oxide particles were never observed separately from UO_2 agglomerates. Precipitates of Mn oxides are characterized by morphology different from that of uranium oxide particles [26, 27]. In addition, the concentrations of oxygen extracted from EDS data were high and the balance could not be reached with U and Mn oxides. Therefore, it was necessary to find another source of large amounts of oxygen. Among the other compounds, manganese acetates [28, 29] could be the potential candidates.

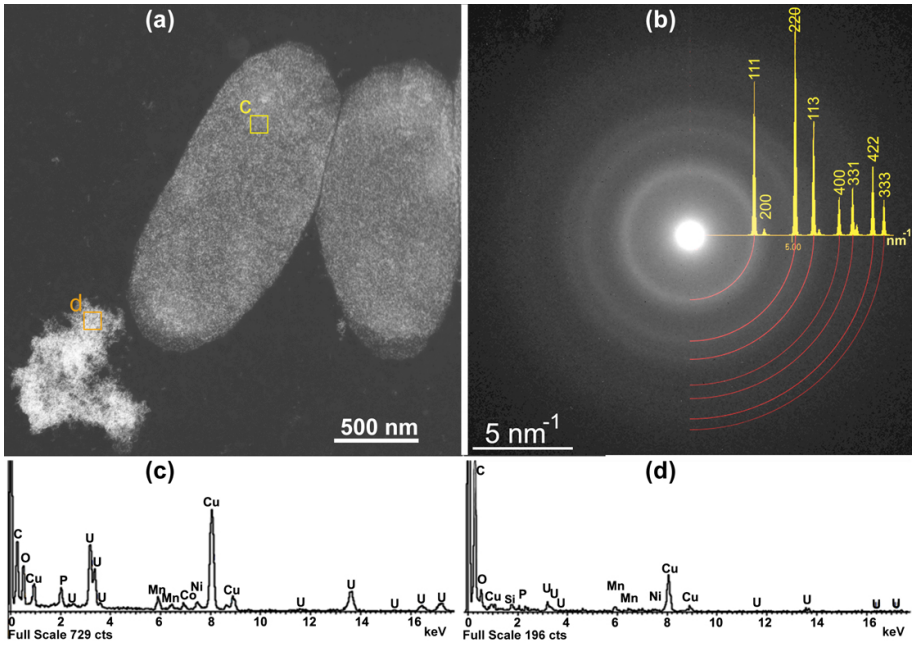

FIG. 2. TEM image of cells covered with UO_2 particles and UO_2 particles with Mn impurities in an extracellular space in a whole mount specimen (a), X-ray EDS spectra obtained from the particle agglomeration and the cell (b and c), SAED pattern obtained from the particle agglomerate (d), UO_2 phase with cubic structure derived using JEMS simulation of the SAED pattern (e)

Acetate ions, being a component of uranyl acetate and one of the major organic acid metabolites [30] after bacterial reduction of U (VI) can interact with Mn^{2+} ions and form hydrated manganese (II) acetates and absorbed on the surface of UO_2 nanoparticles. It is known that simple mono-carboxylates, such as acetate, are able to generate complex extended structures due to the many accessible carboxylate bridging coordination modes [31]. Thus, the heterogeneous medium with UO_2 precipitates facilitates the formation and adsorption of Mn acetates. It also should be noted that in spite that, Mn acetate is considered as water soluble compound (solubility of tetrahydrate and anhydrous Mn acetate is 64.5 g/100 ml and 38.1 100 ml, respectively, at 50 °C) the solubility of $MnCl_2$ is much higher (88.5 g/100 ml at 40 °C) [32, 33] and therefore Cl-ions are much more easily washed out during rinsing with distilled water.

The formation of manganese acetate dihydrate or/and tetrahydrate corresponds well to elemental concentrations expressed in atomic % for the samples of assumed realistic thickness ranged from 10 to 60 nm. The plots (Fig. 3) show the actual oxygen concentrations in at.% depending on thickness for samples containing UO_2 particles with Mn impurities before and after treatment by the NaOH solution. The curve named "remaining oxygen" shows the remaining oxygen concentration of O after subtracting oxygen per uranium dioxide, phosphate group and possible silicon oxide. The lines named "$MnAc_2$ tetra", "$MnAc_2$ dihydr", "$MnAc_2$ anhydr" and "Mn hydroxide" show the oxygen concentration required to satisfy the corresponding stoichiometric formulas of $Mn(CH_3COO)_2 \cdot 4H_2O$, $Mn(CH_3COO)_2 \cdot 2H_2O$, $Mn(CH_3COO)_2$ and $Mn(OH)_2$. The intersection of these lines with the curve of "remaining oxygen" makes it possible to estimate the thickness of the sample.

Thus, the X-ray EDS data helped to maintain the balance of elements in accordance with the stoichiometric formulas to find the composition of a mixture of phases of UO_2 and Mn acetate tetra- or/and dihydrate within the experimental error.

The NaOH treatment of samples can lead to transformation of the part of Mn acetate into Mn hydroxide [34]. However, Mn acetate stays the main component of the adsorption layer and the UO_2 particle shell. This observation is consistent with a well-documented fact of the strong adsorption capacity of Mn^{2+} salts [35].

Figure 4 shows the structure models of UO_2 particles (core) coated by adsorbed manganese acetate tetrahydrate (Fig. 4(a)) on the 2.5-nm carbon film. The profiles of the simulated ring diffraction pattern (Fig. 4(b)) and the simulated ring diffraction patterns (Fig. 4(c)) evidence that the presence of Mn acetates in the given concentrations did not affect the positions of the peaks in electron diffraction patterns and show the good match with the experimental diffraction patterns.

TABLE 1. Crystallographic parameters of U and Mn oxides

Compound	Space group	Parameters [nm]	References
UO_2	Cubic, Fm-3m	$a = 0.547$	[11]
UO	Cubic, Fm-3m	$a = 0.492$	[12]
UO_3	Tetragonal, I41/am	$a = b = 0.6901$, $c = 1.9975$	[13]
U_3O_8	Hexagonal, P-3	$a = b = 0.6815$, $c = 0.4136$	[14]
	Orthorhombic, C222	$a = 0.6704$, $b = 1.195$, $c = 0.4142$	[15]
U_4O_9	Cubic, I-43d	$a = 2.1805$	[16]
MnO	Cubic, Fm-3m Cubic, Fm-3m	$a = 0.441$ $a = 0.454$	[17] [18]
MnO	Hexagonal, P63m	$a = 0.3372$, $c = 0.5386$	[19]
Mn_2O_3	Cub., Ia-3	$a = 0.941$	[20]
Mn_3O_4	Tetragonal, I41/amd	$a = b = 0.5757$, $c = 0.9424$	[21]
	Orthorhombic, Pbca	$a = 0.9412$, $b = 0.9418$, $c = 0.9423$	[22]
MnO_2	Tetr., P 42/mnm	$a = b = 0.4398$, $c = 0.2873$	[23]
	Orthorhombic, Fddd	$a = 1.2207$, $b = 2.0154$, $c = 0.2725$	[24]
	Orthorhombic, Pnma	$a = 0.9273$, $b = 0.2864$, $c = 0.4522$	[25]

The presence of Mn and high content of oxygen in particle agglomeration and nearly the same U/Mn ratio in NaOH treated and untreated samples showed that the tendency of UO_2 particles to strongly agglomerate was preserved as well the major part of manganese acetate was not dissolved. Therefore, the process of biogenic removal of U^{6+} from contaminated water can be efficient also for the simultaneous removal of Mn^{2+} ions.

3.2. EELS characterization

Electron energy loss spectroscopy (EELS) was applied to ascertain if mixed chemical states of uranium (for instance, traces of the remaining U^{6+}) and manganese can be determined after the bacterial reduction.

A typical EEL spectrum for UO_2 (U^{4+}) obtained at room temperature with two U–$M_{5,4}$ edges (3552 eV and 3728 eV, correspondingly) is present in Fig. 5(a). Applying the comparison of the experimental EEL spectra from the biogenic mineral and synthetic UO_2 standard namely M5/M4 white-line ratios [36] led to the conclusion that U^{6+} changed to U^{4+} and UO_2 particles formed.

However, the efforts to determine the valence state of the impurity Mn ion in the presence of large quantity of UO_2 failed. Fig. 5(b) shows the weak U–$N_{7,6}$ edges between 350 and 400 eV and the O–K edge corresponding to the UO_2 phase while Mn–$L_{3,2}$ lines were detected only for the specimens with the highest $MnCl_2$ concentration (8 mM) in the solution. We did not succeed to record clear Mn edges in the specimens with lowest concentration of Mn ion (when the UO_2 particles had the biggest size) [8]. Mn–$L_{3,2}$ lines did not appear in the EEL spectrum due two possible reasons: a very low concentration of Mn ions (0.1 mM in solution) absorbed onto a thick UO_2 particle agglomeration. The increase in Mn concentration allowed detection of the Mn–$L_{3,2}$ edges. However, EELS

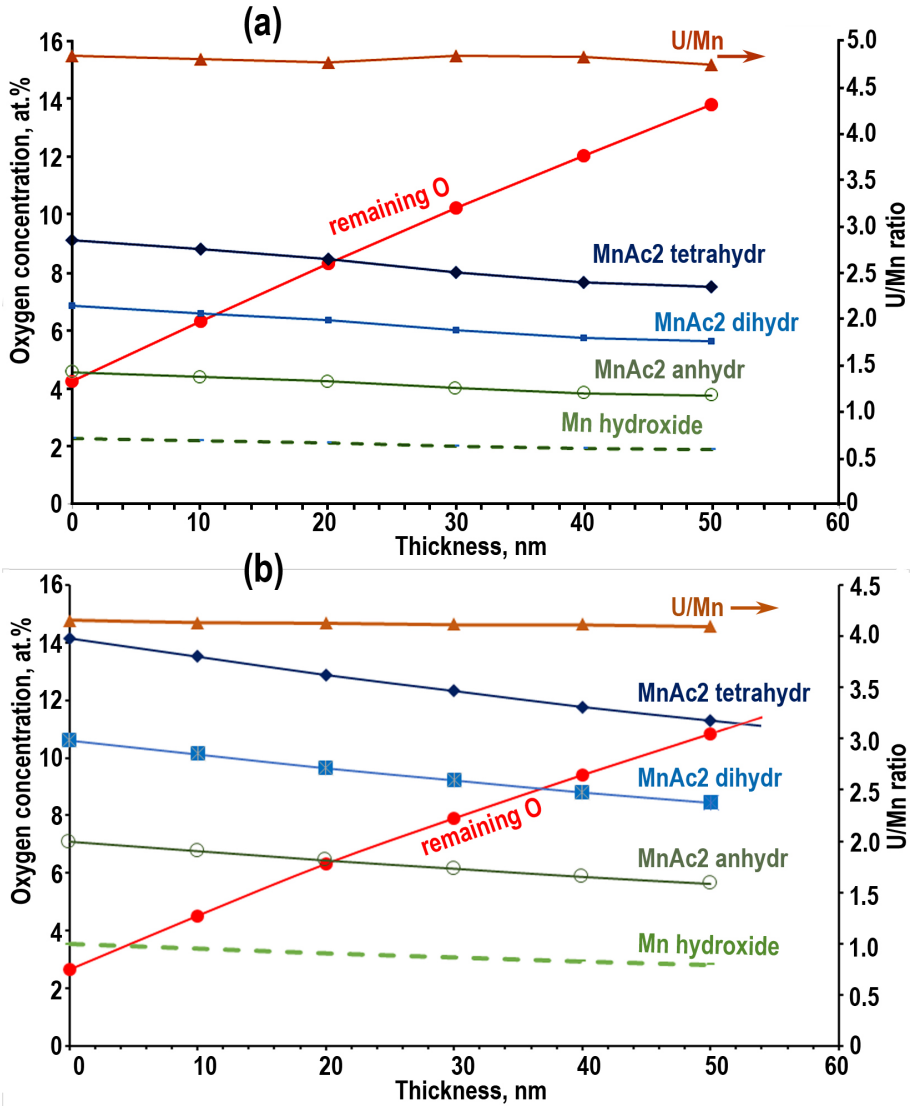

FIG. 3. Oxygen concentration values calculated using absorption correction method in the thickness range from 0 to 60 nm for untreated samples (a) and for NaOH treated samples (b). The ratio U/Mn is nearly constant and equal ≈ 4.7 for untreated samples (a) and ≈ 4.2 for NaOH treated ones (b)

measurements did not give an unambiguous answer to the question of the valence of Mn ions, which, again may be due to the insufficient Mn content and relatively thick UO_2 agglomerated specimens.

The significant effect of sample thickness and carbon on the U oxide spectrum in the low-loss region 0 – 60 eV [37] is shown in Fig. 5(c, d). Spectrum in Fig. 5(c) was obtained from the thick part of the UO_2 particle agglomeration on the carbon support while spectrum in Fig. 5(d) shows the spectrum from the thin part of the agglomeration over a hole in the carbon supporting film.

In contrast to some reports that the electron beam tends to change elemental oxidation state of U during EEL spectra acquisitions [37] we did not observe phase transformations and the appearance of other U phases in detectable quantities.

3.3. Determination of the particle size

One of the main objectives of this study was to determine whether the UO_2 particle sizes change with the addition of Mn impurities. Several techniques were applied to estimate the size of biogenic UO_2 particles. The use of electron diffraction is an indirect way to determine the average size of diffracting grains while (S)TEM imaging

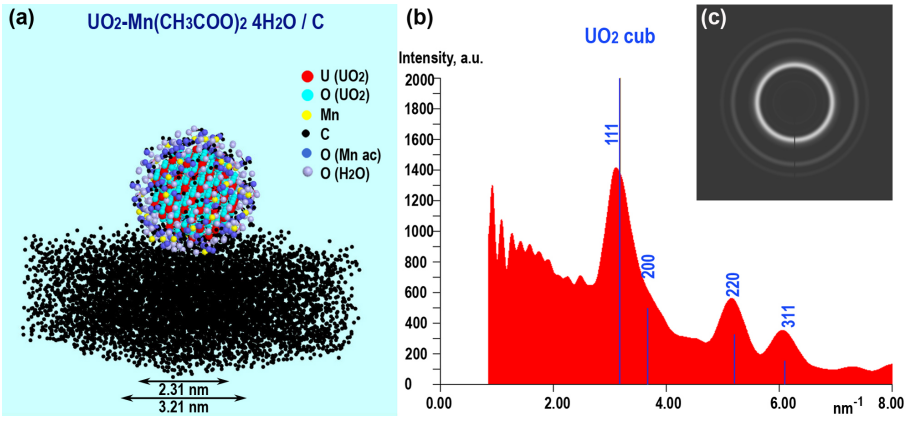

FIG. 4. Structural model of the UO_2 particle of 2.31 nm in diameter (core) coated by $Mn(CH_3CO_2)_2$ tetrahydrate (shell) of 0.9 nm thick on the carbon film of 2.5 nm thick (a), the simulated intensity profile of the diffraction rings with indicated UO_2 reflections (b), the simulated ring diffraction patterns from the $Mn(CH_3CO_2)_2$ tetrahydrate coated UO_2 particles (c)

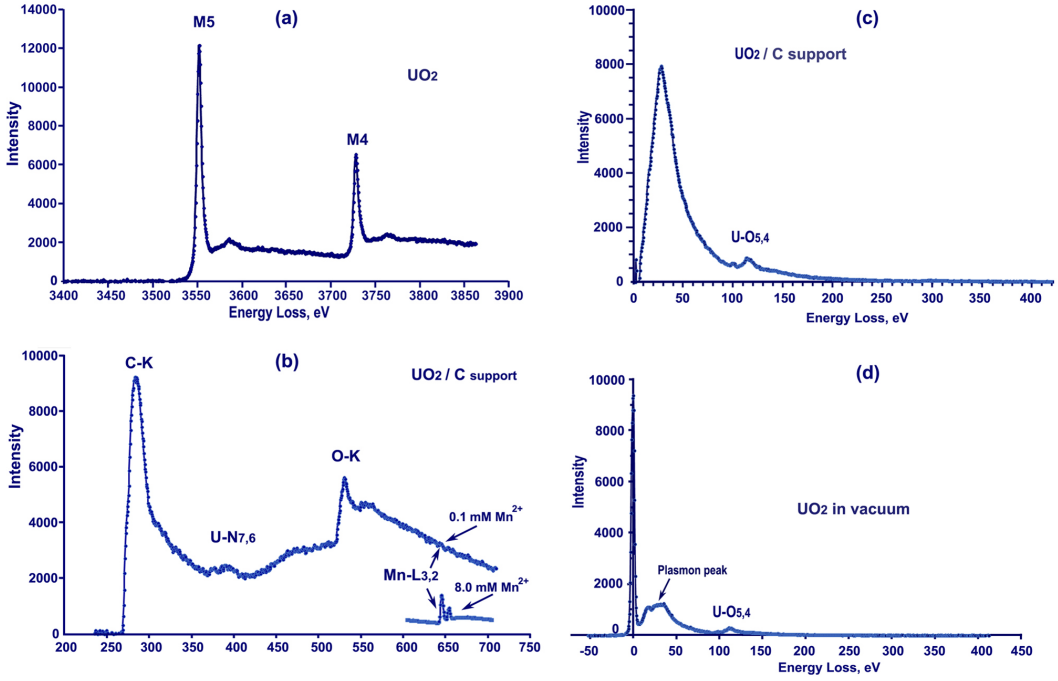

FIG. 5. U–$M_{4,5}$ EEL spectrum after background subtraction for uranium dioxide (a), U–$N_{7,6}$, O–K, C–K and Mn–$L_{3,2}$ (inset) EEL spectrum after background subtraction for uranium dioxide and $MnCl_2$ on a carbon support (b), EEL spectrum obtained from the thick sample on the carbon support (c), EEL spectrum obtained from the thin sample over a hole in the carbon film in vacuum (d)

offers the direct way to measure sizes and particle size distributions. However, measurements using both methods are difficult due to the small particle size and their heavy agglomeration.

The average size of particles can be found by measuring the broadened electron diffraction rings and applying the Scherrer formula. However, if the sizes of the crystal nanoparticles are less than 4 nm, the relative error of the Scherrer formula increases significantly [38]. In this work, the simulation of powder (ring) diffraction patterns for particles with sizes in the range from 3.0 nm to 1.5 nm was performed. Afterwards the profiles of $111 + 200$ rings in experimental electron diffraction patterns were compared with the simulated ones. The 111 reflection was chosen because it is the strongest reflection for UO_2 cubic phase and the corresponding ring is the most intense in

SAED patterns. The other 200 ring is quite close to the 111 ring and both rings start overlapping due to size effect broadening. Therefore, the intensity profile from both reflections were analyzed.

Figure 6 shows the TEM image (Fig. (a)), the corresponding SAED pattern (Fig. 6(b)), the HRTEM image of UO_2 particles (Fig. 6(c)) and the HRTEM FFT (Fig. 6(d)) obtained from the specimen containing 0.5 mM Mn^{2+}. A similar observation is present in Fig. 6(e) for UO_2 particles from the specimen containing 5 mM Mn^{2+}. The intensities of the SAED rings (Fig. 6(f) decrease with the Mn concentrations as well the sizes of particles on the HRTEM image (Fig. 6(g)) also decrease and the rings in the FFTs become practically indistinguishable (Fig. 6(h).

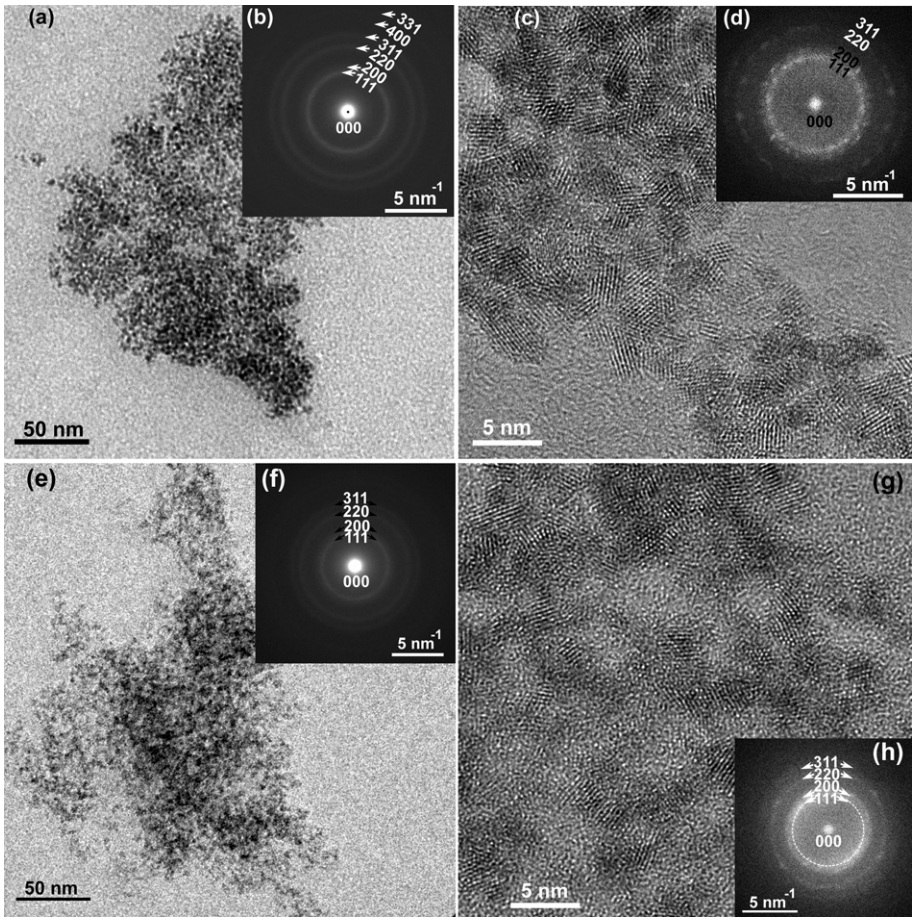

FIG. 6. TEM image of an agglomeration of UO_2 particles with the low concentration of Mn^{2+} impurities (a), ring SAED pattern (b), HRTEM image of UO_2 particles (c), FFT of the HRTEM image of UO_2 particles (d); TEM image of an agglomeration of UO_2 particles with the high concentration of Mn^{2+} impurities (e), ring SAED pattern (f), HRTEM image of UO_2 particles (g), FFT of the HRTEM image of UO_2 particles (h)

Analysis of the intensity profiles from both SAED patterns is shown in Figs. 7 and 8. The corresponding profiles (Figs. 7(b) and 8(b)) were recorded along the directions indicated in the SAED patterns (Figs. 7(a) and 8(a)), the peaks, including the 111 and 200 reflections after polynomial background subtraction, are shown in Figs. 7(c) and 8(c). Finally, fitting the $111 + 200$ simulated peaks (dash lines in Figs. 7(d) and 8(d)) to the experimental ones was obtained for particles with the average size 2.4 nm and 1.9 nm, respectively.

The average particle size (the mode diameter) was also derived from the size distributions obtained from the HRTEM images (Fig. 9(a, c)). In order to recognize the edges of small particles (specimen with higher Mn concentration) the filtered HRTEM image was analyzed (Fig. 9(d)). The smaller the size of the particles, the farther their size distribution from the Gaussian shape (Fig. 9(b, d)), approaching the right skewed lognormal distribution.

The results reported earlier [39] showed that the fastest re-oxidation is characteristic for the smallest (≈ 1.5 nm) biogenic UO_2 particles. Adsorption of Mn acetates on the surface of UO_2 particles and formation of the shell can explain the increase of their stability observed in [6].

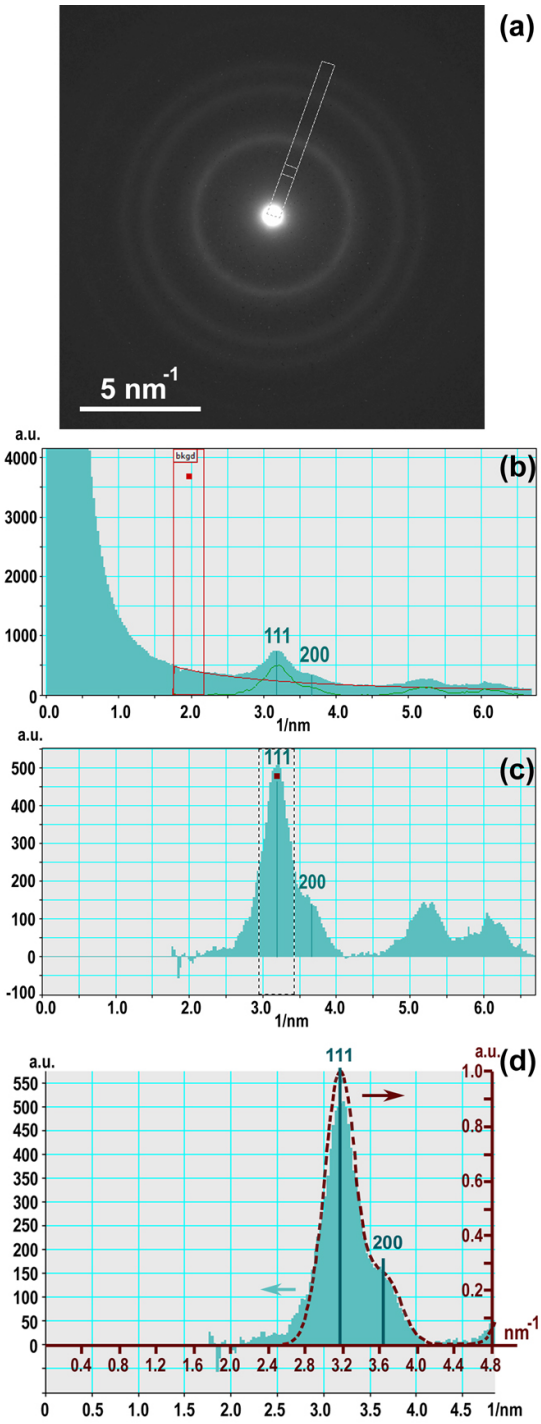

FIG. 7. Ring SAED patterns obtained from UO_2 particles with low Mn^{2+} concentration (a), the corresponding profiles of the SAED rings (b), signal intensity of 111 and 200 reflections after background subtraction (c), fitting the calculated profile of 111 + 200 reflection to the experimental intensity profile (d)

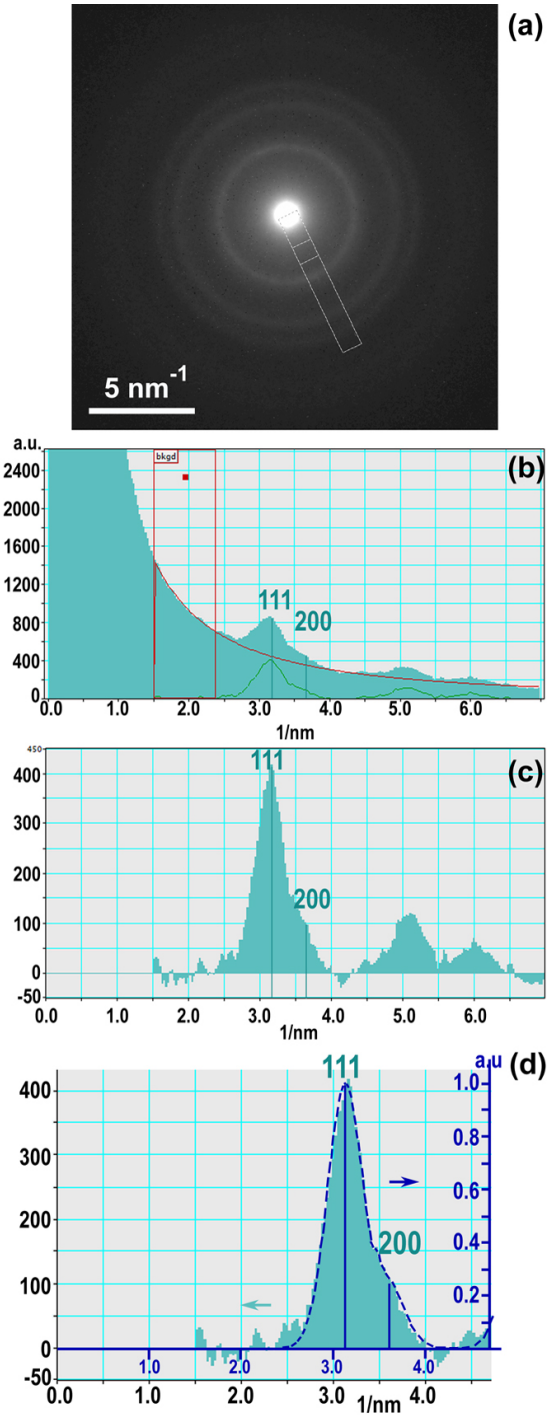

FIG. 8. Ring SAED patterns obtained from UO_2 particles with high Mn^{2+} concentration (a), the corresponding profiles of the SAED rings (b), signal intensity of 111 and 200 reflections after background subtraction (c), fitting the calculated profile of 111 + 200 reflection to the experimental intensity profile (d)

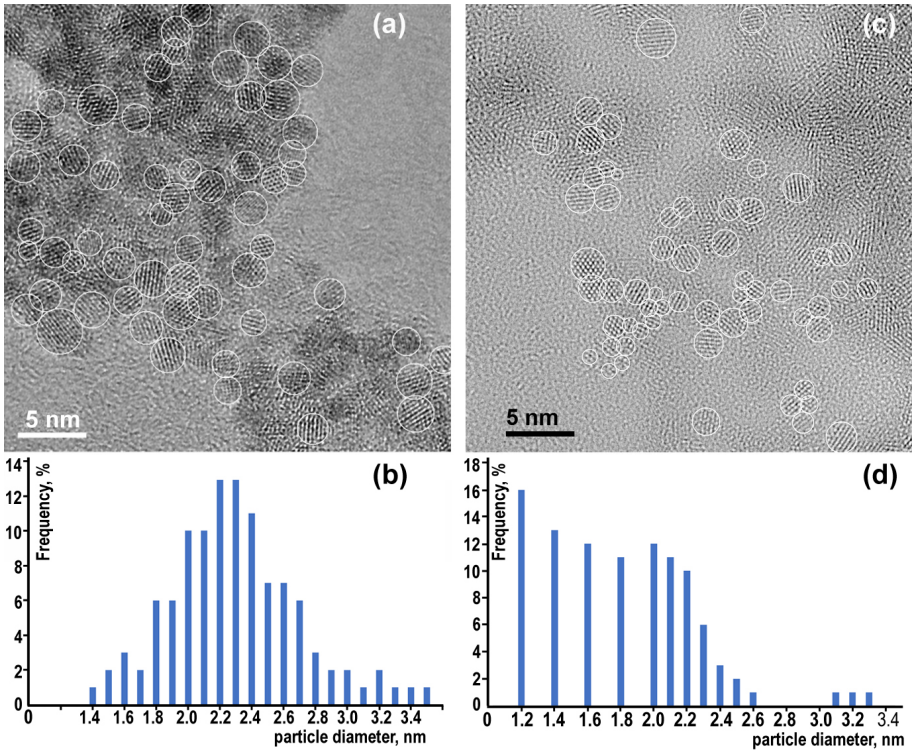

FIG. 9. HRTEM image of counted UO_2 particles with measured sizes with low (a) and high Mn^{2+} concentration (c) and the corresponding histograms (b, d). Histograms were obtained for 100 – 120 particles from several HRTEM images

Burgos et al. [39] reported that estimation of particle sizes with EXAFS (extended X-ray absorption fine-structure spectroscopy) could provide values of about 1.2 nm in diameter and such particles too small to be visualized by TEM what is not entirely true. Modeling the small UO_2 particles and the corresponding simulation of the HRTEM images (Fig. 10) showed that it is possible to visualize particles even smaller than 1 nm using the microscopes without aberration corrections.

The fact is that such small particles are unlikely to survive in solution having the sizes lower than the possible critical nucleus. Simulation of small UO_2 nanoparticles with non-integer number of cells showed a discrete set of sizes and the smallest particles found in HRTEM images had about 1.1 – 1.2 nm in diameter (Fig. 9(a, c)) what correspond to the model with diameter of 1.16 nm. And the next smallest size is about 0.76 nm. Such particles with 4 uranium atoms surrounded by 16 oxygen atoms are unikely to stay independently.

3.4. Effect of the electron beam: Sintering of particles

The efforts to determine the particle size distribution met the problem of the electron irradiation induced sintering. The particle sizes increased with irradiation time or/and beam intensity. Diffractograms from HRTEM images obtained during different exposure time demonstrate the increase of particle size after electron irradiation for 40 s (Fig. 11).

Sintering the UO_2 nanoparticles did not lead to phase transformation and after 5 min of irradiation only 5.0 – 9.0 nm UO_2 irregular particles were found. Mn acetate shells also did not prevent sintering and did not introduce significant effect on the final sizes and phase composition of particles. However, the amount of oxygen lowered due to radiolysis and breaking bounds in Mn acetate structure since the electron diffraction patterns showed the UO_2 cubic structure.

Therefore, low dose and reasonably short exposure time should be used if the final target is to image nanoparticles and estimate their original sizes.

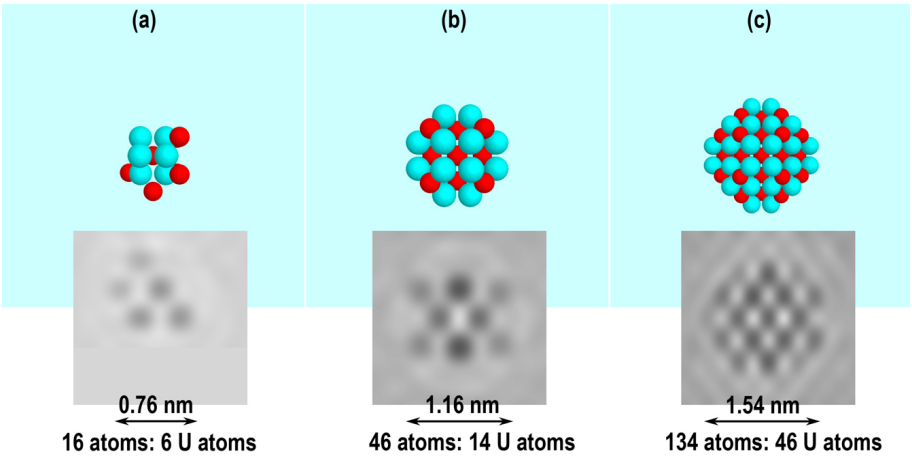

FIG. 10. The structural models of UO_2 particles are built with the help of JEMS (Stadelman, JEMS 2016) with different amount of unit cells embedded in boxes with sizes $2 \times 3 \times 3$ unit cells (a), $3 \times 3 \times 3$ unit cells (b) and $4 \times 4 \times 4$ unit cells (c) with particle diameters 0.76, 1.16 and 1.54 nm respectively. The HRTEM image simulation given under the corresponding model was performed using weak phase object assumption and the following imaging conditions: accelerating voltage 200 kV, spherical aberration coefficient $cs = 1.4$ mm, chromatic aberration coefficient $cc = 1.8$ mm, Scherzer defocus 72.5 nm, energy spread 0.8 eV

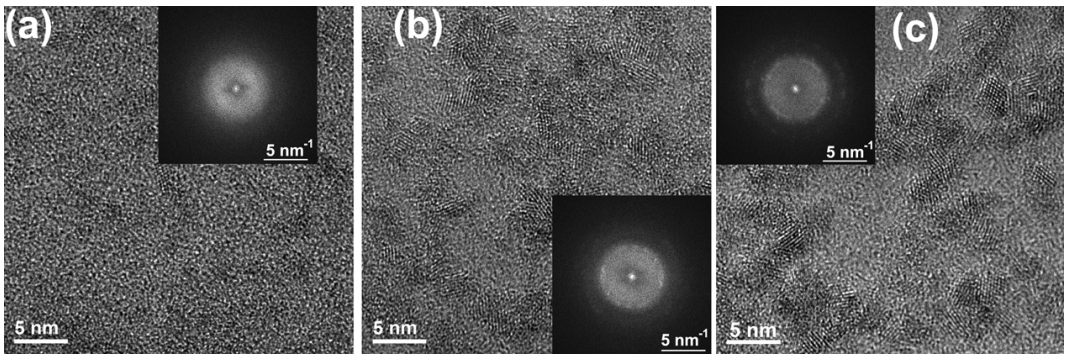

FIG. 11. HRTEM images and FFTs (insets) of UO_2 nanoparticles precipitated in solutions with different concentrations of Mn^{2+} ions: 8.0 mM (a), 1.0 mM (b), 0.1 mM (c)

4. Conclusions

Transmission electron microscopy analyses allowed study of the morphology and structure of biogenic nanoparticles formed during reduction of U(VI) from uranyl acetate using *S. oneidensis* MR-1 in the presence of Mn^{2+} impurities. UO_2 nanoparticles cover the surface of cells and are agglomerated in extracellular space. Their sizes decrease with increase of concentration of impurity Mn^{2+} ions in the solutions. Quantitative X-ray EDS microanalysis showed that Mn acetate tetra- or dihydrate formed and strongly adsorbed on the particle surface, which may explain suppression of UO_2 particle growth and the increase in particle stability and dissolution resistance. The UO_2 particles have a strong tendency to sinter under the electron beam and their size increases markedly while the presence of Mn acetate shell has no effect on the sintering process. Some elongated particles of approximately 8.0 – 9.0 nm long with irregular shape formed during sintering. The UO_2 phase is quite stable under electron beam and does not undergo phase transitions. The process of biogenic removal of U^{6+} from contaminated water can be efficient also for the simultaneous removal of Mn^{2+} ions.

Acknowledgements

All samples were prepared at École Polytechnique Fédérale de Lausanne (EPFL). The help of Prof. Philippe Buffat in discussions of results is acknowledged. This work was also supported by the Ministry of Science and Higher Education of the Russian Federation.

References

[1] Gadd G.M. Microbial influence on metal mobility and application for bioremediation. *Geoderma*, 2004, **122**, P. 109–119.

[2] Newsome L., Morris K., et al. The stability of microbially reduced U(IV); impact of residual electron donor and sediment ageing. *Chemical Geology*, 2015, **409**, P. 125–135.

[3] Post J.E. Manganese oxide minerals: Crystal structures and economic and environmental significance. *Proc. Natl. Acad. Sci. USA*, 1999, **96**, P. 3447–3454.

[4] Taffarel S.R., Rubio J. Removal of Mn^{2+} from aqueous solution by manganese oxide coated zeolite. *Minerals Engineering*, 2010, **23**, P. 1131–1138.

[5] Williams D.B., Carter C.B. *Transmission Electron Microscopy*. A Textbook for Materials Science (Second Ed.), Springer, 2009.

[6] Middleton S.S., Bencheikh Latmani R., et al. Cometabolism of Cr(VI) by *Shewanella oneidensis* MR-1 Produces Cell-Associated Reduced Chromium and Inhibits Growth. *Biotechnology and Bioengineering*, 2003, **83**, P. 627–637.

[7] Schofield E.J., Veeramani H., et al. Structure of Biogenic Uraninite Produced by *Shewanella oneidensis* Strain MR-1. *Environ. Sci. Technol.*, 2008, **42**, P. 7898–7904.

[8] Veeramani H., Schofield E.J., et al. Effect of Mn(II) on the Structure and Reactivity of Biogenic Uraninite. *Environ. Sci. Technol.*, 2009, **43**, P. 6541–6547.

[9] Veeramani H., Alessi D.S., et al. Products of abiotic U(VI) reduction by biogenic magnetite and vivianite. *Geochimica et Cosmochimica Acta*, 2011, **75**, P. 2512–2528.

[10] Stadelmann P. JEMS (Java Electron Microscopy Software); software available at `URL: http://www.jems-saas.ch/`.

[11] Wasserstein B. Ages of uraninites by a new method. *Nature*, 1954, **174**, P. 1004–1005.

[12] Rundle R.E., Baenziger N.C., et al. The Structures of Carbides, Nitrides and Oxides of Uranium. *J. American Chemical Society*, 1948, **70**, P. 99–105.

[13] Loopstra B.O., Taylor J.C., Waugh A.B. Neutron powder profile studies of the gamma uranium trioxide phases. *Journal of Solid State Chemistry*, 1977, **20**, P. 9–19.

[14] Siegel S. The crystal structure of trigonal U_3O_8. *Acta Cryst.*, 1955, **8**, P. 617–619.

[15] Andresen A.F. The structure of U_3O_8 determined by neutron diffraction. *Acta Cryst.*, 1958, **11**, P. 612–614.

[16] Cooper R.I., Willis B.T.M. Refinement of the structure of beta-(U_4O_9). *Acta Cryst. A*, 2004, **60**, P. 322–325.

[17] Levi G.R. The crystal structure of MnO. *Mathematiche e Naturali*, 1924, **57**, P. 619–624.

[18] Radler M.J., Cohen J.B., et al. The defect structures of $Mn_{1-x}O$. *Journal of Physics and Chemistry of Solids*, 1992, **53**, P. 141–154.

[19] Min N.K., Yong-Il K., et al. New crystal structure: synthesis and characterization of hexagonal wurtzite MnO. *Journal of the American Chemical Society*, 2012, **134**, P. 8392–8395.

[20] Klein H., David J. The quality of precession electron diffraction data is higher than necessary for structure solution of unknown crystalline phases. *Acta Cryst. A*, 2011, **67**, P. 297–302.

[21] Baron V., Gutzmer J., Tellgren, R. The influence of iron substitution on the magnetic properties of hausmannite, Mn(2+)(Mn, $Fe)_2(3+)O_4$. *American Mineralogist*, 1998, **83**, P. 786–793.

[22] Norrestam R., *Alpha-manganese (III) oxide – a C-type sesquioxide of orthorhombic symmetry*. Golden Book of Phase Transitions, Wroclaw 2002, **1**, P. 1–123.

[23] Rogers D.B., Shannon R.D., Sleight A.W., Gillson J.L. Crystal chemistry of metal dioxides with rutile-related structures. *Inorganic Chemistry*, 1969, **8**, P. 841–849.

[24] Nuss J., Pfeiffer S., van Smaalen S., Jansen M. Structures of incommensurate and commensurate composite crystals Rb(x)MnO_2 ($x = 1.3711, 1.3636$). *Acta Cryst. B*, 2010, **66**, P. 27–33.

[25] Post J.E., Heaney P.J. Neutron and synchrotron X-ray diffraction study of the structures and dehydration behaviors of ramsdellite and "groutellite". *American Mineralogist*, 2004, **89**, P. 969–975.

[26] Fredrickson J.K., Zachara J.M., et al. Influence of Mn oxides on the reduction of uranium(VI) by the metal-reducing bacterium *Shewanella putrefaciens*. *Geochimica et Cosmochimica Acta*, 2002, **66**, P. 3247–3262.

[27] Saratovsky I., Wightman P.G., et al. Manganese Oxides: Parallels between Abiotic and Biotic Structures. *J. Am. Chem. Soc.*, 2006, **128**, P. 11188–11198.

[28] Bertaut E.F., Duc T.Q., et al. Crystal Structure of Manganese Acetate Tetrahydrate. *Acta Cryst. B*, 1974, **30**, P. 2234–2236.

[29] Cheng C.-Y., Wang S.L. Structure of manganese acetate dihydrate. *Acta Cryst. C*, 1991, **47** (8), P. 1734–1736.

[30] Francis A.J., Dodge C.J., et al. XPS and XANES Studies of Uranium Reduction by *Closfridium* sp. *Environ. Sci. Technol.*, 1994, **28**, P. 636–639.

[31] Martin J.D., Hess R.F. β-$Mn(O_2CMe)_2$: solvothermal synthesis and crystal structure of an unprecedented three-dimensional manganese (II) network. *J. Chem. Soc. Commun.*, 1996, **21**, P. 2419–2420.

[32] Lanovetskiy S.V., Poylov V.Z., Stepanov A.V. Physicochemical Fundamentals of Obtaining High Purity Manganese (II) Acetate Tetrahydrate. *Chemistry for Sustainable Development*, 2012, **20**, P. 173–179.

[33] Linke W.F. *Solubilities, Inorganic and Metal Organic Compounds: A Compilation of Solubility Data from the Periodical Literature*, Band 2, Van Nostrand, 1965.

[34] Wyckoff R.W.G. *Pyrochroite. Crystal Structures 1*, 2nd edition. Interscience Publishers, New York, 1963, P. 239–444.

[35] Taffarel S.R., Rubio J. Removal of Mn^{2+} from aqueous solution by manganese oxide coated zeolite. *Minerals Engineering*, 2010, **23**, P. 1131–1138.

[36] Buck E.C., Fortner J.A. Detecting low levels of transuranics with electron energy loss spectroscopy. *Ultramicroscopy*, 1997, **67**, P. 69–75.

[37] Rice S.B., Bales H.H., Roth J.R., Whiteside A.L. Empirical Identification of Uranium Oxides and Fluorides Using Electron Energy-loss Spectroscopy in the Transmission Electron. *Microscope. Microsc. Microanal.*, 1999, **5**, P. 437–444.

[38] Vorokh A.S. Scherrer formula: estimation of error in determining small nanoparticle size. *Nanosyst. Phys., Chem., Math.*, 2018, **9** (3), P. 364–369.

[39] Burgos W.D., McDonough J.T., et al. Characterization of uraninite nanoparticles produced by Shewanella oneidensis MR-1. *Geochimica et Cosmochimica Acta*, 2008, **72**, P. 4901–4915.

NANO Ф&Х&М

NANOSYSTEMS:

PHYSICS, CHEMISTRY, MATHEMATICS

INFORMATION FOR AUTHORS

The journal publishes research articles and reviews, and also short scientific papers (letters) which are unpublished and have not been accepted for publication in other magazines. Articles should be submitted in English. All articles are reviewed, then if necessary come back to the author to completion.

The journal is indexed in Web of Science Core Collection (Emerging Sources Citation Index), Chemical Abstract Service of the American Chemical Society, Zentralblatt MATH and in Russian Scientific Citation Index.

Author should submit the following materials:

1. Article file in English, containing article title, the initials and the surname of the authors, Institute (University), postal address, the electronic address, the summary, keywords, MSC or PACS index, article text, the list of references.
2. Files with illustrations, files with tables.
3. The covering letter in English containing the article information (article name, MSC or PACS index, keywords, the summary, the literature) and about all authors (the surname, names, the full name of places of work, the mailing address with the postal code, contact phone number with a city code, the electronic address).
4. The expert judgement on possibility of publication of the article in open press (for authors from Russia).

Authors can submit a paper and the corresponding files to the following addresses: nanojournal.ifmo@gmail.com, popov1955@gmail.com.

Text requirements

Articles should be prepared with using of text editors MS Word or LaTex (preferable). It is necessary to submit source file (LaTex) and a pdf copy. In the name of files the English alphabet is used. The recommended size of short communications (letters) is 4-6 pages, research articles– 6-15 pages, reviews – 30 pages.

Recommendations for text in MS Word:

Formulas should be written using Math Type. Figures and tables with captions should be inserted in the text. Additionally, authors present separate files for all figures and Word files of tables.

Recommendations for text in LaTex:

Please, use standard LaTex without macros and additional style files. The list of references should be included in the main LaTex file. Source LaTex file of the paper with the corresponding pdf file and files of figures should be submitted.

References in the article text are given in square brackets. The list of references should be prepared in accordance with the following samples:

[1] Surname N. *Book Title*. Nauka Publishing House, Saint Petersburg, 2000, 281 pp.
[2] Surname N., Surname N. Paper title. *Journal Name*, 2010, **1** (5), P. 17-23.
[3] Surname N., Surname N. Lecture title. In: Abstracts/Proceedings of the Conference, Place and Date, 2000, P. 17-23.
[4] Surname N., Surname N. Paper title, 2000, URL: http://books.ifmo.ru/ntv.
[5] Surname N., Surname N. Patent Name. Patent No. 11111, 2010, Bul. No. 33, 5 pp.
[6] Surname N., Surname N. Thesis Title. Thesis for full doctor degree in math. and physics, Saint Petersburg, 2000, 105 pp.

Requirements to illustrations

Illustrations should be submitted as separate black-and-white files. Formats of files – jpeg, eps, tiff.

NANOSYSTEMS:

PHYSICS, CHEMISTRY, MATHEMATICS

Журнал зарегистрирован
Федеральной службой по надзору в сфере связи, информационных технологий и массовых коммуникаций
(свидетельство ПИ № ФС 77 - 49048 от 22.03.2012 г.)
ISSN 2220-8054

Учредитель: федеральное государственное автономное образовательное учреждение высшего образования
«Санкт-Петербургский национальный исследовательский университет информационных технологий, механики и оптики»

Издатель: федеральное государственное автономное образовательное учреждение высшего образования
«Санкт-Петербургский национальный исследовательский университет информационных технологий, механики и оптики»

Отпечатано в Учреждении «Университетские телекоммуникации»
Адрес: 197101, Санкт-Петербург, Кронверкский пр., 49

Подписка на журнал НФХМ
На второе полугодие 2019 года подписка осуществляется через
ОАО Агентство «Роспечать»
Подписной индекс 57385 в каталоге «Издания органов научно-технической информации»